Non-hydrostatic modelling of large scale tsunamis

Msc. Thesis

P.B. Smit

Caption	:	The Indian Ocean tsunami as it arrives at Koh Jum, Thailand
Cover photograph by	:	A. Grawin (2004)

Title	:	Msc. Thesis Delft University of technology Non-hydrostatic modelling of large scale tsunamis
Author	:	P.B. Smit
Date	:	Oktober 2008
Professor(s)	:	Prof. dr. ir. G.S.Stelling
Supervisor(s)	:	ir. R.J. Labeur ir. J. van Thiel de Vries ir. D. Vatvani

Abstract

The Indian Ocean Tsunami has once again revived the discussion in the tsunami modelling community if the non-linear shallow water equations are a valid model for the propagation of tsunamis. It is suggested that the mechanism of frequency dispersion which is absent in these equations might be important in the correct modelling of large scale tsunamis.

In this master Thesis a non-hydrostatic numerical model based upon the scheme proposed by Stelling and Zijlema (2003) is constructed and it is investigated if it can be an effective and efficient way to include the effect of frequency dispersion in the modelling of tsunamis in their propagation and run-up.

The non-hydrostatic algorithm is incorporated into the existing explicit shallow water solver of XBeach. In this way the model is extended to allow for shorter wave propagation. The main reason for doing this was to show that the employed non-hydrostatic scheme can be easily incorporated as a simple add-on. The depth averaged formulation of the XBeach model prevented an easy extension towards multiple layers but, for a single layer, the addition of the non-hydrostatic pressures was indeed straightforward. No large modifications to the existing code where required.

The numerical model is based on the application of mehrstellen verfahren for the pressure gradients in the vertical. This makes it possible to exactly set the surface pressure to zero which is important for the correct modelling of surface waves. The advective terms have been included in a momentum conservative way based on Stelling and Duinmeijer (2002). This allows for the correct modelling of braking waves.

The resulting 2DV model is validated with analytical solutions available for: (i) an oscillating basin (ii) the propagation of a solitary waves (iii) the run-up of long waves on a beach and (iv) the dambreak solution. Furthermore the model is verified using experimental data by Synolakis (1987) on the run-up of solitary waves on a plane beach. In all cases it is concluded that the results are satisfactory.

The 2DV model is subsequently expanded into a 3D model which is validated with a 3D version of the oscillating basin and verified with the Berkhoff shoal which includes shoaling, refraction and diffraction of waves. A surprising result is that the model using only a single layer is able to satisfactorily reproduce the measurements.

The numerical model is applied to two tsunami benchmark tests conducted by Briggs (1995). The first test consists of the run-up of solitary waves on a vertical wall while the second deals

with the run-up of solitary waves on a conical island. From the first test it is concluded that the model can correctly model these types of waves using only a single layer. Furthermore, when compared to hydrostatic solutions, the model is a dramatic improvement. The over steepening, typical of the non-linear shallow water equations, does not occur.
From the results of the second test it is concluded that the model can accurately predict the inundation heights. However, very fine grids where needed due to the excessive numerical diffusion introduced by the upwind approximations.

It can be concluded that the non-hydrostatic model by Stelling and Zijlema can indeed be an attractive way to include frequency dispersion into large scale tsunami propagation models. It is anticipated that the non-hydrostatic terms add about fifty percent to the duration of a simulation.

Preface and acknowledgements

This thesis concludes the Master of Science program at the faculty of Civil engineering and Geosciences at Delft University of Technology, Netherlands. It was carried out over a period of roughly a year at the section for environmental fluid mechanics.

Working on this master thesis has been very satisfying and, at times, very frustrating. There have been weeks in which little progress was made and weeks in which everything seemed to fall into place. Here I want to thank those who helped me through the rough times with their advise, be it totally wrong, and their support. Thank you Johan, Dirk, Mirza, Martijn and Carolina. I would also like to thank my family, who have always supported me, Sijbrand for the fruitful discussion we had, and the various student assistants and other graduates whom I had the pleasure working with.

Finally I would like to thank the members of my graduating committee and the staff of fluid mechanics for all the support you provided me. I'm afraid you haven't seen the last of me yet.

Delft, November 2008

Pieter Bart Smit

Table of contents

Section I: Introduction

1. Introduction

The December 2004 tsunami in the Indian Ocean has raised public awareness about the dangers this natural phenomenon holds. The enormous damage, loss of life and the human catastrophe in the aftermath of the disaster proved once again the necessity of understanding this phenomenon.

Due to the often complicated bathymetry and the non-linear nature of the mathematical equations involved a principle tool in prediction of tsunami risks are numerical models. Most modern models used to model tsunamis are based upon the depth averaged non-linear shallow water equations (NSWE). In these models vertical accelerations are neglected and the underlying equations are valid for shallow water waves where the wavelengths involved are much larger than the depth. However, the Indian Ocean tsunami revived an old discussion in the tsunami community if the NSWE are sufficiently descriptive of the physics involved to characterize the coastal impact of tsunamis. There is some concern that frequency dispersion, which is absent in the NSWE, might be important.

Frequency dispersion causes waves of different wavelength to travel with different speeds. Generally speaking longer waves will travel with a higher velocity than shorter waves. Besides the wavelength the propagation velocity is also dependent on the depth. Large scale tsunamis usually have wavelengths which are much larger than the water depth. In this case the influence of frequency dispersion becomes physically small and the wave velocity is essentially only dependent on the local water depth. When frequency dispersion is neglected altogether all waves, irrespective of their wavelength, will travel with the same velocity.

One of the first to claim that frequency dispersion might be of importance for the Indian Ocean tsunami was Kulikov (2005). He performed an analysis of satellite altimetry data and his conclusion was that the propagation of the tsunami in the south-western direction was dispersive. Numerical studies performed by Horrillo et al. (2006) and by Grilli et al. (2007) seem to confirm this. They report inundation height differences of up to twenty percent when comparing models based on the NSWE with models which incorporate dispersive behaviour.
Previously Sato (1996), in his study of the 1993 Okushiri Island tsunami found that local tsunami enhancement could be explained by a series of dispersive waves which ride on the main tsunami front. Together with reports by Ortiz et al. (2001), Imamura et al. (1988,1990) and Lui et al. (1995) among others this has revived the discussion in the tsunami community about the validity of the non dispersive NSWE under large scale tsunamis.

The traditional alternative for the NSWE when considering wave propagation are the Boussinesq models which are based on an a priori assumption of the vertical distribution of the horizontal velocity. These models are formulated in a depth averaged way and they are quite efficient for mildly dispersive waves. However, the strongest point of the Boussinesq equations is also their weakness. Wave problems can be efficiently tackled but other non-hydrostatic phenomena can not be modelled.

Besides the Boussinesq models there are also the non-hydrostatic models based on the incompressible Navier-Stokes equations. These models are able to correctly model dispersive waves but have always suffered from the need of a high resolution in the vertical. Traditionally in the order of ten layers are needed to achieve similar results to the depth averaged Boussinesq models.

However, in Stelling and Zijlema (2003) an interesting alternative is presented which is based on the Navier Stokes equations but is tailored towards wave propagation studies. They are able to include dispersive effects similar to a first order Boussinesq model using a depth averaged approach. Furthermore using two layers much shorter waves can also be correctly modelled.

The main advantage with regard to the Boussinesq models is its simplicity. It is conceptually closer to the physics as it is a direct numerical implementation of the Navier Stokes equations. It also allows for a single model to handle wave propagation and other non-hydrostatic effects. Finally, it should be very easy to integrate into an existing explicit shallow water solver.

Most of the applications of this model thus far have been focused on relatively short waves. It would be very interesting to see if this model can efficiently be applied to the problem of tsunami propagation and run-up and form a viable alternative to the Boussinesq equations in these situations. If this is the case it could then be used to further investigate the importance of dispersion under large scale tsunamis.

1.1. Objective

The objective of this study is to construct a non-hydrostatic numerical model based upon the scheme proposed by Stelling and Zijlema (2003) and investigate if it can be an effective and efficient way to include the effect of frequency dispersion in the modelling of tsunamis in their propagation and run-up.

Secondly it is the intention to show that the employed non-hydrostatic scheme can be easily integrated into an existing explicit shallow water solver in the form of an add-on. For this purpose the algorithm is added to the XBeach model.

1.2. Readers guide

In order to fulfil the objective first a study into the importance of dispersion under large scale tsunamis is conducted. This is the subject of **section I**. An introduction into tsunami waves and the relevant physical processes is given in chapter two. In chapter three the importance of frequency dispersion under large scale tsunamis is discussed.

Subsequently the construction of a numerical model which can reproduce the various physical processes found under tsunamis is discussed. **Section II** deals with development of a 2DV numerical model. In chapter four the fundamental equations together with the numerical approximations used are presented. In chapter five the model is validated and verified using various existing analytical solutions and experimental data.

In **section III** the existing model is extended into three dimensions. Chapter six deals with the necessary adaptations and the solutions for some of the problems this raises while chapter seven deals with the verification and validation of the three dimensional model.

In **section IV** the model is applied to two tsunami benchmark cases. Chapter eight deals with the run-up of solitary waves on a vertical wall while chapter nine deals with the run-up of solitary waves on a conical island.

Finally in **section V** the conclusions and recommendations resulting from this study are presented and discussed.

2. Tsunamis

2.1. Introduction

In many respects tsunami waves are similar to common sea waves generated by the wind. They undergo similar physical processes and many conclusions regarding shorter waves are also applicable to tsunami waves. What truly sets them apart from regular waves are their magnitude and in direct relation to this the potential for destruction they hold. Whereas a typical sea wave will have wavelengths in the order tens of metres a large scale tsunami can have a wavelength in the order of a hundred kilometres.

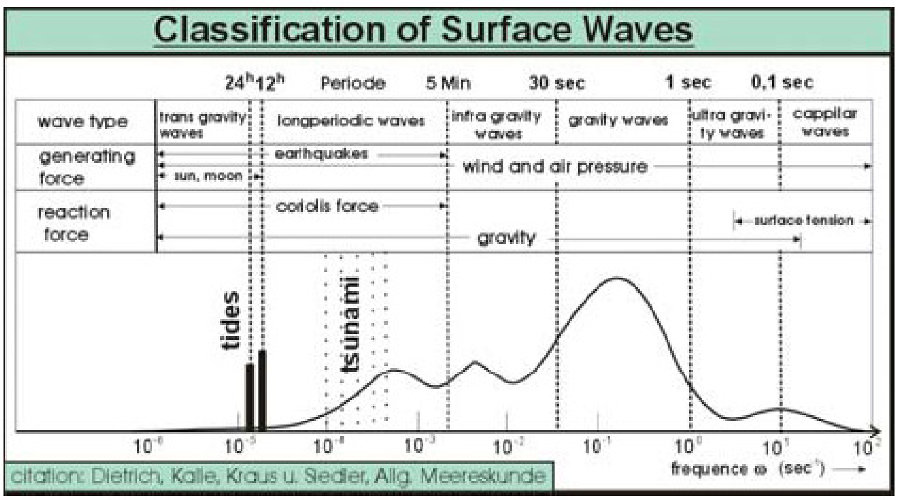

Figure 2-1 Classification of surface waves according to their period. (Kinsman, 1965)

To put them into perspective a classification of surface waves according to their period is given in Figure 2-1. From the figure it is seen that the periods of tsunami waves range from five minutes to twelve hours. This explains why the longer tsunamis used to be referred to as tidal waves.

The word tsunami itself was chosen by oceanographers to prevent confusion with the tides and comes from Japanese where it means "harbour wave". Japanese fishermen often spend the daytime fishing on the deeper parts of the ocean where a tsunami is hardly noticeable, and when they came home they found there villages destroyed. They thus theorized that these large waves only happen in harbours and elsewhere near shore.

This also illustrates that the danger a tsunami poses is not related to its wave height on the ocean, but rather to its wavelength. Due to shoaling a initial small surface elevation of a metre can grow to a massive ten metre high wave near shore. And because they are long waves tsunamis can travel vast differences without loosing significant amounts of energy and wreak havoc on a distant shoreline.

2.1.1. Tsunami sources

The large wavelengths found with tsunamis are a consequence of the way they are generated. While most surface waves are wind generated tsunamis are typically created by sudden shifts in the ocean floor which displace large amounts of water. These could be underwater landslides, volcanic explosion or earthquakes. Due to the often large source areas the wave generated is much larger than a wind generated wave.

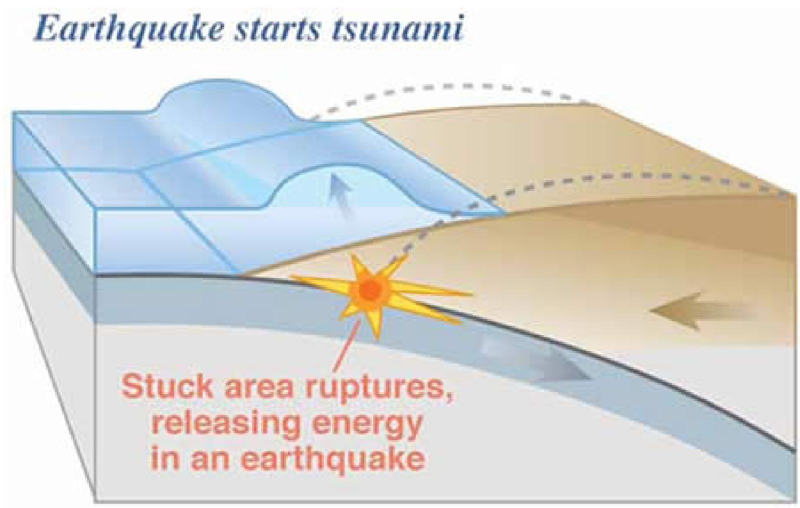

Figure 2-2 Earthquake in a subduction zone causing a tsunami. (NGDC)

Most large scale tsunamis occur in the pacific basin as here the pacific plate collides with the North American, Filipino and Australian plates. In these so called subduction zones one of the plates is forced under the other plate under great tension. The friction between the two plates is enormous causing them to become almost stuck and the upper plate starts to bent. The result is very similar to energy being stored in a spring. At some point the frictional force is no longer large enough to hold back the upper plate and the energy which was accumulated is suddenly released. The upper plate snaps back and raises often several metres displacing millions of cubic metres of water in the process and transferring large amounts of energy. The effect on the water surface is like an instantaneous raise of the water surface.

The Atlantic ocean suffers from far less tsunamis as the tectonic plates move away from each other here, though recently the scientific community has speculated on the potential for large landslide generated tsunamis[1]. The conventional view is that tsunamis caused by either landslides or volcanic eruptions result in waves which have smaller wavelengths. These waves can be extremely destructive locally but, due to the point like source, they quickly loose much of their danger when they propagate over larger distances.

Since the discussion in the tsunami community regarding the importance of dispersion is focused on whether this plays a role under large scale earthquake generated tsunamis these form the main focus of the rest of this study. When the term tsunami is used reference is therefore made to an earthquake generated tsunami, unless stated otherwise.

2.1.2. Historical tsunamis

The occurrence of an tsunami is not as rare as is commonly thought. However, most tsunamis usually go unnoticed as their impact is small. The National Geophysical data center (NGDC) has listed thirteen occurrences of tsunamis in 2007. The tsunami at 1 April near the Solomon Islands was the most deadly one with 57 casualties.

year	Earthquake magnitude	Country	Maximum inundation height	Estimated number of casualties
1906	8.8	Ecuador	5.00	1000
1923	7.9	Japan	12.10	2144
1933	8.4	Japan	29.30	3064
1941	7.6	India	-	5000
1944	8.1	Japan	10.00	1223
1946	8.1	Dom. Rep.	5.00	1790
1946	8.1	Japan	6.60	1362
1960	9.5	Chile	25.00	1260
1976	8.1	Philippines	4.48	2349
1992	7.8	Indonesia	26.20	2500
2004	9.0	Indonesia	50.00	250000

Table 2-1 Tsunamis generated by earthquakes in the last century with more then a thousand casualties.

To illustrate the importance of being able to predict the risk a tsunami poses, an overview of tsunamis with more then a thousand casualties is given in Table 2-1. The actual number of tsunamis that caused damage is far larger than the selected few which are shown here.

[1] There are some claims that, most notably by Davis and Ward (2001), that a landslide tsunami near La Palma might result into a mega tsunami which could seriously affect the eastern seaboard of the United States. However their claims are controversial. See for instance van Nieuwkoop 2007 for a description of the case.

Without any doubt the Indian Ocean tsunami of December 2004 stands out as the most destructive tsunami ever. Besides the enormous amount of casualties the economic damage was well into the billions of US dollars.

2.2. Initially generated waves

The interaction between the sea bottom and the body of water on top can be very complicated locally. The irregularity of the rise, the difference in geographic features along the fault line, and the duration and frequency of the earthquake all contribute to the response of a body of water that finally results in some sort of deformation of the ocean surface. The correspondence between the rise of the sea floor and the (local) rise of the free surface is especially of importance as this sets the initial conditions for the waves which then can be propagated using an appropriate model.

In classical tsunami theory one usually considers the response of the sea surface to a bottom excitation in an ocean of uniform depth. Especially the case of a sudden rise of a block at the bottom has seen extensive investigation using linear theory and experimental verification. In this context especially the investigation by Hammock (1973) has been instrumental in the understanding of this. Here some of his results will be presented in a descriptive manner.

Consider the sudden uniform rise of a section of the ocean floor with a width of B, amplitude of d_0 and a characteristic time scale t_c [1]. Furthermore let the water depth in an undisturbed condition be given by H. The response of the free surface to such an event can be fairly well described by linear theory as was verified experimentally by Hammock and can be characterized by two dimensionless parameters: the ratio between the water depth and the width of the disturbance and the Hammack number.

Starting with the Hammock number that is given by

$$C_h = \frac{t_c}{B / \sqrt{gH}} \tag{2.1}$$

The Hammack number describes the ratio between the time scale of generation and the time scale of propagation out of the disturbed region. For Hammock numbers much larger than one the tsunami leaves the area before the motion of the seafloor has stopped. Since the movement of the ocean floor is relatively slow this type of movement is often referred to as a creeping event.

[1] Let t_c for instance be time necessary to reach two thirds of the final bottom excitation.

For earthquake generated tsunamis where the width of the affected area is usually large and the characteristic time scales small the Hammock number is much smaller than one. In this case the rise of the ocean floor is felt as almost instantaneous by the body of water on top as the disturbance doesn't have time to leave the generation area during the uplift of the seafloor. Ocean floor movements that correspond to small Hammack number are also referred to as impulsive events.

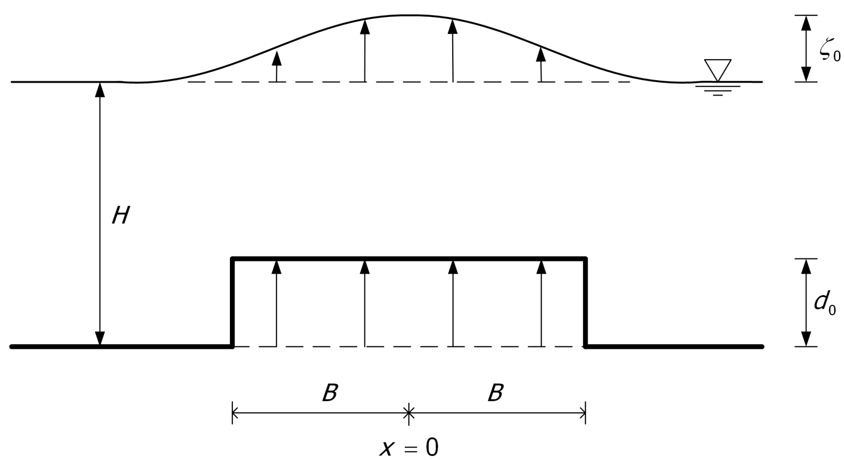

Figure 2-3 The bottom movement is often schematized with a block like shape which suddenly starts to move upward. The resulting free surface is dependent on the upwards velocity , amplitude and width of the block,

The second important parameter is the ratio between the depth of the ocean and the width of the disturbance. For small scale events, where $B/H \ll 1$, the resulting response of the free surface will be much smaller than the amplitude of the bottom excitation. On the other hand for large scale events, where $B/H \gg 1$, the raise of the ocean floor at the centre is essentially translated one to one to the ocean surface.

In Figure 2-4 experimental results from Hammack (1973) are shown that give the relative surface response for different combinations of the relative depth and the Hammack number. Both experimental and theoretical results clearly show that impulsive movements do indeed lead to a larger initial surface response. However, when the size of the source is small compared to the depth, the relative response diminishes considerably. For the smallest width to depth ratio ($b/h \approx 0.61$) found in the figure the maximum response under impulsive conditions is only half of the maximum bottom excitation. Smaller ratios will result in an even smaller response

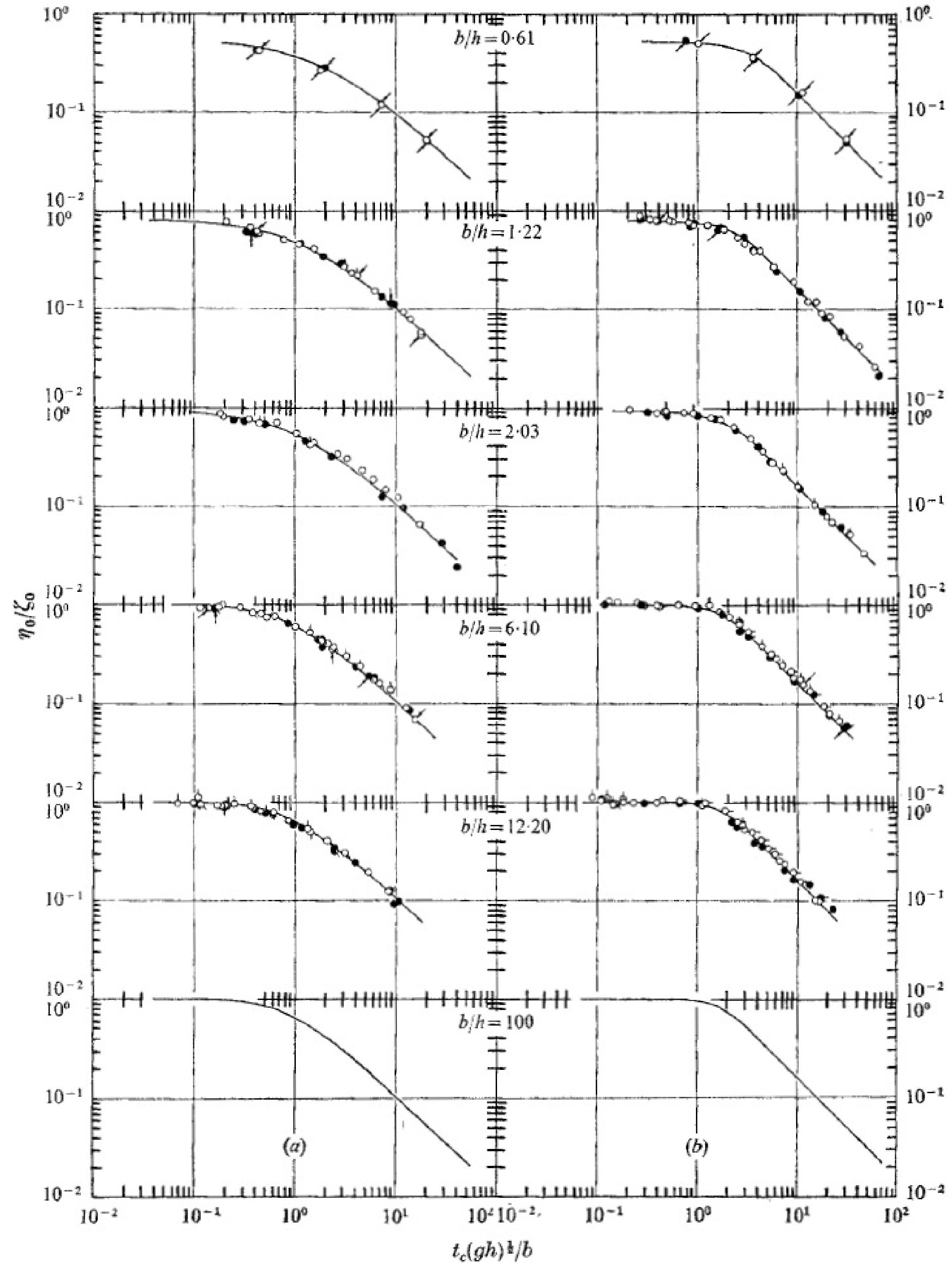

Figure 2-4 Experimental results from Hammack(1973) at the centre of a block like disturbance for different values of the Hammack number and the relative depth. Dots indicate the measured relative surface response while the solid line represents the surface elevation predicted by linear theory. In **(a)** an exponential movements was used while in **(b)** the motion represented half a sine. Be aware that in the graph η_0 is the free surface displacement and ζ_0 the amplitude of the bottom rise.

For large scale events, where the width to depth ratio is much larger then one, the response will be similar to the amplitude of the bottom movement. Note that this only holds for a position right above the centre of the disturbance, at either end the response will roughly be half of the amplitude at the bottom.
A very interesting result from the experiments by Hammack is that the linear theory gives a good approximation of the relative amplitude. This makes the results more easily applicable to real world tsunamis as a superposition of linear solutions is also a solution.

When considering a large scale earthquake the bottom rise will most likely not be uniform along the fault. However, if this is approximated by a combination of block like raises some conclusion regarding the initial wave and its components can still be made. The most important one is that local raises of the sea floor which are substantially larger or smaller than the average raise, but have dimensions smaller than the water depth, will not make a significant contribution to the relative amplitude. From Figure 2-4 it is clearly seen that the response at the free surface reduces for smaller ratios of the width to the depth. Furthermore, due to the smaller width the Hammack number will be much less and although the average bottom raise is impulsive the local bottom raise might be creeping.

Thus although the bottom raise is non-uniform only large scale features, with sizes larger or equal to the water depth, will have a significant impact on the resulting free surface. The sizes of these disturbances can be seen as indicative for the wavelengths they generate. The shortest wavelengths with significant amplitude present in the initial wave will have a size comparable to the local water depth. And more importantly the dominant wave lengths will correspond to the large average movements along the fault. These will therefore have sizes much larger than the water depth.

2.3. Wave propagation

In this section the physical processes involved during the propagation of the tsunami wave trough the ocean and in coastal waters will discussed. The aim of this section is to describe these processes qualitatively and the theory will be presented in a descriptive manner without a formal mathematical derivation. Much of the processes can be justified in a more fundamental manner using either linear wave theory or appropriate non-linear theories. For a more comprehensive introduction into (non-) linear wave theory the reader is referred to Holthuijsen (2007), Dingemans (1997) or Mei (2005).

Although some remarks regarding dispersion under tsunamis will also be presented in this section a full discussion on when this might be important is postponed until the next chapter.

2.3.1. Linear dispersion

One of the most fundamental results from linear wave theory is that it predicts that the frequency of a freely propagating wave component[1] is dependent on the local depth and its wavelength. This essentially means that at each depth there is a one to one relation between the wave period and its corresponding wave length. Such a coupling, which for instance also exists for light waves travelling through a medium, is called a dispersion relation. Linear wave theory predicts that this relation, in the absence of ambient currents, is given by

$$\omega^2 = gk \tanh kH \tag{2.2}$$

Where k is the wave number, ω the angular frequency, g the gravitational acceleration and H the water depth. The wave number and the angular frequency are related to the wave period and wave length by

$$k = \frac{2\pi}{L}, \qquad \omega = \frac{2\pi}{T} \tag{2.3}$$

For very long waves kH is much smaller than one. In this case $\tanh kH \approx kH$ and the dispersion relation reduces to

$$\omega_s^2 = gk^2H \tag{2.4}$$

This is consistent with the expressions found in long wave theory. Linear long waves can therefore be regarded as a limiting case.

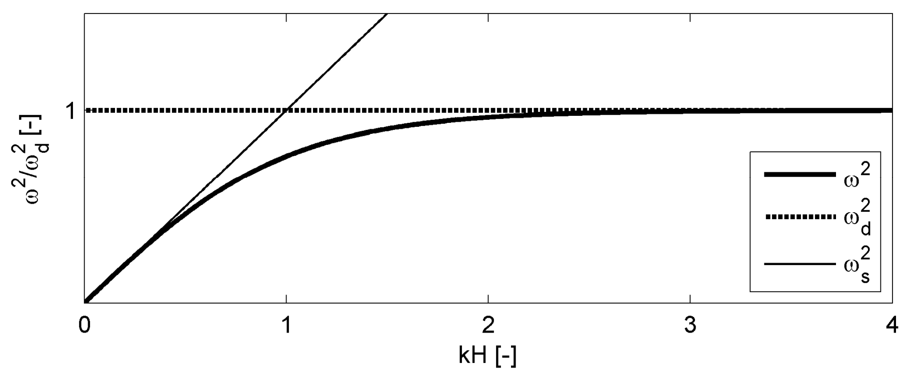

Figure 2-5 A plot of the dispersion relation together with the deep and shallow water limits.

The other useful limit is called the deep water limit and it is applicable to waves which have wavelengths which are much shorter than the depth. In this case kH is much larger than one and the dispersion relation reduces to

---

[1] Note that waves which are subject to external forcing can have arbitrary combinations of the angular frequency and wave number.

$$\omega_d^2 = gk \tag{2.5}$$

Now the waves no longer feel the bottom and the water depth is therefore no longer of influence.

A very interesting consequence of the existence of a dispersion relation is that the wave celerity is now also dependent on the wavelength. Dividing (2.2) by the wave number squared and taking the root results in:

$$c = \sqrt{\frac{g}{k}\tanh kH}\ ,\ c_d = \sqrt{\frac{g}{k}}\ \text{if}\ kH \gg 1\ ,\ c_s = \sqrt{gH}\ \text{if}\ kH \ll 1 \tag{2.6}$$

Where c is the wave celerity, c_s the wave celerity for the shallow water approximation and c_d the deep water approximation. This clearly shows that the deep water wave celerity is fully dependent on the wavelength, while in the shallow water limit the wave celerity is only dependent on the depth.

Since the focus of this study are essentially shallow water waves the main area of interest is the behaviour in the transition zone near the shallow water limit wave. In this transition zone the fundamental difference between the wave celerity approximation of the linear theory and the shallow water approximation is the absence of a dependence of the wavelength in the shallow water limit. Therefore all linear waves travel with the same celerity regardless of their wavelength.

From paragraph **Error! Reference source not found.** it is known that the initial wave only contains wavelengths which are larger or equal to the depth. Furthermore the dominant wavelengths for large scale tsunamis are much larger than the local depth. In this case $kH \ll 1$ and the shallow water approximation seems justified.

2.3.2. Shoaling

Regardless if the shallow water wave theory applies the wave celerity will decrease with decreasing water depth. When approaching the shore the front of the wave will generally speaking be shallower water then the back of the wave. Using c_s as an estimate for the wave celerity the difference in propagation speed between the front and the back of the wave is highlighted in Table 2.

Normally the difference will be less extreme but it highlights an important aspect, the wavelength will decrease due to the speed differential. A consequence of this is that the wave amplitude begins to grow. This process is often referred to as the shoaling and may transform what appears to be a small disturbance in the deep ocean into a ten meter high wave.

	Depth [m]	$c \approx \sqrt{gh}$ [km/h]
Front of wave	100	110
Back of wave	4100	710

Table 2 Difference in propagation speed between the front and back of a tsunami wave propagating over a sloping bottom.

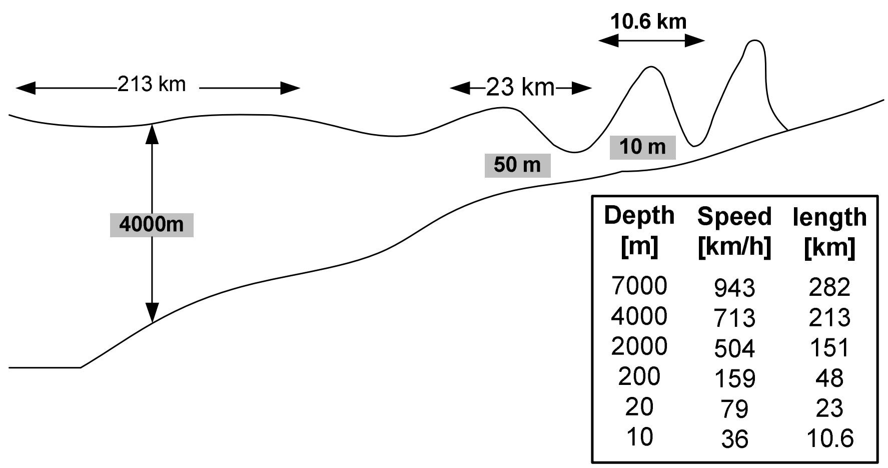

Figure 2-6 As the wave approaches the coastline the length and celerity of the wave decrease while the amplitude increases. This is also known as shoaling.

Near the coast ratio between crest height and depth has grown to such an extent that linear wave theory is no longer applicable and we have to use non-linear approximations.

2.3.3. Refraction

Besides shoaling the wave will also be affected by refraction. Refraction is the tendency of waves to change their direction to a perpendicular orientation towards depth lines. This is caused by the dependency of the wave celerity on the depth.

Refraction occurs due to variations of the wave celerity along wave crests. Parts of the wave crest which are in deeper water will propagate faster than those in shallower water. This causes the waves to turn into a direction perpendicular towards the depth lines. Besides variations in depth currents can also induce wave refraction. Due to refraction the wave energy is redistributed and at places where wave rays converge the wave amplitude increases while at places of diverging wave rays the amplitude decreases (see Figure 2-7).

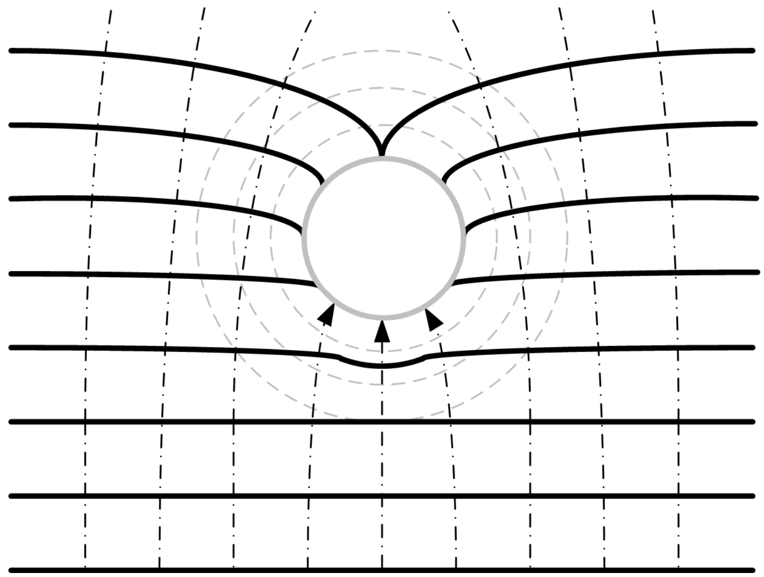

Figure 2-7 Impression of wave refraction around a conical island.

Refraction causes tsunami waves that start out in a direction of travel parallel to a coastline to turn towards the coast. Furthermore refraction can cause parts of the wave to become trapped to the coastline.

2.3.4. Diffraction

Diffraction occurs when waves meet an obstacle in the flow and the crests bend around the obstacle and thus penetrate into the zone to the lee of the obstacle. In Figure 2-8 for instance a breakwater in a region of uniform depth interrupts the incoming wave field.

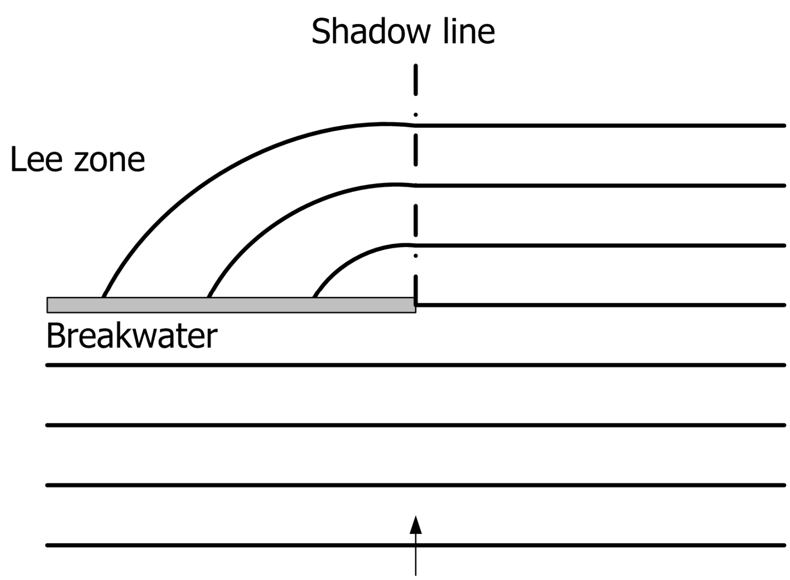

Figure 2-8 Impression of the diffraction of an incoming regular wave field around around a breakwater located in a region of uniform depth.

Due to the breakwater the waves penetrating in the lee zone are significantly reduced in height. In this (academic) case the wave height at the shadow line will be exactly half of the incoming wave height. In the shadow zone the amplitude decreases monotonically with increasing distance from the shadow line.

The degree of diffraction which occurs depends on the ratio of a characteristic lateral dimension of the obstacles and the wave length. For a tsunami this means that only objects of significant length (order of kilometres) will show a significant reduction of wave height on the lee side as for smaller object the tsunami will almost fully diffract around the object. Thus for instance islands with similar or larger length scales than the incoming tsunami wave will have reduced wave height at the lee of the islands.

2.3.5. Non-linear behaviour

In the linear theory of water waves it is assumed that the wave amplitude ζ_0 is small when compared to the total water depth or $\zeta_0 / H \ll 1$. When this is no longer valid another approximation is required which takes the influence of the amplitude into account.

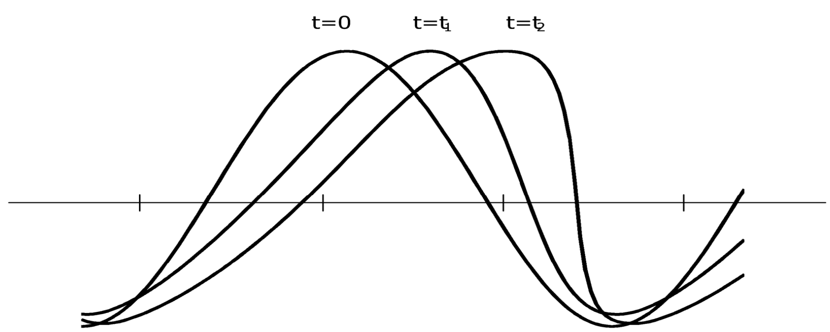

Figure 2-9 When an initial sinusoidal disturbance is propagated with the NSWE the wave will steepen until the front slope has become almost vertical.

The most profound consequence of non-linearity is that parts of the wave itself will now propagate with different speeds, even when travelling over a horizontal bottom. This is most easily shown for a shallow water wave although the results are valid for dispersive waves as well. Lets assume that an initial sinusoidal wave is travelling over a flat section of the bed, furthermore $\zeta_0 / H \approx O(1)$. In this case the troughs of the wave travels with a shallow water celerity $c_{trough} = \sqrt{g(H - \zeta_0)}$ while the tops travels with $c_{top} = \sqrt{g(H + \zeta_0)}$. Assuming an initial wavelength *L*, this means that the distance between a trough leading a top decreases with

$$x_{trough} - x_{top} \sim \tfrac{1}{2} L + \sqrt{gH}\left(\sqrt{\left(1 - \frac{\zeta_0}{H}\right)} - \sqrt{\left(1 + \frac{\zeta_0}{H}\right)}\right) t$$

Since the factor between parentheses is always negative this means that the top of the wave will, in a finite duration, catch up with the trough of the wave. Therefore the front of the wave will steepen until the top has caught up with the trough and the front has become vertical. At that point the wave travels as a discontinuity in the equations and this is often interpreted as the braking of the wave. A result of non-linearity's is thus that higher parts of the wave travel faster than lower parts, and higher waves travel faster than lower waves. This is the reason why it is also referred to as amplitude dispersion.

In the absence of frequency dispersion any sinusoidal wave will in a finite time, even when $\zeta_0 / H \ll 1$, start to steepen and develop into a discontinuity. Therefore the NSWE, which include non-linearity but neglect frequency dispersion, do not have permanent wave forms as a solution.

With the inclusion of frequency dispersion the behaviour will change. Starting again with a sinusoidal disturbance which can safely be approximated with the shallow water theory, the wave again begins to steepen due to the non-linear effects. As it steepens the waveform begins to differ significantly from a sinusoidal wave (see Figure 2-9). In this case steepening of the wave means that a description in Fourier modes needs more harmonics. Thus apart from the initial sinusoidal wave the non-linear effects are the cause of the appearance of higher harmonic components. In the dispersive linear case the higher harmonics, which are shorter, have more dispersion and the waves travel slower than the basic wave. This counteracts the steepening of the wave.

In certain situations the effects of amplitude dispersion and frequency dispersion will balance each other and waves of permanent form become possible. Well know examples of this are Stokes waves, which have sharper higher peaks and shallower troughs, and the cnoidel waves. For a description of these types of waves and the theory behind them the reader is referred to Dingemans (1997) or Mei (2005).

2.4. Leading wave

When considering the initial evolution of a rise of the sea surface it is usually assumed that (1) the surface raise is instantaneous and (2) that the initial horizontal velocity is zero. From this initial disturbance two waves emerge, each travelling in the opposite direction. In Hammack and Segur (1974) the evolution of one of these waves is investigated. When the net volume of displaced water is positive they showed experimentally and theoretically that, eventually, the disturbance will separate into solitary waves with a following dispersive wave train. Interestingly this even occurs for initial profiles which contain a leading depression. An example of some of their experimental results is given in Figure 2-10.

This discovery explains the frequent use of the solitary wave at the off-shore boundary as a model for the leading wave of a far field tsunami. It should be recognized that this model only holds if there is a sufficient propagation distance between the source and the region in question. For near field tsunamis, such as the wave which hit Sumatra in the Indian Ocean Tsunami, there is insufficient time for the wave to evolve into this shape.

Another reason for the frequent application of a solitary wave as model for the leading wave of a tsunami is the relative ease and consistency with which it can be generated under laboratory conditions. Numerous experimental studies with regard to tsunami run up where conducted with solitary waves as a model for the tsunami. Examples of this are Synolakis (1987), Briggs (1994) and Briggs (1995). All of these will later on feature as verification of the numerical model constructed in this study.

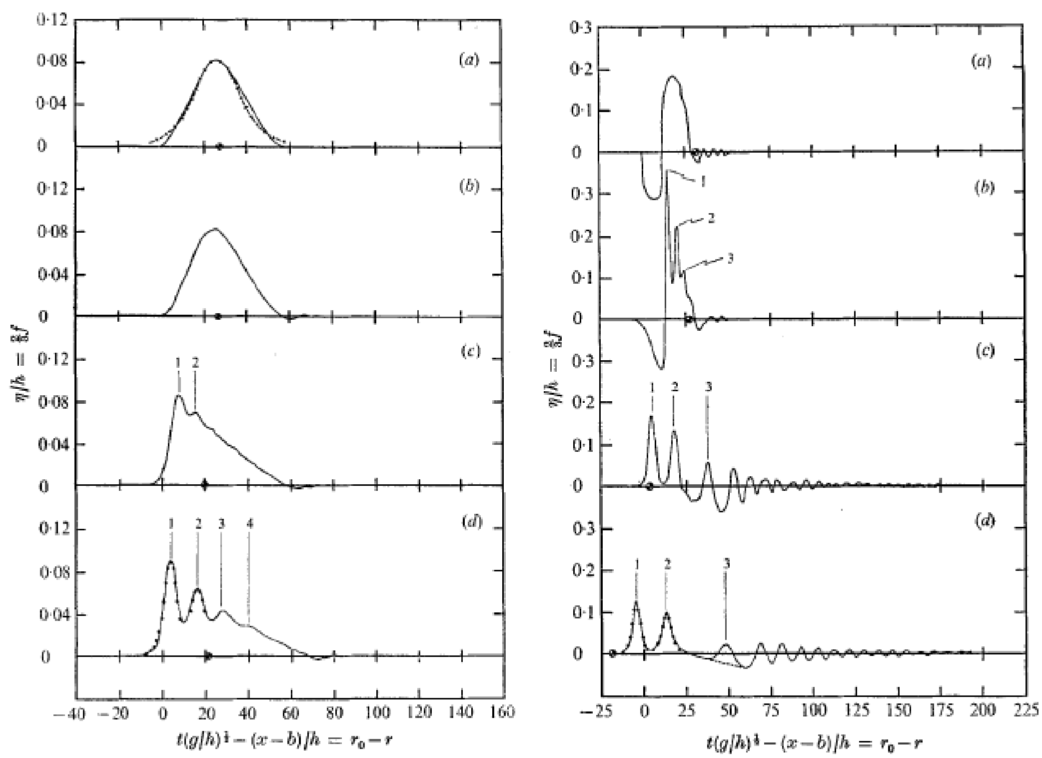

Figure 2-10 Some results from Hammack and Segur (1973) illustrating the evolution of the initial disturbance into a series of solitary waves. On the left a completely positive wave and on the right an initial profile containing a depression. In both cases the net volume under the wave was positive.

However, the solitary wave paradigm has recently come under criticism as the only model for leading waves. Under the Nicaraguan and Indian Ocean tsunami leading depression waves where observed. It appears that the dynamics of a leading depression wave during run-up might be totally different than that of a leading elevation wave.

3. Dispersion of large scale tsunamis

When considering the propagation of tsunamis there are basically two regions of interest which have different characteristics. Tsunamis generated far from the region of interest first need to cross large parts of the worlds oceans. Here the depth is typically in the order of several kilometres. In this case the ocean is usually sufficiently deep to neglect non-linear effects.

On the other hand when a tsunami propagates into coastal waters the depth rapidly decreases and the height of the wave increases. Here non-linear effects become important and linear wave theory usually breaks down.

In either case it is customary to neglect dispersive effects on the propagation of the tsunami. However, since the Indian Ocean Tsunami the discussion regarding the importance of frequency dispersion under large scale tsunamis has resurfaced. In this chapter the importance of dispersion is investigated for transoceanic propagation and for propagation over the continental shelf.

3.1. Oceanic propagation

When investigating the relative importance of frequency dispersion and non-linear effects usually the non-dimensional forms of the equations are considered. In this case the importance of the non-linear terms and frequency dispersion are indicated by

$$\varepsilon = \frac{\zeta_0}{H} \text{ and } \mu^2 = \left(\frac{H}{L}\right)^2 \tag{3.1}$$

where ε gives the importance of nonlinearity and μ is a measurement for the importance of dispersion (Mei, 2005). Furthermore ζ_0 is a typical measure of the amplitude of the wave, H a typical water depth and L a typical horizontal length scale for the wave. When $\varepsilon \ll 1$ or $\mu^2 \ll 1$ either non-linear or dispersive effects are small and can be neglected. Both parameters are frequently combined to form the Ursell parameter

$$U_r = \frac{\varepsilon}{\mu^2} = \frac{\zeta_0 L^2}{H^3} \tag{3.2}$$

Sometimes also called the Stokes parameter (Dingemans 1997) this dimensionless number describes the relative importance of non-linear and dispersive effects. For $U_r = O(1)$ both are of equal importance while for $U_r \ll 1$ or $U_r \gg 1$ either dispersion or non-linear effects dominate.

When deciding if dispersion and non-linearity are important a final important consideration is the propagation distance considered. Initially small effects might have a cumulative contribution which is still substantial.

A qualitative analysis involving the Korteweg-de Vries (KdV) equation, which incorporates dispersion and non-linearity to the leading order, given in Mei (2005, p. 689) shows that dispersive effects remain small when:

$$t_d \ll \sqrt{\frac{g}{H}}\left(\frac{L}{H}\right)^3 \tag{3.3}$$

While for non-linear effects to remain small

$$t_n \ll \sqrt{\frac{g}{H}}\frac{L}{\zeta_0} \tag{3.4}$$

Combining these two time scales with the shallow water wave celerity results in a typical distance for which either non-dispersive or non-linear theories brake down.

Let's consider a large scale tsunami[1] where the typical rupture length is of the order of 1000km while the bottom rises over a width in the order of 100km. A typical response of the sea surface for these types of events is around 1m. Assuming the earthquake occurred in the deep ocean where the depth is about 4km an estimate for the initial importance of both dispersion and non-linearity is: $\varepsilon = 2.5 * 10^{-4}$ and $\mu^2 = 1.6 * 10^{-3}$ which are both much smaller than one. Therefore initially linear long wave theory is sufficient. To investigate when linear non-dispersive wave theory brakes both time scales (3.3) and (3.4) are calculated. The smallest of the two results in $t \sim 2{,}5 \times 10^6 s$, this means the fastest wave has propagated over distance proportional to $x = t\sqrt{gh} \sim 5 \times 10^5 km$ before the linear non-dispersive wave theory brakes down. This distance is far larger than the typical dimensions of the world oceans. This justifies the application of non-dispersive linear theory for transoceanic propagation.

[1] In the Indian Ocean tsunami of 2004 the rupture length was about 1200 km while the zone where either uplift or subduction occurred had typical width of 100 km.

When considering a smaller scale tsunami with a characteristic length scale of say $L = 10km$ the dispersive terms will become important over much smaller length scales (in this case $x \sim 500km$).

Approximate ranges for when dispersive and or non-linear effects are important are given in Table 3-1, which is taken from Mei (2005) and based on the investigations by Hammack and Segur (1978).

U_r	$\tau = \frac{1}{6}\sqrt{\frac{g}{h}}t$	**Approximate equation**
$\gg 1$	$\ll \frac{L}{\zeta_0}$	Linear nondispersive
	$O\left(\frac{L}{\zeta_0}\right)$	Nonlinear nondispersive
$\ll 1$	$\ll \left(\frac{L}{\zeta_0}\right)^3$	Linear nondispersive
	$O\left(\frac{L}{\zeta_0}\right)^3$	Linear dispersive
$O(1)$	$\left(\frac{H^2}{\zeta_0 L}\right)^3 \gg \tau \gg \left(\frac{L}{H}\right)^3$	Linear dispersive for leading waves
	$O\left(\frac{H^2}{\zeta_0 L}\right)^3$	Nonlinear dispersive for leading waves

Table 3-1 Choice of approximate equations, adapted from Mei (2005)

None of these results are considered controversial in the tsunami community when modelling the leading wave of a tsunami. There is however a growing discussion if the correct modelling of the leading wave(s) is sufficient, or that some of the shorter wave components can be significant.

From the investigation by Hammack (1973) it is known that the smallest wave lengths with a significant amplitude present in the initial wave have a size proportional to the depth. There is no doubt that wave components which have lengths of up to ten times the depth will be affected by frequency dispersion. These waves will eventually be left behind by the leading wave when considering transoceanic propagation. However, the question remains if this significantly reduces the leading wave, or if these trailing waves can be destructive on their own.

In Ortiz et al (2000) a transoceanic propagation model including frequency dispersion is compared to a non-dispersive model. They used a wave profile computed by a dislocation model from the 1960 Chilean tsunami as an initial condition. This earthquake had a typical width of 200km and resulted in an initial wave with an amplitude of roughly a metre. After 6000 km of transoceanic propagation they found differences in amplitude of more than 60% between the dispersive and non-dispersive model. They concluded that the dispersive effects are important in a correct estimation of the amplitude.

In Horrillo et al. (2006) the argument is made that the trailing wave train will interact with the primary wave during its run-up, drawdown, and reflection from shelf or land, introducing strong modifications to the leading wave effects. Furthermore they argue that the length scales of the trailing wave components are more likely to induce resonance in harbours and bays.

Following the Indian Ocean Tsunami numerous numerical simulations using Boussinesq models have been performed. In the remaining section of this paragraph some results regarding the dispersion of the Indian Ocean tsunami as it propagated in the westward direction are presented.

The Indian Ocean tsunami of December 2004 was the first ever major tsunami detected by satellite altimeter data. Moreover, the tsunami was detected by over four satellite systems (TOPEX/POSEIDON, Jason, Envisat and Geosat) rather then just a single system. However, it was the Jason satellite operated by NASA and the French space agency (CNES) which was located strategically placed, providing accurate measurement of the tsunami wave height in the Indian ocean. Both the track and measured profile are given in Figure 3-1.

In Kulikov (2005) the first analysis of this data was presented. He performed a wavelet analysis on the wave profile along the Jasons track on data captured 2 hours after the generating earthquake. The results of his analysis are presented in Figure 3-2. It shows that for the waves travelling in the South-western direction the shorter wave components where significantly delayed with regards to the longer wave components. And the location of the wave fronts is in good agreement with the theoretical dispersion curve (presented by a solid line).

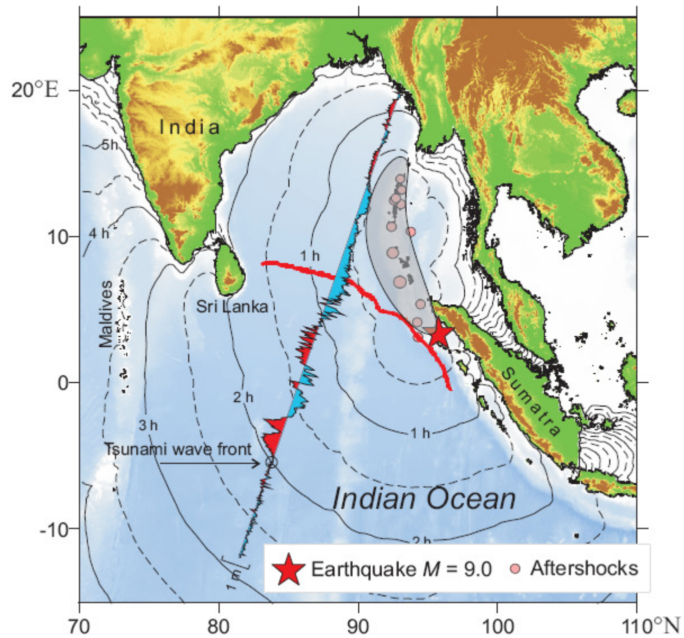

Figure 3-1 Calculated tsunami wave in the Indian Ocean about two hours after the Sumatra Earthquake. Kulikov (2005).

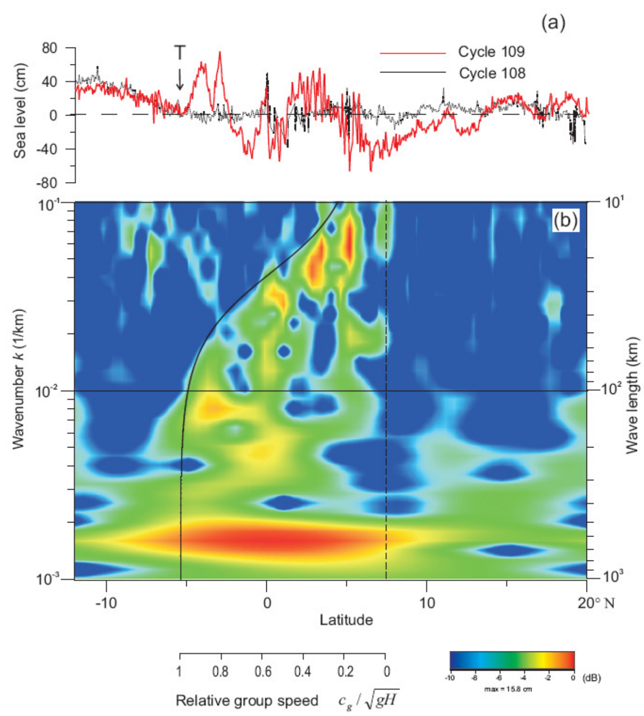

Figure 3-2 (a) Altimetry sea-level taken along the 129 track of the Jason-1 satellite for Cycle 109 and 10 days earlier along the same track for Cycle 108. The letter T indicates the tsunami wave front. (b) Wavelet analysis of the 109 Cycle sea-level. The solid line indicates the theoretical group velocity. Kulikov (2005).

Following the study by Kulikov numerous researchers have tried to model the IOT using Boussinesq models. In Horrillo et al (2006) a comparison was made between a Boussinesq model, a non-hydrostatic model, and a model based on the NSWE. Here it was found that the leading waves of the tsunami where usually overestimated by the NSWE model while the following waves where underestimated or even absent in the model.

Grilli et al. (2007) used their Boussinesq model Funwave to model the bay of Bengal and compared the results to a version solving the NSWE. They found differences of up to 20 percent in surface elevations between the Boussinesq and NSWE simulations for the westward propagated wave.

Glimsdal et al (2006) also used a Boussinesq model. The results where again compared to a NSWE model. In Figure 3-3 the results for the wave near Africa are shown, at about seven hours after the earthquake. The leading wave is much lower and wider due to the dispersive effects.

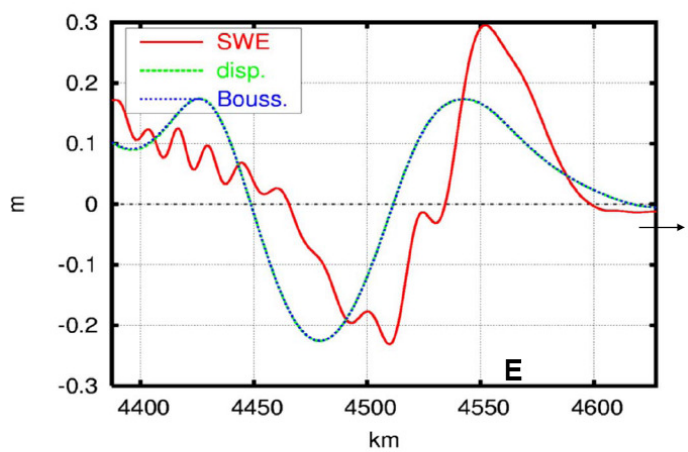

Figure 3-3 The IOT after 7 hours propagated in the westward direction (near Africa). The wave front as predicted by the NSWE is in red and by the Boussinesq model in blue. Glimsdal et al. (2006)

The general opinion from these articles is that especially the westward directed part of the tsunami was altered by dispersion. This is easily understood when considering that the tsunami travelled considerable distances over deep water while propagating in this direction. When compared with both measured data and Boussinesq models the NSWE usually predicted the time of arrival of the front well. The differences where mainly found in the details of, for example, a sequence of wave crests in the tsunami wave packet.

3.2. Coastal waters

When the tsunami propagates from the deep ocean into shallower zones the wave will start to shoal. At this point the importance of non-linear effects begins to grow, and it is generally accepted that at least a non-linear theory is needed to correctly model the tsunami wave in this case. The question remains if dispersive effects need to be included in this case.

3.2.1. Solitary wave fission

When a soliton travels from one constant depth to another constant smaller depth it disintegrates into several solitons of varying sizes, trailed by an oscillatory tail. Thus from the single solitary wave multiple waves emerge with a trailing dispersive tail. This is often referred to as solitary wave fission (Mei 2005).

Fission of solitary waves can occur under tsunamis for waves travelling from the deep ocean onto the continental shelf. A key aspect here is that the continental shelf is wide enough to allow the fission to occur.

On may 26 1983, an earthquake of magnitude 7.7 occurred in the Japan Sea, generating a large tsunami, known as the 1983 Nihonkai-Chubu earthquake tsunami. During this event soliton fission was observed on the gentle seabed slope in the shallow water along the coast (Shuto 1985). Interestingly enough the leading soliton was larger in amplitude than the initial disturbance and it subsequently broke.

Fission of waves in models can only occur when both dispersion and non-linear effects are included in the equations. This means that, if this effect is deemed important, the NSWE cannot be used anymore and an alternative theory including dispersive effects has to be used.

3.2.2. Non-linearity and wave breaking

When a tsunami is incident on a river mouth, estuary or a coast with a mild slope, the wave will often form a bore. The steep, turbulent and rapidly moving wave front is formed after breaking due to the nonlinear processes of the front in shallow water. For small scale tsunamis with large amplitudes this breaking occurs faster and it almost certainly occurs for tsunamis travelling up rivers.

There have been question in the tsunami community if wave breaking occurs for large scale tsunamis. The Indian Ocean Tsunami has provided some confirmation that this indeed happens. Numerous eyewitness accounts of breaking fronts are available and there is also photographic evidence of what appears to be breaking tsunami waves. In Figure 3-4 the tsunami is captured on photo as it approaches the shore of Krabi in Thailand. The Tsunami clearly transformed into a bore.

Figure 3-4 The 2004 Indian Ocean tsunami as it approaches the shore of Krabi, Thailand. The wave clearly has transformed into a bore and appears to have broken somewhere off-shore.

In paragraph 2.3.5 the remark was made that the non-linear shallow water equations do not have permanent wave forms as a solutions. For tsunami waves which are not to steep this forms no real problem as the distance it takes for the non-linear effects to transform the solution to a bore far exceeds the width of most continental shelves.

When a fairly steep leading wave travels a significant distance over the continental shelf the absence of frequency dispersion might become a problem. In this case the NSWE might distort the wave significantly from its physical appearance. Thus, as the waves move into shallower parts, shoaling causes the non-linear effects to become more dominant. The onset of breaking will happen at different locations when comparing a non-dispersive non-linear theory to a dispersive non-linear theory. And more importantly, waves which appear to brake in the NSWE, might actually propagate without breaking when the correct physics are used. The question now is if tsunami waves ever become steep enough to either cause the NSWE to fail or to actually cause wave breaking.

Finally there is the possibility that the tsunami wave bore forms a weak or undular bore. In this case the initial wave front breaks up into a train of smooth waves. This phenomenon has been known to occur for tsunamis travelling upriver. Tsuji et. Al. (1990) reported this phenomenon in the 1983 Japan Sea tsunami. For practical purposes they noted that the undular bore which develops might be one and a half times larger than the initial height of the bore. This could be of importance for the height of the flood defences.

Figure 3-5 The tsunami as it arrives at Koh Jum, Thailand (A. Grawin 2004). The front has developed into an undular bore.

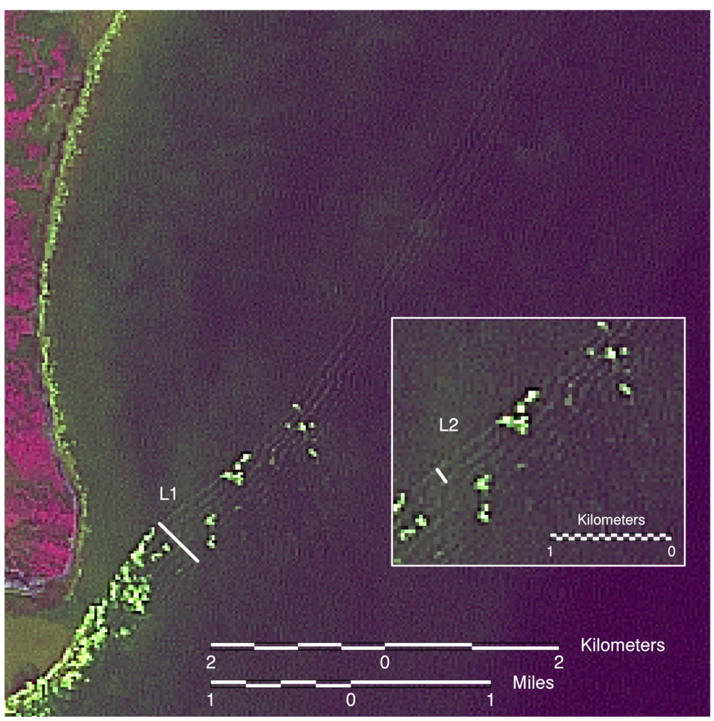

Figure 3-6 Satellite image taken by the Landsat Satellite near Devi Point at the east coast of India. It reportedly shows an undular bore.

However, it appears that an undular bores can also develop when a large scale tsunami hits a mildly sloping coastline. Spectacular evidence for this is found in the photo's by Grawin in Figure 3-5. In the photo the leading wave has clearly transformed into a leading bore with a trailing train of smooth waves.

A somewhat controversial source which does show the occurrence of undular bores during the IOT is found from satellite imagery taken by the Landsat satellite near Devi Point at the east coast of India shown in Figure 3-6. The time the photo was taken (10.17H local time) corresponds with the arrival of the second wave front at the Indian shore. The distance between the leading wavelet and the last (L1) is about 650 metre while the distance between individual wavelets (L2) is about 95 metre.

Previously Sato (1996), in his study of the 1993 Okushiri Island tsunami found that local tsunami enhancement could be explained by a series of dispersive waves which ride on the main tsunami front.

3.3. Discussion

In this chapter various examples have been presented of situations where dispersion might be important under tsunamis. For trans oceanic propagation some authors are claiming that the short wave components which are left behind significantly lower the amplitude of the leading wave. Furthermore the argument is made that the inter arrival time between successive tsunami waves is important in assessing the impact on a distant coast.

There is however little confirmation that the large differences in amplitude after transoceanic propagation reported in these studies are physical. Direct comparison with for example tide gages is difficult as there is a great deal of uncertainty regarding the initial wave. In this way any discrepancy between the model and measured data can be attributed to uncertainty in the initial data. This means that the only verification material is comparison between models as for instance done in Horillo (2006). It is encouraging that models based on the Boussinesq equations give similar results to a non-hydrostatic model while both give different results compared to the model based on the NSWE.

There seems to be consensus that the prediction of the arrival time is excellent when using the NSWE. Furthermore it appears that the amplitude for far field tsunamis are over predicted using the NSWE.

In shallower waters the verification material available for some of the effects caused by dispersion is more profound. There is for instance good evidence that undular bores indeed

do occur. In this case however the question whether or not these are significant immediately rises. It seems very unlikely that the short wave components with typical lengths of a hundred metres have a significant influence in comparison to the main wavelengths. Furthermore to capture this phenomenon a very fine grid resolution is needed. In this case this would lead to grid sizes in the order of five metres which is much to detailed for large scale applications where grid sizes in the order of kilometres are typical.
For the development of the undular bore on a river due to a tsunami it seems far more efficient to use a hydrostatic model up to the river mound and then use the results of this model as boundary condition into a non-linear dispersive model.

There appears to be sufficient evidence to at least make the occurrence of wave breaking under large scale tsunamis plausible. As the only physical effect which opposes the steepening of the wave front is dispersion the inclusion of this is important for the correct breaking behaviour. Especially when the continental shelf in front of the coast is extensive and shallow the NSWE might seriously distort the wave form and lead to premature breaking. This could lead to different inundation heights when compared to solutions which remain unbroken over a large part of the shelf. Whether or not this leads to large differences will depend greatly on the incoming wave length and the local bathymetry.

The effects of frequency dispersion appear to be quite subtle and its importance is difficult to predict before hand. Furthermore the intended usage of the model will also play an important role. For early warning systems it is important that the model predicts the arrival times fast and accurately. For this purpose the (non-) linear shallow water equations should be sufficient as these predict the arrival of the leading wave accurately. Unfortunately, due to the coarse grid sizes, any information regarding wave heights and maximum run-up will be inaccurate from these models.
To allow for a more detailed analysis a better approach might be to model many different earthquake scenarios beforehand and base risk evaluation and evacuation scenarios on these calculations. The runtime of the model is now less crucial and finer grids can be used. Furthermore the inclusion of frequency dispersion now becomes viable. Of coarse this should be done efficiently as the amount of scenarios can be very large.

It can be concluded that there is a great deal of uncertainty regarding the importance of frequency dispersion under large scale tsunamis. In this context a model which would easily allow for the efficient inclusion of frequency dispersion could be very useful.

Section II: 2DV numerical model

4. Model description

4.1. Governing equations

Although the principal subject of this chapter is the construction of a 2DV model including non-hydrostatic pressures it is convenient to introduce the underlying mathematical equations in three dimension in preparation for the three dimensional model which is presented in chapter 6. The two dimensional equations are easily retrieved from these equations as this simply involves dropping one of the two horizontal dimension.

4.1.1. Navier-Stokes equations

Using the physical principle of conservation momentum one is able to derive the well known Navier-Stokes equations for a Newtonian fluid which form the basis of a large part of the field of fluid mechanics.

$$\begin{aligned}
&\frac{\partial \rho u}{\partial t}+\frac{\partial \rho u^2}{\partial x}+\frac{\partial \rho v u}{\partial y}+\frac{\partial \rho w u}{\partial z}=-\frac{\partial P}{\partial x}+\nu\nabla^2 u\\
&\frac{\partial \rho v}{\partial t}+\frac{\partial \rho u v}{\partial x}+\frac{\partial \rho v^2}{\partial y}+\frac{\partial \rho w v}{\partial z}=-\frac{\partial P}{\partial y}+\nu\nabla^2 v\\
&\frac{\partial \rho w}{\partial t}+\frac{\partial \rho u w}{\partial x}+\frac{\partial \rho v w}{\partial y}+\frac{\partial \rho w^2}{\partial z}=-\frac{\partial P}{\partial z}+\nu\nabla^2 w
\end{aligned} \tag{4.1}$$

Where u, v and w denote the velocity components [m/s] in the x, y and z-direction respectively, ρ the density [kg/m^3], P the pressure [N/m^2] and ν the kinematic viscosity [m^2/s]. Furthermore ∇^2 is the Laplacian defined as

$$\nabla^2(\ )=\frac{\partial^2}{\partial x^2}(\ )+\frac{\partial^2}{\partial y^2}(\ )+\frac{\partial^2}{\partial z^2}(\ ).$$

Besides the conservation of momentum one usually also considers the conservation of mass.

$$\frac{\partial \rho}{\partial t}+\frac{\partial}{\partial x}(\rho u)+\frac{\partial}{\partial y}(\rho v)+\frac{\partial}{\partial z}(\rho w)=0 \tag{4.2}$$

This equation almost always accompanies the Navier-Stokes equations. Together they describe a wide variety of flows found, for both gases and fluids.

4.1.2. Basic assumptions

fluid properties

The area of interest in which (approximate) solutions to the Navier-Stokes equations are sought involves wave like phenomena in the coastal zone. This justifies some assumptions with regard too the fluid which can simplify the Navier Stokes equations. The fluid will be assumed to be: (i) Incompressible, (ii) Homogeneous and (iii) Inviscous.

The assumption that the fluid is incompressible is not restricted to our domain but very common when the fluid in question is water. It is justified when the flow velocities are much lower than the speed of sound in the medium which is usually the case in naturally occurring flows[1]. An interesting property which results directly from the incompressibility assumption is that sound (pressure) waves travel with infinite speed through the medium

The fluid is furthermore assumed to be homogenous. This means that both variations in density, which for example result from different salinity levels, and differences in temperatures are ignored. These differences do occur in nature but the situations where density differences play a role in wave propagation (e.g. fluid mud deposits in front of the coast) are not considered here.

Finally the fluid is treaded as in viscous. This means that the viscous stresses are neglected in the equations and no turbulent stresses are introduced. This is mainly done for convenience as the (turbulent) viscosity plays a minor role in wave propagation. If needed the viscosity can be incorporated into the numerical model and the fluid is not necessarily assumed to be rotation free.

Description of the free surface and bottom

The domain of interest considered is vertically bounded by the free surface and the bottom. The free surface acts as an air water interface which, due to for example wave overturning, can assume complex shapes. Due to the mixing between air and water in breaking waves the interface is sometimes hard to define. These effects are difficult to include into a numerical model. Models which can deal with this are usually based on the Marker and Cell scheme or the Volume of fluid method. These methods have to resolve very small scales in both time and space. This makes large scale applications impossible.

[1] This is usually expressed in the Mach number, $Ma = u / c$ where u is the fluid velocity and c the speed of sound in water. With $c \approx 1480 m / s$ this means that $Ma \ll 1$ and the fluid can be assumed to be incompressible.

An alternative approach to deal with the free surface is to use a single valued function $\zeta(x,y,t)$ to describe the location of the free surface. This excludes overtopping waves. Rather than resolving this phenomenon it is considered to be a sub-grid effect that has to be captured by a proper conservation principle. This is the approach taken here.

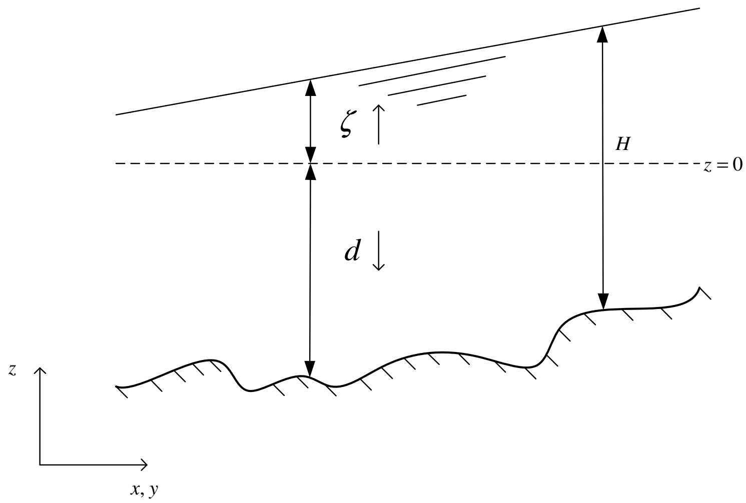

Figure 4-1 Coordinate system used

The bottom is assumed to be an immobile bed. Changes of the bathymetry due to sedimentation and erosion are neglected. The location of the bottom is measured positive downwards. The total water depth is now given by:

$$H(x,y,t)=\zeta(x,y,t)+d(x,y) \tag{4.3}$$

Similar to the free surface the choice to use a single valued function to represent the location of the bottom excludes complex bathymetries where for example arches are present.

4.1.3. Euler equations

Using the assumptions as outlined in the previous paragraph we are now able to simplify the Navier-Stokes equations in (4.1). Neglecting the viscous contributions and treating the density as constant in space and time leads to the incompressible Euler equations

$$\frac{D\mathbf{u}}{Dt}=-\frac{1}{\rho}\nabla P-\mathbf{g} \tag{4.4}$$

Where the material derivative is used defined as:

$$\frac{D}{Dt}(\ )\equiv\frac{\partial}{\partial t}(\ )+u\frac{\partial}{\partial x}(\ )+v\frac{\partial}{\partial y}(\ )+w\frac{\partial}{\partial z}(\ )$$

And

$$\mathbf{u}=\begin{pmatrix}u\\v\\w\end{pmatrix},\qquad \mathbf{g}=\begin{pmatrix}0\\0\\g\end{pmatrix}$$

The conservation of mass reduces to the conservation of volume as the density is now constant in both space and time and can be divided out of the equation

$$\nabla \bullet \mathbf{u} = \frac{\partial u}{\partial x} + \frac{\partial v}{\partial y} + \frac{\partial w}{\partial z} = 0 \tag{4.5}$$

This equation will be referred to as the local continuity equation.

4.1.4. Pressure decomposition

In (4.4) the total pressure is used in the equations. Usually the largest contribution to the pressure in a water column is due to the weight of the water above, or the hydrostatic pressure component. This can be made explicit in the equations by decomposing the pressure in a hydrostatic and hydrodynamic part or

$$P = p_d + p_h = \rho p + \rho g\left(\zeta - z\right) \text{ with } p = \frac{p_d}{\rho} \tag{4.6}$$

Where p_d is the dynamic pressure, p_h the hydrostatical part of the pressure and p the dynamic pressure normalized with the reference density ρ . The pressure at the free surface has been assumed zero in (4.6). Substituting (4.6) into (4.4) gives

$$\begin{aligned} \frac{Du}{Dt} &= -g\frac{\partial \zeta}{\partial x} - \frac{\partial p}{\partial x} \\ \frac{Dv}{Dt} &= -g\frac{\partial \zeta}{\partial y} - \frac{\partial p}{\partial y} \\ \frac{Dw}{Dt} &= -\frac{\partial p}{\partial z} \end{aligned} \tag{4.7}$$

If the dynamic pressure component is neglected in these equations they reduce to the well known non-linear shallow water equations (NSWE).

4.1.5. Free surface equation

To obtain an expression for the free surface the continuity equation is integrated over the depth:

$$\int_{-d}^{\zeta} \nabla \cdot \mathbf{u} dz = \int_{-d}^{\zeta} \frac{\partial u}{\partial x} dz + \int_{-d}^{\zeta} \frac{\partial v}{\partial y} dz + w(x, y, \zeta, t) - w(x, y, -d, t) \tag{4.8}$$

Now it is assumed that the water surface is always composed of the same particles. This is justified due to exclusion of wave overturning. The vertical velocity of a particle located at the free surface is therefore equal to the material derivative of the free surface. This results in the kinematic boundary condition of the free surface:

$$w(x,y,\zeta,t)=\frac{D\zeta}{Dt}=\frac{\partial\zeta}{\partial t}-u\frac{\partial\zeta}{\partial x}-v\frac{\partial\zeta}{\partial y} \tag{4.9}$$

Something similar holds at the bottom where only the partial time derivative drops out as the bottom profile is constant in time. The kinematic boundary condition at the bottom is given by

$$w(x,y,-d,t)=-u\frac{\partial d}{\partial x}-v\frac{\partial d}{\partial y} \tag{4.10}$$

When the equations (4.9) and (4.10) are substituted into equation (4.8) and use is made of the Leibniz rule of integration the integrated continuity equation becomes

$$\frac{\partial\zeta}{\partial t}+\frac{\partial UH}{\partial x}+\frac{\partial VH}{\partial y}=0 \tag{4.11}$$

Where U and V are the depth averaged velocities given by

$$U=\frac{1}{H}\int_{-d}^{\zeta}udz, V=\frac{1}{H}\int_{-d}^{\zeta}vdz \tag{4.12}$$

From now on equation (4.11) is referred to as the global continuity equation. This equation gives a relationship between the depth averaged velocity and the surface elevation.

4.2. Grid schematization

4.2.1. Vertical coordinate system

The numerical model will cover areas where the bathymetry is irregular. Furthermore the free surface will vary as a function of time. The coordinate system must be able to accommodate both of these when we discretise the governing equations in the vertical. Both z-planes and sigma planes are suitable candidates for this.

Using z-planes the usual practice is to discretise the computational domain into a set of strictly horizontal planes on which the variables are defined in the vertical. Due to the variation in bathymetry and the movement of the free surface the number of active grid points does not remain constant in space and time. In Figure 4-2 we see a situation in which the lowest horizontal plane is partly located below the bottom level and in this situation some of the grid points on this domain will remain inactive. Furthermore points might become dry due to the movement of the free surface. A further disadvantage is that the number of points in the vertical reduces from four in the deepest part too only two in the shallower areas. As the shallowest areas are often the area of interest this loss off accuracy is rather unfortunate. Note that much of the problems raised here can be solved if unstructured grids are employed.

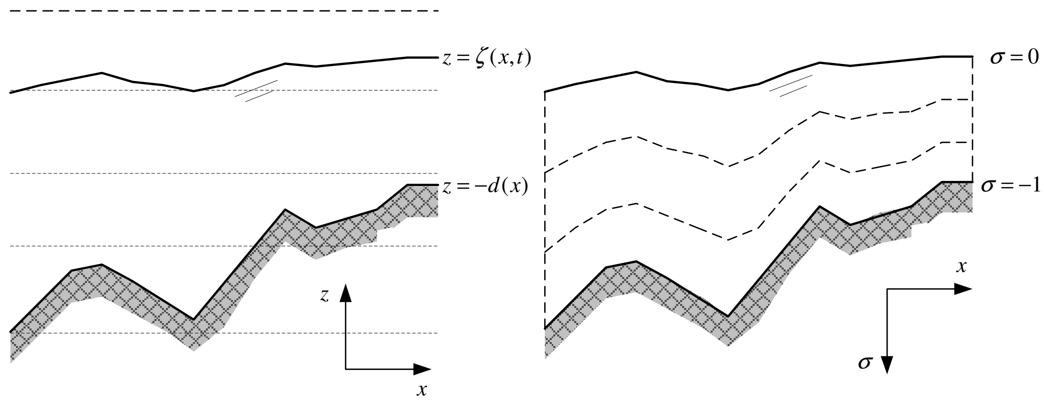

Figure 4-2 A vertical cross section divided into z-layers on the left and sigma layers on the right. Notice that the number of layers in the sigma formulation remains constant along the x-axis while in the z-layer model the number of layers reduces from four to two.

An alternative to z-planes can be found in the so called sigma coordinates. The sigma transformation was first introduced by Phillips (1957) and it introduces a transformation of the vertical z-axis.

$$\sigma = \frac{z-\xi}{\xi - z_0} = \frac{z-\xi}{H_i}\,,\ \sigma = \{-1,0\} \tag{4.13}$$

where σ is the sigma coordinate and z_0 the location of the bottom. The free surface is now located at $\sigma = 0$ while the bottom is located at $\sigma = -1$.

Under the sigma transformation the vertical domain no longer varies in the horizontal. In practise this mean it is now possible to discretise the entire horizontal domain using the same number of points in the vertical. However, the differential equations must contain extra terms which account for the grid movement and these are not present in the Cartesian formulation.

In the present study the equations will not be transformed into σ-co-ordinates. Instead following Zijlema (1998,2000) and Stelling and Van Kester (1994) a sigma grid is generated by choosing a layer distribution over the vertical. The sigma lines will consequently be regarded as boundaries of the time varying volumes in Cartesian co-ordinates. The resulting equations are very similar but are formulated in terms of x,z,t instead of x,σ,t. Furthermore the moving coordinate system results in apparent vertical advection terms which are identical to the relative vertical velocity ω encountered in the sigma transformation.

4.2.2. Variable layout

The staggered arrangement is the classical variable layout used by most non-hydrostatic models. It does not suffer from spurious oscillations in the pressure compared to the collocated grid. Furthermore several terms which require interpolation in the collocated arrangement, are very naturally approximated by central differences without interpolation.

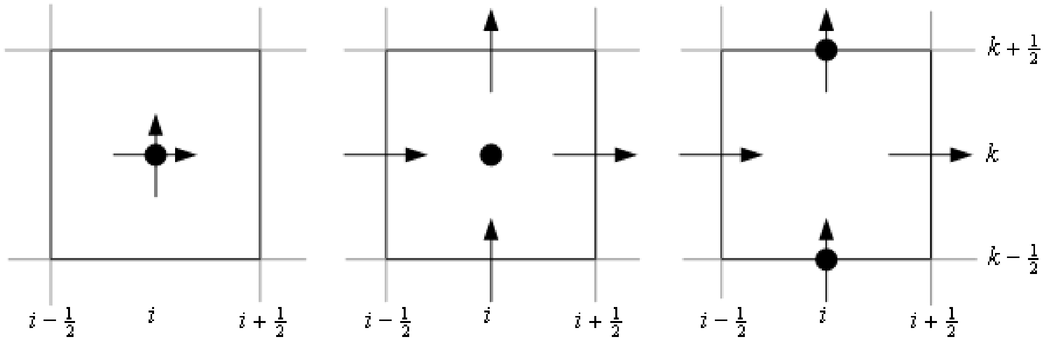

Figure 4-3 Collocated arrangement on the left, classical staggered arrangement in the middle and the arrangement as proposed by Stelling and Ziijlema on the right.

Both the staggered and collocated approach share the disadvantage that the surface pressure cannot be included easily. And it appears that a correct approximation of the pressure distribution in the top cell is key to modelling dispersive waves correctly. This lead Stelling and Zijlema (2003) to introduce the Keller box scheme in the vertical. Here the pressure points are no longer located in the cell centre but at the top and bottom cell face. In Figure 4-3 the three arrangements are depicted.

Adopting this approach results in a hybrid between a staggered grid in the horizontal and a compact approach in the vertical. Horizontal velocity components are staggered when compared to pressure points and the free surface location. In the vertical the pressure points are located at the same position as the vertical velocities.

4.2.3. Grid description

The horizontal gridlines are formed by a set of vertical planes numbered from $i = 1,..,I$ located on x_i. The distance between x_{i+1} and x_i is indicated with $\Delta x_{i+\frac{1}{2}}$ while Δx_i is the distance between $x_{i+\frac{1}{2}}$ and $x_{i-\frac{1}{2}}$. The vertical gridlines are formed by the sigma isolines numbered from $k = 0,...,K$ located at σ_k. Here the bottom is located at σ_0 and the free surface at σ_K. The area between two sigma lines will often be referred to as a computational layer and the sigma lines separating the layers as layer interfaces. The layers are numbered from $k = 1,...,K$ and the layer interfaces of layer k are $\sigma_{k+\frac{1}{2}}$ and $\sigma_{k-\frac{1}{2}}$.

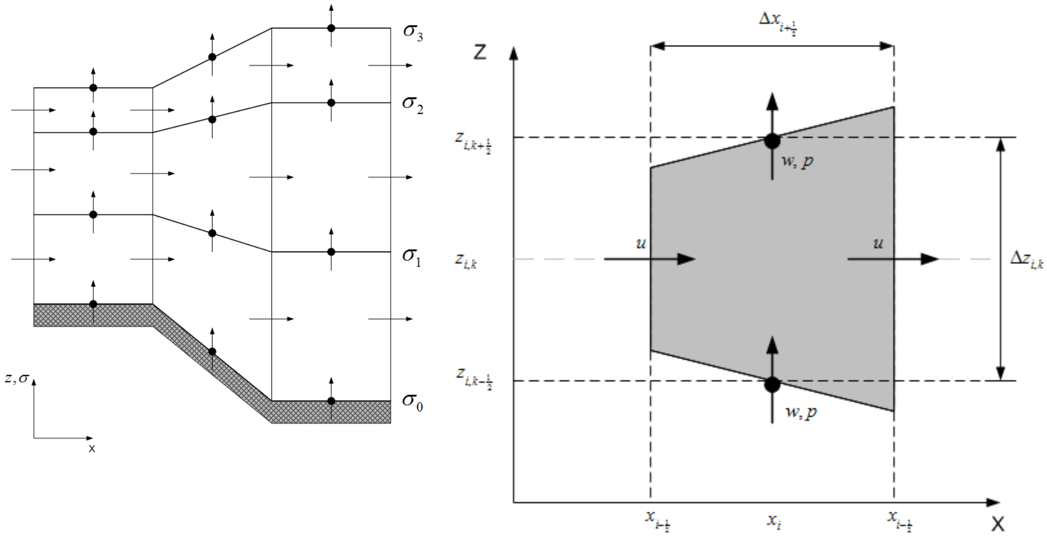

Figure 4-4 An overview of the grid employed. On the left an impression of a typical grid and on the right a detailed view of the variable layout.

The free surface ζ is located in the cell centre (i) while the non-hydrostatic pressure p and vertical velocity w are defined on the cell face ($i, k+\frac{1}{2}$). The horizontal velocity is located at the cell face ($i+\frac{1}{2}, k$). The relative layer thickness can now be described by:

$$\Delta\sigma_k = \sigma_{k+\frac{1}{2}} - \sigma_{k-\frac{1}{2}} \quad k = 1,...,K \tag{4.14}$$

Multiplying with the water depth H_i gives the absolute layer thickness $h_{i,k} = H_i \Delta\sigma_k$. From this the location of the layer interfaces can be calculated using

$$z_{i,k+\frac{1}{2}} = z_{i,k-\frac{1}{2}} + h_k, \quad k = 1,...,K \tag{4.15}$$

Where $z_{i,\frac{1}{2}}$ is the location of the bottom and $z_{i,K+\frac{1}{2}}$ denotes the location of the free surface.

4.2.4. Relative vertical velocity[1]

Before introducing the numerical approximations it is convenient to introduce the relative vertical velocity ω. This vertical velocity is due to the vertical schematizations and is defined as the rate of change of the vertical distance between a water particle and an observer moving along the projection of the water particle on the sigma isoline. The vertical velocity ω is defined as

$$\omega = \frac{DL}{Dt} = \frac{Dz_p}{Dt} - \frac{Dz_\sigma}{Dt} \tag{4.16}$$

[1] Portions of the text in this paragraph are taken from Van Reeuwijk (2002)

Where L is the distance between the observer and the water particle. This distance is defined as the difference between the z location of the particle z_p and the location of the sigma isoline z_σ .Thus the vertical velocity ω can now be written as:

$$\omega = w - \frac{\partial z}{\partial t} - u\frac{\partial z}{\partial x} \tag{4.17}$$

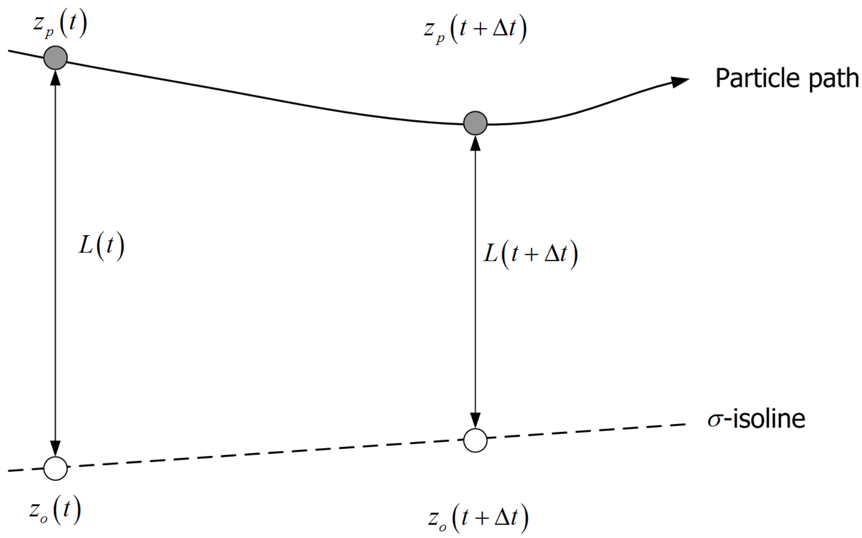

Figure 4-5 Definition of the vertical velocity ω. Van Reeuwijk (2002)

Notice that the relative velocity ω introduces a coupling between the horizontal and vertical velocities. Using (4.17) and the definitions of the kinematic boundary conditions it is easy to show that at the free surface:

$$(z = \zeta) \qquad w = \frac{\partial \zeta}{\partial t} + u\frac{\partial \zeta}{\partial x} \Leftrightarrow \omega = 0 \tag{4.18}$$

And at the bottom:

$$(z = -d) \qquad w = u\frac{\partial \zeta}{\partial x} \Leftrightarrow \omega = 0 \tag{4.19}$$

4.3. *Space discretisation*

With the grid defined the equations can now be discretized in both space and time. As this is a crucial step in the development of the model the methods used will be dealt with in detail. As a discretisation technique the method of lines has been used which clearly distinguishes between discretisation in space and time. This is certainly not the only method available but its clarity and relative simplicity was seen as an advantage in developing the model.

The discretization in space was initially based on a compromise between the layer averaged method as given by Zijlema (1998) for the momentum equations, and a finite volume discretisation for the pressure gradient and the continuity equations. Due to the nature of the structured grid employed the layer averaged derivation and the finite volume discretisation of the continuity equations and the pressure gradient result in virtually identical numerical expressions. It was later found that when the model was fully recast into a finite volume method (including the momentum equations) the dam break problem performed marginally better. To keep the derivations consistent the layer averaged derivation is presented here as this model formed the basis of most cases presented later on.

The derivation based on the layer averaged equations makes extensive use of the Leibniz Rule of integration which is therefore repeated here for convenience.

$$\int_{a(t)}^{b(t)} \frac{\partial}{\partial t} f(z,t)dz = \frac{\partial}{\partial t}\int_{a(t)}^{b(t)} f(z,t)dz - f(b(t),t)\frac{\partial}{\partial t}b(t) + f(a(t),t)\frac{\partial}{\partial t}a(t) \tag{4.20}$$

4.3.1. Global continuity equation

As was outlined in the previous chapter the global continuity equation, which describes the relation between the free surface and the depth averaged discharge, is given by

$$\frac{\partial \zeta}{\partial t} + \frac{\partial}{\partial x}(UH) = 0 \tag{4.21}$$

A simple semi-discretisation of (4.21) using central differences for the space derivative is given by:

$$\frac{d\zeta_i}{dt} + \frac{U_{i+\frac{1}{2}}H_{i+\frac{1}{2}} - U_{i-\frac{1}{2}}H_{i-\frac{1}{2}}}{\Delta x} = 0 \tag{4.22}$$

The depth averaged velocity can be approximated by using the midpoint rule for the integration over a single layer and then summation over all the layers. Dividing by the depth results in a second order accurate approximation of the depth average velocity:

$$U_{i+\frac{1}{2}} = \frac{1}{H_{i+\frac{1}{2}}}\sum_{k=1}^{K} h_{i+\frac{1}{2},k} u_{i+\frac{1}{2},k} = \sum_{k=1}^{K} u_{i+\frac{1}{2},k}\Delta\sigma_k \tag{4.23}$$

where $\Delta\sigma_k$ is the relative layer thickness. A problem with (4.22) is that the water depth is not defined in a velocity point and thus needs to be interpolated from surrounding points. Here a simple first order accurate upwind interpolation is employed defined as

$$H_{i+\frac{1}{2}} = \begin{cases} \zeta_i + d_{i+\frac{1}{2}} & \text{if } \mathrm{U}_{\mathrm{i}+\frac{1}{2}} > 0 \\ \zeta_{i+1} + d_{i+\frac{1}{2}} & \text{if } \mathrm{U}_{\mathrm{i}+\frac{1}{2}} < 0 \\ \max(\zeta_i, \zeta_{i+1}) + d_{i+\frac{1}{2}} & \text{if } \mathrm{U}_{\mathrm{i}+\frac{1}{2}} = 0 \end{cases} \tag{4.24}$$

The resulting scheme is only first order accurate by virtue of the upwind interpolations and mass conservative. To increase the accuracy of the scheme higher order interpolations can be used but this will be the subject of 4.6.

4.3.2. Local continuity equation

The local continuity equation is integrated vertically over a layer. This results in a layer averaged equation. Using the Leibniz rule of integration this becomes:

$$\int_{z_{k-\frac{1}{2}}}^{z_{k+\frac{1}{2}}} \left(\frac{\partial u}{\partial x} + \frac{\partial w}{\partial z} \right) dz = \frac{\partial}{\partial x}\left(h_k u_k\right) - u_{k+\frac{1}{2}} \left.\frac{\partial z}{\partial x}\right|_{k+\frac{1}{2}} + u_{k-\frac{1}{2}} \left.\frac{\partial z}{\partial x}\right|_{k-\frac{1}{2}} + w_{k+\frac{1}{2}} - w_{k-\frac{1}{2}} = 0 \tag{4.25}$$

Notice that this expression can be rewritten using equation (4.17) into

$$\frac{\partial h_k}{\partial t} + \frac{\partial}{\partial x}\left(h_k u_k\right) + \omega_{k+\frac{1}{2}} - \omega_{k-\frac{1}{2}} = 0 \tag{4.26}$$

This equation is more compact and will be used later on in the derivation of the layer averaged momentum equations. Furthermore it is used in the determination of the relative velocity. A simple second order accurate discretisation of (4.26) is given by:

$$\frac{\partial h_{i,k}}{\partial t} + \frac{h_{i+\frac{1}{2},k} u_{i+\frac{1}{2},k} - h_{i-\frac{1}{2},k} u_{i-\frac{1}{2},k}}{\Delta x_{i+\frac{1}{2}}} + \omega_{i,k+\frac{1}{2}} - \omega_{i,k-\frac{1}{2}} = 0 \tag{4.27}$$

However, for the local continuity equation we retain the form of equation (4.25) as this uses the physical velocity w. This has certain advantages when deriving an expression for the non-hydrostatic pressure.

Thus continuing with equation (4.25) discretisized using central differences, multiplying the equation with Δx this results in:

$$\begin{aligned} & u_{i+\frac{1}{2},k} h_{i+\frac{1}{2},k} - u_{i-\frac{1}{2},k} h_{i-\frac{1}{2},k} + w_{i,k+\frac{1}{2}} \Delta x_{i+\frac{1}{2}} - w_{i,k-\frac{1}{2}} \Delta x_{i+\frac{1}{2}} \\ & -\left(z_{i+\frac{1}{2},k+\frac{1}{2}} - z_{i-\frac{1}{2},k+\frac{1}{2}}\right) u_{i,k+\frac{1}{2}} + \left(z_{i+\frac{1}{2},k-\frac{1}{2}} - z_{i-\frac{1}{2},k-\frac{1}{2}}\right) u_{i,k-\frac{1}{2}} = 0 \end{aligned} \tag{4.28}$$

Expression (4.28) was derived using a layer averaged approach and then applying finite differences to the result. However, inspecting (4.28) in more detail reveals that it constitutes a mass balance for a control volume located at i,k. This is consistent with a finite volume discretisation and is mass conservative.

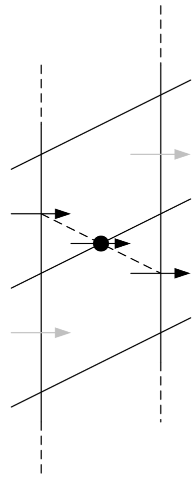

Figure 4-6 Interpolating the horizontal velocity component from its surrounding points

Notice that in equation (4.28) the velocity at $u_{i,k+\frac{1}{2}}$ is not known and therefore needs to be interpolated. For interior points this velocity is given by

$$u_{i,k+\frac{1}{2}} = \begin{cases} \dfrac{u_{i+\frac{1}{2},k} + u_{i-\frac{1}{2},k+1}}{2}, \text{ if } z_{i+\frac{1}{2},k+\frac{1}{2}} - z_{i-\frac{1}{2},k+\frac{1}{2}} \geq 0 \\ \dfrac{u_{i+\frac{1}{2},k+1} + u_{i-\frac{1}{2},k}}{2}, \text{ if } z_{i+\frac{1}{2},k+\frac{1}{2}} - z_{i-\frac{1}{2},k+\frac{1}{2}} < 0 \end{cases} \tag{4.29}$$

At the free surface and at the bottom the velocities follow from the discretisation of the kinematic boundary conditions.

4.3.3. Horizontal momentum equation

The horizontal momentum equations in conservative form for a 2DV framework are given by

$$\frac{\partial u}{\partial t} + \frac{\partial u^2}{\partial x} + \frac{\partial wu}{\partial z} = -g\frac{\partial \zeta}{\partial x} - \frac{\partial p_d}{\partial x} \tag{4.30}$$

In order to arrive at a conservative approximation of the horizontal momentum equations they will be first integrated over a layer to arrive at the layer averaged equations. Subsequently these equations will be approximated with a finite difference like approach to arrive at the final expressions.

Treating consecutively the integration over a layer of (i) the time derivative, (ii) the surface gradient (iii) the advective terms and (iv) the integration of the non-hydrostatic pressure gradient.

Time derivative

The time derivative of the momentum equation is integrated over the layer k and using the Leibniz rule of integration we obtain

$$\int_{z_{k-\frac{1}{2}}}^{z_{k+\frac{1}{2}}} \frac{\partial u}{\partial t} \partial z = \frac{\partial h_k u_k}{\partial t} - u_{\,k+\frac{1}{2}} \left.\frac{\partial z}{\partial t}\right|_{k+\frac{1}{2}} + u_{k-\frac{1}{2}} \left.\frac{\partial z}{\partial t}\right|_{k-\frac{1}{2}} \tag{1.31}$$

The second and third terms on the right hand side are a result of the movement of the grid.

Advective terms

Layer averaging of the advective terms gives

$$\int_{z_{k-\frac{1}{2}}}^{z_{k+\frac{1}{2}}} \frac{\partial u^2}{\partial x} + \frac{\partial uw}{\partial z} dz = \int_{z_{k-\frac{1}{2}}}^{z_{k+\frac{1}{2}}} u^2 \partial z + u\,(w - u\frac{\partial z}{\partial x})\Big|_{z_{k-\frac{1}{2}}}^{k+\frac{1}{2}} \tag{1.32}$$

In (1.32) we substitute the expression for ω, as given in (4.17), which yields

$$\int_{z_{k-\frac{1}{2}}}^{z_{k+\frac{1}{2}}} \frac{\partial u^2}{\partial x} + \frac{\partial uw}{\partial z} dz = \frac{\partial}{\partial x} \int_{z_{k-\frac{1}{2}}}^{z_{k+\frac{1}{2}}} u^2 dz + u_{k+\frac{1}{2}} \left(\omega_{k+\frac{1}{2}} + \frac{\partial z_{k+\frac{1}{2}}}{\partial t} \right) - u_{k-\frac{1}{2}} \left(\omega_{k-\frac{1}{2}} + \frac{\partial z_{k-\frac{1}{2}}}{\partial t} \right) \tag{1.33}$$

Finally we rewrite the integral on the right hand side of equation (1.33) using

$$\int_{z_{k-\frac{1}{2}}}^{z_{k+\frac{1}{2}}} u^2 dz = h_k u_k^2 + \int_{z_{k-\frac{1}{2}}}^{z_{k+\frac{1}{2}}} \left(u - u_k\right)^2 dz \tag{1.34}$$

to obtain

$$\begin{aligned} \int_{z_{k-\frac{1}{2}}}^{z_{k+\frac{1}{2}}} \frac{\partial u^2}{\partial x} + \frac{\partial uw}{\partial z} dz &= \frac{\partial}{\partial x} \left(h_k u_k^2 + \int_{z_{k-\frac{1}{2}}}^{z_{k+\frac{1}{2}}} \left(u - u_k\right)^2 dz \right) \\ &+ u_{k+\frac{1}{2}} \left(\omega_{k+\frac{1}{2}} + \frac{\partial z_{k+\frac{1}{2}}}{\partial t} \right) - u_{k-\frac{1}{2}} \left(\omega_{k-\frac{1}{2}} + \frac{\partial z_{k-\frac{1}{2}}}{\partial t} \right) \end{aligned} \tag{4.35}$$

The integral term in the right hand side of equation (1.34) is the dispersion term which results from the vertical non-uniformities in the flow. A common practice to deal with this term is to model it as diffusion. When the vertical distribution of the flow over the layer does not vary to much the integral can be safely approximated with the first term on the right hand side of (1.34) and the contribution of the integral term can be neglected. When this assumption is violated the best remedy is to using a higher grid resolution in the vertical. This is then most likely needed anyway for the correct resolution of the vertical momentum equation.

To summarize the layer averaged advection terms now read:

$$\int_{z_{k-\frac{1}{2}}}^{z_{k+\frac{1}{2}}} \frac{\partial u^2}{\partial x} + \frac{\partial uw}{\partial z} dz = \frac{\partial h_k {u_k}^2}{\partial x} + u_{k+\frac{1}{2}} \left(\omega_{k+\frac{1}{2}} + \frac{\partial z_{k+\frac{1}{2}}}{\partial t} \right) - u_{k-\frac{1}{2}} \left(\omega_{k-\frac{1}{2}} + \frac{\partial z_{k-\frac{1}{2}}}{\partial t} \right) \tag{1.36}$$

This is approximated as:

$$\int_{z_{k-\frac{1}{2}}}^{z_{k+\frac{1}{2}}} \frac{\partial u^2}{\partial x} + \frac{\partial uw}{\partial z} dz \approx \frac{q_{i+1,k}u_{i+1,k} - q_{i,k}u_{i,k}}{\Delta x}$$
$$+u_{i+\frac{1}{2},k+\frac{1}{2}}\left(\omega_{i+\frac{1}{2},k+\frac{1}{2}} - \frac{\partial z_{k+\frac{1}{2}}}{\partial t}\right) - u_{i+\frac{1}{2},k-\frac{1}{2}}\left(\omega_{i+\frac{1}{2},k-\frac{1}{2}} + \frac{\partial z_{k-\frac{1}{2}}}{\partial t}\right) \tag{4.37}$$

Where $q_{i,k}$ represents the discharge through the face of layer k. The velocity $u_{i,k}$ is given by either a first order upwind scheme as defined in equation (4.38) or a limited scheme as described in 4.6.

$$u_{i,k} = \begin{cases} u_{i-\frac{1}{2},k}, \text{ if } q_{i,k} \geq 0 \\ u_{i+\frac{1}{2},k}, \text{ if } q_{i,k} < 0 \end{cases} \tag{4.38}$$

We will leave the definition of $q_{i,k}$ rest for the time being for reasons which will become apparent later in this section. The values of u at the layer interfaces are given by a simple first order upwind approximation:

$$u_{i+\frac{1}{2},k+\frac{1}{2}} = \begin{cases} u_{i+\frac{1}{2},k} & \text{if } \omega^z_{i+\frac{1}{2},k+\frac{1}{2}} \geq 0 \\ u_{i+\frac{1}{2},k+1} & \text{if } \omega^z_{i+\frac{1}{2},k+\frac{1}{2}} < 0 \end{cases} \quad \text{where} \quad \bar{\omega}^z_{i+\frac{1}{2},k+\frac{1}{2}} = \frac{\omega_{i,k+\frac{1}{2}} + \omega_{i+1,k+\frac{1}{2}}}{2} \tag{4.39}$$

This proved to be a more stable approach as apposed to central differences which gave erroneous results in the case of shockwaves.

Free surface gradient

As the free surface gradient is not dependent on the depth the term can be easily written as

$$\int_{z_{k+\frac{1}{2}}}^{z_{k+\frac{1}{2}}} g\frac{\partial \zeta}{\partial x} dz = h_k g \frac{\partial \zeta}{\partial x} \tag{1.40}$$

The gradient is very naturally approximated with a central scheme which results in

$$h_k g \frac{\partial \zeta}{\partial x} \approx h_{i+\frac{1}{2},k} g \frac{\zeta_{i+1} - \zeta_i}{\Delta x_{i+\frac{1}{2}}} \tag{4.41}$$

Non-hydrostatic pressure gradient

Finally the non-hydrostatic pressure is integrated over the layer as follows

$$\int_{z_{k-\frac{1}{2}}}^{z_{k+\frac{1}{2}}} \frac{\partial p}{\partial x} dz = \frac{\partial}{\partial x}\int_{z_{k-\frac{1}{2}}}^{z_{k+\frac{1}{2}}} p dz - p_{k+\frac{1}{2}}\frac{\partial z_{k+\frac{1}{2}}}{\partial x} + p_{k-\frac{1}{2}}\frac{\partial z_{k-\frac{1}{2}}}{\partial x} \tag{1.42}$$

The integral on the right hand side is approximated with the midpoint rule, combined with central differences and reordering of the terms this results in

$$\int_{z_{k-\frac{1}{2}}}^{z_{k+\frac{1}{2}}} \frac{\partial p}{\partial x} dz \approx \frac{h_{i+1,k}\bar{p}^z_{i+1,k} - h_{i,k}\bar{p}^z_{i,k}}{\Delta x_{i+\frac{1}{2}}} - \bar{p}^x_{i+\frac{1}{2},k+\frac{1}{2}} \frac{z_{i+1,k+\frac{1}{2}} - z_{i,k+\frac{1}{2}}}{\Delta x} + \bar{p}^x_{i+\frac{1}{2},k-\frac{1}{2}} \frac{z_{i+1,k-\frac{1}{2}} - z_{i,k-\frac{1}{2}}}{\Delta x} \tag{4.43}$$

where

$$\bar{p}^x_{i+\frac{1}{2},k+\frac{1}{2}} = \frac{p_{i,k+\frac{1}{2}} + p_{i+1,k+\frac{1}{2}}}{2} \text{ and } \bar{p}^z_{i,k} = \frac{p_{i,k+\frac{1}{2}} + p_{i,k-\frac{1}{2}}}{2} \tag{4.44}$$

Substituting the definition of $h_{i+\frac{1}{2},k}$ and some reordering of the terms shows that equation (4.43) is equivalent to a finite volume approximation of the non-hydrostatic pressure term.

Layer averaged momentum equation

Combining the equations (1.31), (4.37), (4.41) and (4.43) the layer averaged equation will now read

$$\begin{aligned} &\frac{\partial \bar{h}_{i+\frac{1}{2},k} u_{i+\frac{1}{2},k}}{\partial t} + \frac{\bar{q}^x_{j+1,k} u_{i+1,k} - \bar{q}^x_{j,k} u_{i,k}}{\Delta x_{i+\frac{1}{2}}} + u_{i+\frac{1}{2},k+\frac{1}{2}} \bar{\omega}^x_{i+\frac{1}{2},k+\frac{1}{2}} - u_{i+\frac{1}{2},k-\frac{1}{2}} \bar{\omega}^x_{i+\frac{1}{2},k-\frac{1}{2}} + \bar{h}_{i+\frac{1}{2},k} g \frac{\zeta_{i+1} - \zeta_i}{\Delta x_{i+\frac{1}{2}}} + \\ &\frac{h_{i+1,k}\bar{p}^z_{i+1,k} - h_{i,k}\bar{p}^z_{i,k}}{\Delta x_{i+\frac{1}{2}}} - \bar{p}^x_{i+\frac{1}{2},k+\frac{1}{2}} \frac{z_{i+1,k+\frac{1}{2}} - z_{i,k+\frac{1}{2}}}{\Delta x} + \bar{p}^x_{i+\frac{1}{2},k-\frac{1}{2}} \frac{z_{i+1,k-\frac{1}{2}} - z_{i,k-\frac{1}{2}}}{\Delta x} = 0 \end{aligned} \tag{4.45}$$

Unfortunately this equation is not expressed in the primitive variable u. To achieve this we consider a different version of the layer averaged continuity equation (4.25). This can be rewritten using the definition of ω to

$$\frac{\partial \bar{h}_k}{\partial t} + \frac{\partial q_k}{\partial x} + \omega_{k+\frac{1}{2}} - \omega_{k-\frac{1}{2}} = 0 \tag{4.46}$$

Now similar to Stelling and Duinmeijer [5.13] we consider a discrete version of the layer averaged continuity equation centered on an u-point.

$$\frac{d\bar{h}_{i+\frac{1}{2},k}}{dt} + \frac{\bar{q}^x_{i+1,k} - \bar{q}^x_{i,k}}{\Delta x} + \bar{\omega}^x_{i+\frac{1}{2},k+\frac{1}{2}} - \bar{\omega}^x_{i+\frac{1}{2},k-\frac{1}{2}} = 0 \tag{4.47}$$

Where

$$\bar{h}^x_{i+\frac{1}{2},k} = \frac{h_{i+1,k} + h_{i,k}}{2},\ \bar{q}^x_{i,k} = \frac{q_{i+\frac{1}{2},k} + q_{i-\frac{1}{2},k}}{2},\ q_{i+\frac{1}{2},k} = h_{i+\frac{1}{2},k} u_{i+\frac{1}{2},k} \text{ and } \bar{\omega}^x_{i+\frac{1}{2},k} = \frac{\omega_{i,k} + \omega_{i+1,k}}{2} \tag{4.48}$$

Multiplying equation (4.47) with $u_{i+\frac{1}{2},k}$ and substracting the result from equation (4.45)

$$\frac{du_{i+\frac{1}{2},k}}{dt}+\frac{\bar{q}^x_{j+1,k}u_{i+1,k}-\bar{q}^x_{j,k}u_{i,k}}{\bar{h}^x_{i+\frac{1}{2},k}\Delta x_{i+\frac{1}{2}}}-\frac{u_{i+\frac{1}{2},k}\left(\bar{q}^x_{j+1,k}-\bar{q}^x_{j,k}\right)}{\bar{h}^x_{i+\frac{1}{2},k}\Delta x_{i+\frac{1}{2}}}+\frac{u_{i+\frac{1}{2},k+\frac{1}{2}}\bar{\omega}^x_{i+\frac{1}{2},k+\frac{1}{2}}-u_{i+\frac{1}{2},k-\frac{1}{2}}\bar{\omega}^x_{i+\frac{1}{2},k-\frac{1}{2}}}{\bar{h}^x_{i+\frac{1}{2},k}}$$
$$-\frac{u_{i+\frac{1}{2},k}}{\bar{h}_{i+\frac{1}{2},k}}\left(\bar{\omega}^x_{i+\frac{1}{2},k+\frac{1}{2}}-\bar{\omega}^x_{i+\frac{1}{2},k-\frac{1}{2}}\right)+\frac{h_{i+1,k}\bar{p}^z_{i+1,k}-h_{i,k}\bar{p}^z_{i,k}}{\Delta x_{i+\frac{1}{2}}}-\bar{p}^x_{i+\frac{1}{2},k+\frac{1}{2}}\frac{z_{i+1,k+\frac{1}{2}}-z_{i,k+\frac{1}{2}}}{\Delta x} \tag{4.49}$$
$$+\bar{p}^x_{i+\frac{1}{2},k-\frac{1}{2}}\frac{z_{i+1,k-\frac{1}{2}}-z_{i,k-\frac{1}{2}}}{\Delta x}=0$$

This is our final expression for the semi-discrete momentum equation. It is (momentum) conservative and thus appropriate for the modelling of bores and breaking waves. Furthermore it does not contain a bed slope source term which prevents artificial circulations due to this term (see also Stelling and Duinmeijer 2002). As shown in Stelling and Duinmeijer (2002) equation (4.49) can be further simplified when upwind approximations are used which results in a very simple first order scheme for the advective terms.

4.3.4. Vertical momentum equation

The derivation of the semi-discrete vertical momentum equation is, unsurprisingly, very similar to the derivation of the semi-discrete horizontal momentum equation. The derivation is therefore treated in less detail. The only exception to this is the treatment of the pressure gradient term which will be dealt with in detail. The vertical momentum equation is given by

$$\frac{Dw}{Dt}+\frac{\partial p}{\partial z}=0 \tag{4.50}$$

Again the semi-discrete version of (4.50) is derived by considering separately (1) the time derivative (2) the advective terms and (3) the non-hydrostatic pressure terms.

Time derivative and advective terms

The time derivative is integrated over z_k to z_{k+1}.

$$\int_{z_k}^{z_{k+1}}\frac{\partial w}{\partial t}dz=\frac{\partial h_{k+\frac{1}{2}}w_{k+\frac{1}{2}}}{\partial t}-w\left.\frac{\partial z}{\partial t}\right|_{z_k}^{z_{k+1}} \tag{4.51}$$

Integrating the advective terms over the layer results in

$$\int_{z_k}^{z_{k+1}}\frac{\partial uw}{\partial x}+\frac{\partial w^2}{\partial z}dz=\frac{\partial}{\partial x}\left(h_{k+\frac{1}{2}}u_{k+\frac{1}{2}}w_{k+\frac{1}{2}}\right)+\left.w^2\right|_{z_k}^{z_{k+1}}-w\left.\frac{\partial z}{\partial x}\right|_{z_k}^{z_{k+1}} \tag{4.52}$$

Now similarly to the horizontal momentum equation ω is substituted into equation(4.52), combined with central differences this gives,

$$\int_{z_k}^{z_{k+1}} \frac{\partial uw}{\partial x} + \frac{\partial w^2}{\partial z} dz \approx \frac{\bar{q}^z_{i+\frac{1}{2},k+\frac{1}{2}} w_{i+\frac{1}{2},k+\frac{1}{2}} - \bar{q}^z_{i-\frac{1}{2},k+\frac{1}{2}} w_{i-\frac{1}{2},k+\frac{1}{2}}}{\Delta x} + \bar{\omega}^z_{i,k+1} w_{i,k+1} - \bar{\omega}^z_{i,k} w_{i,k}$$
$$+ w_{i.k+1} \left.\frac{\partial z}{\partial t}\right|_{z_{i.k+1}} - w_{i.k} \left.\frac{\partial z}{\partial t}\right|_{z_{i.k}} \tag{4.53}$$

Combining the equations (4.51) and (4.53) while subtracting the layer averaged continuity equation centred around the vertical velocity multiplied with $w_{i,k+\frac{1}{2}}$ results in:

$$\frac{dw_{i,k+\frac{1}{2}}}{dt} + \frac{\bar{\omega}^z_{i,k+1} w_{i,k+1} - \bar{\omega}^z_{i,k} w_{i,k}}{h^z_{i,k+\frac{1}{2}}} - \frac{w_{i,k+\frac{1}{2}}}{h^z_{i,k+\frac{1}{2}}} \left(\bar{\omega}^z_{i,k+1} - \bar{\omega}^z_{i,k} \right)$$
$$+ \frac{\bar{q}^z_{i+\frac{1}{2},k+\frac{1}{2}} w_{i+\frac{1}{2},k+\frac{1}{2}} - \bar{q}^z_{i-\frac{1}{2},k+\frac{1}{2}} w_{i-\frac{1}{2},k+\frac{1}{2}}}{\Delta x} - \frac{w_{i,k+\frac{1}{2}}}{\bar{h}^z_{i,k+\frac{1}{2}} \Delta x} \left(\bar{q}^z_{i+\frac{1}{2},k+\frac{1}{2}} - \bar{q}^z_{i-\frac{1}{2},k+\frac{1}{2}} \right) = 0 \tag{4.54}$$

Where

$$\bar{\omega}^z_{i,k} = \frac{\omega_{i,k+\frac{1}{2}} + \omega_{i+1,k-\frac{1}{2}}}{2}, \quad \bar{q}^z_{i+\frac{1}{2},k+\frac{1}{2}} = \frac{q_{i+\frac{1}{2},k} + q_{i+\frac{1}{2},k+1}}{2} \text{ and } \bar{h}^z_{i,k+\frac{1}{2}} = \frac{h_{i,k} + h_{i,k+1}}{2} \tag{4.55}$$

Finally we approximate the face values of w using a simple first order upwind approach.

Vertical pressure gradient

The vertical pressure gradient still needs to be approximated. In Stelling and Zijlema (2004) the Keller box scheme is employed which yields good results. However, in Haiyang (2007) it is concluded that when introducing advection and viscosity the resulting system sometimes becomes ill-posed[1]. To circumvent this here a compact method, or mehrstellen verfahren, is adopted. This is identical to the Keller box when advection is not included, and performs equally well for modelling waves.

The basis of this method lies in the coupling of the pressure gradients from two different interfaces given by

$$\left.\frac{\partial p}{\partial z}\right|_{z_{k+\frac{1}{2}}} + \left.\frac{\partial p}{\partial z}\right|_{z_{k-\frac{1}{2}}} \approx 2 \frac{p_{k+\frac{1}{2}} - p_{k-\frac{1}{2}}}{h_k} \tag{4.56}$$

Substituting this relation into the vertical momentum equation this gives

[1] Note that in the current implementation with an explicit scheme for the advective terms and no viscosity there is no risk of the system ever becoming ill-posed. However with future implementations in mind where this might change the compact method is adopted none the less.

$$\frac{dw_{k+\frac{1}{2}}}{dt} + 2\frac{p_{k+\frac{1}{2}} - p_{k-\frac{1}{2}}}{h_k} - \left.\frac{\partial p}{\partial z}\right|_{z_{k-\frac{1}{2}}} = F_{k+\frac{1}{2}}(w) \tag{4.57}$$

where $F_{k+\frac{1}{2}}(w)$ denotes a linear algebraic operator arising from the space discretisation of the convective terms.

This seems to be of little use as the problem now shifts to the determination of the vertical pressure gradient in the lower layer interface. However, by continuously substituting (4.56) for the unknown pressure gradient the vertical velocity is coupled to all pressure points below.

$$\frac{dw_{i,k+\frac{1}{2}}}{dt} + 2\sum_{m=0}^{k-1}\left[(-1)^m\left(\frac{p_{i,k+\frac{1}{2}-m} - p_{i,k-\frac{1}{2}-m}}{h_{i,k-m}}\right)\right] + (-1)^k \left.\frac{\partial p}{\partial z}\right|_{z_{i,\frac{1}{2}}} = F^w_{i,k+\frac{1}{2}} \tag{4.58}$$

To close the system an expression is needed for the vertical pressure gradient at the bottom. This is readily obtained when the bed is horizontal as the pressure gradient is zero in this case (in the absence of viscosity). When the bed has a slope this term can be eliminated using the kinematic boundary condition and the vertical momentum equation at the bottom.

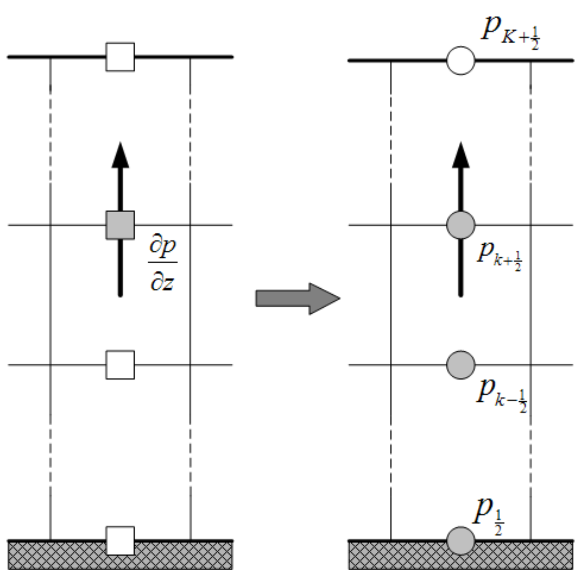

Figure 4-7 Substituting the Hermitian relation for the vertical pressure gradient couples the vertical momentum equation to all the lower pressure points.

The discrete version of the kinematic boundary condition at the bottom is given by:

$$w_{i,\frac{1}{2}} = u_{i,\frac{1}{2}} \frac{z_{i+\frac{1}{2},\frac{1}{2}} - z_{i-\frac{1}{2},\frac{1}{2}}}{\Delta x_i} \tag{4.59}$$

This combined with the vertical momentum equation at the bottom gives the expression for the non-hydrostatic pressure gradient at the bottom:

$$\left.\frac{\partial p}{\partial z}\right|_{z_{i,\frac{1}{2}}} = -\frac{du_{i,\frac{1}{2}}}{dt}\frac{z_{i+\frac{1}{2},\frac{1}{2}} - z_{i-\frac{1}{2},\frac{1}{2}}}{\Delta x_i} + F^w_{i,\frac{1}{2}} \tag{4.60}$$

Combining the equations in (4.58) and (4.60) leads to the semi-discrete vertical momentum equation.

$$\begin{gathered}\frac{dw_{i,k+\frac{1}{2}}}{dt} + 2\sum_{m=0}^{k-1}\left[(-1)^m\left(\frac{p_{i,k+\frac{1}{2}-m} - p_{i,k-\frac{1}{2}-m}}{h_{i,k-m}}\right)\right] \\ +(-1)^{k-1}\left(\frac{du_{i,\frac{1}{2}}}{dt}\frac{z_{i+\frac{1}{2},\frac{1}{2}} - z_{i-\frac{1}{2},\frac{1}{2}}}{\Delta x_i} - F(w)_{i,\frac{1}{2}}\right) + F(w)_{i,k+\frac{1}{2}} = 0\end{gathered} \tag{4.61}$$

The advective terms are here again summarized using $F_{i,k+\frac{1}{2}}(w)$. Notice that all the vertical momentum equations now contain a contribution from the bottom advective term due to the applied relation.

4.4. Time discretisations

In principle there are many variants possible for the time discretisation of equations which where presented in 4.3. Here a variant of the well known explicit Leapfrog scheme combined with a first order explicit time step for the advective terms and a first order implicit time step for the non-hydrostatic terms is used. The main reasons for doing this where: (1) ease of implementation (2) accuracy of the scheme with regards to wave propagation and (3) the accurate simulation of the waves required a relatively small time stepping anyway.

For the coupling between the momentum equations and the free surface gradient the scheme by Hansen (1956) is used. This scheme is an adaptation of the well known Leapfrog scheme. In the traditional Leapfrog scheme both the velocity and surface elevation are evaluated at the same time level. The Hansen scheme distinguishes itself by evaluating the velocity components at half time steps while the surface elevation is still evaluated at whole time steps.

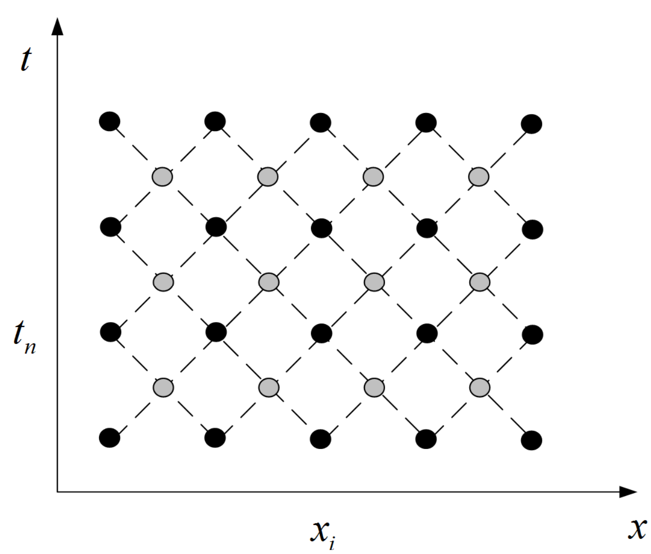

Figure 4-8 The Hansen scheme introduces a staggering in both space and time between the free surface (Black dots) and the horizontal velocity (grey points).

This eliminates the need to store three time levels which is needed in the traditional leapfrog scheme and makes the algorithm easy to implement. As the Hansen scheme is a variant of the Leapfrog scheme it shares the property of this scheme that it dampens wave like solutions only very weakly.

For the advective terms a first order accurate explicit scheme is used while for the non-hydrostatic pressures a first order implicit scheme is employed. Interestingly the backward Euler method did not result in any observable wave dampening in any of the test cases and was found to be sufficiently accurate for time steps approaching the stability limit of the explicit schemes.

Due to the explicit approximations the stability of the resulting model is bound by the Courant-Friedrichs-Levy (CFL) condition. This places a stability restriction on the maximum time step. Especially when considering steady state solutions this can place an unacceptable restriction on the time step which has lead many authors to consider implicit time stepping techniques (for instance Cassulli 1999). However, it is expected that the accurate simulation of propagating and breaking waves will lead to time steps which are well below the limit set by the CFL condition. This means that this condition is not restrictive in the current case. In a more general setting with larger variations in depth it is probably wise to use an implicit stepping instead.

4.4.1. Discrete momentum and continuity equations

Applying the Leapfrog method to the global continuity equation given in (4.24) will result in

$$\frac{\zeta_i^{n+1}-\zeta_i^n}{\Delta t}+\frac{H_{i+\frac{1}{2}}^n U_{i+\frac{1}{2}}^{n+\frac{1}{2}}-H_{i-\frac{1}{2}}^n U_{i-\frac{1}{2}}^{n+\frac{1}{2}}}{\Delta x_i}=0 \tag{4.62}$$

Notice that to remove the non-linearity the discharge at the half time step is approximated with $H_{i+\frac{1}{2}}^{n+\frac{1}{2}} U_{i+\frac{1}{2}}^{n+\frac{1}{2}} \approx H_{i+\frac{1}{2}}^n U_{i+\frac{1}{2}}^{n+\frac{1}{2}}$. For a moment ignoring the non-hydrostatic pressures the horizontal momentum equation is written as follows.

$$\frac{u_{i+\frac{1}{2},k}^{*}-u_{i+\frac{1}{2},k}^{n+\frac{1}{2}}}{\Delta t}+g\frac{\zeta_{i+\frac{1}{2}}^{n+1}-\zeta_{i-\frac{1}{2}}^{n+1}}{\Delta x}+F\left(u\right)_{i+\frac{1}{2},k}^{n+\frac{1}{2}}=0 \tag{4.63}$$

Where $F\left(u\right)_{i+\frac{1}{2},k}^{n+\frac{1}{2}}$ denotes the advection evaluated at the current time. The fact that the non-hydrostatic pressures have not been taken into account is indicated with an asterisk. If the model is run in the hydrostatic mode these are the equations which are solved and $u_{i+\frac{1}{2},k}^{n+\frac{3}{2}}$ is taken to be equal to $u_{i+\frac{1}{2},k}^{*}$. The vertical velocities are then approximated directly from the local continuity equation (4.28).

Using equation (4.63) as the definition of $u^*_{i+\frac{1}{2},k}$ the horizontal momentum equation with the non-hydrostatic pressure included becomes

$$\frac{u^{n+\frac{3}{2}}_{i+\frac{1}{2},k}-u^*_{i+\frac{1}{2},k}}{\Delta t}+\frac{h^{n+1}_{i+1,k}p^{n+\frac{3}{2}}_{i+1,k}-h^{n+1}_{i,k}p^{n+\frac{3}{2}}_{i,k}}{\Delta x_{i+\frac{1}{2}}}-p^{n+\frac{3}{2}}_{i+\frac{1}{2},k+\frac{1}{2}}\frac{z^{n+1}_{i+1,k+\frac{1}{2}}-z^{n+1}_{i,k+\frac{1}{2}}}{\Delta x_{i+\frac{1}{2}}}+p^{n+\frac{3}{2}}_{i+\frac{1}{2},k-\frac{1}{2}}\frac{z^{n+1}_{i+1,k-\frac{1}{2}}-z^{n+1}_{i,k-\frac{1}{2}}}{\Delta x_{i+\frac{1}{2}}}=0 \quad (4.64)$$

Where the non-hydrostatic pressure terms are taken on new time level. Here it should be noted that the time step the pressure belongs to is somewhat arbitrary. If the pressure gradient is considered to be part of the current time step (or $n+\frac{1}{2}$) nothing changes in the solution method presented in 4.5 (apart from a replacement of $p^{n+\frac{3}{2}}_{i,k+\frac{1}{2}}$ by $p^{n+\frac{1}{2}}_{i,k+\frac{1}{2}}$).

Similar to the horizontal advection equation the vertical momentum equation can now be written as

$$\begin{aligned}&\frac{w^{n+\frac{3}{2}}_{i,k+\frac{1}{2}}-w^{n+\frac{1}{2}}_{i,k+\frac{1}{2}}}{\Delta t}+2\sum_{m=0}^{k-1}\left[(-1)^m\left(\frac{p^{n+\frac{3}{2}}_{i,k+\frac{1}{2}-m}-p^{n+\frac{3}{2}}_{i,k-\frac{1}{2}-m}}{h^{n+1}_{i,k-m}}\right)\right]\\&+(-1)^{k-1}\left(\frac{w^{n+\frac{3}{2}}_{i,\frac{1}{2}}-w^{n+\frac{1}{2}}_{i,\frac{1}{2}}}{\Delta t}-F(w)^{w,n+\frac{1}{2}}_{i,\frac{1}{2}}\right)+F(w)^{n+\frac{1}{2}}_{i,k+\frac{1}{2}}=0\end{aligned} \quad (4.65)$$

Where again an explicit stepping is used for the advective terms while the non-hydrostatic pressure is included implicitly. Equation (4.65) is solved for every vertical velocity including the one located at the free surface but excluding the vertical velocity at the bottom. The vertical velocity at the bottom is simply prescribed to be equal to the kinematic boundary condition (4.59).

Finally the form of the local continuity equation as given in (4.27) is integrated in time as:

$$\frac{h^{n+1}_{i,k}-h^n_{i,k}}{\Delta t}+\frac{h^n_{i+\frac{1}{2},k}u^{n+\frac{1}{2}}_{i+\frac{1}{2},k}-h^n_{i-\frac{1}{2},k}u^{n+\frac{1}{2}}_{i-\frac{1}{2},k}}{\Delta x_{i+\frac{1}{2}}}+\omega^{n+\frac{1}{2}}_{i,k+\frac{1}{2}}-\omega^{n+\frac{1}{2}}_{i,k+\frac{1}{2}}=0 \quad (4.66)$$

This expression will be used to determine $\omega^{n+\frac{1}{2}}_{i,k+\frac{1}{2}}$. From (4.19) is is known that $\omega_{i,\frac{1}{2}}=0$ and using (4.66) the other values can be calculated from the bottom up.

4.4.2. Stability

As noted before the explicit nature of the time stepping with regard to the free surface gradient and advection introduces a constraint on the maximum time step. This constraint is often referred to as the Courant-Friedrichs-Levy (CFL) condition. It expresses that the domain of dependence of the differential equation should be entirely contained in the numerical domain of dependence of the discretised equations. In other words, the numerical scheme defining the approximation in mesh point i must be able to include all the physical information which influences the behaviour of the system in this point. As the expressions for mesh point i as defined in 4.4.1 only contain contributions from its direct neighbours it follows that information can only be allowed to travel a distance of Δx in a time of Δt. This leads to the usual definition of the CFL condition[1]:

$$\sigma = \frac{c\Delta t}{\Delta x} \leq 1 \tag{4.67}$$

Where C is the velocity of information in the system which is given by the summation of the shallow water wave phase velocity and the contribution of the current:

$$C = \sqrt{gd} + |u_k| \tag{4.68}$$

Although in general the free surface waves will not travel with their shallow water velocity it does provide an upper bound and is thus a safe approximation. Equation (4.68) allows us to rewrite equation (4.67) into the wave courant number and the advection courant number or:

$$\sigma = \sigma_{adv} + \sigma_{wave} \leq 1 \text{ where } \sigma_{adv} = \frac{|u|\Delta t}{\Delta x} \text{ and } \sigma_{wave} = \frac{\sqrt{gH}\Delta t}{\Delta x} \tag{4.69}$$

The wave courant number is the dominant contribution under most circumstances and this can therefore safely be used to estimate the time step beforehand. Due to vertical advection the time step is also restricted by:

$$\frac{\omega \Delta t}{h} \leq 1 \tag{4.70}$$

Only under very small water layers and bore like solutions this forms any restriction on the time step.

4.4.3. Dynamic time step

Usually a time step is chosen beforehand which satisfies the CFL condition. This has the disadvantage that the worst case scenario determines the maximum time step which can be taken. During most of the simulation it is likely that a much larger time step is possible which means that the simulation is quite inefficient. To circumvent this problem the XBeach model uses a dynamically adjusted time step. The user supplies a value for the CFL condition beforehand and the program dynamically adjust the time step taken to adhere to this

[1] A more formal derivation based on the von Neumann method for stability analysis for the Leapfrog and explicit Euler scheme can be found in Hirsch (2007).

condition using the most up to date system state. In this way the largest possible time step is taken and more efficient time integration is the result.

With the extension to multiple layers and the addition of the non-hydrostatic pressure correction this mechanism was left in place. Only an additional check was added to ensure that condition (4.70) was also full filled.

4.5. Determining the non-hydrostatic pressure

From the previous paragraph it is clear that the evolution of the free surface location in time is determined by equation (4.63). In turn both velocity components at the new time level are determined from their respective momentum equations. In contrast to this the non-hydrostatic pressure does not have an equation which relates the new pressure to the pressure at the previous time level. This lack of an explicit equation is due to the assumption of incompressible flow which means there is no longer an equation of state which relates density to pressure.

In order to determine the pressure a different route has to be taken. From the principle of conservation of mass it was shown that the incompressible Euler equations have a divergence free flow field. Generally speaking equations (4.64) and (4.65) do not result in a divergence free field when neglecting the non-hydrostatic pressure terms. Thus the only term which ensures that the flow stays divergence free is the non-hydrostatic pressure.

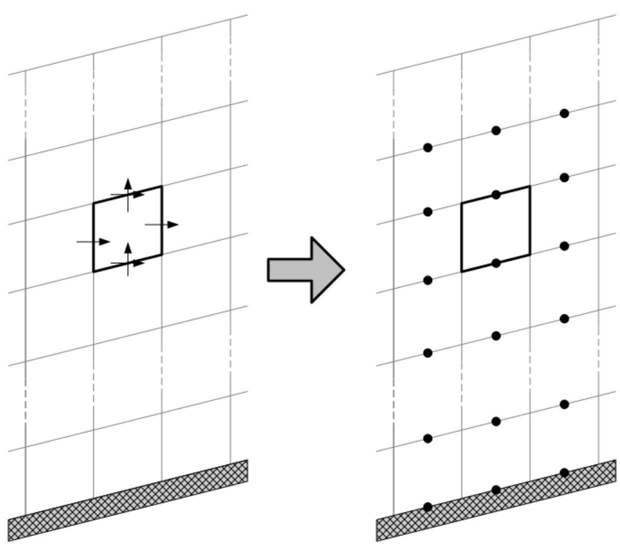

Figure 4-9 Substitution of the momentum equations for the velocities in the continuity equation gives the dependence of a cell on its surrounding pressure points.

The non-hydrostatic pressure can be calculated through the demand that the new velocity field is divergence free. To achieve this consider a control volume centered at i,k where the discrete local continuity equation reads

$$u^{n+\frac{3}{2}}_{i+\frac{1}{2},k} h^{n+1}_{i+\frac{1}{2},k} - u^{n+\frac{3}{2}}_{i-\frac{1}{2},k} h^{n+1}_{i-\frac{1}{2},k} + w^{n+\frac{3}{2}}_{i+\frac{1}{2},k+\frac{1}{2}} \Delta x_{i+\frac{1}{2}} - w^{n+\frac{3}{2}}_{i+\frac{1}{2},k-\frac{1}{2}} \Delta x_{i+\frac{1}{2}} \\ -\left(z^{n+1}_{i+\frac{1}{2},k+\frac{1}{2}} - z^{n+1}_{i-\frac{1}{2},k+\frac{1}{2}}\right) u^{n+\frac{3}{2}}_{i,k+\frac{1}{2}} + \left(z^{n+1}_{i+\frac{1}{2},k-\frac{1}{2}} - z^{n+1}_{i-\frac{1}{2},k-\frac{1}{2}}\right) u^{n+\frac{3}{2}}_{i,k-\frac{1}{2}} = 0 \tag{4.71}$$

Now substituting the momentum equations and kinematic boundary condition at the bottom into equation (4.71) for u and w results in an equation which relates the surrounding pressure points to the current control volume. Subsequently doing this for every control volume results into a system with $I \times K$ equations. This is the system which needs to be solved to calculate the pressure.

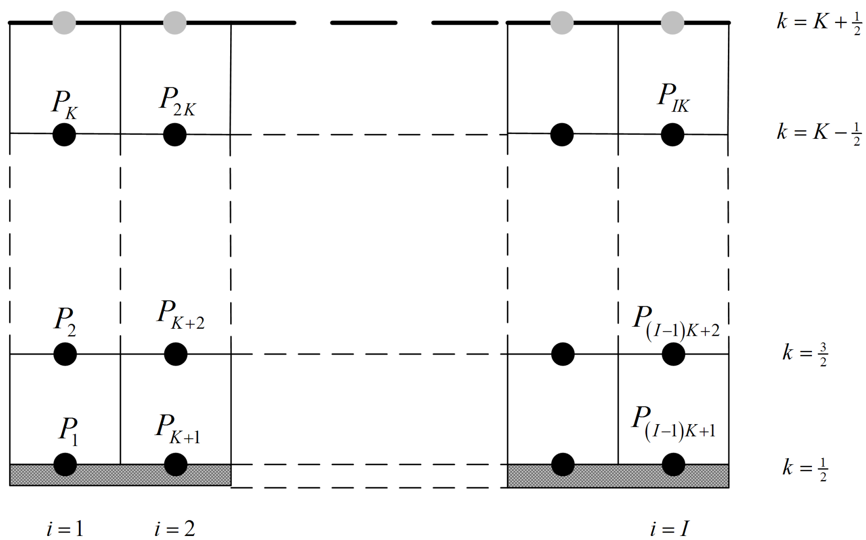

Figure 4-10 Renumbering the pressure points. Pressure points located at the free surface are excluded as they are known to be zero.

To solve this system it is convenient to first map the pressure points onto a single vector as this allows us to use standard linear algebra . Using

$$p_m = p_{i,k+\frac{1}{2}} \text{ with } m = (i-1)(K) + (k+1) \text{ where } i = 1....I \text{ and } k = 0...K-1 \tag{4.72}$$

The resulting system can be written in Matrix form. Let $\mathbf{A}$ denote the pressure coefficient matrix and $\mathbf{x}$ the vector containing the pressure points. Then the system is written as:

$$\mathbf{Ax} = \mathbf{q} \tag{4.73}$$

Where $\mathbf{q}$ is the right hand side resulting from equation (4.71) that contains the all the explicit contributions. The resulting matrix $\mathbf{A}$ has a block like structure as shown in Figure 4-11 for a case with two computational layers (or $K = 2$). Generally speaking the blocks have a width of $3K$ and a height of K. This means that the bandwidth of the matrix increases considerably when multiple layers are used. On the other hand for the case of a single layer the system reduces exactly to a tridiagonal system.

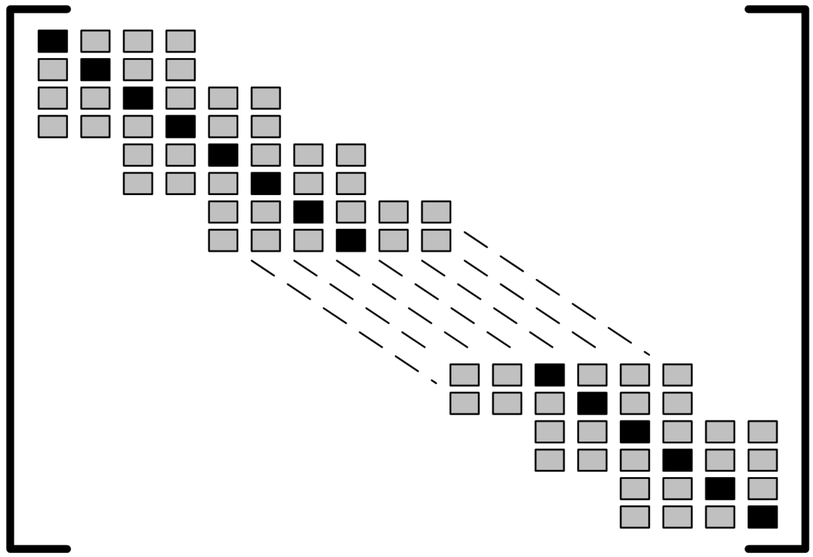

Figure 4-11 The resulting matrix after the momentum equations have been substituted into the local continuity equation

Solving the discrete version of the pressure Poisson equation thus obtained forms the largest computational burden for all but the single layer case. To solve this system a direct method has been used based on Gaussian elimination which sweeps the matrix into an upper triangular system and then uses back substitution to find the solution. Usually for large sparse matrices iterative solvers are employed as Gaussian elimination is far too expensive. However, the special block like structure of the matrix prevents fill in from becoming a problem. Therefore, as long as the bandwidth is not too large, Gaussian elimination proved to be sufficiently fast for the 2DV case.

4.6. Higher order spatial approximations

Up until now extensive use has been made of upwind approximation when interpolation of a variable was required. This in turn has lead to the situation that most expressions which are second order approximation in their own right are reduced to first order accuracy in space. (See for instance paragraph 4.3.1). These first order approximations might lead to unacceptably small grid sizes as upwind discretisations are known to introduce large amounts of numerical diffusion.

A logical step to improve this is to use higher order interpolation instead and the obvious choice is to use an central scheme to interpolate the variable in question. This is an acceptable choice when the variable in question is sufficiently smooth. Unfortunately the application of a central scheme on the advective terms will give rise to unphysical behaviour near discontinuities. The most striking result of this is the appearance of new maxima (or wiggles) in the solution, which were not present in the initial situation. This can be especially harmful when the considered variable is physically bounded, such as concentration, and the numerical oscillations can lead to negative values.

The generation of these unwanted maxima is closely related to the notion of monotonicity introduced by Gudonov. This essentially states that a numerical solution should have monotone behaviour, whereby the new solution value u_i^{n+1} should not reach values outside the range covered by the solution values u_{i+j}^n . If the scheme is monotone, no new extrema are created other than those already present in the solution.
It was also Gudonov who showed that all linear monotone schemes for the convection equation are at most first order. A proof of this can be found in Hirsch (2007).

In the current application the free surface and velocity field are usually smooth enough that the application of a higher order scheme will not cause any problems. The one exception to this is when the waves brake and propagate as bores. In this case a discontinuity in the variables is introduced and the higher order approximations can no longer be used. Thus the possibility of discontinuities forces the use of upwind approximations in order to accurately represent such a discontinuity with the side effect that a small grid spacing is required in order to control numerical diffusion.

To solution to this dilemma was first introduced by Van Leer and revolves around the notion that nonlinear schemes can fulfill the concept of monotonicity and still be of higher order then one. The basic idea is to control the generation of the over- and undershoots by preventing gradients to exceed certain limits. To achieve this certain functions are introduced, called limiters, which when encountering a discontinuity, locally reduce to scheme to first order. On the other hand when the field is locally smooth the limiter applies the second order approximation.

4.6.1. The minmod limiter

In the traditional sense limiters are mainly used as so called flux-limiters where they control the accuracy of the finite difference scheme. In the current implementation they have been implemented as a way to control the interpolation of the various variables in the model. In this case they are usually referred to as slope limiters, but the effect they have is very similar.

One of the simplest limiters which is often applied is the so called minmod limiter. This limiter bases the choice to use either second order upwind, first order upwind or central interpolation, on the ratio between successive gradients. Let's for instance assume the free surface location $\zeta_{i+\frac{1}{2}}$ need to be interpolated from the surrounding points. Furthermore, let

$U > 0$, then the two successive gradients are: $\Delta\zeta_{i+\frac{1}{2}} = \zeta_{i+1} - \zeta_i$ and $\Delta\zeta_{i-\frac{1}{2}} = \zeta_i - \zeta_{i-1}$. The ratio of these two gradients is given by

$$r_i = \frac{\zeta_{i+1} - \zeta_i}{\zeta_i - \zeta_{i-1}} \tag{4.74}$$

The choice between central, first order upwind or second order upwind interpolation is now made on the basis of the value of r_i, where an important condition is that the value of the interpolated $\zeta_{i+\frac{1}{2}}$ is contained between $\min(\zeta_{i-1}, \zeta_i, \zeta_{i+1}) \le \zeta_{i+\frac{1}{2}} \le \max(\zeta_{i-1}, \zeta_i, \zeta_{i+1})$. In other words, no new extreme value is introduced.

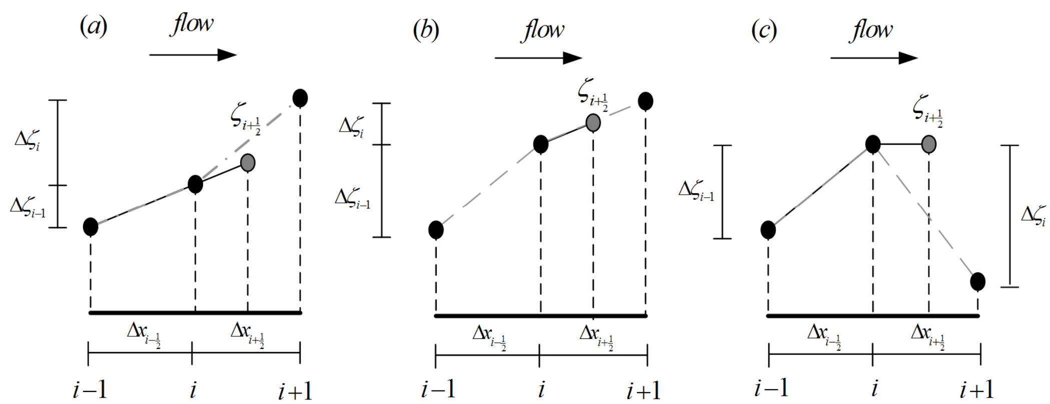

Figure 4-12 Minmod limiter with the three scenario's for the successive gradients for positive flow and the scheme applied. (a) second order upwind extrapolation (b) central interpolation and (c) upwind interpolation

If $r \le 0$ there might be a discontinuity present and to avoid the generation of unwanted wiggles the scheme is reduced to first order (Figure 4-12c) . Note that this also means that near the top of for instance a sinusoidal wave, which is continuous, the limiter still detects a possible discontinuity and switches to first order.

When $0 < r_i \le 1$, the upwind gradient is larger than the central gradient. In this case the smallest of the two (central) is used to interpolate (Figure 4-12b). Finally for $r_i > 1$ the second order upwind scheme is used (Figure 4-12a).

The minmod limiter as described above can be defined as:

$$\Psi(r) = \begin{cases} \min(r,1) & \text{if } r > 0 \\ 0 & \text{if } r \le 0 \end{cases} \tag{4.75}$$

where r is the ratio between the successive gradients. Using this definition the interpolation of the free surface location as described above can be given by

$$\zeta_{i+\frac{1}{2}} = \zeta_i + \tfrac{1}{2}\Psi(r_i)(\zeta_i - \zeta_{i-1}) \qquad (4.76)$$

Where r_i is defined as in (4.74). This expression for the free surface is second order accurate when the solution is smooth and only reduces to first order in the case of a discontinuity. Note that the water depth the limiter is only applied to the free surface, and not to location of the bottom to ensure positive water depths (see 4.7.2).

The minmod limiter is certainly not the only limiter available and a good overview of the available choices and their derivation is present in Hirch (2007). It was found that the minmod limiter performed adequately in most test cases and no investigation was made if other alternatives might be better candidates.

4.6.2. Second order interpolations

Interpolation in the horizontal when needed was performed with the minmod limiter as described in the previous paragraph. An overview of the slope limiter when applied to different variables is given in Table 5-1. Expressions are given for both positive and negative flow directions.

		Extrapolation	r_i
$\zeta_{i+\frac{1}{2},k}$	$U \geq 0$	$\zeta_i + \frac{1}{2}\Psi(r)(\zeta_i - \zeta_{i-1})$	$\dfrac{\zeta_{i+1} - \zeta_i}{\zeta_i - \zeta_{i-1}}$
	$U < 0$	$\zeta_{i+1} - \frac{1}{2}\Psi(r)(\zeta_{i+2} - \zeta_{i+1})$	$\dfrac{\zeta_{i+1} - \zeta_i}{\zeta_{i+2} - \zeta_{i+1}}$
$u_{i,k}$	$U \geq 0$	$u_{i-\frac{1}{2}} + \frac{1}{2}\Psi(r)\left(u_{i-\frac{1}{2}} - u_{i-\frac{3}{2}}\right)$	$\dfrac{u_{i+\frac{1}{2},k} - u_{i-\frac{1}{2},k}}{u_{i-\frac{1}{2}} - u_{i-\frac{3}{2}}}$
	$U < 0$	$u_{i+\frac{1}{2},k} - \frac{1}{2}\Psi(r)\left(u_{i+\frac{3}{2},k} - u_{i+\frac{1}{2},k}\right)$	$\dfrac{u_{i+\frac{1}{2},k} - u_{i-\frac{1}{2},k}}{u_{i+\frac{3}{2},k} - u_{i+\frac{1}{2},k}}$
$w_{i+\frac{1}{2},k+\frac{1}{2}}$	$U \geq 0$	$w_{i,k+\frac{1}{2}} + \frac{1}{2}\Psi(r)\left(w_{i,k+\frac{1}{2}} - w_{i-1,k+\frac{1}{2}}\right)$	$\dfrac{w_{i+1,k+\frac{1}{2}} - w_{i,k+\frac{1}{2}}}{w_{i,k+\frac{1}{2}} - w_{i-1,k+\frac{1}{2}}}$
	$U < 0$	$w_{i+1,k+\frac{1}{2}} - \frac{1}{2}\Psi(r)\left(w_{i+2,k+\frac{1}{2}} - w_{i+1,k+\frac{1}{2}}\right)$	$\dfrac{w_{i+1,k+\frac{1}{2}} - w_{i,k+\frac{1}{2}}}{w_{i+2,k+\frac{1}{2}} - w_{i+1,k+\frac{1}{2}}}$

Table 4-1 Various extrapolations based on the minmod limiter.

Notice that switching between upwind approximations and the approximations using the minmod limiter can be achieved by simply returning zero for the limiter for all values of r_i when a certain flag is set in the program code.

Interpolation in the vertical direction is necessary to obtain $u_{i+\frac{1}{2},k+\frac{1}{2}}$ and $w_{i,k}$ which are used in the momentum equations. Usually the number of layers in the vertical will be very small and it therefore doesn't make much sense to use higher order limited schemes. In this case a simple second order accurate central scheme was chosen when higher accuracy was demanded.

4.7. Flooding and drying

For the calculation of wave run-up and run-down on the beach, use of a moving boundary condition is required. Several strategies are available for the representation of the shoreline motion and examples which are often used in Boussinesq type models are: (1) allowing the grid to move in the horizontal similar to the grid movement in the vertical (2) a permeable-bed technique or (3) a Riemann solver based algorithm. A somewhat more detailed treatment on each of these techniques can be found in Stelling and Zijlema (2008) who also point out references for further reading into each of the techniques. In the present work the method proposed in Stelling and Duinmeijer (2003) is used which tracks the moving shoreline accurately using a very simple approach while guaranteeing non-negative water depths.

4.7.1. Staircase like bottom

Depth points are only defined at water level points and, just as the free surface, need to be interpolated to velocity points. For a positive downward defined depth the minimum of the surrounding depth points is taken or:

$$d_{i+\frac{1}{2}} = \min\left(d_i, d_{i+1}\right) \tag{4.77}$$

Using this definition the bottom can be represented as a series of tiles centred around a water level point with a width of Δx . An example is shown in Figure 4-13 which shows that the bottom has a staircase like appearance in this case.

This definition might seem a bit awkward as the bottom is assumed to be constant and therefore a second order interpolation seems more appropriate. It certainly is the case that second order interpolation will give more accurate results during simulations where flooding and drying isn't involved. However, when considering the possibility of a moving shoreline the definition in equation (4.77) leads to a smoother behaviour.

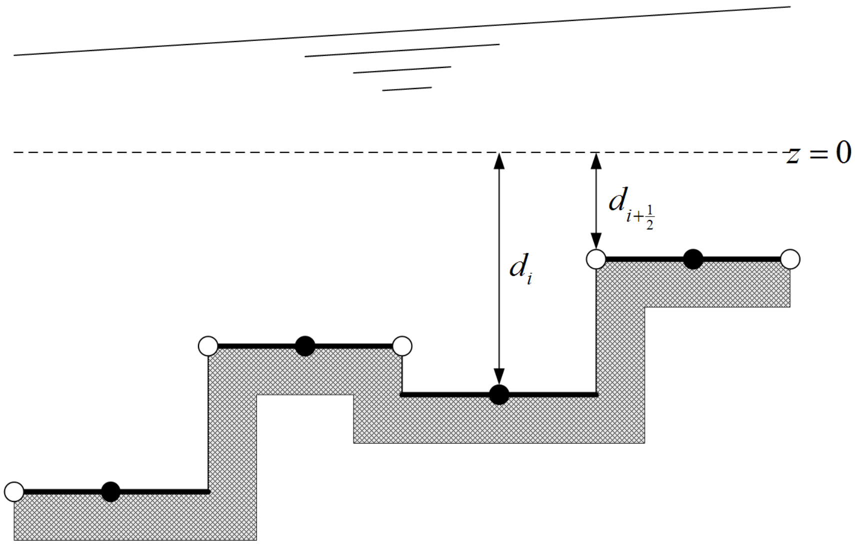

Figure 4-13 The bottom is represented as a series of tiles centred around a waterlevel point. This gives the description of the bottom a staircase like appearance.

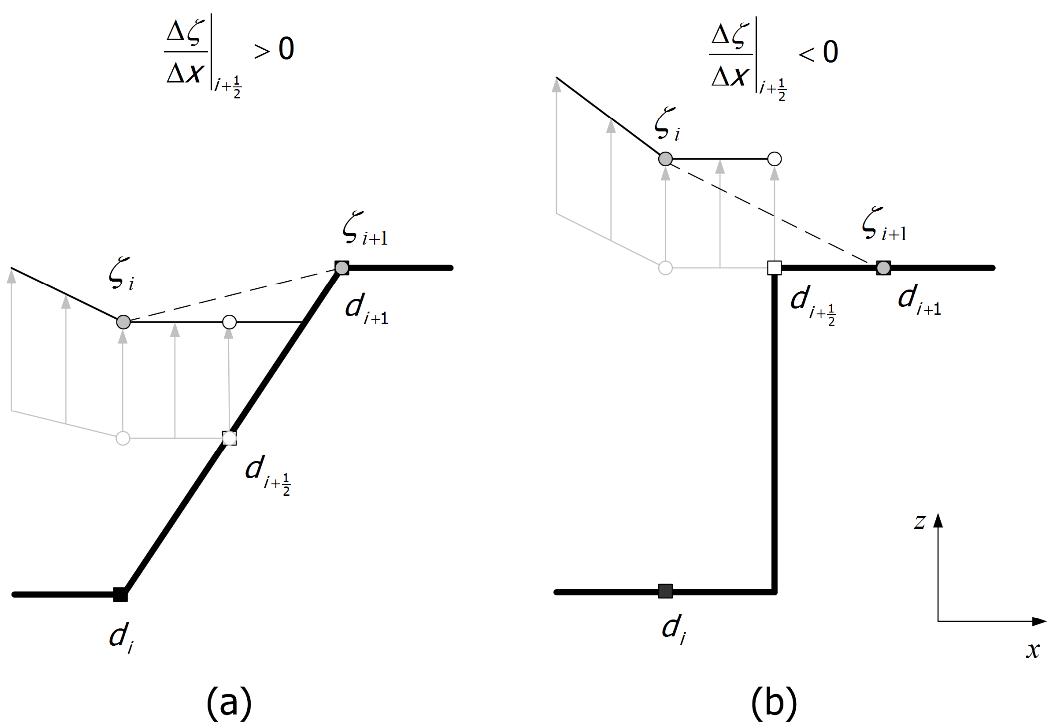

Figure 4-14 (a) Bottom at velocity point interpolated by central differences. When the velocity point becomes dry the free surface gradient works in the opposite direction to the incoming wave. (b) Interpolation using the minimum depth of the surrounding points. In this case the free surface gradient never opposes the incoming wave.

This can be illustrated by considering a rising water level near shore as depicted in Figure 4-14. As the water level in H_i increases it eventually rises above the bottom $d_{i+1/2}$. At this point the velocity $u_{i+1/2}$ becomes active. When $d_{i+1/2}$ is interpolated using a central scheme its value will lie below d_{i+1}. Since at this moment this point is still dry the free surface ζ_{i+1} is also located at the level d_{i+1}. Therefore

$$\frac{\zeta_{i+1} - \zeta_i}{\Delta x} > 0$$

But this means that, in the absence of advection, the velocity at $u_{i+1/2}$ will, for a short period in time, actually oppose the incoming current. This unphysical behaviour can be avoided if the bottom is interpolated using (4.77). This is visually illustrated in Figure 4-14b.

Other examples can be constructed during run off which also show that the current definition leads to better results and a much smoother behaviour during flooding and drying.

4.7.2. Positive water depths

An important consideration is that the water depth always has a positive value since negative water depths have no physical meaning. If negative water depths do occur special flooding and drying procedures are required which can be difficult to implement correctly and the loss of mass is a frequently encountered problem.

In Stelling and Duinmeijer (2003) a scheme is constructed which guarantees positive water depths. Following their derivation a slightly adapted form of the discrete global continuity equation (4.62) is considered:

$$H_i^{n+1} = H_i^n - \frac{U_{i+\frac{1}{2}}^{n+\frac{1}{2}}\Delta t}{\Delta x} H_{i+\frac{1}{2}}^n + \frac{U_{i-\frac{1}{2}}^{n+\frac{1}{2}}\Delta t}{\Delta x} H_{i-\frac{1}{2}}^n \tag{4.78}$$

For $U_{i+\frac{1}{2}}^{n+\frac{1}{2}} > 0$, assuming positive water depths, the new water depth will always be larger then zero if

$$1 - \frac{U_{i+\frac{1}{2}}^{n+\frac{1}{2}}\Delta t}{\Delta x} \frac{H_{i+\frac{1}{2}}^n}{H_i^n} \geq 0 \tag{4.79}$$

When upwind interpolation is used $H_{i+\frac{1}{2}}^n = \zeta_i^n + d_{i+\frac{1}{2}}$, combined with equation (4.77) this gives $H_{i+\frac{1}{2}}^n \leq H_i^n$. Using $H_{i+\frac{1}{2}}^n = H_i^n$ equation (4.79) becomes

$$1 - \frac{U_{i+\frac{1}{2}}^{n+\frac{1}{2}}\Delta t}{\Delta x} \geq 0 \tag{4.80}$$

This shows that positive water levels are guaranteed when the following condition is adhered to

$$\frac{U_{i+\frac{1}{2}}^{n+\frac{1}{2}}\Delta t}{\Delta x} \leq 1 \tag{4.81}$$

But equation (4.81) is precisely the CFL condition related to the stability of the advection and therefore poses no new time step limitation. This also shows that, using upwind interpolations, no special flooding and drying procedures are required. A similar expression can be derived for the case when $U_{i+\frac{1}{2}}^{n+\frac{1}{2}} < 0$.

When the limited expressions are used the easiest way to ensure positive water levels is to comply with (4.79), or for positive flow:

$$\frac{U_{i+\frac{1}{2}}^{n+\frac{1}{2}}\Delta t}{\Delta x} \leq \frac{H_i^n}{H_{i+\frac{1}{2}}^n} \tag{4.82}$$

This condition is more restrictive as the right hand side can now become smaller then one.
As the limiter is applied only to the water level and it generates no new maxima it is known that $\zeta_{i+\frac{1}{2}}^n$ is bounded by

$$\min\left(\zeta_i, \zeta_{i+1}^n\right) \leq \zeta_{i+\frac{1}{2}}^n \leq \max\left(\zeta_i^n, \zeta_{i+1}^n\right) \tag{4.83}$$

And since $d_{i+\frac{1}{2}} = \min\left(d_i, d_{i+1}\right)$ this shows that:

$$H_{i+\frac{1}{2}}^n \leq \max\left(H_i^n, H_{i+1}^n\right) \tag{4.84}$$

Therefore if the water depth does not chance drastically between two consecutive grid points equation (4.82) doesn't impose a heavy restriction on the time step. Generally speaking due to the wave CFL condition (4.69) the left hand side will be much lower than the right hand side anyway. Only when considering discontinuities there might be a problem. Fortunately, when considering discontinuities the scheme locally reduces to first order, which means (4.81) is once again applicable.

4.7.3. Flooding and drying criteria

If a point is either wet or dry is largely based on a very simple criteria. A velocity point is considered wet if the water level H_i is larger than an a priori determined threshold depth ε. Defining wet as one and dry as zero the function *wetu* is introduced defined as

$$wetu = \begin{cases} 1 \text{ if } H_{i+\frac{1}{2}} > \varepsilon \\ 0 \text{ if } H_{i+\frac{1}{2}} \leq \varepsilon \end{cases} \tag{4.85}$$

Notice that this function is only given for velocity points as a different criteria is used for water level points. If the velocity point under consideration is marked as being dry, all the horizontal velocities in the vertical are set to zero, and the momentum equations for this point are skipped. This also means that no coupling is introduced in the pressure coefficient matrix between i and $i+1$.

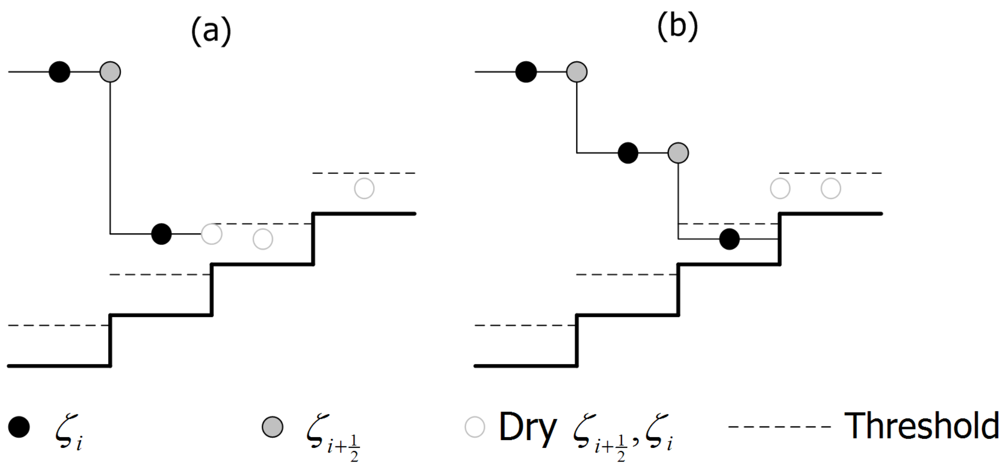

Figure 4-15 (a) A velocity point is considered dry if the total water depth is under a certain threshold. (b) A water level point is considered wet if any of the surrounding velocity points are wet, even if the water depth itself is below the threshold.

For ζ-points the global continuity equation is always applied, irrespective of if the point is considered wet or dry. Thus the state of the particular point only influences whether or not the vertical momentum equations and the pressure are calculated. Again the criteria could be similar as in (4.85). However, this could lead to some ambiguity regarding the pressure gradient in the bordering horizontal momentum equations. Therefore water level points are only set dry if both surrounding velocity points are dry. In this way the non-hydrostatic pressure gradient in the horizontal momentum equations is always defined and no artificial boundaries (e.g. $\frac{\partial p}{\partial x}=0$) need to be introduced. Similar to the function *wetu* the function *wet*ζ is introduced which is defined as:

$$wet\zeta_i = \begin{cases} 1 \text{ if } 1\text{-}\left(1\text{-}wetu_{i+\frac{1}{2}}\right)\left(1\text{-}wetu_{i-\frac{1}{2}}\right)=1 \\ 0 \text{ if } 1\text{-}\left(1\text{-}wetu_{i+\frac{1}{2}}\right)\left(1\text{-}wetu_{i-\frac{1}{2}}\right)=0 \end{cases} \tag{4.86}$$

If the point is considered dry (or $wet\zeta_i = 0$) then the vertical momentum equations are skipped and all the vertical velocities and non-hydrostatic pressures are set to zero. Furthermore the entries on the main diagonal in the pressure coefficient matrix are set to one and the right hand side is set to zero to prevent an undetermined system of equations in (4.73).

4.8. Boundary conditions

For the boundary conditions a distinction is made between open boundaries and closed boundaries. At open boundaries characteristics can either enter or leave the domain while at a closed boundary full reflection takes place. Of the two open boundary conditions proved to be the more challenging to implement and these will therefore be treated more extensively.

4.8.1. Incoming boundary

An unfortunate consequence of addition of non-hydrostatic pressures is that an extra degree of freedom is introduced in the equations. This means that if a time series of the free surface is used as an incoming wave signal the pressure has to be defined as well. This poses a problem as most measurements only include the free surface at the ocean boundary.

For fairly long incoming waves, where the non-hydrostatic pressures only play a role after the wave shoals, a reasonable approximation is to set the dynamic pressure to zero at the boundary and assume a hydrostatic pressure profile in the vertical. This approach becomes more problematic when short waves are considered. In Van Reeuwijk (2002) it is shown that the energy flux this boundary generates is:

$$F = Ec_o \text{ with } E = \tfrac{1}{2}\rho g a^2 \text{ and } c_0 = \sqrt{gd} \tag{4.87}$$

According to linear wave theory the time-averaged power transported through a vertical plane is equal to:

$$F = Enc \text{ With } n = \tfrac{1}{2} + \frac{kH}{\sinh 2kH} \tag{4.88}$$

Where n varies between $\tfrac{1}{2} \leq n \leq 1$. Since the shallow water phase velocity is always larger then the one obtained from the linear dispersion relation this means that the boundary will always generate to much wave power. This means a redistribution of the pressure will occur as soon as the wave enters the domain which results in an increase of the amplitude.

The easiest way to deal with this problem is to use the velocity as a boundary condition instead of the free surface. In this case no momentum equation is solved at the boundary. Therefore there is no more need to prescribe the free surface and pressure at the boundary anymore. This type of forcing works very well and does not introduce an increase in amplitude for linear waves. It does however require that the velocity is known at the boundary and, if multiple layers are used, information about the vertical distribution of the velocity. If no information on the vertical structure is present the same average velocity is used for all layers.

4.8.2. Absorbing boundary conditions

It is often beneficial if disturbances are allowed to freely leave the computational domain with minimal reflection. To achieve this so called absorbing boundary conditions are applied which are often based on the Sommerfeld radiation condition:

$$\frac{\partial f}{\partial t}+c\frac{\partial f}{\partial x}=0 \tag{4.89}$$

Where f represents the surface elevation and the velocity components and c is the wave phase velocity vector. Under long waves the phase velocity is set equal to the shallow water wave velocity and the Sommerfeld condition performs very well. In this case the Sommerfeld condition for very shallow water reads

$$u_{i+\frac{1}{2},k}-\sqrt{\frac{g}{H_{i+\frac{1}{2}}}}\zeta_{i+\frac{1}{2}}=0 \tag{4.90}$$

For short waves however the phase velocity is not easily extracted from the model results and the application of the Sommerfeld condition will lead to reflection. Instead of trying to improve condition (4.90) the choice was made to combine it with a so called sponge layer. When using a sponge layer a dampening term $\nu_{i+\frac{1}{2}}u_{i+\frac{1}{2}}$ is added to the horizontal momentum equation (4.63)

$$\frac{\delta u_{i+\frac{1}{2}}}{\delta t}+....+\nu_{i+\frac{1}{2}}u_{i+\frac{1}{2},k}=0 \tag{4.91}$$

Where ν is a dampening parameter for which the following form is chosen (Dingemans, 1997)

$$\nu=\hat{\nu}f_s\left(\frac{x-L_0}{L}\right)\equiv\hat{\nu}f_s\left(y\right) \tag{4.92}$$

With the shape function given by

$$f_s\left(y\right)=\begin{cases}\frac{1}{2}\tanh\left(\dfrac{\sin\left(\frac{\pi}{2}\left(4y-1\right)\right)}{1-\left(4y-1\right)^2}\right)+\frac{1}{2} & \text{if } 0\le y\le\frac{1}{2}\\ \frac{1}{2}\tanh\left(\dfrac{\sin\left(\frac{\pi}{2}\left(-4y-3\right)\right)}{1-\left(-4y-3\right)^2}\right)+\frac{1}{2} & \text{if } \frac{1}{2}\le y\le 1\\ 0 & \text{if } y<0 \text{ or } y>1\end{cases} \tag{4.93}$$

Where L denotes the length of the sponge layer which starts at $x=L_0$. This function is shown in shown in Figure 4-16.

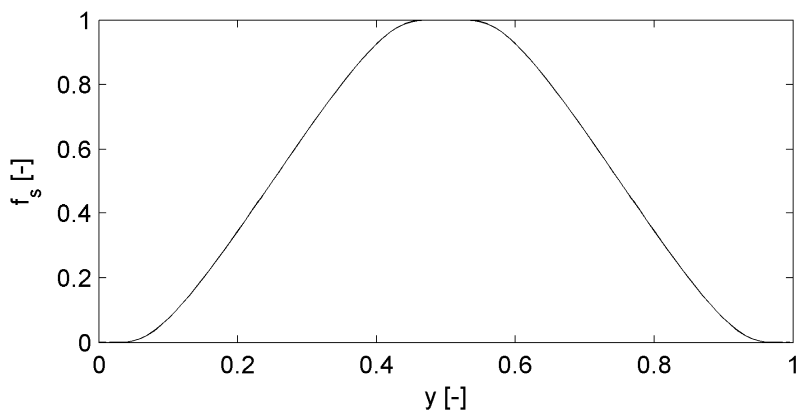

Figure 4-16 The shape function $f_s\left(y\right)$

Notice that the shape function goes to zero again towards the end of the sponge layer. This reduces the reflection of the sponge layer. It is important that the length of the sponge layer compared to the waves leaving the domain is not to short for two reasons: (1) if the sponge layer is not long enough there will be insufficient damping of the waves and (2) for short sponge layers the gradients in the dampening coefficient are large. This means that the dampening coefficient can vary substantially between grid points and this might induce reflection.

The combination of the Sommerfeld radiation condition (4.90) with the sponge layer results in a considerable reduction of the reflected waves. Incoming waves are first damped significantly by the sponge layer, which is most effective on the higher frequencies. The longer waves are then allowed to leave the domain using the radiation condition. Any reflected signal must then pass through the sponge layer again and the amplitudes are therefore diminished substantially. (Dingemans, 1997)

5. Validation and verification

In order to asses if the model is correctly implemented and to show that it can cope with the physically relevant processes the numerical model is compared to several problems which have an (approximate) analytical solution and results from experiments. In the next paragraphs the following cases will be considered:

1. Linear dispersion relation
2. Solitary wave propagation in a straight canal
3. The run-up of long waves on a plane beach
4. The dam break problem
5. Run-up of solitary waves on a plane beach

The first and second test consider the correct implementation of the non-hydrostatic model and its properties concerning wave propagation. The third test is used to verify the flooding and drying algorithm. The dam break problem is used to asses the accuracy of momentum conservative approximations. Finally the model is compared to experimental data of the run-up of solitary waves.

5.1. Linear dispersion relation

5.1.1. Numerical dispersion relation

The inclusion of the non-hydrostatic pressures introduces a coupling between the wave number and frequency into the classical NSWE. However, the dispersion relation that is represented by the numerical model in not exact and it is therefore necessary to asses how well the approximations perform. It is known that models based on the non-hydrostatic approach improve their dispersion relations by increasing the number of layers present in the model. But due to limited available processing power it is usually preferred to keep the number of layers as small as possible.

In order to investigate the dispersion relation present in the scheme a semi-discretisation in the vertical has been carried out for the linearized equations. Substituting harmonic solutions for the variables one is able to show that for the single layer case the dispersion relation resulting from the application of the compact scheme in the vertical is (see appendix A.2 for a full derivation)

$$\omega^2 = k\frac{gkH}{1+\frac{1}{4}(kH)^2} \tag{5.1}$$

This solution is very similar to the dispersion relations present in lower order Boussinesq models. For two computational layers the dispersion relation is given by (see appendix A.3 for a derivation)

$$\omega^2 = k\frac{\frac{1}{16}g(kH)^3 + gkH}{1+\frac{3}{8}(kH)^2+\frac{1}{256}(kH)^4} \tag{5.2}$$

Both solutions are drawn in Figure 5-1. It is immediately clear that using two layers improves the solution dramatically. In this case the error in the predicted phase velocity stays below 1% for $kh < 7.8$.

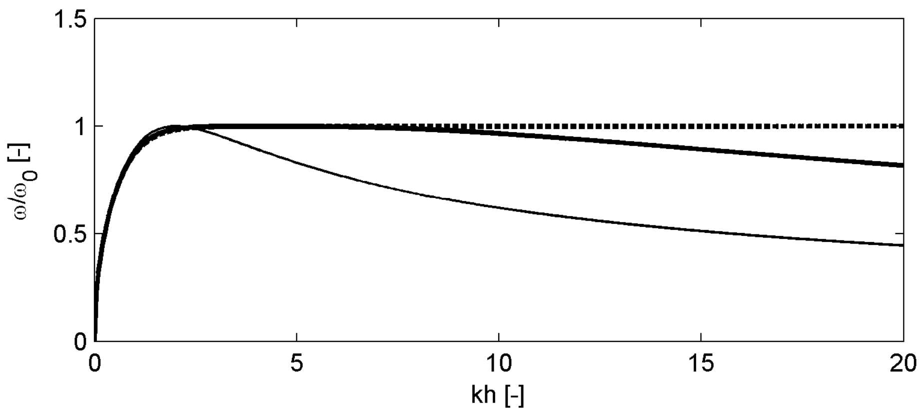

Figure 5-1 The analytical dispersion relation from linear wave theory (dotted line) compared against the dispersion relation using one layer (thin solid line) and the dispersion relation using two layers (thick solid line). Solution scaled with the deep water frequency.

Increasing the number of layers will result in an even better correspondence between the analytical solution and the numerical dispersion relations. It is expected that for waves considered in this study the two layer approach should be more than sufficient. Note that due to the semi-discrete approach the results obtained here are only truly valid for an exact scheme in the horizontal. Due to the approximations in the horizontal the results here can only be compared to solutions which have a high resolution in the horizontal.

5.1.2. Standing wave in basin

One of the standard tests in literature to test the dispersive properties of both models based on Boussinesq like equations and on the Non-hydrostatic approach is a standing linear wave in a basin.

In this test a closed two dimensional basin is considered with a depth a still water depth d and a width B . As an initial condition a sinusoidal wave is imposed as (see Figure 5-2). It is easily shown that the basin will display a standing wave pattern for waves with a wavelength of

$$L = \frac{B}{\frac{1}{2}n} \tag{5.3}$$

Where n is any positive integer. Since the dispersive characteristics are a function of the wavelength with regard to the depth, but independent of the standing wave pattern, n is set to one, which corresponds to the fundamental mode.

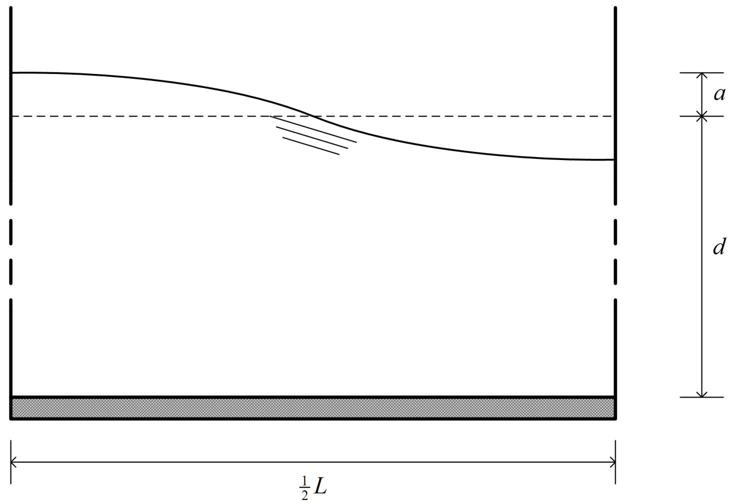

Figure 5-2 Initial condition for the standing wave in a basin

Choosing as an initial condition the sinusoidal wave

$$\zeta(x,0) = a\cos(kx) \tag{5.4}$$

The analytical solution is now given by equation (5.5) where a represents the amplitude of the standing wave, ω the angular frequency and k the wave number.

$$\zeta(x,t) = a\cos(\omega t)\cos(kx) \tag{5.5}$$

From linear wave theory the relation between ω and k is known and given by

$$\omega^2 = gk\tanh kh \tag{5.6}$$

Thus if both the width and the depth of the basin are known the movement of the initial disturbance given by (5.4) is completely determined by equation (5.5). The only restrictions are that the wave amplitude is small compared to the depth and that the wave steepness is small. Thus $\frac{a}{d} \ll 1$ and $\frac{a}{L} \ll 1$. $\Delta t \approx 0.002$

The dimensions of the basin are given in Table 5-1 together with the relative parameters which determine the wave movement. Notice that both the wave steepness and the ratio between the water depth and the wave height are taken to be much smaller as one, such that the wave can be regarded as a linear wave.

d [m]	a [m]	L [m]	$\frac{a}{d}$ [-]	$\frac{a}{L}$ [-]	kh [-]
10	0.001	20	0.0001	0.00005	π

Table 5-1 Parameters for the basin test

The domain is discretised using one hundred grid points with fully reflective closed boundaries. Furthermore the CFL condition is set to 0.1 which roughly corresponds with a mean time step of s. As an initial condition (5.4) is imposed with the velocities set to zero. The simulation is run for five wave periods using one and two computational layers.

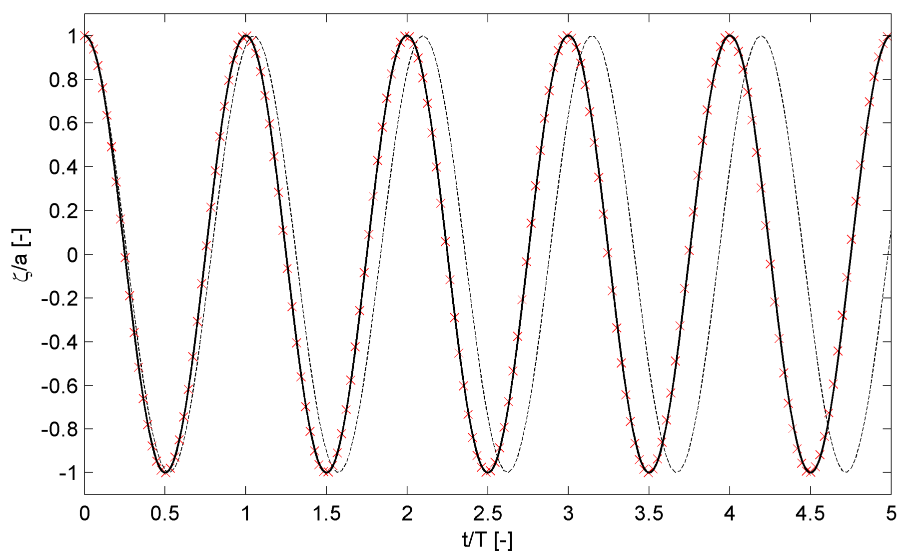

Figure 5-3 Free surface elevation at the start of the basin. Shown are the analytical solution (thick black line), results with one layer (thin black line) and the results with two layers (red crosses). Axis are made dimensionless with the analytical period T and the initial wave amplitude a.

In Figure 5-3 the free surface elevation as a function of time at the start of the basin is compared to the analytical solution. It appears that the solution using only a single layer has a slightly longer period which results in the ever increasing phase difference between the numerical and analytical solution. Using two computational layers there is no more visual difference between the analytical solution and the numerical results. Furthermore for both cases the amplitude of the wave remains constant in time, even when the simulation is extended.

Although the single layer model has a wave period which is slightly to long it is a considerable improvement with the hydrostatic model run. As the wave is already in relative deepwater the ratio between the analytical period and the period obtained using the shallow water equations is about $\frac{T_h}{T} = 0.5631$. This means that in this particular case using the hydrostatic assumption would result in a wave with a frequency which is almost twice as fast. In this light the improvement of the single layer model is already substantial.

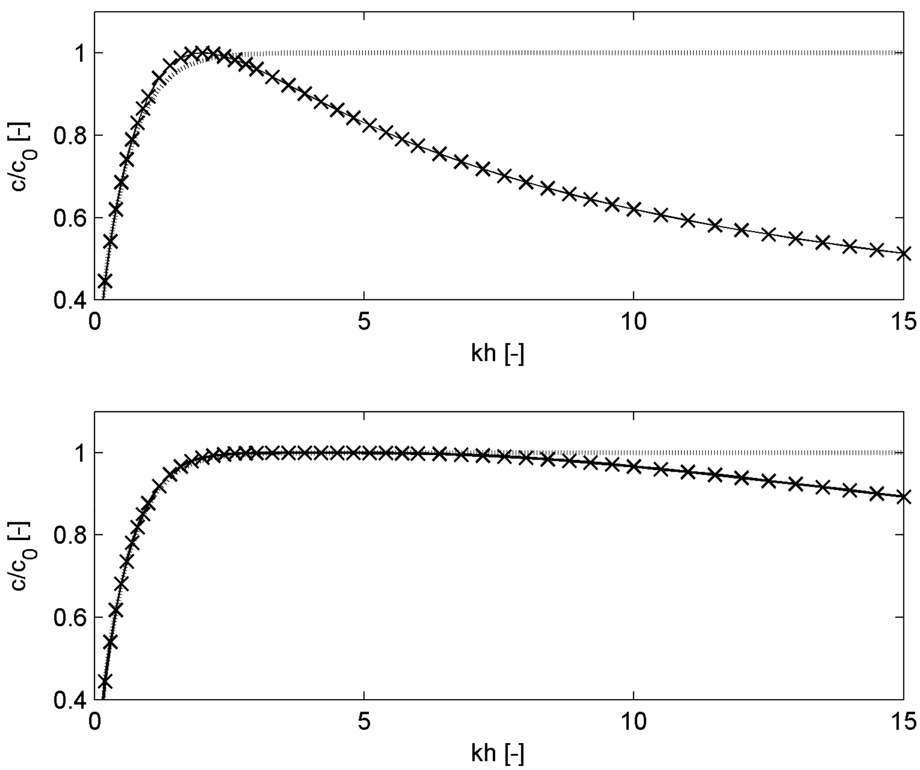

Figure 5-4 (**Top figure**) Comparing the wave celerity from the one layer model (solid line) with the analytical solution (dotted line) and the dispersion relation from (5.1) (Crosses). (**Bottom figure**) Comparing the wave celerity from the two layer model (solid line) with the analytical solution (dotted line) and the dispersion relation from (5.2) (Crosses).

In order to investigate the range for which the one and two layer model return valid results a similar setup as in Table 5-1 is used for a range of kh values. Keeping the wave length, and thus the basin width, constant the depth is gradually increased. In this way standing waves with a range of $0.1 \leq kh \leq 10$ where modelled with an interval of $\Delta kh = 0.1$. Thus a total of two hundred runs where performed for a setup with one- and two layers. Each of the individual runs had a length of ten wave periods. Using the distance between two consecutive upward zero-crossings in the time-signal as a measurement for the wave period the wave celerity for each run is determined. The results are made dimensionless with the deep water wave celerity given by:

$$c_0 = \frac{gT^2}{2\pi} \tag{5.7}$$

The results are presented in Figure 5-4 where the top figure represents result from the one layer case and the bottom figure the results using two layers. In both figures the solid line represents the model results, the dotted line the solution from linear wave theory and the crosses the solutions from paragraph 5.1.

The figure clearly shows that using two computational layers improves the results considerably and the model stays valid over a longer range. For values up to $kh \approx 1$ the single layer setup performs well.

A more objective measurement is found in Figure 5-5 which shows the relative error defined by

$$\varepsilon = \frac{c_n - c_a}{c_a} \tag{5.8}$$

Where c_n is the wave celerity as computed by the model and c_a the wave celerity from linear wave theory.

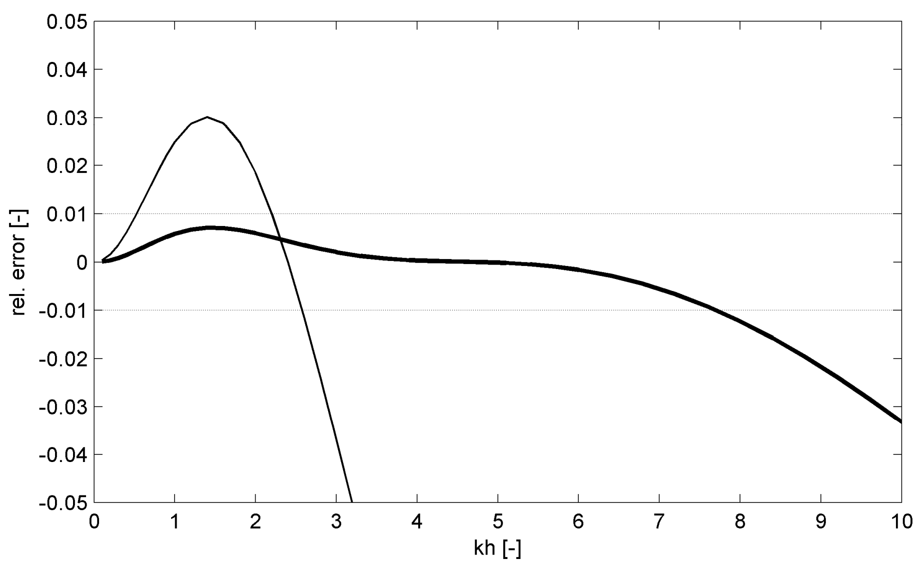

Figure 5-5 Relative error between respectively the analytical solution and the model using one layer (thin solid line), the analytical solution and the model using two layers (thick solid line) .

The relative error remains under 1% for the two layer model for values of kh of up to $kh \approx 7.8$. This is much less the case in the one layer setup which already has errors larger than 1% for $kh > 0.5$. Thus the two-layer model is more accurate and has a wider range of applicability at the cost of an increase in computing time. Therefore for long waves with $kh < 0.5$ the single layer model is appropriate while when shorter waves are expected two layers need to be used. If even more accuracy is required than the two-layer setup provides the number of layers can be increased even further, at the cost of more work per time step.

5.2. Solitary wave in channel

The solitary wave is a non-linear wave of finite amplitude with the characteristic property that it is neither preceded nor followed by any surface disturbance. An interesting aspect of this test is that the solitary wave is not a solution of the shallow water equations and, as such, cannot be reproduced in models based on the hydrostatic pressure assumption.

Furthermore, many laboratory experiments concerning tsunami run-up (including some featured in this report) use solitary waves as these are easy to generate under laboratory conditions. This makes that correct propagation of solitary waves is important.

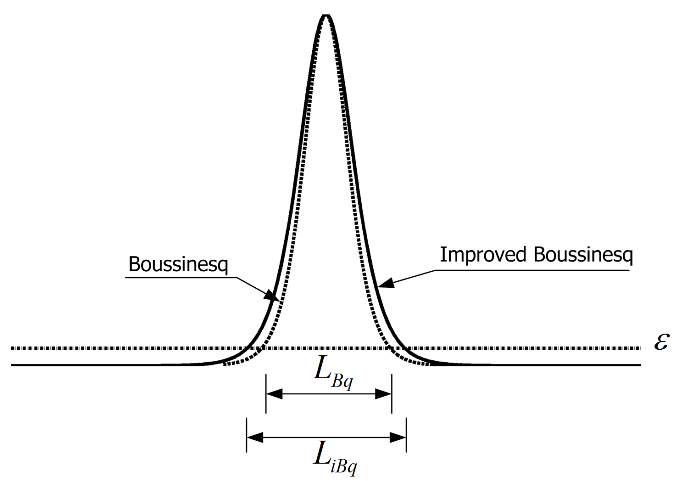

Figure 5-6 The solitary wave profile according to the Boussinesq (Bq) and improved Boussinesq equations (iBq). The iBq profile is slightly wider.

The explicit expressions for the surface elevation are dependent on the fundamental equations considered (e.g. de Korteweg de Vries equations or the improved Boussinesq equations) but all usually have a similar shape of the free surface elevation. An example is shown in Figure 5-6 comparing the solitary wave profile obtained from the Boussinesq and improved Boussinesq equations. More details regarding the various solitary wave solutions can be found in Dingemans (2000 p.p. 701-708).

The solitary wave solutions mentioned are only accurate for small waves where

$$\varepsilon \equiv \frac{\zeta_0}{d_0} \ll 1 \tag{5.9}$$

here ζ_0 is the amplitude of the solitary wave and d_0 the still water depth. As it is anticipated that larger waves need to be dealt with as well here a third order accurate solution is used due to Grimshaw (1971). This solution is obtained from a series expansion of the non-linear equation where all terms of order ε^4 are neglected. In this case the expression for the surface elevation becomes:

$$\begin{aligned}\frac{\zeta(x,t)}{d_0} &= \varepsilon s^2 - \tfrac{3}{4}\varepsilon^2 s^2 t^2 + \varepsilon^3\left(\tfrac{5}{8}s^2t^2 - \tfrac{101}{80}s^4t^2\right)\\ \alpha &= \sqrt{\tfrac{3}{4}\varepsilon}\left(1-\tfrac{5}{8}\varepsilon+\tfrac{71}{128}\varepsilon^2\right)\end{aligned} \tag{5.10}$$

Where $s = \operatorname{sech}\alpha x$ and $t = \tanh\alpha x$. The horizontal and vertical velocities become:

$$\begin{aligned}\frac{u}{\sqrt{gd_0}} &= \varepsilon s^2 + \varepsilon^2\left[\tfrac{1}{4}s^2 - s^4 + y^2\left(\tfrac{9}{4}s^4 - \tfrac{3}{2}s^2\right)\right]\\ &\quad+\varepsilon^3\left[-\tfrac{19}{40}s^2 - \tfrac{1}{5}s^4 + \tfrac{6}{5}s^6 + (1+z)^2\left(\tfrac{3}{2}s^2 + \tfrac{15}{4}s^4 - \tfrac{15}{2}s^6\right) + (1+z)^4\left(\tfrac{3}{8}s^2 - \tfrac{45}{16}s^4 + \tfrac{45}{16}s^6\right)\right]\\ \frac{w}{\sqrt{gd_0}} &= \sqrt{3\varepsilon}\,(1+z)\,t\left\{\varepsilon s^2 + \varepsilon^2\left[-\tfrac{3}{8}s^2 - 2s^4 + (1+z)^2\left(\tfrac{3}{2}s^4 - \tfrac{1}{2}s^2\right)\right]+\right.\\ &\quad\left.\varepsilon^3\left[-\tfrac{49}{640}s^2 + \tfrac{17}{20}s^4 + \tfrac{18}{5}s^6 + (1+z)^2\left(\tfrac{13}{16}s^2 + \tfrac{25}{16}s^4 - \tfrac{15}{2}s^6\right) + (1+z)^4\left(\tfrac{3}{40}s^2 - \tfrac{9}{8}s^4 + \tfrac{27}{16}s^6\right)\right]\right\}\\ \frac{c}{\sqrt{gd_0}} &= 1 + \tfrac{1}{2}\varepsilon - \tfrac{3}{20}\varepsilon^2 + \tfrac{3}{56}\varepsilon^3\end{aligned} \tag{5.11}$$

When terms of order ε^2 and above are ignored the Boussinesq solitary wave is retrieved.

Before continuing with the description of the test first a measurement for the width of the solitary wave is introduced. Since, in theory, the wavelength of the solitary wave is infinite another measure for the practical length of the wave is needed. Here an effective length is adopted which is defined as the distance between points of the profile, for which the height ζ is some small fraction of the wave height, or

$$L = 2\sqrt{\frac{3\zeta_0}{4d_0^3}}\,arc\cosh\left(sqrt\left(\frac{1}{\varepsilon}\right)\right) \tag{5.12}$$

where ε is a small fraction which is set to $\frac{1}{20}$. (See also Figure 5-6). For practical purposes the length is defined according to the Boussinesq profile. As this wavelength will only be used as a scaling parameter this is a reasonable approximation.

For the first test the channel is set to a depth of ten metres, with a length of fourteen wavelengths the initial profile is prescribed by the equations (5.10) and (5.11). The wave heights is set to one metre, which results in a depth to height ratio of 0.1 and a wavelength of $L \approx 79.5m$. The domain is discretised using 200 points per wavelength. At $t = 0s$ the wave is located at $x_0 = 2L$. The wave is now allowed to propagate over a distance of ten wavelengths and at the end of the test the resulting profile is compared to the theoretical profile. Simulations are run using one and two layers and the results are presented in Figure 5-8 to Figure 5-10.

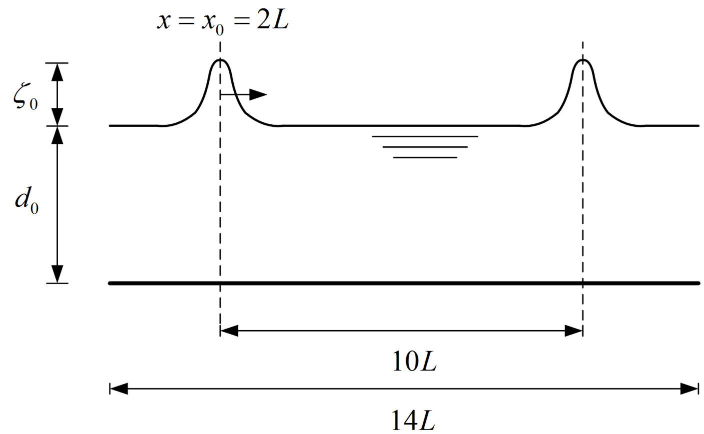

Figure 5-7 Overview of the solitary wave test

In Figure 5-8 the free surface obtained from the numerical simulations is compared to that of the theoretical profile as described by (5.10). First looking at the solution obtained with a single layer a small growth in amplitude of the wave is observed. Furthermore the wave has still not evolved into its final shape as it is still loosing some of the higher harmonics which are not correctly propagated. This also explains the change in profile of the wave as with the loss of these harmonics the wave is deformed. If the wave is allowed to propagate even further it does obtain a stable shape with a height comparable to the one in the figure. Finally it is noted that the propagation velocity is slightly too high.

When using two layers the situation is improved considerably as the wave now still has the correct shape and amplitude when compared to the analytical wave. Now there are now more visible trailing waves although at the start of the simulation the solitary wave still adapts itself slightly.

In Figure 5-9 the depth averaged velocity compared to the analytical solution is shown while in Figure 5-10 the comparison is made for the vertical velocities. Note that for the single layer model the vertical velocity is only shown at the free surface as there are no interior points in this case. Also be aware the vertical velocity points are defined on sigma iso-lines and not on planes of constant z.

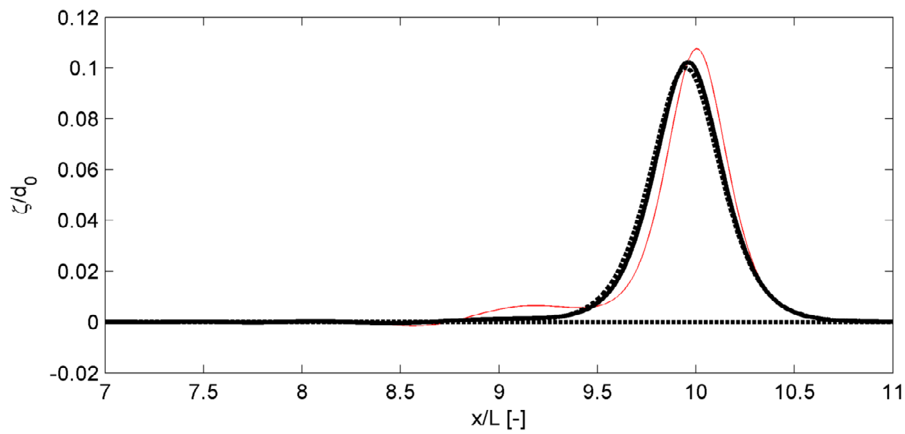

Figure 5-8 Free surface profile after propagation over ten wave lengths. Shown are the analytical solution (dotted line), the numerical solution using one layer (thin red line) and the numerical solution using two layers (thick black line).

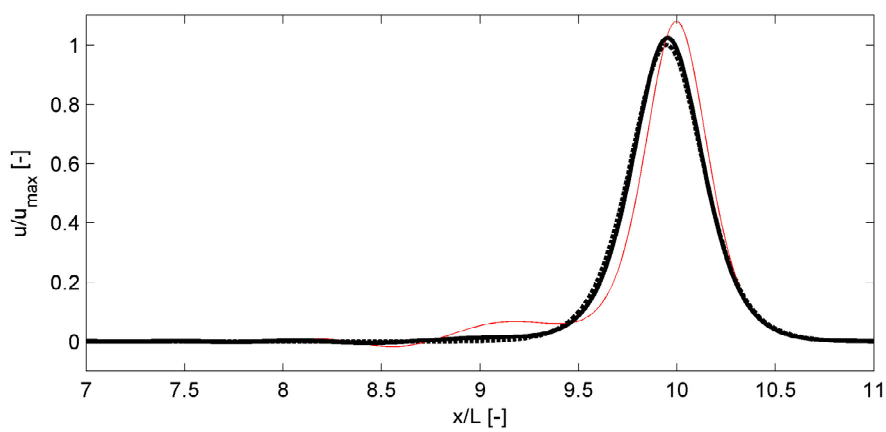

Figure 5-9 Velocity profile after propagation over ten wave lengths. Shown are the analytical solution (dotted line), the numerical solution using one layer (thin red line) and the numerical solution using two layers (thick black line).

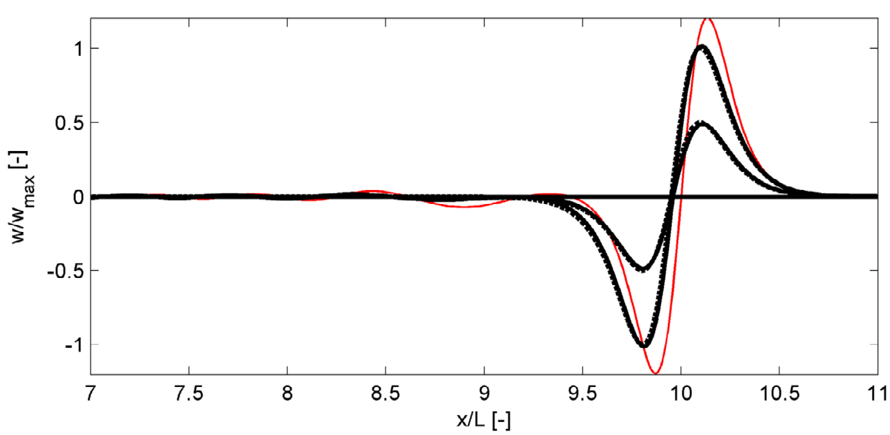

Figure 5-10 The vertical velocity profile after propagation over ten wave lengths. Shown are the analytical solution (dotted line), the numerical solution using one layer (thin red line) and the numerical solution using two layers (thick black line). Results are scaled with the maximum vertical velocity of the analytical solution. Notice that for the single layer model only the vertical velocity at the free surface is given.

With increasing height to depth ratios the nonlinearities play an increasingly vital role. Not only is the wave height now a significant portion of the total depth, but there is also a shortening of the typical horizontal length scales (see (5.12)).

Two more cases where modelled with $\varepsilon = 0.2$ and $\varepsilon = 0.3$. The free surface profiles at the end of the run are shown in Figure 5-11 and Figure 5-12.

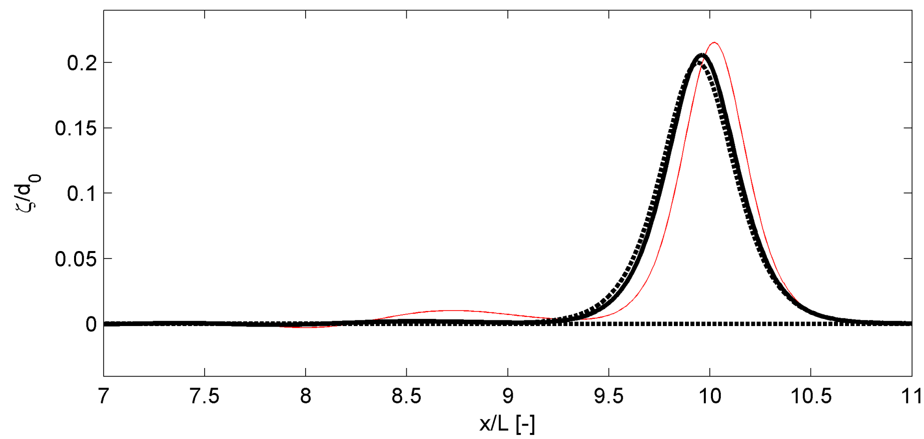

Figure 5-11 Solitary wave profile for $\varepsilon = 0.2$ Analytical solution by Grimshaw (striped black line) compared to the depth averaged model (red line) and the two layer model (thick solid black line).

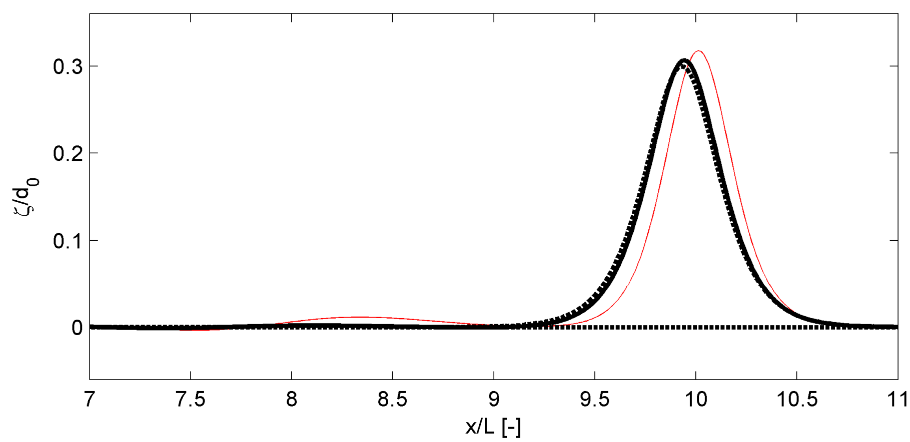

Figure 5-12 Solitary wave profile for $\varepsilon = 0.3$ Analytical solution by Grimshaw (striped black line) compared to the depth averaged model (red line) and the two layer model (thick solid black line).

The figures show a similar situation as before, where the depth averaged model shows a smaller higher wave profile while the two layer model fits the analytical solution very well. Furthermore the two layer model has no trailing waves which do show up in the depth averaged model.

5.3. Long waves on a beach

In order to asses the accuracy of the model in capturing the moving shoreline the model results are compared to an analytical solution by Carrier and Greenspan (1958). This case has been frequently considered in literature and recent examples of this include Zijlema and Stelling (2008) and Fuhrman and Madsen (2008).

The case considers an incoming long wave approaching a uniformly sloping beach with a steep slope relative to the wave. The wave fully reflects and a standing wave pattern is produced. Due to the non-linearity and the moving shoreline the resulting pattern differs significantly from a sinusoidal pattern. Carrier and Greenspan solved this situation for the dimensionless shallow water equations by means of a coordinate transformation. A derivation of their solution is presented in Mei (1989).

As the Carrier and Greenspan solution is based on the shallow water equations it only considers long waves for which the dispersive terms are physically small. It is therefore quite common to consider this case without either the Boussinesq or non-hydrostatic terms (e.g. Zijlema and Stelling, 2008). In contrast to this Fuhrman and Madsen (2008) did model the case with the Boussinesq approximations and concluded that these effects did indeed have a negligible impact on the result.

The model as described in this chapter is largely based on the formulations of Stelling and Zijlema (2008) and thus there is no reason to expect any difference in the results between the models. However, it is interesting to see if the non-hydrostatic pressure approach also has a negligible effect on the results. Therefore the model is run with the non-hydrostatic pressures enabled and using two computational layers.

The model area consisted of a sloping ($1/25$) beach with a still water depth of 5 m on the ocean boundary. On the boundary an incoming long wave was prescribed from linear wave theory with a wave height of 0.12 m and a wave period of 32 s. This corresponds to an incoming wave with a wavelength of 223.4 m and $kh \approx 0.14$. The area had a length (including dry areas) of 150 m and was simulated on a 1500 point grid. The CFL condition was set to 0.1 which roughly translates to a time step of $\Delta t \approx 0.001$ s. The relatively small grid spacing of $\Delta x = 0.1$ m was chosen so that a very high resolution was available in the run-up region. This was necessary to capture the solution with sufficient accuracy. The simulation was run for 400 seconds with the initial velocity field set to zero.

In Figure 5-13 the surface elevation from the numerical model and the analytical solution is drawn at different stages of the wave period. Figure 5-14 gives a similar picture for the depth averaged velocities while Figure 5-15 presents the horizontal location of the shoreline as a function of time.

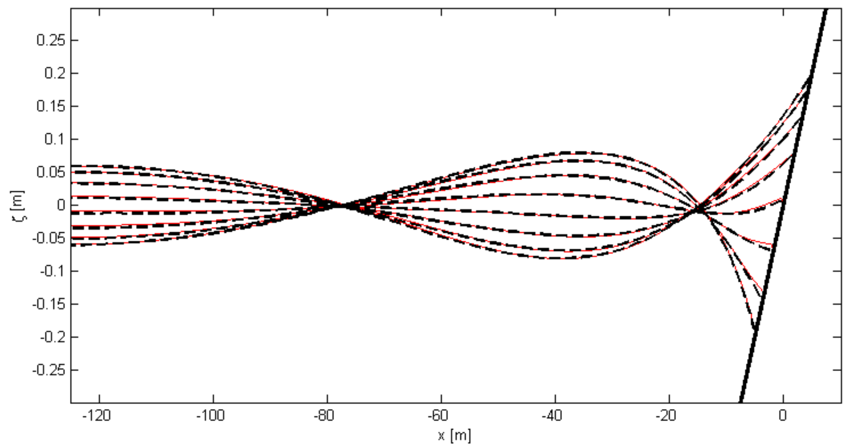

Figure 5-13 Surface elevation at different stages of the wave period. The analytical solution (black dashed line) is compared to the numerical results (solid red line).

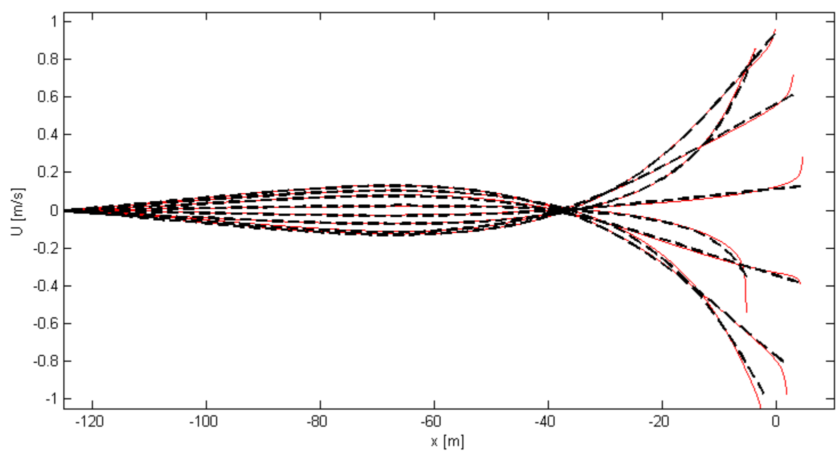

Figure 5-14 Depth averaged velocity at different stages of the wave period. The analytical solution (black dashed line) is compared to the numerical results (solid red line).

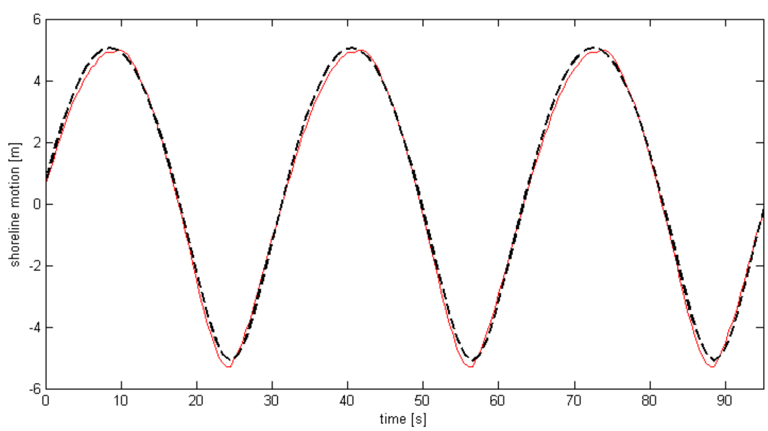

Figure 5-15 Location of the shoreline as a function of time. The analytical solution (black dashed line) is compared to the numerical results (solid red line).

The free surface profile shows an excellent agreement with the analytical solution. The location of maxima and the nodes is well represented. For the depth averaged velocities the agreement is good in the deeper part where the location of the node at the boundary and the second node is correctly reproduced. Near the shoreline the numerical model has a tendency to somewhat overestimate the depth averaged velocities, especially during the draw down of the wave. This is most likely due to the staircase like approximation of the bottom which in

this case results in smaller water depths in velocity points. Normally this difference is negligible when compared to the total water depth but near the shoreline this difference is more pronounced. Fortunately, due to the relatively small water depths involved, these differences with the analytical solution have a small impact on the overall solution. The movement of the shoreline is still represented very well as can be seen in Figure 5-15.

Finally it is observed that running the model with the non-hydrostatic approximations did not result in large differences with the analytical solution. This is as expected as was noted before since the dispersive terms are very small and is in agreement with the results obtained by Fuhrman and Madsen in a comparable configuration.

5.4. Dam break

In order to test if the implementation of the advection scheme is indeed momentum conservative the dam break case is considered. This case was also considered in Stelling and Duinmeijer (2003) where they showed that the depth averaged version of there conservative scheme indeed reproduces the dam break wave well.

The case considers two regions of fluid with different water levels and fluid velocities which are initially separated by a vertical wall. This mimics for example the case of a reservoir used for the generation of hydroelectric current where there is a small discharge through the structure. At t=0 the wall is suddenly removed and a flood wave enters the downstream portion of the canal.

The so called dry bed case was first considered by Ritter(1892) and considers a flat bed where the downstream region is completely dry and the initial velocities are zero in the upstream portion. He derived an analytical solution to this problem from the Saint-Venant equations. His solutions were later extended to incorporate a non-zero water level downstream with non-zero initial velocities (see for example Stoker 1952). Later contributions by Dresler(1952) and Whitham(1954) also added the influence of friction.

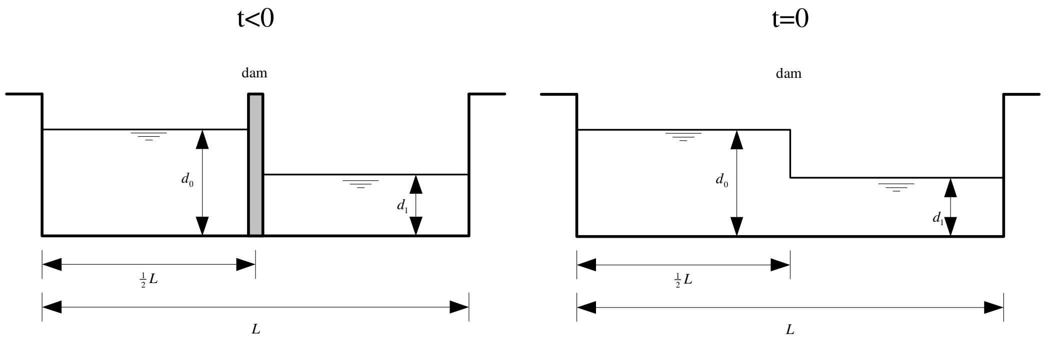

Figure 5-16 Dam break case. Two reservoirs are separated by a structure (left), but at t=0 suddenly the structure is removed (right).

For our purposes the friction is ignored and the model results are only compared to the wet and dry bed analytical solutions. For convenience only zero initial velocities are considered in the wet bed case.

In the absence of friction the only driving force is the gradient of the piezometric level. But since this gradient is zero in the vertical there shouldn't be any gradients in the horizontal velocities in the vertical. When a depth averaged approach is used this condition is naturally always met. However, when more layers are added, this can be violated when the numerical approximations are not considered carefully. Especially when using z-layers this is notoriously difficult to achieve in the presence of a jump discontinuity. Here it will be shown that in the hydrostatic case the sigma transformation very naturally conforms to this condition, even in the presence of a shock.

As noted the analytical solutions where derived from the Saint-Venant equations which in turn means that they implicitly contain the hydrostatic pressure assumption. As vertical accelerations are negligible everywhere except in the region of the discontinuity this seems justified. However, comparisons between the analytical solution and the non-hydrostatic version of the model are also made to see how the pressure correction technique behaves in the case of a discontinuity.

The computational domain consisted of two thousand grid points with an uniform grid spacing of $\Delta x = 0.05m$ and a total length of $L = 100m$. The dam was located at the centre of the domain ($x = 50m$). For both the dry and wet bed case the upstream water level was $d_0 = 1m$ while the downstream water level in the wet bed case was initially $0.1m$. The CFL condition was set to 0.1 which resulted in an average time step of about $\Delta t \approx 0.0014s$. Finally the flooding and drying threshold was set to $10^{-10}m$. This was necessary to capture the wave celerity in the dry bed case correctly.

Dry bed

Initially two different depth averaged scenario's where run for the dry bed case. One using upwind approximations while the other used a second order limited scheme. From Stelling and Duinmeijer (2002) it is already known that the momentum conservative depth averaged advection scheme should perform rather well and these tests where mainly used to verify the implementation. The results for the upwind scheme can also be considered representative for the original XBeach[1] code. The results for the dry bed case after seven seconds can been seen in Figure 5-17.

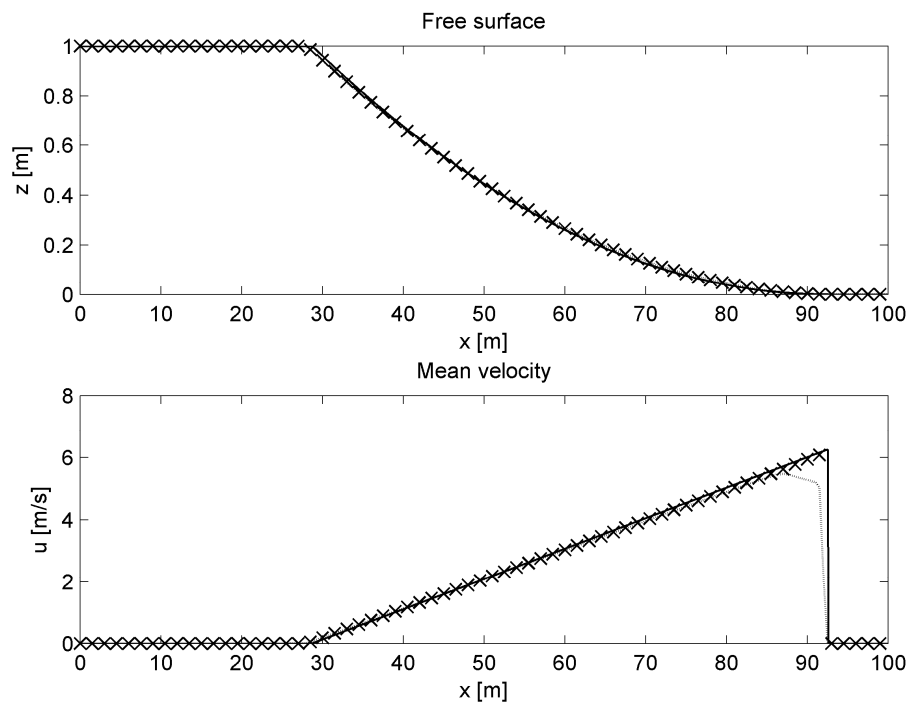

Figure 5-17 The location of the free surface (top figure) and the depth averaged velocity (bottom figure) at t=7 for the analytical solution(black solid line), upwind scheme(dotted line) and the minmod limited scheme(crosses).

The figure shows that both the upwind and limited schemes predict the free surface shape rather well. The velocity profile is less sharp in the case of upwind approximations while the second order limited scheme shows a small improvement in this respect. It should be noted that the differences become more profound when using a larger grid spacing. The second order scheme remains quite accurate when increasing the grid spacing while the first order upwind scheme becomes very inaccurate. This difference in behaviour is hardly surprising and well documented in literature.

[1] Although the expressions used are quite different in appearance they converge to the same solution when upwind interpolation is used.

Finally it is worthwhile mentioning that the minmod limiter successfully avoids the generation of wiggles near the discontinuity in the velocity which are typically generated when central difference schemes are used.

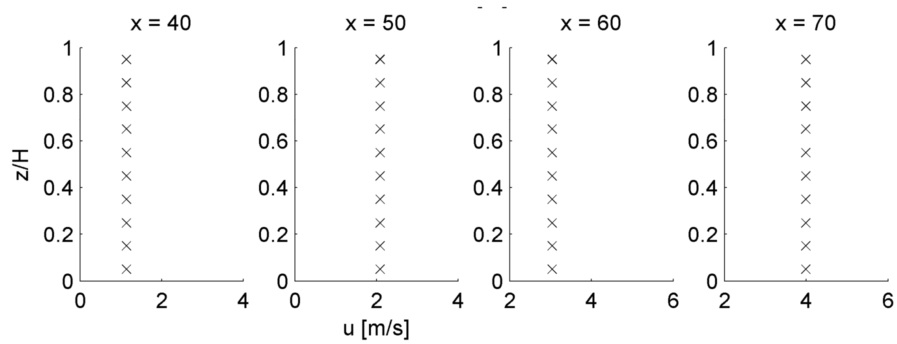

Figure 5-18 The vertical velocity profiles for the model using the minmod limiter at the indicated locations.

In Figure 5-18 the vertical velocity profiles are shown for a run using the minmod limiter with ten computational layers. The profiles clearly show that there is no variation in the horizontal velocity in the vertical. As was explained before this is correct in the absence of friction and this shows that the numerical model artificial gradients when confronted with shocks..

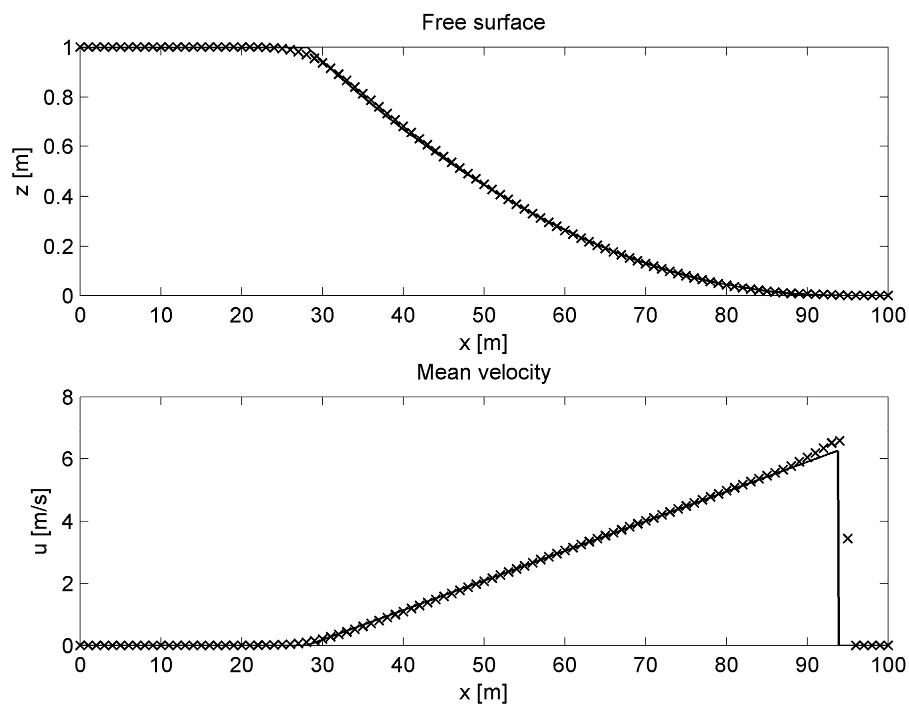

Figure 5-19 The location of the free surface (top figure) and the depth averaged velocity (bottom figure) at t=7 for the analytical solution(black solid line) and the minmod limited scheme(crosses) with the non-hydrostatic pressure correction enabled.

In Figure 5-19 the results with the non-hydrostatic pressure correction technique enabled is shown. Here again the free surface is predicted rather well. However, when looking at the depth averaged velocities, the wave front seems to have covered a larger distance. Furthermore it appears that the maximum attained velocities are higher when compared to the analytical solution. At this point it is yet unclear if the difference can be attributed to the hydrostatic pressure assumption in the analytical method, or if this is either a result from the numerical approximations used or implementation errors.

Wet bed

The results for the wet bed case are represented in Figure 5-20. Here the difference between the limited solution and the upwind approach are negligible which is due to the fine grid and therefore only the results using the minmod limiter are shown. The agreement with the analytical solution is excellent, also when the ratio between the up- and downstream levels is varied. Of more interest are the undulations which are produced by the non-hydrostatic solution. Here we can distinguish two different regions, (1) the undulations which remain stationary around the middle of the canal and (2) the undulations at the wave front.

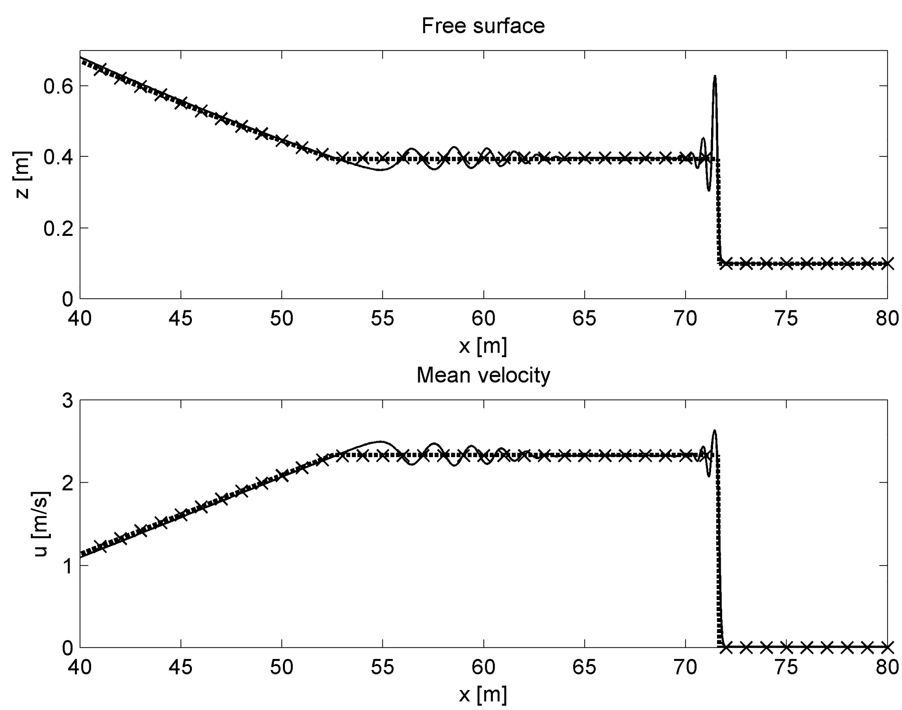

Figure 5-20 Depth integrated wet bed dam break. Upstream dept was one metre while the downstream depth was set to one tenth of a metre. Shown are the limited hydrostatic solution (crosses), the non-hydrostatic solution (solid line) and the analytical solution (thick black stripped line).

The initial straight front mathematically contains an infinite number of harmonics which propagate in both directions. Those harmonics for which the wave celerity equals the current velocity cannot travel upstream and show up as stationary waves in both space and time, these are the source of the undulations in region one. The source for the undulations in region two are most likely the leading harmonic, which travels with the front celerity and the trailing harmonics which do travel in the same direction as the front but whose celerity is lower. The absence of both types of undulations in the hydrostatic solutions is readily explained with the fact that all waves travel at the same velocity in hydrostatic models.

The extend and occurrence of the undulations is depended on the ratio d_0 / d_1. Furthermore the number of undulations which show up is dependent on the grid spacing, as this determines which wave components can be represented on the grid.

5.5. Run up of solitary waves

Synolakis (1986) performed several experiments involving the run-up of solitary waves on a beach. In these experiments solitary waves with depth to height ratios between $0.009 \leq \hat{\zeta} \leq 0.633$ ($\hat{\zeta} = \zeta_0 d_0^{-1}$) where generated and sent into the direction of a plane beach. For each of the depth to height ratios the maximum run-up was recorded. In the original experiment the water depth varied between $0.0625m \leq d_0 \leq 0.38m$. This was mainly done to investigate if the relative wave height is indeed a defining variable for the maximum run-up of solitary waves. As the measurements showed that the relative wave height, as a first approximation, does indeed define the relative run up the variance in the still water depth will be ignored from now on.

Unfortunately only the relative run-up heights compared to the relative wave heights where available for comparison. The wave data recorded by the wave gages and the snapshots of the free surface taken from video data where not listed in the rapport which was available. This means that there was little sense to try and model the experiment in detail as there was no data to compare to. Instead the choice was made to only keep the bathymetry information identical to the original experiment and then model a series of solitary waves with relative wave heights comparable as the ones in the experiment. Since the relative wave height is the dominant variable for the definition of the relative run-up these can be compared to the original experimental data. A definition sketch is given in Figure 5-21.

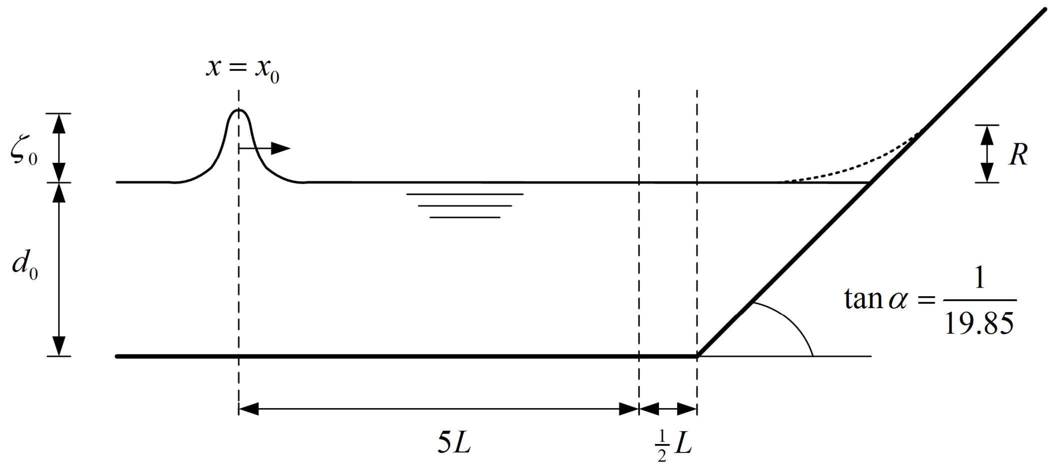

Figure 5-21 Sketch defining the run up of a solitary wave on a plane beach

For all experiments the still water depth was fixed at $d_0 = 0.1\text{m}$ and only the incoming wave height was varied. At $t = 0s$ the solitary wave was prescribed from the Boussinesq solitary wave profile as an initial condition in the free surface, horizontal and vertical velocity. The top of the wave was located five and a half wavelengths away from the toe of the beach (with the wavelength as defined in equation (5.12)). In this way the initial profile had a chance to evolve into its final stable form. This does mean that most waves (except the smallest ones) contained a small spurious tail. However, the front of the waves was smooth and therefore the maximum run up was most likely not significantly affected by the spurious oscillations.

Similar to the experiment the final wave height was measured at a distance of half a wave length away from the toe of the beach. Due to the varying solitary waves the total length of the area varied from experiment to experiment. However, each wave was modeled using the same number of 250 points per wavelength. The large number of points per wavelength where necessary because the higher approximations using the limiter resulted in less smooth run up behavior[1] during the run-up and run down of the wave. Using upwind approximations these instabilities where not encountered but now a high resolution was required until the simulations converged due to excessive numerical diffusion.

Using a CFL condition of $\sigma = 0.1$ the model was run long enough for the wave to leave the domain again. To facilitate this a non-reflective boundary was applied at the open end of the

[1] Using the minmod limiter with higher relative wave heights resulted in a small hump on the tip of the wave during run-up. Furthermore the draw down was accompanied with irregular flooding and drying, patches of the slope would fall dry while higher up the slope there was still water according to the model.

domain. All the simulations where run in the depth averaged mode of the model. A total of 63 waves where modeled starting with $\hat{\zeta} = 0.02$ and ending with $\hat{\zeta} = 0.65$

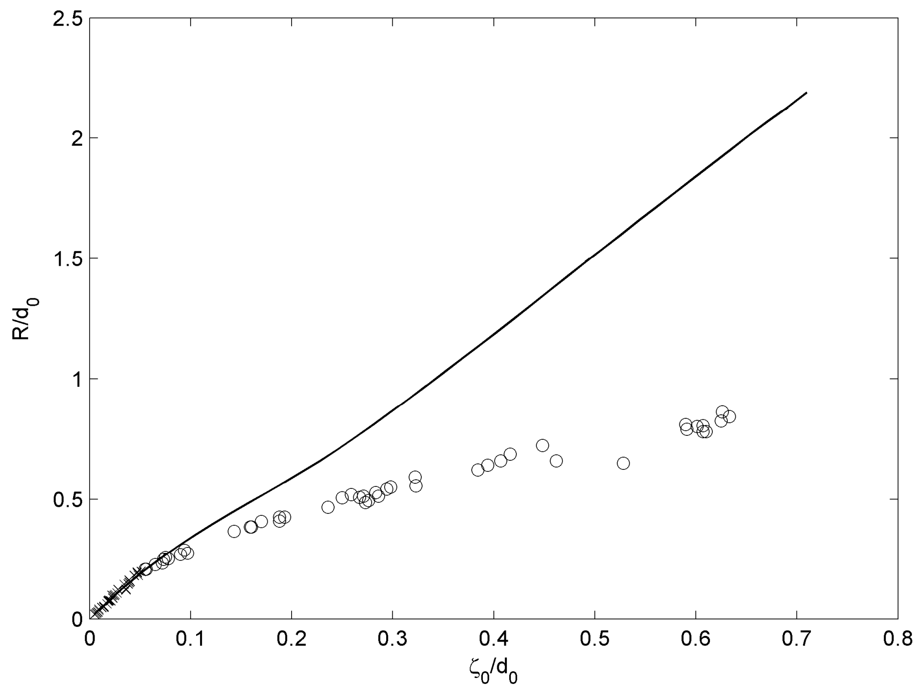

Figure 5-22 The relative run up of solitary waves on a plane 1/19.85 beach as a function of the relative wave height . Wave heights where measured half a wave length away from the toe of the beach. Breaking waves are marked with a circle while non-breaking waves are marked with a cross.

The results are presented in Figure 5-22 which shows the relative run up height as a function of the relative incoming wave height. It is immediately clear that the run up for the higher waves is grossly overestimated. For the highest waves modeled the run up as calculated by the model is more than two and a half times larger than the run-up that was measured. Interestingly it appears that the run-up is modeled accurately up to relative wave heights of about 0.1, which is also the point where breaking of the waves started to occur in the measurements.

The most likely cause for the large difference in computed and observed run-up is found in the absence of friction in the numerical model. As the broken wave runs up a mild slope, it travels as a fairly thin layer of water moving with a high speed. The front can be considered highly turbulent and this combined with the small water depths and high speeds means that friction indeed becomes important. This is also consistent with the results obtained by Lynett et al. (2002) who used a Boussinesq model to compute the run-up. They also found that the inclusion of bottom friction is indeed important in this case and their results without bottom friction where similar to the results obtained here.

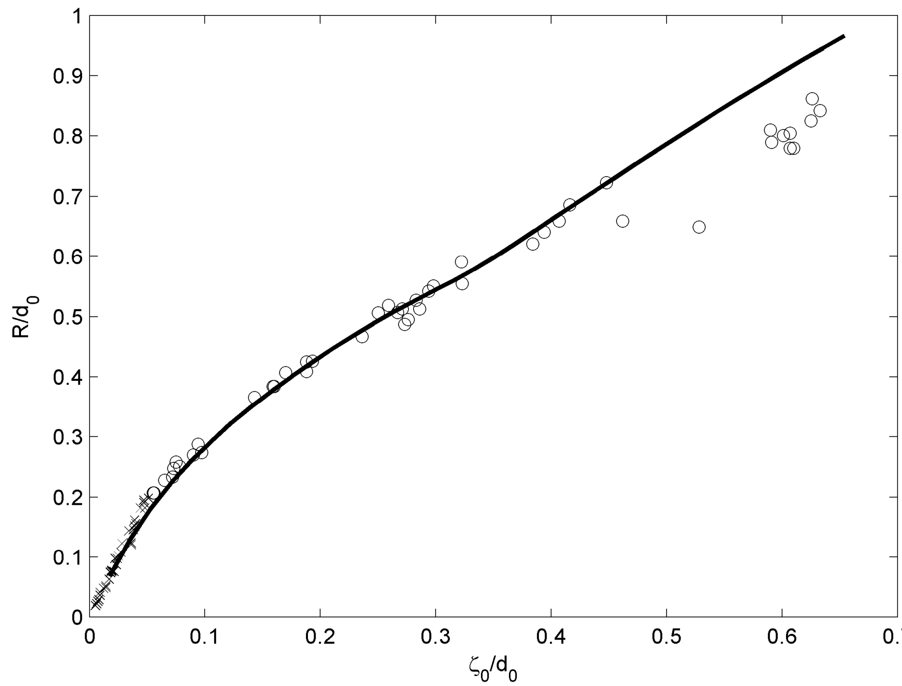

Figure 5-23 The relative run up of solitary waves on a plane 1/19.85 beach as a function of the relative wave height . Wave heights where measured half a wave length away from the toe of the beach.

Fortunately the addition of friction can be achieved relatively easy for the depth averaged model by the inclusion of a simply friction law into the horizontal momentum equation. As the original XBeach code already featured a friction term based on a Chezy formulation this was also chosen in the current case. Therefore the momentum equation in the depth averaged case becomes

$$\frac{\partial u}{\partial t} + \ldots + \frac{g}{C^2}\frac{|U|U}{h} = 0 \tag{5.13}$$

Where C is the Chezy friction coefficient. No information was available regarding the material used to construct the slope, however it is assumed that the slope was constructed of a smooth material and the Chezy coefficients where therefore sought in the range $60 < C < 80$ which is similar to the range reported by Lynett et al. After some trial an error a Chezy coefficient of $C = 65$ appeared to give a fit which was quite good.

The results are presented in Figure 5-23 and show that the agreement with the measurements is excellent for relative wave heights of up to 0.4. It appears to confirm that friction is indeed important in the run up of waves, which, in hindsight, is not very surprising.

For values of $\hat{\zeta}$ larger than 0.4 the measurements and the computed results begin to diverge more significantly, a trend which appears to start around $\hat{\zeta} = 0.35$ where the slope of the line suddenly begins to increase again.

Using more than one layer in the computations produced similar results to the depth averaged runs without friction. This is not to surprising as the effect of the non-hydrostatic pressures was only expected to be mild. Unfortunately no comparison to the runs with friction could be made as the inclusion of bottom friction is non-trivial in the case of more than one computational layer. In this case (turbulent) viscosity needs to be included in the model which also means some sort of turbulence closure model has to be introduced. This was not further pursued.

5.6. Discussion

In this chapter the numerical 2DV model as described in the previous chapter has been validated against a variety of test cases. The test cases considered where (i) an oscillating basin (ii) a solitary wave in channel, (iii) long waves on a beach, (iv) a dam break wave and (v) the run-up of solitary waves on a plane beach.

The oscillating basin test showed the excellent linear dispersion characteristics present in the model. The model propagates waves up to $kH = 7.8$ with an error in wave celerity of less than one percent for the two layer model while, using a single layer, the model has a similar error for waves up to $kH = 0.5$. Furthermore the dispersion relation reproduced by the model agreed very well with the theoretical dispersion relation derived for a semi discretisation in the vertical.

The solitary wave test confirmed that the model can accurately propagate solitary waves without any trailing waves. The solitary waves have a constant shape with little to no wave damping. Furthermore when compared to an approximate analytical solution the agreement with the two layer model was excellent.

The carrier and Greenspan test was used to validate the flooding and drying algorithm. Although the model produced results which agree well with the analytical solution, a very fine grid was needed to capture the run-up and drawdown of the waves in sufficient detail. This is most likely due to the staircase like appearance of the bottom. Furthermore the use of the second order limited approximations appears to lead to less smooth behavior in this case.

The Dam break test served as verification for the momentum conservation properties of the model and as a way to verify the ability of the scheme to deal with shock like solutions. The wet and dry bed hydrostatic runs confirmed the correct implementation of the momentum conservative scheme. These runs also showed the improvement the limited second order approximations bring when compared to the first order upwind approximations. When the non-hydrostatic terms where enabled for the dry bed case the flood wave appears to move faster than the analytical solution. Since the analytical solution is based on the hydrostatic pressure assumption it is difficult to tell if the difference is physical or due to implementation / numerical errors.

Finally the model was verified against the run-up of solitary waves on a plane beach. In this tests serious problems where found with flooding and drying when the higher order interpolations where used. Portions of the slope would fall dry while the parts above and below would still remain wet. This lead to unstable behavior and from this point onward it was therefore decided to only use upwind discretisations in the case of flooding and drying. This however meant that the grid resolution had to be increased considerably as the upwind approximations introduce significant amounts of numerical diffusion.
Without friction run-up heights up to a factor of two too large where found for the higher incoming waves. When a simple friction law is introduced the results agree very well with the measurements. This large difference between solutions with and without friction was also reported by Lynett et al. (2002).

Section III: 3D Numerical model

6. Model description

In this chapter the 2DV model is extended towards a full three dimensional model. The governing equations where already described for a three dimensional case in paragraph 4.1 and will not be repeated in this chapter. Furthermore the methodology of deriving the layer averaged equations and the subsequent discretisation in both space and time remains unchanged, apart from the addition of extra terms. Therefore this derivation will not be repeated here. Instead the resulting equations will be presented and the major focus will be the influence the addition of the extra dimension has on the resulting system of equations and the consequences this has on how to solve this.

6.1. Grid

The grid layout is kept similar to the 2DV numerical model and the horizontal velocity variables in the horizontal are still staggered with respect to water level points. This does mean that u-velocities are defined in different points than *v*-velocities. The resulting layout in the horizontal is shown in Figure 6-1, where also the resulting control volumes for each variable are indicated.

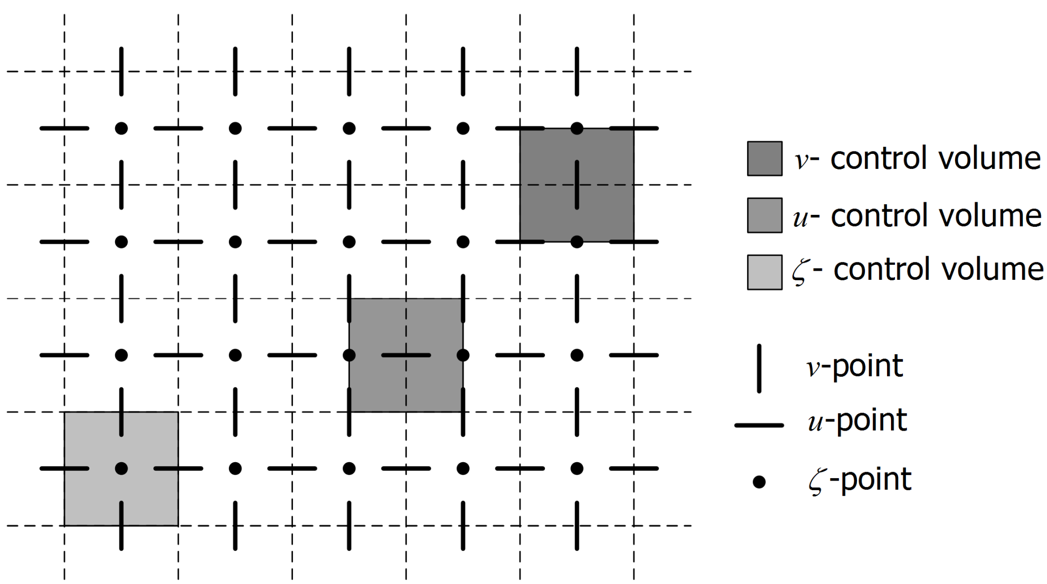

Figure 6-1 The staggered grid in the horizontal.

In the vertical the staggered arrangement is maintained for the velocities, but again the pressure points are located on the cell interfaces for accurate wave propagation. The resulting layout is sketched in Figure 6-2.

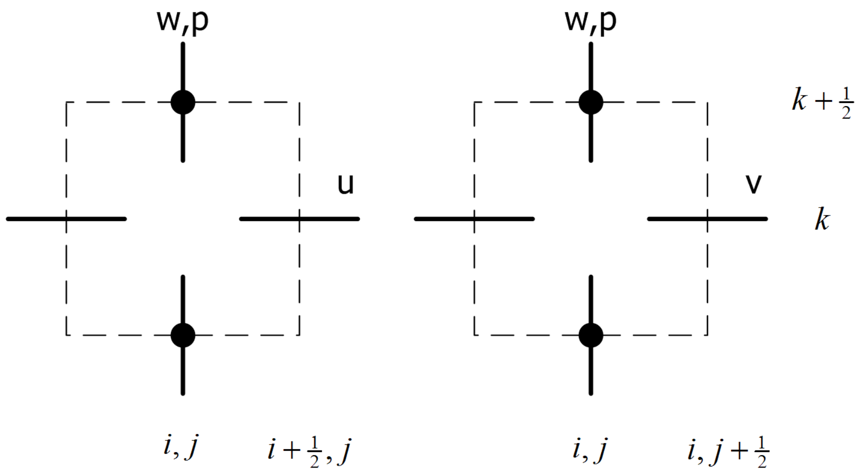

Figure 6-2 Vertical variable arrangement for u variables on the left and v variables on the right

The addition of the y-direction also introduces an extra index variable for each of the variables. Thus the location of a variable is now indicated with the subscript (i,j,k), where again half indices will be used for variables located on cell faces.

6.1.1. Variable grid size

A notable feature of the grid which was not dealt with in detail in the previous chapter is that a non-uniform grid spacing will be allowed. This means that the horizontal grid size $\Delta x, \Delta y$ will now also vary in space. This makes it possible to increase the number of points locally in regions where strong variation in the flow is expected, and thus a large number of grid points is required. On the other hand region with a relatively smooth variance in flow behaviour can be dealt with using fewer grid points. An example can be seen in Figure 6-3.

As the grid is still orthogonal the freedom this allows is rather limited and it is expected that for complex domains there will still be a considerable amount of overhead. An unstructured method based on the finite element or finite volume method is more efficient. However, the adoption to handle non-uniform grids is relatively easy to make as the existing code needed little modification.

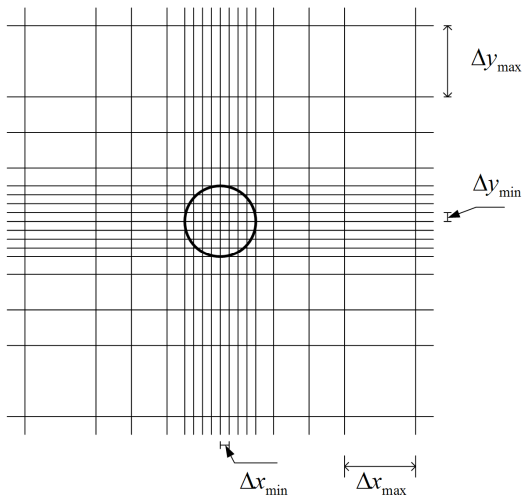

Figure 6-3 An example of a non-uniform grid where the grid spacing is locally reduced to capture a region of the domain in more detail.

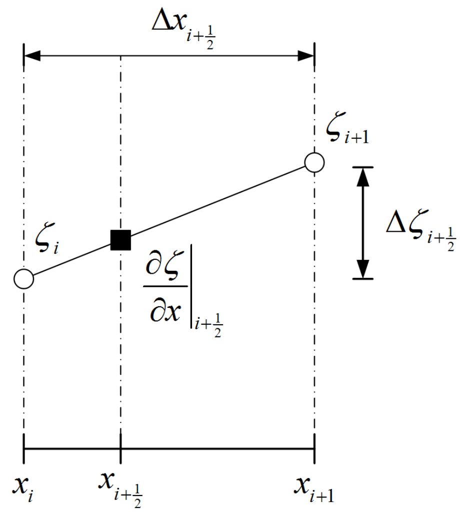

Figure 6-4 The gradient of the free surface is no longer evaluated midway between waterlevel points. Therefore the central approximation reduces locally to first order accuracy

A consequence of using non-uniform grids is that locally the central approximations reduce to first order accuracy (Hirch 2007). This is due to the fact that the derivative approximated is no longer located midway between the variables. As long as the changes in the grid are not sudden the error made is still substantially smaller than those made in a forward or backward difference scheme. Here the changes in the grid spacing will often follow

$\Delta x_{i+1} = r_i \Delta x_i$ and $\Delta y_{j+1} = r_j \Delta y_j$ (6.1)

As long as the expansion (or contraction) parameter r is close to unity the first order truncation error made will indeed be small and the scheme is of almost second order[1]. The use of a smoothly varying grid as described in equation (6.1) also creates a smooth transition between zones with a fine grid resolution and regions where a coarser grid is appropriate.

6.2. Discretised equations

The addition of the extra horizontal dimension adds extra convective terms to the global and local continuity equations and each of the momentum equations. Besides these extra terms there is also the addition of an extra momentum equation for the *y*-direction. However, as noted before, the appearance of these extra terms and the extra equation is very similar to the existing equations. Therefore the complete derivation will not be repeated as the procedure outlined in 4.3 and 4.4 is easily extended.

[1] See also Ferziger and Peric 2002, p 48-49.

6.2.1. Global continuity equation

The global continuity equation including the extra horizontal dimension now becomes:

$$\frac{\zeta_{i,j}^{n+1}-\zeta_{i,j}^{n}}{\Delta t}+\frac{H_{i+\frac{1}{2},j}^{n}U_{i+\frac{1}{2},j}^{n+\frac{1}{2}}-H_{i-\frac{1}{2},j}^{n}U_{i-\frac{1}{2},j}^{n+\frac{1}{2}}}{\Delta x_i}+\frac{H_{i,j+\frac{1}{2}}^{n}V_{i,j+\frac{1}{2}}^{n+\frac{1}{2}}-H_{i,j-\frac{1}{2}}^{n}V_{i,j-\frac{1}{2}}^{n+\frac{1}{2}}}{\Delta y_j}=0 \tag{6.2}$$

With:

$$U_{i+\frac{1}{2},j}=\frac{1}{H_{i+\frac{1}{2},j}}\sum_{k=1}^{K}h_{i+\frac{1}{2},j,k}u_{i+\frac{1}{2},j,k} \text{ and } V_{i,j+\frac{1}{2}}=\frac{1}{H_{i,j+\frac{1}{2}}}\sum_{k=1}^{K}h_{i,j+\frac{1}{2},k}v_{i,j+\frac{1}{2},k} \tag{6.3}$$

Furthermore $H_{i+\frac{1}{2},j,k}$ and $H_{i,j+\frac{1}{2},k}$ are determined using upwind interpolation similar to equation (4.24) or the limited higher order expressions.

6.2.2. Local continuity equation

In the local continuity equation two new terms appear due to the time and space dependent grid in the vertical

$$\begin{aligned}&\frac{u_{i+\frac{1}{2},j,k}h_{i+\frac{1}{2},j,k}-u_{i-\frac{1}{2},j,k}h_{i-\frac{1}{2},j,k}}{\Delta x_{i+\frac{1}{2}}}+\frac{v_{i,j+\frac{1}{2},k}h_{i,j+\frac{1}{2},k}-v_{i,j-\frac{1}{2},k}h_{i,j-\frac{1}{2},k}}{\Delta y_{j+\frac{1}{2}}}+w_{i,j,k+\frac{1}{2}}-w_{i,j,k-\frac{1}{2}}\\&-\frac{\left(z_{i+\frac{1}{2},j,k+\frac{1}{2}}-z_{i-\frac{1}{2},j,k+\frac{1}{2}}\right)u_{i,j,k+\frac{1}{2}}-\left(z_{i+\frac{1}{2},j,k-\frac{1}{2}}-z_{i-\frac{1}{2},j,k-\frac{1}{2}}\right)u_{i,j,k-\frac{1}{2}}}{\Delta x_{i+\frac{1}{2}}}\\&-\frac{\left(z_{i,j+\frac{1}{2},k+\frac{1}{2}}-z_{i,j-\frac{1}{2},k+\frac{1}{2}}\right)v_{i,j,k+\frac{1}{2}}-\left(z_{i,j+\frac{1}{2},k-\frac{1}{2}}-z_{i,j-\frac{1}{2},k-\frac{1}{2}}\right)v_{i,j,k-\frac{1}{2}}}{\Delta y_{j+\frac{1}{2}}}=0\end{aligned} \tag{6.4}$$

The velocity $u_{i,j,k+\frac{1}{2}}$ is still acquired using equation (4.29) while for $v_{i,j,k+\frac{1}{2}}$ a similar expression in the *y*-direction is used.

6.2.3. Horizontal momentum equations

Let $F(u)_{i+\frac{1}{2},j,k}$ represent the advective terms in the *u*-momentum equation so that

$$\begin{aligned}F(u)_{i+\frac{1}{2},j,k}=&\frac{\bar{q}_{i+1,j,k}^{x}u_{i+1,j,k}-\bar{q}_{i,j,k}^{x}u_{i,j,k}}{\bar{h}_{i+\frac{1}{2},j,k}^{x}\Delta x_{i+\frac{1}{2}}}-\frac{u_{i+\frac{1}{2},j,k}\left(\bar{q}_{i+1,j,k}^{x}-\bar{q}_{i+1,j,k}^{x}\right)}{\bar{h}_{i+\frac{1}{2},j,k}^{x}\Delta x_{i+\frac{1}{2}}}\\&+\frac{\bar{q}_{i+\frac{1}{2},j+\frac{1}{2},k}^{y}u_{i+\frac{1}{2},j+\frac{1}{2},k}-\bar{q}_{i+\frac{1}{2},j-\frac{1}{2},k}^{y}u_{i+\frac{1}{2},j-\frac{1}{2},k}^{n+\frac{1}{2}}}{\bar{h}_{i+\frac{1}{2},j,k}^{x}\Delta y_j}-\frac{u_{i+\frac{1}{2},j,k}^{n+\frac{1}{2}}\left(\bar{q}_{i,j+\frac{1}{2},k}^{y}-\bar{q}_{i,j-\frac{1}{2},k}^{y}\right)}{\bar{h}_{i+\frac{1}{2},j,k}^{x}\Delta y_j}\\&+\frac{u_{i+\frac{1}{2},j,k+\frac{1}{2}}\bar{\varpi}_{i+\frac{1}{2},j,k+\frac{1}{2}}^{x}-u_{i-\frac{1}{2},j,k-\frac{1}{2}}\bar{\varpi}_{i+\frac{1}{2},j,k-\frac{1}{2}}^{x}}{\bar{h}_{i+\frac{1}{2},j,k}^{x}}-\frac{u_{i+\frac{1}{2},j,k}}{\bar{h}_{i+\frac{1}{2},j,k}^{x}}\left(\bar{\varpi}_{i+\frac{1}{2},j,k+\frac{1}{2}}^{x}-\bar{\varpi}_{i+\frac{1}{2},j,k-\frac{1}{2}}^{x}\right)\end{aligned} \tag{6.5}$$

Where

$$\overline{q}^{x}_{i,j,k} = \frac{q^{x}_{i+\frac{1}{2},j,k} + q^{x}_{i-\frac{1}{2},j,k}}{2}, \; q^{x}_{i+\frac{1}{2},j,k} = h_{i+\frac{1}{2},j,k} u_{i+\frac{1}{2},j,k}$$
$$\overline{q}^{y}_{i+\frac{1}{2},j+\frac{1}{2},k} = \frac{q^{y}_{i,j+\frac{1}{2},k} + q^{y}_{i+1,j+\frac{1}{2},k}}{2}, \; q^{y}_{i,j+\frac{1}{2},k} = h_{i,j+\frac{1}{2},k} v_{i,j+\frac{1}{2},k} \tag{6.6}$$

While $u_{i+\frac{1}{2},j,k}$, $\omega^{x}_{i+\frac{1}{2},j,k+\frac{1}{2}}$ and $\overline{h}^{x}_{i+\frac{1}{2},j,k}$ are defined similarly to the two dimensional case (see 4.3.3). Now the hydrostatic approximation for *u* on the next time level is

$$\frac{u^{*}_{i+\frac{1}{2},j,k} - u^{n+\frac{1}{2}}_{i+\frac{1}{2},j,k}}{\Delta t} + g\frac{\zeta^{n+1}_{i+1,j,k} - \zeta^{n+1}_{i,j,k}}{\Delta x_{i+\frac{1}{2}}} + F(u)^{n+\frac{1}{2}}_{i+\frac{1}{2},j,k} = 0 \tag{6.7}$$

And the horizontal momentum equation for *u* including the non-hydrostatic pressured becomes

$$\frac{u^{n+\frac{3}{2}}_{i+\frac{1}{2},j,k} - u^{*}_{i+\frac{1}{2},j,k}}{\Delta t} \frac{h^{n+1}_{i+1,j,k}\overline{p}^{n+\frac{3}{2}}_{i+1,j,k} - h^{n+1}_{i,j,k}\overline{p}^{n+\frac{3}{2}}_{i,j,k}}{\overline{h}^{n+1}_{i+\frac{1}{2},j,k}\Delta x_{i+\frac{1}{2}}}$$
$$-\frac{\overline{p}^{n+\frac{3}{2}}_{i+\frac{1}{2},j,k+\frac{1}{2}}}{\overline{h}^{n+1}_{i+\frac{1}{2},j,k}}\frac{z^{n+1}_{i+1,j,k+\frac{1}{2}} - z^{n+1}_{i,j,k+\frac{1}{2}}}{\Delta x_{i+\frac{1}{2}}} + \frac{\overline{p}^{n+\frac{3}{2}}_{i+\frac{1}{2},j,k-\frac{1}{2}}}{\overline{h}^{n+1}_{i+\frac{1}{2},j,k}}\frac{z^{n+1}_{i+1,j,k-\frac{1}{2}} - z^{n+1}_{i,j,k-\frac{1}{2}}}{\Delta x_{i+\frac{1}{2}}} = 0 \tag{6.8}$$

Notice that the expression for the horizontal *u*-momentum equation only contains extra advective terms, in all other aspects it is identical to equation (4.64).

For the *v*-momentum equation a similar situation holds. Let $F(v)_{i,j+\frac{1}{2},k}$ denote the advective terms given by

$$F(v)_{i,j+\frac{1}{2},k} = \frac{\overline{q}^{y}_{i,j+1,k}v_{i,j+1,k} - \overline{q}^{y}_{i,j,k}v_{i,j,k}}{\overline{h}^{n+1}_{i,j+\frac{1}{2},k}\Delta y_{j+\frac{1}{2}}} - \frac{v_{i,j+\frac{1}{2},k}\left(\overline{q}^{y}_{i,j+1,k} - \overline{q}^{y}_{i,j+1,k}\right)}{\overline{h}^{n+1}_{i,j+\frac{1}{2},k}\Delta y_{j+\frac{1}{2}}}$$
$$+\frac{\overline{q}^{x}_{i+\frac{1}{2},j+\frac{1}{2},k}v_{i+\frac{1}{2},j+\frac{1}{2},k} - \overline{q}^{x}_{i+\frac{1}{2},j-\frac{1}{2},k}v_{i+\frac{1}{2},j-\frac{1}{2},k}}{\overline{h}^{n+1}_{i,j+\frac{1}{2},k}\Delta x_{i}} - \frac{v_{i,j+\frac{1}{2},k}\left(\overline{q}^{x}_{i,j+\frac{1}{2},k} - \overline{q}^{x}_{i,j-\frac{1}{2},k}\right)}{\overline{h}^{n+1}_{i,j+\frac{1}{2},k}\Delta x_{i}}$$
$$+\frac{v_{i,j+\frac{1}{2},k+\frac{1}{2}}\overline{\omega}_{i,j+\frac{1}{2},k+\frac{1}{2}} - v_{i,j+\frac{1}{2},k-\frac{1}{2}}\overline{\omega}_{i,j+\frac{1}{2},k-\frac{1}{2}}}{\overline{h}_{i,j+\frac{1}{2},k}} - \frac{v_{i,j+\frac{1}{2},k}}{\overline{h}_{i,j+\frac{1}{2},k}}\left(\overline{\omega}_{i,j+\frac{1}{2},k+\frac{1}{2}} - \overline{\omega}_{i,j+\frac{1}{2},k-\frac{1}{2}}\right) \tag{6.9}$$

Where the variables, when needed, are interpolated using similar expressions as in the *u*-momentum case. The hydrostatic approximation $v^{*}_{i,j+\frac{1}{2},k}$ on the next time level is

$$\frac{v^{*}_{i,j+\frac{1}{2},k} - v^{n+\frac{1}{2}}_{i,j+\frac{1}{2},k}}{\Delta t} + g\frac{\zeta^{n+1}_{i,j+1,k} - \zeta^{n+1}_{i,j,k}}{\Delta y_{j+\frac{1}{2}}} + F(v)^{n+\frac{1}{2}}_{i,j+\frac{1}{2},k} = 0 \tag{6.10}$$

While the *v*-momentum equation including non-hydrostatic pressures now becomes

$$\frac{v^{n+\frac{3}{2}}_{i,j+\frac{1}{2},k}-v^{*}_{i,j+\frac{1}{2},k}}{\Delta t}+\frac{h^{n+1}_{i,j+1,k}\bar{p}^{n+\frac{3}{2}}_{i,j+1,k}-h^{n+1}_{i,j,k}\bar{p}^{n+\frac{3}{2}}_{i,j,k}}{\bar{h}^{n+1}_{i,j+\frac{1}{2},k}\Delta y_{j+\frac{1}{2}}}$$
$$-\frac{\bar{p}^{n+\frac{3}{2}}_{i,j+\frac{1}{2},k+\frac{1}{2}}}{\bar{h}^{n+1}_{i,j+\frac{1}{2},k}}\frac{z^{n+1}_{i,j+1,k+\frac{1}{2}}-z^{n+1}_{i,j,k+\frac{1}{2}}}{\Delta y_{j+\frac{1}{2}}}+\frac{\bar{p}^{n+\frac{3}{2}}_{i,j+\frac{1}{2},k-\frac{1}{2}}}{\bar{h}^{n+1}_{i,j+\frac{1}{2},k}}\frac{z^{n+1}_{i,j+1,k-\frac{1}{2}}-z^{n+1}_{i,j,k-\frac{1}{2}}}{\Delta y_{j+\frac{1}{2}}}=0 \tag{6.11}$$

6.2.4. Vertical momentum equation

Let $F\left(w\right)_{i,j,k+\frac{1}{2}}$ represent the advective terms in the vertical momentum equation:

$$F\left(w\right)_{i,j,k+\frac{1}{2}}=\frac{\bar{\omega}_{i,j,k+1}w_{i,j,k+1}-\bar{\omega}_{i,j,k}w_{i,j,k}}{\bar{h}^{z}_{i,j,k+\frac{1}{2}}}-\frac{w_{i,j,k+\frac{1}{2}}}{\bar{h}^{z}_{i,j,k+\frac{1}{2}}}\left(\bar{\omega}_{i,j,k+1}-\bar{\omega}_{i,j,k}\right)$$
$$+\frac{\bar{q}^{x}_{i+\frac{1}{2},j,k+\frac{1}{2}}w_{i+\frac{1}{2},j,k+\frac{1}{2}}-\bar{q}^{x}_{i-\frac{1}{2},j,k+\frac{1}{2}}w_{i-\frac{1}{2},j,k+\frac{1}{2}}}{\bar{h}^{z}_{i,j,k+\frac{1}{2}}\Delta x_{i}}-\frac{w_{i,j,k+\frac{1}{2}}}{\bar{h}^{z}_{i,j,k+\frac{1}{2}}\Delta x_{i}}\left(\bar{q}^{x}_{i+\frac{1}{2},j,k+\frac{1}{2}}-\bar{q}^{x}_{i-\frac{1}{2},j,k+\frac{1}{2}}\right)$$
$$+\frac{\bar{q}^{y}_{i,j+\frac{1}{2},k+\frac{1}{2}}w_{i,j+\frac{1}{2},k+\frac{1}{2}}-\bar{q}^{y}_{i,j-\frac{1}{2},k+\frac{1}{2}}w_{i,j-\frac{1}{2},k+\frac{1}{2}}}{\bar{h}^{z}_{i,j,k+\frac{1}{2}}\Delta y_{i}}-\frac{w_{i,j,k+\frac{1}{2}}}{\bar{h}^{z}_{i,j,k+\frac{1}{2}}\Delta x}\left(\bar{q}^{y}_{i,j+\frac{1}{2},k+\frac{1}{2}}-\bar{q}^{y}_{i,j+\frac{1}{2},k+\frac{1}{2}}\right) \tag{6.12}$$

Using (6.12) the vertical momentum equation can now be written as

$$\frac{w^{n+\frac{3}{2}}_{i,k+\frac{1}{2}}-w^{n+\frac{1}{2}}_{i,k+\frac{1}{2}}}{\Delta t}+2\sum_{m=0}^{k-1}\left[\left(-1\right)^{m}\left(\frac{p^{n+\frac{3}{2}}_{i,j,k+\frac{1}{2}-m}-p^{n+\frac{3}{2}}_{i,j,k-\frac{1}{2}-m}}{h^{n+1}_{i,k-m}}\right)\right]$$
$$+\left(-1\right)^{k-1}\left(\frac{u^{n+\frac{3}{2}}_{i,j,\frac{1}{2}}-u^{n+\frac{1}{2}}_{i,j,\frac{1}{2}}}{\Delta t}\frac{z^{n+1}_{i+\frac{1}{2},j,\frac{1}{2}}-z^{n+1}_{i-\frac{1}{2},j,\frac{1}{2}}}{\Delta x_{i}}+\frac{v^{n+\frac{3}{2}}_{i,j,\frac{1}{2}}-v^{n+\frac{1}{2}}_{i,j,\frac{1}{2}}}{\Delta t}\frac{v^{n+1}_{i+\frac{1}{2},j,\frac{1}{2}}-v^{n+1}_{i-\frac{1}{2},j,\frac{1}{2}}}{\Delta x_{i}}-F\left(w\right)^{n+\frac{1}{2}}_{i,j,\frac{1}{2}}\right)$$
$$+F\left(w\right)^{n+\frac{1}{2}}_{i,j,k+\frac{1}{2}}=0 \tag{6.13}$$

It is interesting too see that, through the kinematic boundary condition at the bottom, the horizontal velocities are introduced in the vertical momentum equation. This implies that, when the bottom is uneven, the *w*-momentum equation introduces a coupling between the surrounding pressure points at the bottom.

6.3. Non-hydrostatic pressure

The solution method for the non-hydrostatic pressure is essentially equivalent to the two dimensional case. Again the momentum equations (6.5),(6.11) and (6.13) are substituted into the local continuity equation (6.4) to enforce a divergence free velocity field. The resulting system of equations must then be solved in order to obtain the non-hydrostatic pressures. With these pressures the updated velocities can be calculated as now all terms in the momentum equations are known. When the velocities are substituted into the local continuity equation this equation takes a form similar to

$$\sum_{k=\frac{1}{2}}^{K-\frac{1}{2}} \left(A^{n}_{i,j-1,k} p_{i,j-1,k} + A^{w}_{i-1,,j,k} p_{i-1,j,k} + A_{i,j} p_{i,j} + A^{e}_{i+1,,j,k} p_{i+1,j,k} + A^{s}_{i,,j+1,k} p_{i,j+1,k} \right) = Q_{i,j,k} \tag{6.14}$$

Where *A* are the coefficients for the pressure resulting from the substitution and *Q* contains all the explicit terms. Notice that even for a single layer ($K = 1$) equation (6.14) couples five pressure points. For two layers each equation contains ten strongly coupled pressure points and the matrix resulting from this takes a shape like in Figure 6-5.

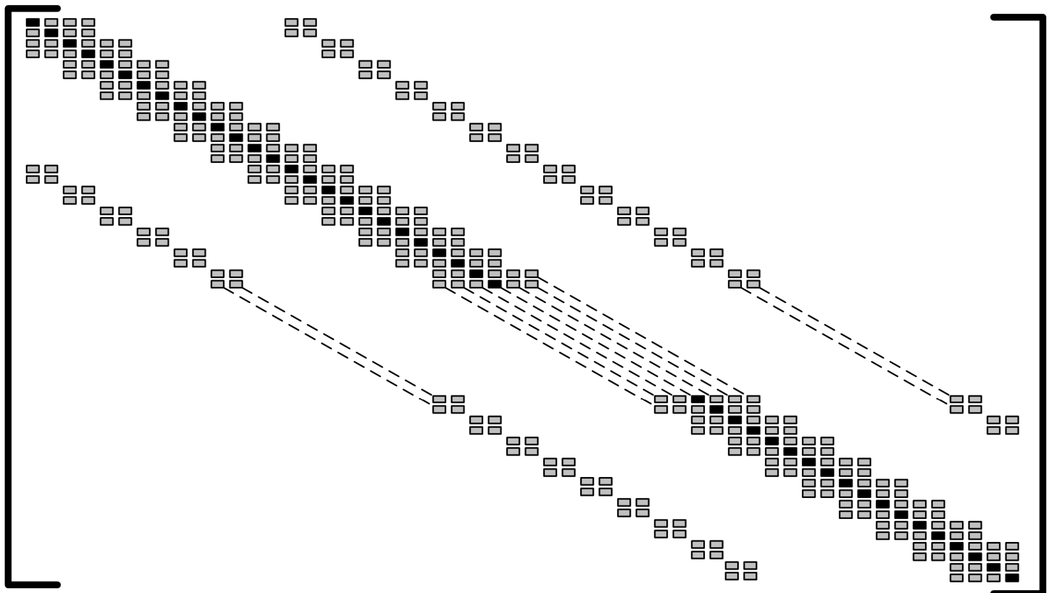

Figure 6-5 An example of a matrix resulting from the discretised system for two computational layers.

The main difference with the matrix obtained in the 2DV model is the appearance of the extra diagonals to the left and right. Due to these diagonals the block solver based on Gaussian elimination used in the 2DV model is no longer a viable option. Even in the depth averaged case this would lead to extensive fill in which makes the application of Gauss elimination inefficient for even modest systems.

For the shallow water equations a similar situation is found when the free surface gradient is treated in an implicit manner. Here a very attractive alternative is found in a splitting method like alternate direction implicit (ADI). This method reduces the full matrix to a set of tri-diagonal systems by alternately switching the direction which is treated implicitly. However, the absence of a time derivative for the pressure in the local continuity equation means that the ADI method can only be implemented by adding a pseudo time derivative for the pressure to the equations. In this way the elliptic problem is transformed into a hyperbolic problem which is solved until a steady state is reached. At that point the time derivative is zero and the original elliptic problem is satisfied (see for instance Ferziger and Peric 2002). Due to an incorrect implementation the ADI which produced excessive dampening the method was rejected. However, when implemented correctly, it might still form a viable alternative.

.

Two other methods where considered, the strongly implicit procedure (SIP) by Stone (1968) and the preconditioned BiConjugate Gradient Stabilized (BiCGSTAB) method by van den Vorst (1992). They will be summarized briefly below, but for a more detailed description the reader is referred to Ferziger and Peric (2002).

The strongly implicit procedure is based on an incomplete lower-upper factorization of the matrix **A**. This factorization is constructed in such a way that it has the same sparsity as the original matrix. The resulting system can then be solved very efficiently in an iterative manner using forward and backward substitutions. The implementation of the SIP method used is based on a five point computational molecule and is therefore only applicable to the pressure Poisson system generated in the depth averaged case.

When multiple layers are used a different method needed. Because of the application of a vertical boundary-fitted coordinate system the pressure Poisson systems involved are always non-symmetric. This means that the preconditioned conjugate gradient methods are no longer applicable. Therefore, following Zijlema and Stelling (2004), a popular method appropriate for solving non-symmetric matrices is used, namely BiCGSTAB. This method is combined with a preconditioner based on incomplete LU decompositions to improve efficiency.
The BiCGSTAB method is applicable for the solution of general systems and can be applied to both structured and unstructured grids. However, for additional computational speed, the method used was tailored for the use on a structured grid with a maximum of two layers.

The choice to either use the BiCGSTAB method or the SIP method, which is only relevant in the depth averaged case, is made on the bases of efficiency. Usually the SIP method will require more iterations per time step than the preconditioned BiCGSTAB method. However, the work done per iteration is much lower and on balance the SIP method is faster than the BICGSTAB method. This is the reason that, whenever a single layer is used, the SIP method is employed. The BiCGSTAB method is applied to problems involving two layers.

Both methods rely on iterative solution of the pressure Poisson equation and will therefore generate intermediate solutions which improve in accuracy when more iterations are taken. There is usually no need to continue this procedure until machine precision is reached, since the errors made in the underlying discretisation process are usually much larger than the accuracy of the computer arithmetic. A stopping criteria is needed that determines when the solution is considered to be sufficiently accurate. Here the following criterium is adopted

$$\frac{\left\| \mathbf{Ap}^s \text{ - } \mathbf{Q} \right\|}{\left\| \mathbf{Q} \right\|} < \alpha \tag{6.15}$$

Where α is a pre determined threshold $\mathbf{Q}$ the right hand side of the linear problem and $\| \ \|$ is the L_2 norm of the respective vector. Interestingly it appears that the solution of the pressure matrix is not very sensitive to the threshold α and it usually suffices to set it to about $\alpha = 10^{-2}$ (see Stelling and Zijlema, 2002).

6.4. Flooding and drying

Most remarks made in the previous chapter regarding flooding and drying still hold and most concepts are easily extended in a setting with two horizontal directions. Here only an extension to the criterion for positive water depths is given as this is considered an essential part of the flooding and drying algorithm.

6.4.1. Positive water depths in two dimensions

Again, in order to investigate under which conditions the water depth never falls below zero, the global continuity equation is considered.

$$\frac{\zeta_{i,j}^{n+1} - \zeta_{i,j}^{n}}{\Delta t} + \frac{H_{i+\frac{1}{2},j}^{n} U_{i+\frac{1}{2},j}^{n+\frac{1}{2}} - H_{i-\frac{1}{2},j}^{n} U_{i-\frac{1}{2},j}^{n+\frac{1}{2}}}{\Delta x_i} + \frac{H_{i,j+\frac{1}{2}}^{n} V_{i,j+\frac{1}{2}}^{n+\frac{1}{2}} - H_{i,j-\frac{1}{2}}^{n} V_{i,j-\frac{1}{2}}^{n+\frac{1}{2}}}{\Delta y_j} = 0 \tag{6.16}$$

However, in contrast to the previous derivation now a situation is considered where all velocities are directed outward of the cell. This situation can be thought of as the worst case scenario for the algorithm. Using the tile like description of the bottom again we have:

$$z_{i+\frac{1}{2},j,\frac{1}{2}} = \max\left(z_{i,j,\frac{1}{2}}, z_{i+1,j,\frac{1}{2}}\right) \text{ and } z_{i,j+\frac{1}{2},\frac{1}{2}} = \max\left(z_{i,j,\frac{1}{2}}, z_{i,j+1,\frac{1}{2}}\right) \tag{6.17}$$

This means that the water depth at velocity points, when using upwind approximations, is always smaller or equal to the water depth in the free surface point. Again picking the worst case scenario entails using the maximum water depth. Now equation (6.16) can be rewritten as:

$$H_{i,j}^{n+1} = H_{i,j}^{n}\left(1 - \Delta t\left(\frac{U_{i+\frac{1}{2},j}^{n+\frac{1}{2}}}{\Delta x_i} - \frac{U_{i-\frac{1}{2},j}^{n+\frac{1}{2}}}{\Delta x_i} + \frac{V_{i,j+\frac{1}{2}}^{n+\frac{1}{2}}}{\Delta y_j} - \frac{V_{i,j-\frac{1}{2}}^{n+\frac{1}{2}}}{\Delta y_j}\right)\right) \tag{6.18}$$

Obviously, as long as the water depths at the current time step are positive this is always positive if

$$\Delta t\left(\frac{U^{n+\frac{1}{2}}_{i+\frac{1}{2},j}}{\Delta x_i}-\frac{U^{n+\frac{1}{2}}_{i-\frac{1}{2},j}}{\Delta x_i}+\frac{V^{n+\frac{1}{2}}_{i,j+\frac{1}{2}}}{\Delta y_j}-\frac{V^{n+\frac{1}{2}}_{i,j-\frac{1}{2}}}{\Delta y_j}\right)\leq 1 \tag{6.19}$$

However, when the velocities are directed into the cell they transport mass into the control volume and they thus have a positive contribution.

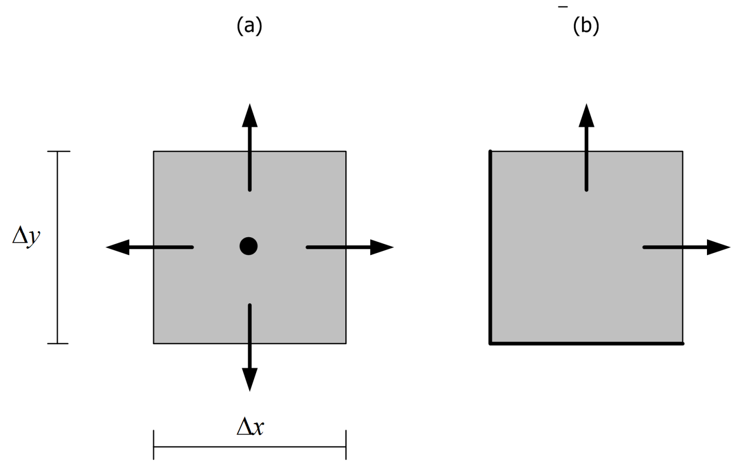

Figure 6-6 (a) Worst case scenario for a particular mass control volume, all velocities are pointed outward. (b) Situation where only two velocities are directed outward while the other boundaries are closed.

A sufficient condition can be derived by neglecting any positive contributions into the cell, this means condition (6.18) becomes

$$\Delta t\left(-\frac{\min\left(U^{n+\frac{1}{2}}_{i-\frac{1}{2},j},0\right)}{\Delta x_i}+\frac{\max\left(U^{n+\frac{1}{2}}_{i+\frac{1}{2},j},0\right)}{\Delta x_i}-\frac{\min\left(V^{n+\frac{1}{2}}_{i,j-\frac{1}{2}},0\right)}{\Delta y_j}+\frac{\max\left(V^{n+\frac{1}{2}}_{i,j+\frac{1}{2}},0\right)}{\Delta y_j}\right)<1 \tag{6.20}$$

This condition has a very simple physical interpretation. It basically checks that the amount of water leaving through the faces in a single time step is never greater than the volume of water contained the cell (multiply both sides of (6.20) with the volume will immediately make this clear). The condition for the dynamic time step therefore becomes

$$\Delta t<\frac{\Delta y_j\Delta x_i}{-\Delta y_j\min\left(U^{n+\frac{1}{2}}_{i-\frac{1}{2},j},0\right)+\Delta y_j\max\left(U^{n+\frac{1}{2}}_{i+\frac{1}{2},j},0\right)-\min\left(V^{n+\frac{1}{2}}_{i,j-\frac{1}{2}},0\right)+\Delta x_i\max\left(V^{n+\frac{1}{2}}_{i,j+\frac{1}{2}},0\right)} \tag{6.21}$$

In some circumstances, especially when considering overflow situations, this condition becomes more restrictive than the stability condition. Lets for a moment in time assume that the velocity is dominant in the propagation of information (e.g. supercritical flow) and assume only two boundaries are open (see Figure 6-6b). Furthermore let $U^{n+\frac{1}{2}}_{i+\frac{1}{2},j}=V^{n+\frac{1}{2}}_{i,j+\frac{1}{2}}$ and $\Delta y_j=\Delta x_i$

In this case equation (6.21) becomes

$$\Delta t<\frac{\Delta x_i}{2U^{n+\frac{1}{2}}_{i+\frac{1}{2},j}} \tag{6.22}$$

Comparing this to a time step criteria obtained from the CFL condition:

$$\Delta t \leq \frac{\Delta x}{U + \sqrt{gH}} \tag{6.23}$$

This shows that if $U > \sqrt{gH}$ the flooding and drying criteria of (6.22) becomes dominant. Notice that if more velocities are directed outward this can becomes even worse. However, this is a situation that is rarely encountered and usually the time step is restricted by the courant number.

7. Validation and verification

The numerical model as described in chapter 6 is validated against two test. First the oscillating basin is used to verify the correct implementation of the non-hydrostatic pressure routine in three dimensions. After this the Berkhoff Shoal is used as verification of the model.

7.1. Oscillating basin

As a validation test of the correct implementation of the pressure corrections in three dimensions we return to the oscillating basin test which was also used as a verification of the 2DV model. (see section 5.1.2). However, now the basin is extended in the *y*-direction and the initial condition will also slightly change.

Consider a three dimensional basin which has a square shape horizontally with sides of length *L*. The fundamental mode of such a basin can be described with a wave like solution given by:

$$\zeta(x,y,t) = \zeta_0 \cos(k_x x)\cos(k_y y)\cos(\omega t) \tag{7.1}$$

Where $k_x = k_y = \pi L^{-1}$ and ω is determined by the linear dispersion relation:

$$\omega^2 = gk \tanh kh \text{ with } k = \sqrt{k_y^2 + k_x^2} = \sqrt{2}\pi L^{-1} \tag{7.2}$$

As again only waves with a small steepness are considered the velocities can be approximated safely with linear wave theory and are given by:

$$\begin{aligned}
u(x,y,z,t) &= \frac{\zeta_0 g k_x}{\omega}\frac{\cosh(k(H+z))}{\cosh(kH)}\sin(k_x x)\cos(k_y y)\sin(\omega t)\\
v(x,y,z,t) &= \frac{\zeta_0 g k_y}{\omega}\frac{\cosh(k(H+z))}{\cosh(kH)}\cos(k_x x)\sin(k_y y)\sin(\omega t)\\
w(x,y,z,t) &= -\frac{\zeta_0 g k_x}{\omega}\frac{\sinh(k(H+z))}{\cosh(kH)}\cos(k_x x)\cos(k_y y)\sin(\omega t)
\end{aligned} \tag{7.3}$$

The sides of the basin where set at $L = 250m$ while the still water depth was also chosen to be $d_0 = 250m$. In such basin $kH = \sqrt{2}\pi$ and the wave is therefore in relatively deep water. As an initial condition the solution at *t=0* is prescribed. This means a zero velocity field is used. The free surface is given by (7.1) where the amplitude was $\zeta_0 = 0.01m$. An impression of the initial condition is found in Figure 7-1.

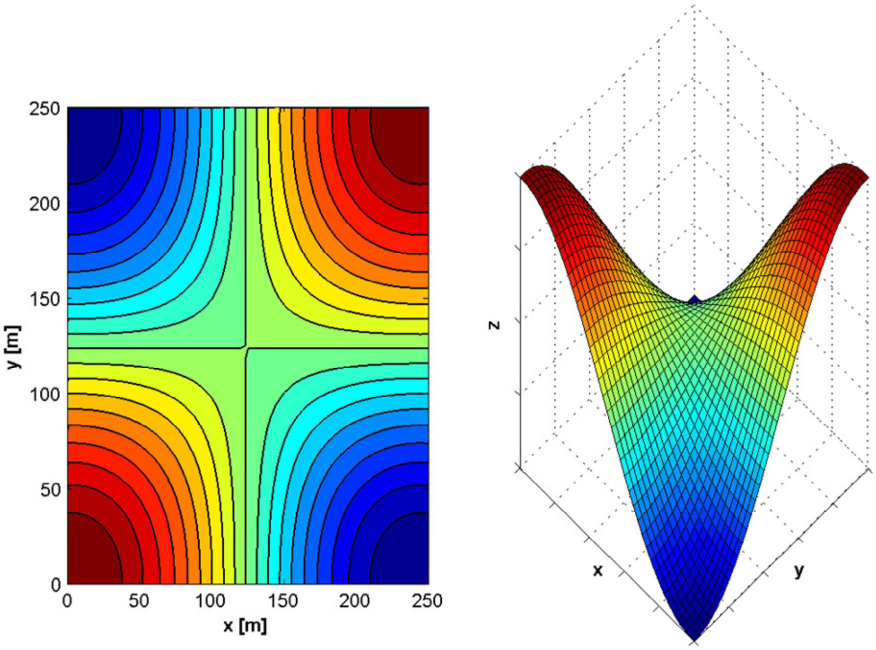

Figure 7-1 Overview of the basin together with the contours of the initial condition at t=0s at the left. At the right a three dimensional impression of the free surface at t=0s..

The basin was discretised using an uniform 81 by 81 grid while in the vertical either one or two layers where used. For the depth averaged case the SIP solver was used while the BiCGSTAB method was employed when using multiple layers. In both cases the convergence criteria (6.15) was set to $\alpha = 10^{-2}[-]$. The simulation was run for a total of six periods of the analytical solution and the CFL condition was set to $CFL = 0.2$ which corresponds to a mean time step of roughly $\Delta t \approx 0.0043s$. As no flooding and drying occurred the second order expressions could safely be used.

Depth averaged run

In Figure 7-2 time series are given for the free surface, the depth averaged horizontal velocities and the vertical velocity at the free surface. They were taken at a point located at *x=50m, y=50m* and are compared to the analytical solutions[1].

The solutions obtained for the free surface shows the expected behaviour already found in the 2dV basin test. Here the numerical solution also lags the analytical solution due to the inaccurate dispersion relation. After about three periods the analytical and numerical solution

[1] Note that both analytical solutions for the horizontal velocities where integrated over the depth and then divided by the depth to obtain a depth average velocity.

are actually in anti-phase. However, the amplitude is correctly reproduced and no sign of numerical dampening is found. For the velocity components something similar holds although in there the amplitudes are also different. This can be explained by the difference in frequency. In the expressions for the amplitudes in (7.3) ω is present in the denominator. For longer periods this means that the amplitudes are smaller, which explains the observed differences.

In Figure 7-3 contours are shown for six different times during the first period, together with the velocity vectors and the contours of the analytical solution at the same time. Aside from the difference in phase the numerical solution does reproduce the correct behavior. The solution stays symmetric around the diagonals and the velocity pattern is correct. Remembering that the wave modeled here is essentially in too deep water for a depth averaged solution and all errors found can be attributed to this. It is expected that for solutions in shallower water the depth averaged solution will perform better.

Finally it is worth mentioning that both the SIP method and the BiCGSTAB method reproduced a very similar solution which provides some confidence in the correct integration of these two methods in the model. Furthermore, hardly any improvement was found when the stopping criteria was set to achieve more accurate solutions, which is consistent with the remarks in Stelling and Zijlema (2003).

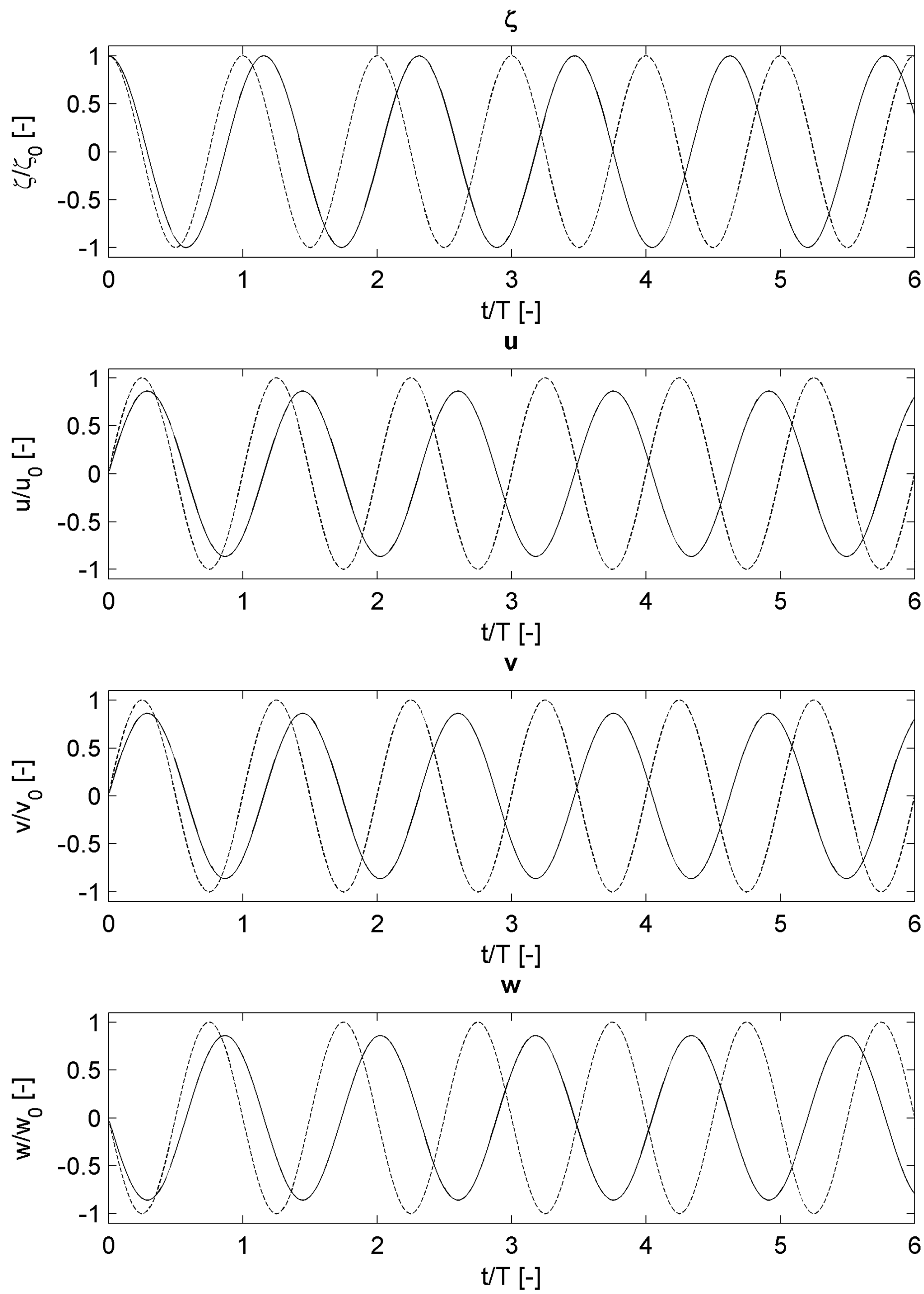

Figure 7-2 The free surface, horizontal depth averaged velocities *u,v* The free surface, horizontal depth averaged velocities *u,v* and the vertical velocity w compared to the analytical solutions at x=50,y=50. The analytical solution is indicated with a dotted line while the analytical solution is given by a solid line.

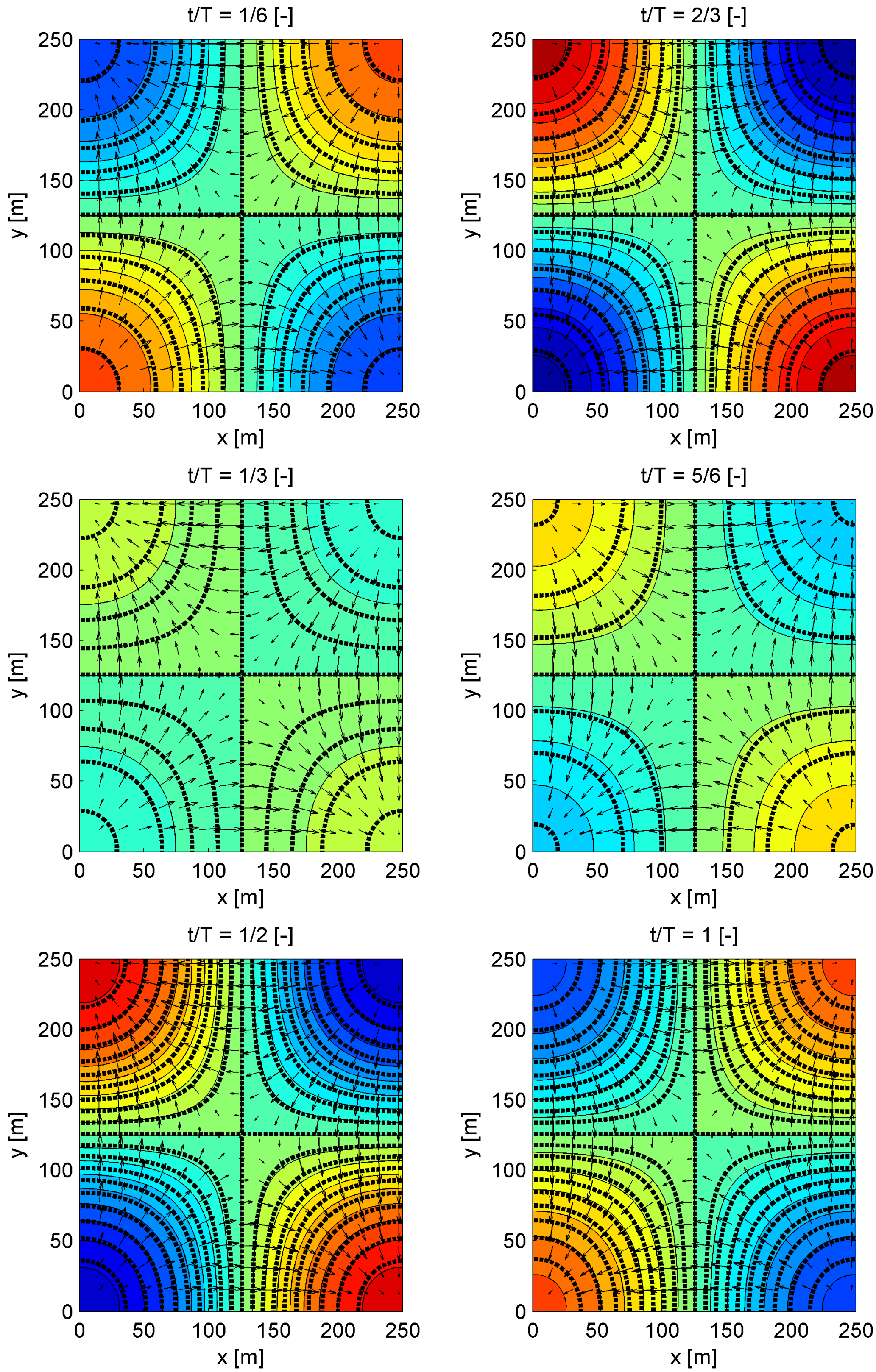

Figure 7-3 Contours of the free surface and velocity vectors of the numerical solution obtained during the first numerical wave period for the depth averaged solution. Contour lines of the analytical solution are indicated by the thick dotted lines.

Two layers

From the depth average case it was already observed that the major source in the discrepancies between the analytical solution and the numerical solution was the inaccurate dispersion contained in the numerical model. From paragraph 5.1 it is known that the linear dispersion relation present in the model improves enormously when using two layers. As the expansion with the extra horizontal dimension does not change this (a similar expression can be obtained in three dimension) the addition of an extra layer should improve the results.

Figure 7-4 gives the time series for the free surface, depth averaged horizontal velocities and the vertical velocity at the free surface (at *x=50m, y=50m*). The figure clearly show that, using two layers, the solution obtained is virtually identical to the analytical solution. The amplitudes and phases are now correctly modelled and again no numerical dampening is observed.
In Figure 7-5 contours are shown for six different times during the first period, together with the velocity vectors and the contours of the analytical solution at the same time. These show that correspondence between the analytical solution and the numerical solution is good throughout the basin. Furthermore the flow pattern is still correct and the solution is still symmetric around the diagonal which reinforces the notion that, in this particular case, the dominant terms are modeled well.

As the runtime of a single run is quite long (about thirty minutes) no attempt was made to test the dispersive relation over a wider range of *kH* values. However, since the behavior observed is similar to the results in the 2DV model (the depth averaged run has a period which is slightly too long while the two layer solution has the correct period) it seems safe to assume that a similar picture as in Figure 5-5 can be produced.

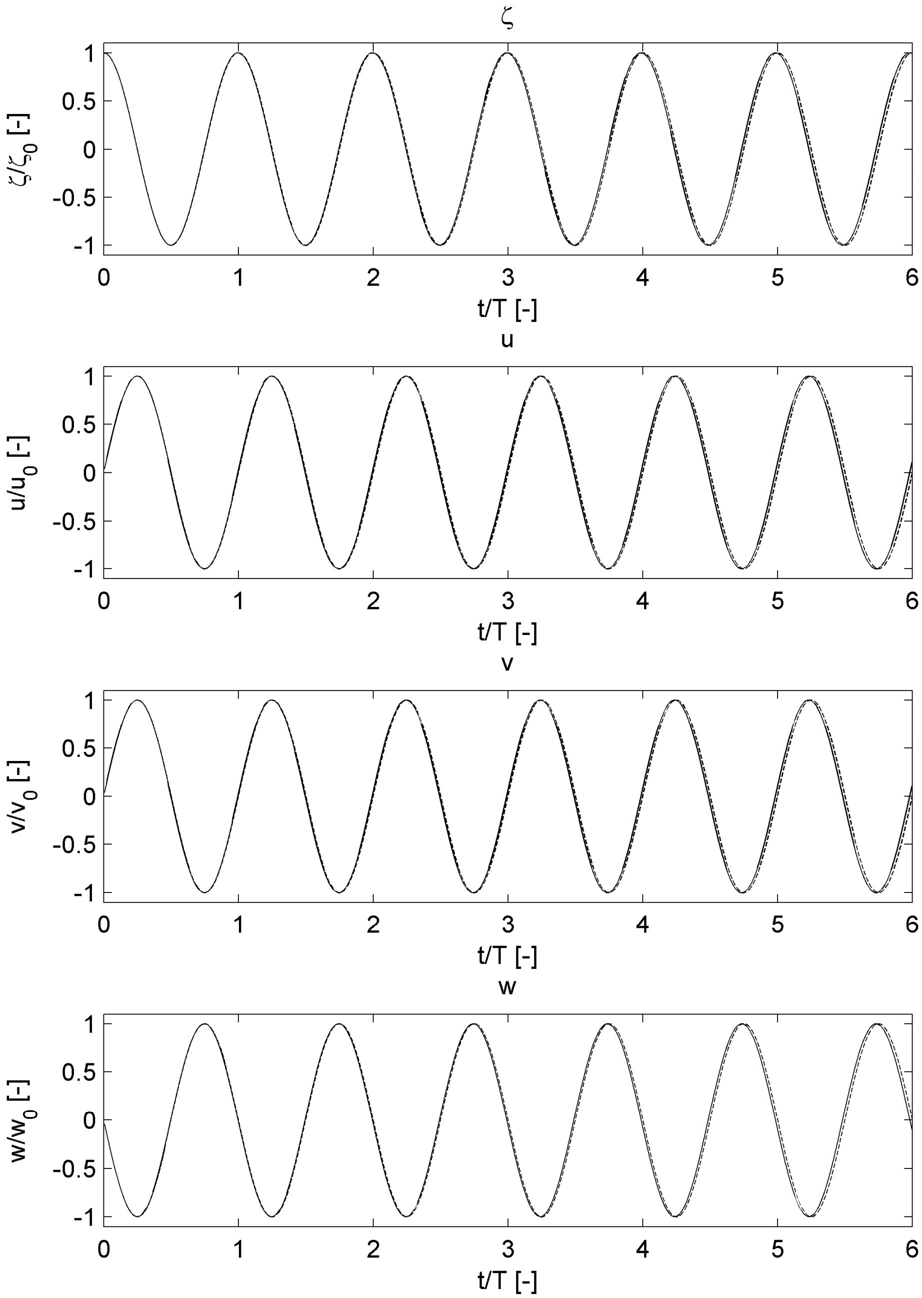

Figure 7-4 The free surface, horizontal depth averaged velocities *u*, *v* and the vertical velocity *w* compared to the analytical solutions at x=50, y=50 for a model run with two computational layers. The analytical solution is indicated with a dotted line while the analytical solution is given by a solid line.

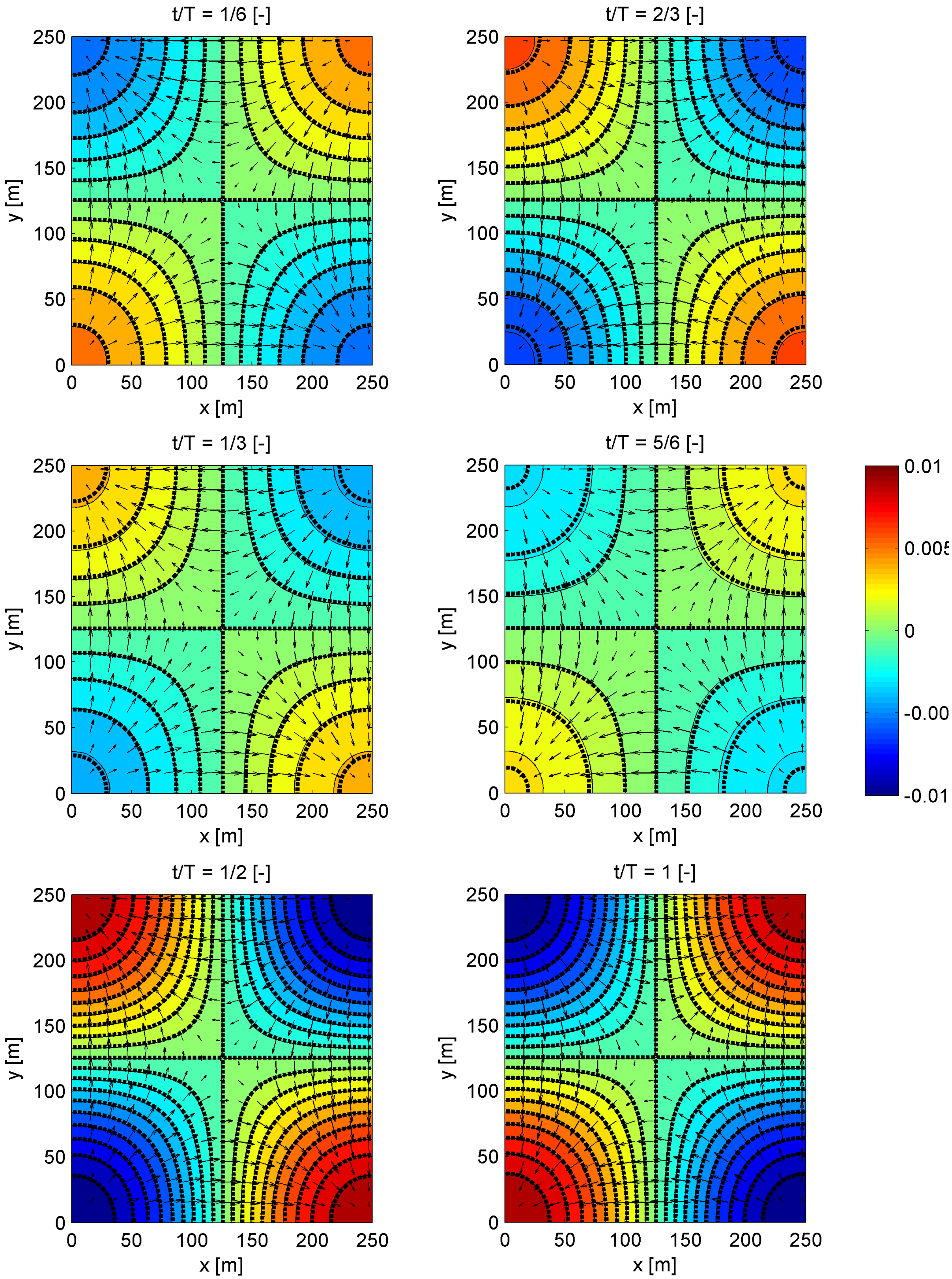

Figure 7-5 Contours of the free surface and velocity vectors of the numerical solution obtained during the first wave period for the model with two computational layers. Contour lines of the analytical solution are indicated by the thick dotted lines.

7.2. Wave deformation by an elliptic shoal on sloped bottom[1]

The Berkhoff Shoal is a classic test conducted in 1982 by Berkhoff et al. which combines refraction, diffraction and shoaling of waves over a complex bathymetry. It was originally setup for a comparison of laboratory measurements with linear wave propagation models but has widely been used to verify models based on Boussinesq like equations. It was also discussed in Stelling and Zijlema (2003) where excellent agreement was found between their model results and the measurements.

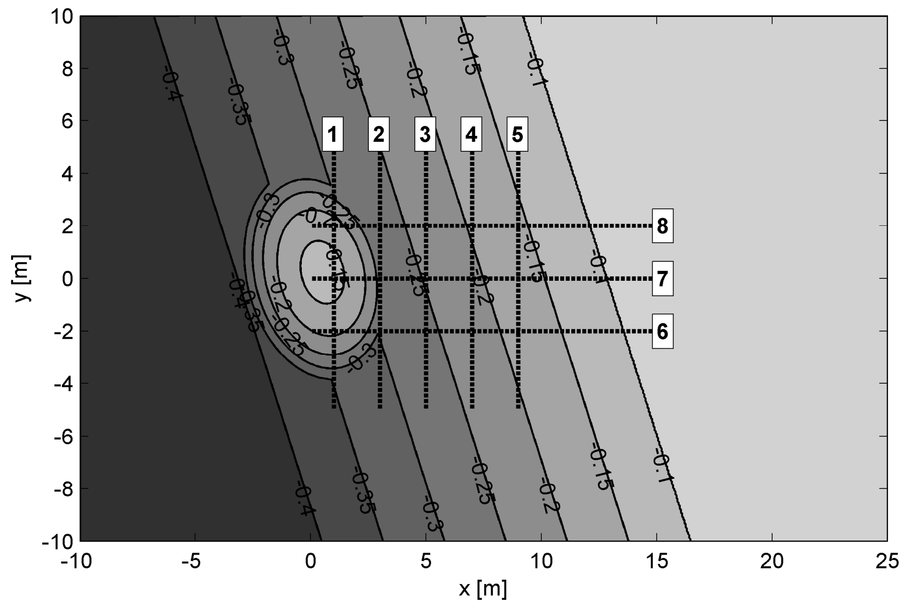

Figure 7-6 Bathymetry of the experiment carried out by Berkhoff et. Al and the location of the transects along which measurements where conducted.

Here the test will be used to verify the correct implementation of the current model. Furthermore the accuracy of the depth averaged model will also be compared to one using multiple layers. Stelling and Zijlema (2003) never considered the depth averaged model in their paper because the kH value of the waves which propagate into the domain is about 1.9 which is relatively large. From this they concluded they needed two layers to accurately model this problem.

The bathymetry can be described using slope oriented coordinates (x', y') which are related to the (x, y) coordinates by means of rotation over -20^o. The water depth in the undisturbed condition without the shoal is then given by:

[1] The description of the test is taken from Stelling and Zijlema (2003)

$$\begin{aligned} &H = 0.45 && , \quad y' < -5.484 \\ &H = \max(0.10, 0.45 - 0.02(5484 + y')) && , \quad y' \geq -5.484 \end{aligned} \tag{7.4}$$

An overview of the bathymetry is presented in Figure 7-6. The shoal is bound by:

$$\left(\frac{x'}{4}\right)^2 + \left(\frac{y'}{3}\right)^2 = 1 \tag{7.5}$$

And the thickness of the shoal is given by:

$$d = -0.3 + 0.5\sqrt{1 - \left(\frac{x'}{5}\right)^2 - \left(\frac{y'}{3.75}\right)^2} \tag{7.6}$$

Monochromatic waves with a frequency of 1 Hz. and wave height of 4.64 cm are generated at the lower boundary and propagate into the domain. At x=-10 and x=10 a closed boundary is present. The grid size is set to $\Delta x = \Delta y = 0.05m \approx \lambda / 30$, where λ denotes the wavelength in the deeper part. A simulation period of 30 s is chosen so that a stationary solution is obtained while the CFL condition is set to 0.2.

In the experiment wave heights where measured along eight transects starting just behind the shoal. Three where placed in the x-direction and five in the y-direction. Along each transect ten wave gauges where deployed which where used to measure the wave height after a steady state was reached. In the numerical model the wave heights where measured straightforwardly by recording the maximum and minimum water level which occurred during five periods when the stationary solution was achieved. Locations of each of the transects are shown in Figure 7-6 where they are numbered from one to eight.

Depth averaged model

Due to refraction the shoal acts like a lens in the experiment and focuses the incoming waves to a point behind the shoal. Therefore the highest waves where found behind the shoal, and not at the top of the shoal, which would have been the case if only shoaling was taken into account. Figure 7-7 clearly shows that the highest waves are concentrated into relatively narrow region just behind the shoal, which is exactly which was observed in the experiments.

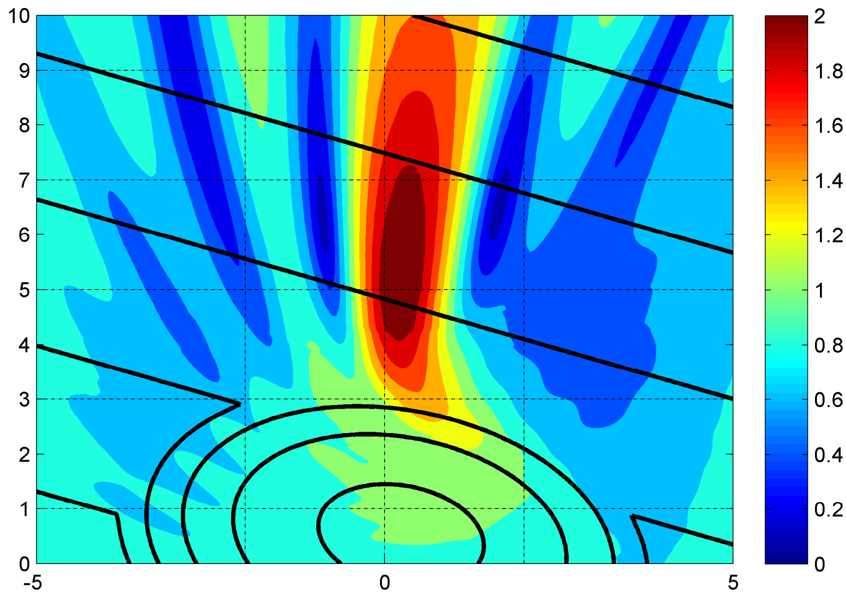

Figure 7-7 Result from the depth averaged run. Shown are the relative wave heights captured in the region just after the shoal.

In Figure 7-8 the results from the model along transects indicated in Figure 7-6 are shown and compared to the measurements. In the results from sections three to five both the width and height of the focal point behind the shoal is adequately represented. The secondary maxima shown in the measurements are also reasonably captured. Only the minima in section five are clearly under predicted. Good agreement between model results and measurements is also found in the sections directed in the stream wise direction (5-7) where the global behaviour found in the measurements is reproduced. A notable exception to this is found in section six, where the model fails to resolve the caustic present in the measurements. This is a featured shared with lower ordered Boussinesq models which also overestimate the wave heights in this region. Usually Boussinesq models with an improved dispersion relation are needed to capture this minimum, and it is therefore not surprising that the depth averaged version fails to capture this point as its dispersive relation is comparable to that of lower order Boussinesq models. In general the depth averaged approach already performed above expectations capturing most of the physical processes well.

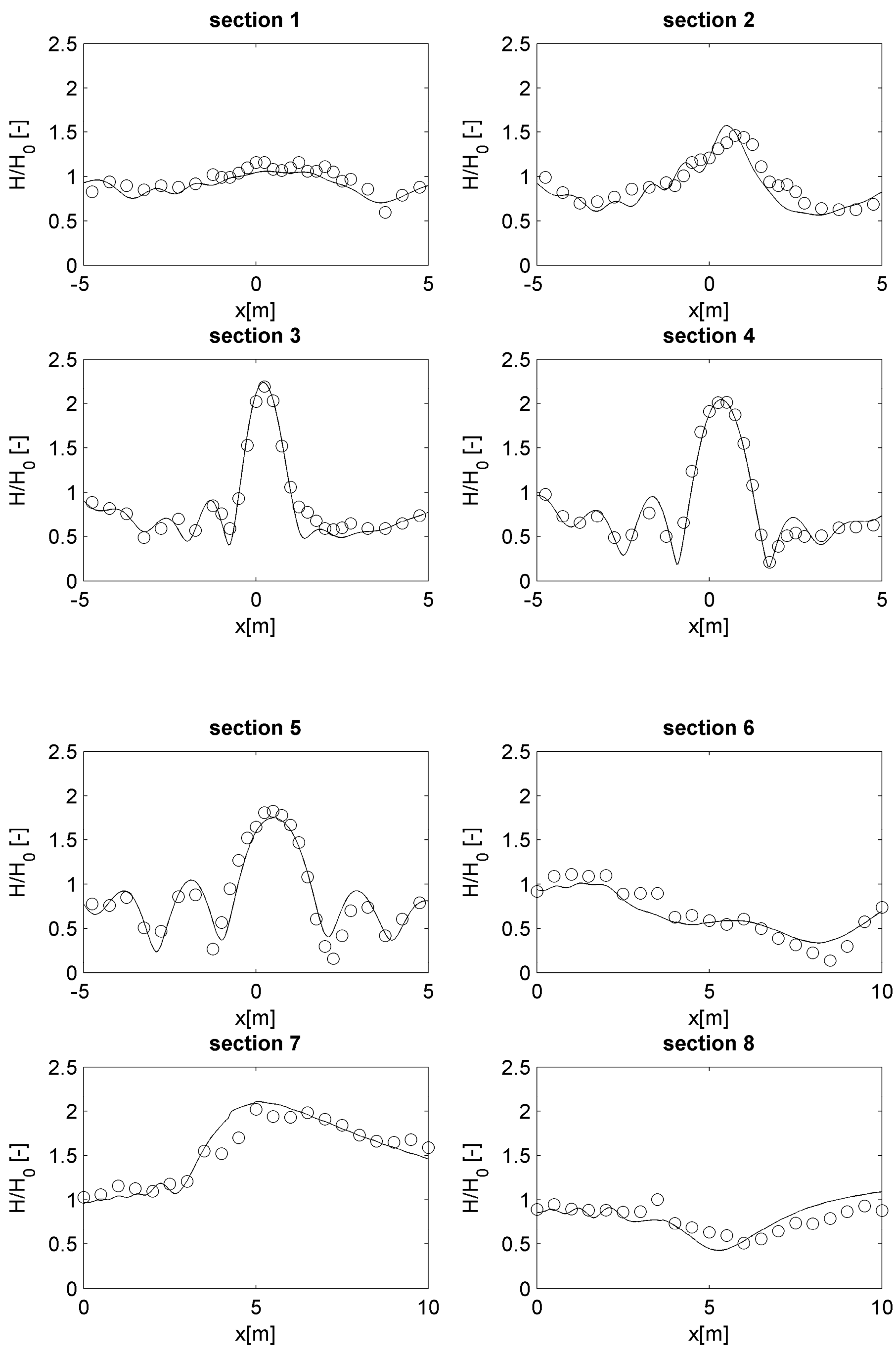

Figure 7-8 Comparison between measurements (symbols) and the results using a depth averaged approach. Shown are the relative wave heights along the eight transects (waves scaled with the incoming wave height). Sections one to five are parallel to the incoming waves fronts while sections six to eight are perpendicular to the waves.

Two layers

Keeping all other parameters identical the number of computational layers was now increased from one to two which is expected to improve the model results. An overview of the resulting relative wave heights behind the shoal is presented in Figure 7-9

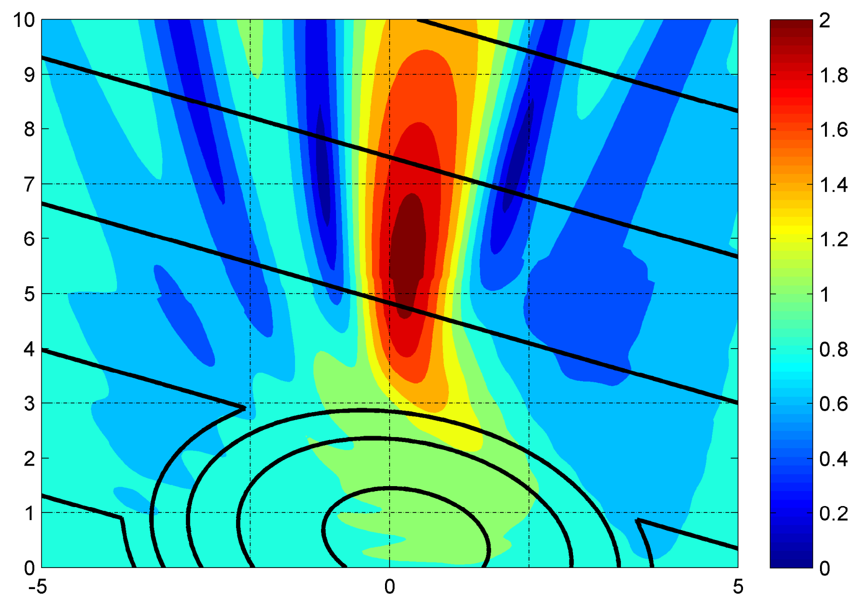

Figure 7-9 Result from the model using two layers. Shown are the relative wave heights captured in the region just after the shoal.

Comparing this figure to the depth averaged version (Figure 7-7) shows little differences. The relative position of the various maxima and minima is slightly changed and there sizes differ somewhat but overall the model results are consistent with each other. A comparison with the measured data is presented in Figure 7-10 which shows results similar to the ones published by Stelling and Zijlema (2003, 2008). The caustic in section six is now present and the secondary maxima in sections three to six are better resolved. Only the maximum behind the shoal in sections three and five is slightly to low.

In general the two layer model predicts the wave heights more accurately than the one layer model but the differences are relatively minor. The depth averaged model is therefore quite attractive. It does reproduce the global trends surprisingly well. Especially considering that the incoming wave was relatively short. The most staggering difference can be found in the computational time, where the twofold increase of grid points resulted in an 300% increase in computational time (from around two hours to around six).

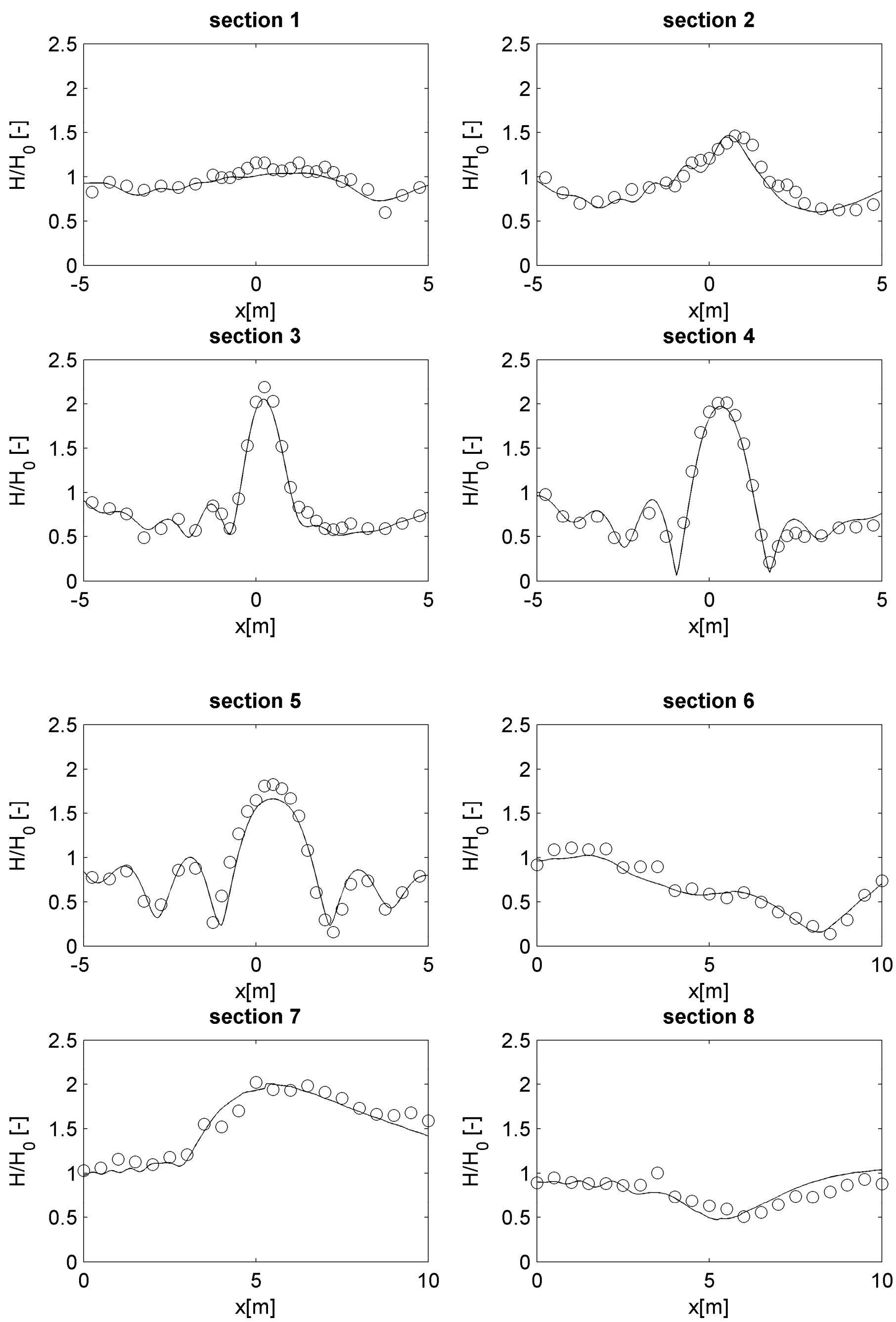

Figure 7-10 Comparison between measurements (symbols) and model using two layers. Shown are the relative wave heights along the eight transects (waves scaled with the incoming wave height). Sections one to five are parallel to the incoming waves fronts while sections six to eight are perpendicular to the waves.

7.3. Discussion

To test the implementation of the three dimensional model it has been validated against an academic test case for which analytical solutions exist, and against measurements performed in laboratory conditions. The validation of the three dimensional model was less extensive than in the 2DV case due to time constraints. Especially the lack of a flooding and drying test in two horizontal dimensions is something which is unfortunate. Nevertheless, all of the 2DV flooding and drying cases gave similar results when run in the other horizontal direction which gives some confidence in the correct implementation.

In the basin test the model showed similar behaviour as found in the 2DV test. With a single layer linear dispersion is less accurately represented in the model than using two layers. Although only a single basin was tested, as opposed to several basins of varying depth, it seems plausible that the dispersion relations found in the previous chapters are also valid in a three dimensional setting.

It is encouraging though that the depth averaged model offers a significant improvement over the hydrostatic model. Furthermore it does qualitatively reproduce the solution with the correct surface amplitude and a qualitatively correct velocity field . However, the periods of the solution are slower than those of the analytical solution and the amplitudes of the velocity components are over predicted.

Finally the performance of both of the matrix solvers seems to be satisfactory. Both gave similar solutions for the depth averaged case and both appear to give sufficiently accurate results for a relatively large threshold. In general the BiCGSTAB solver needed roughly a single iteration per time step while the SIP solver used about three. However, the SIP solver was, due to its smaller memory footprint and simpler algorithm still faster when it could be used.

The Berkhoff test was used to verify that the effects of shoaling, diffraction and refraction could be successfully modelled. It featured relatively small waves on the off shore boundary which propagated over a shoal located on a slope.

The results achieved with both the depth averaged model and the two layer model are considered to be very good. Especially the results in the depth averaged case where far above expectations. The depth averaged model was able to reproduce the shoaling and refraction on top of the shoal and the wave focussing behind the shoal very well. When compared to these results the improvements the two layer model gave where not spectacular. The caustic, which was not well resolved in the depth averaged model, now appears to be correctly modelled and the wave focussing is marginally better. Other than this the results for both models are quite similar.

This is a quite favourable result when considering the propagation of tsunami waves. Since in this case the waves will have larger relative wavelengths it appears that a depth averaged approach should be sufficient to correctly represent these effects.

Section IV: Application to tsunami benchmark experiments

8. Run up on a vertical wall

The numerical model as constructed and verified in the previous chapters appears to be able to reproduce most of the physically relevant processes for wave propagation and run up reasonably well. Although the model needs more verification when considering short wave propagation and run-up it appears that, at least qualitatively, the model gives good results under long waves. It therefore seems appropriate to test the model against measurements of tsunami like waves.

The National Science Foundation (NSF) funded a study beginning in 1992 to identify important physical parameters involved in 3D tsunami run-up. Over the course of this study, several flumes and basins were used to conduct four physical models of a plane beach, vertical wall, and a circular island. Of these four experiments the measurements from the vertical wall and circular island case are freely available[1] and where featured in a workshop on tsunami run-up where several long wave models where used to reproduce the data.

8.1. Experimental setup

In 1995 two-dimensional (2D) flume experiments of solitary wave run-up on a vertical wall were conducted by Briggs et al. at the U.S. Army Engineer Waterways Experiment Station, Vicksburg, Mississippi. .The wave flume used was $23.23\mathrm{m}$ long and $0.45\mathrm{m}$ wide and contained a compound slope fixed bed bathymetry simulating the bottom profile at Revere Beach, Massachusetts. The bathymetry consisted of a deep section and three different slopes (1/50, 1/150./1:13). At the start of the domain a wave maker was located which generated the solitary waves.

Ten capacitance wave gages were used to measure surface wave elevations along the centerline of the flume (Y=0). The origin of the x-axis was at the wavemaker. The first four gages were located in the constant depth region to measure incident wave conditions. Gages 1 to 3 remained at fixed positions for all tests. Prior to each run, gage 4 was moved seaward from the toe of the 1:53 slope a distance equivalent to half-a-wavelength (i.e. L/2) of the wave to be generated. This procedure ensured that the tsunami wave was always measured at the same relative stage of evolution. Gages 5, 7, and 9 were located over the toes and the remaining gages were spaced approximately midway up each slope of the compound-slope beach profile.

[1] At the time of writing these were available at: http://chl.erdc.usace.army.mil/

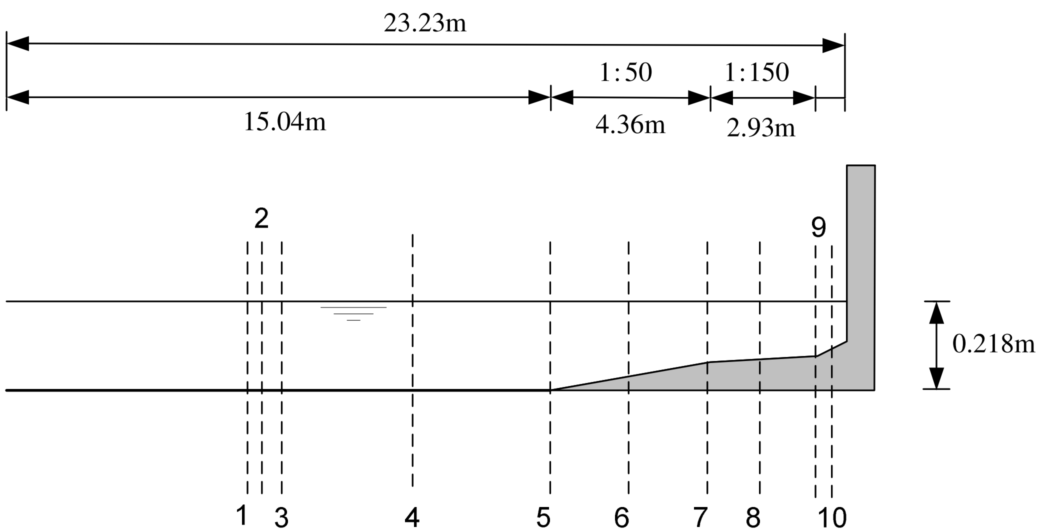

Figure 8-1 Schematic overview of the experiment conducted by Briggs et. Al.

Gage	4A	4B	4C	5	6	7	8	9	10
X (m)	12.64	14.06	14.40	15.04	17.22	19.40	20.86	22.23	22.80

Table 8-1 The locations of the different used wave gages and the three cases which where run.

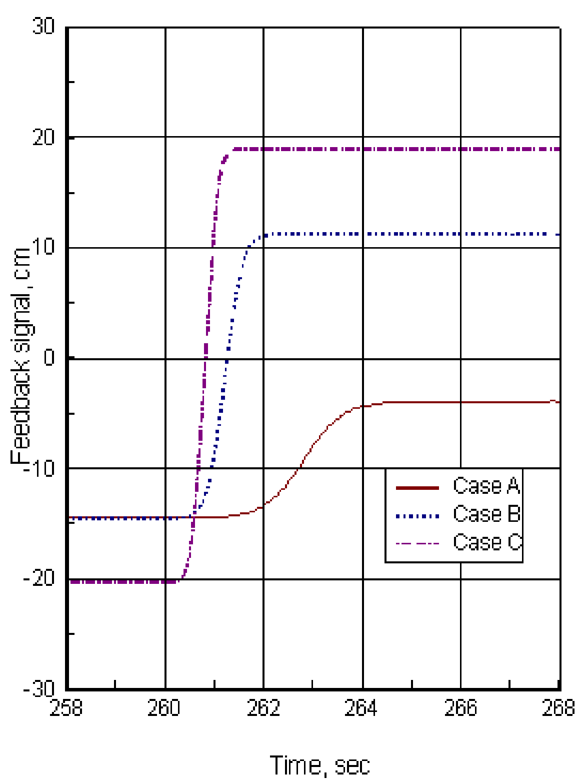

Figure 8-2 Wave paddle trajectories for the cases A. B and C.

The maximum run-up near the wall was also visually recorded. When the waves reached the vertical wall, a plume of water would shoot upward. The highest point of this excursion was visually noted through the glass walls of the flume and manually recorded after each run.

Case	**A**	**B**	**C**
Target ζ_0 / d_0	0.05	0.30	0.70
Achieved ζ_0 / d_0	0.039	0.246	0.696
ζ_0 / L	0.0022	0.0178	0.1164
d / L	0.044	0.088	0.166

Table 8-2 Target and achieved waveheights for the three cases.

As a model for tsunami waves solitary waves of different amplitudes where generated by the wave maker. A total of three different cases where simulated and the target and achieved relative wave heights are listed in Table 8-2. The paddle trajectories for each of the cases are shown in Figure 8-2.

Of the three cases only case A can be considered to roughly represent a tsunami of geophysical scale. Taking for instance a typical wavelength of 10 kilometers at a depth of 100m with a maximum wave height of ten metres leads to a wave steepness of roughly 0.001 and a relative shortness of $d / L = 0.01$. These parameters are of the same order of magnitude as the wave in case A. Case B has a wave steepness which is one order of magnitude larger and can be considered as an upper limit. Case C is two orders of magnitude steeper and much shorter and cannot be considered as being representative for the leading wave of a tsunami.

8.2. Numerical model setup

Although the wave paddle trajectories where available, these where not used as a forcing in the model, as the correct implementation of such a boundary can be complicated. Instead it was decided to use a similar procedure as was used in the modeling of the run-up of solitary waves on a plane beach. The solitary wave was prescribed three wavelengths away from the first gage as an initial profile on the water surface. Here again the definition for a wavelength under a solitary wave given by equation (5.12) was used. This initial profile was then propagated in the direction of the vertical wall. The arrival time of the peak of the solitary wave was matched to the measured peak at the first wave gage.

Unfortunately no data was available from the first three wave gages and it therefore little sense to include the full wave tank in the modeled domain. Instead the choice was made to put the boundary of the domain five wavelengths in front of the fourth gage. In this way the peak of the initial solitary wave was located two wavelengths away from the boundary. The larger solitary waves have a tendency to deform a little from their starting profile and in doing so some wave components are send in the opposite direction to the wave propagation. To allow these waves to leave the computational domain a weakly reflective boundary was placed on the side of the wavemaker.

The domain was discretisized using an uniform grid spacing which was coupled to the wavelength of the solitary waves. The grid resolution was coupled to the wavelength such that each of the waves was modeled with at least a hundred points per wavelength. The number of grid points and the grid spacing was therefore dependent on the incoming wave. The CFL condition was set at 0.1 which roughly corresponded to an average time step of $\Delta t = 0.07\mathrm{s}$, although this varied between the runs due to the differences in the grid spacing.

Each of the cases was modelled using one and two computational layers. Furthermore a model run was done without the non-hydrostatic pressure corrections. Since this experiment was 2DV in nature the block solver was used as a matrix solver. Furthermore as no flooding and drying was encountered the limited second order expressions where used.

8.3. Results

8.3.1. Case A

Of the three cases considered case A had the lowest incoming wave and in this case it was expected that the hydrostatic model still should perform reasonable. The first run was therefore performed using the model without the non-hydrostatic pressures and this case functions as a benchmark for the improvements, if any, the inclusion of the non-hydrostatic pressure brings.

In Figure 8-3 results are presented for the gages five, seven, nine and ten. The results for the other gages can be found in appendix D.1.1. Starting at the toe of the slope (at gage five) it appears the hydrostatic solution gives virtually identical results to the measurements. Both wave height and width are consistent with the measurements. There does appear to be a small mismatch in the still water level between measurements and the model which is also observed in the measurements of the other gages. The still water level is slightly too high in the model in gages five seven and nine while somewhat too low in gage ten.

Traveling in the direction of the wall the wave starts to shoal and begins to steepen. The correspondence between the wave and the measurements is still good at gage seven and the results are also reasonable at gage nine, At the wall near gage ten the wave has steeped too much and immediately breaks upon reflection. Traveling back in the direction of the boundary it is apparent that the hydrostatic solution is no longer similar to the measurements as the wave form is totally different. In the experiments the reflected wave still clearly represents a solitary wave while in the numerical model the wave travels as a bore.

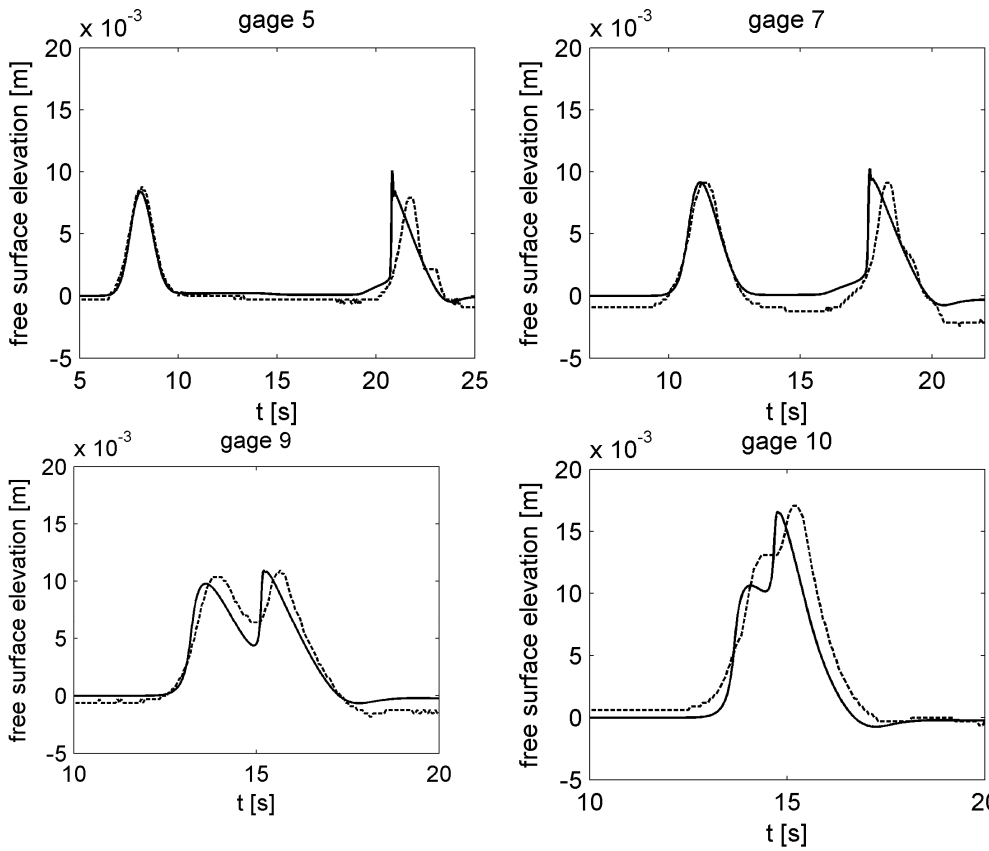

Figure 8-3 Case A: Hydrostatic results for the gages 5,7,9 and 10, Solid line indicates model results while the broken line indicates measurements.

The lack of dispersion to combat the wave steepening due to the non-linearities apparently already has a substantial influence. It should be noted that the wave only fully broke at the vertical wall. If, instead of a wall there would have been a mildly sloping beach the results probably would have been more favorable for the hydrostatic model.

Enabling the non-hydrostatic pressures the case is rerun in the depth averaged mode. The results for the gages five, seven, nine and ten are presented in Figure 8-4 while the results for the other gages can again be found in the appendix. The large difference between the non-hydrostatic and hydrostatic solutions is immediately apparent as the reflected wave now is unbroken. The wave now has a shape similar to the wave found in the measurements.

There is a difference in phase and amplitude as the reflected wave in the model is slightly higher and faster than the wave in the measurements.

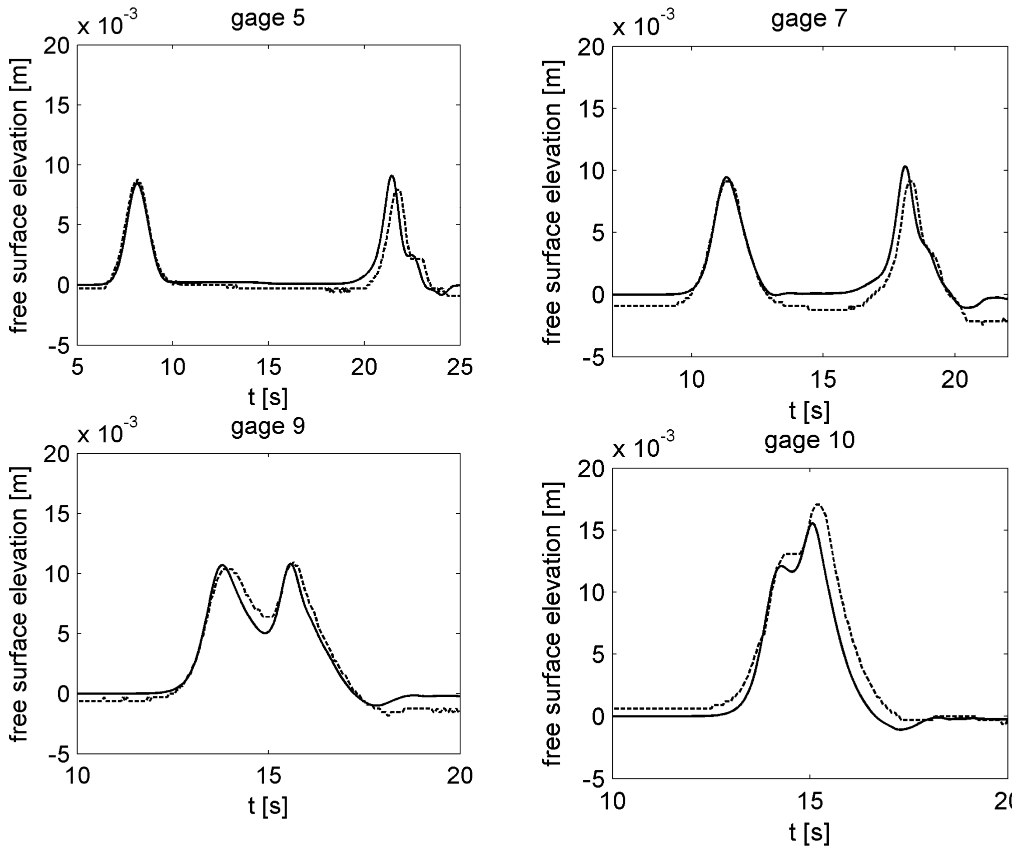

Figure 8-4 Case A: Depth averaged non-hydrostatic results for the gages 5,7,9 and 10, Solid line indicates model results while the dotted line indicates measurements.

There are also some minor improvements found in the shoaling process of the wave as can be seen from comparing the gages seven and nine from the hydrostatic to the non-hydrostatic runs.

Finally it is noted this first case was also modelled using two layers. This did not produce any significant differences with the depth averaged runs and the results are not presented here. They are available in appendix D.1.1.

8.3.2. Case B

The incoming wave specified in case B is significantly higher than in case A. Due to the nature of solitary waves this means that the wavelength has decreased leading to a much steeper incoming wave. The wave in case A had a wavelength L of about 2.80m while the wavelength for the incoming wave in case B is about 1.11m. Thus, not only is the wave almost five times as high, it is more than twice as short as well. This clearly indicates that the wave is much steeper than in the first case and the balance between frequency dispersion and amplitude dispersion becomes much more critical.

This is confirmed when looking at the results from a hydrostatic run at gage six in Figure 8-5. Gage six is located midway on the primary slope and the measured wave starts to show signs of shoaling here. In contrast to this the wave in the numerical model has already broken. This clearly shows that the hydrostatic pressure assumption is no longer valid in this case.

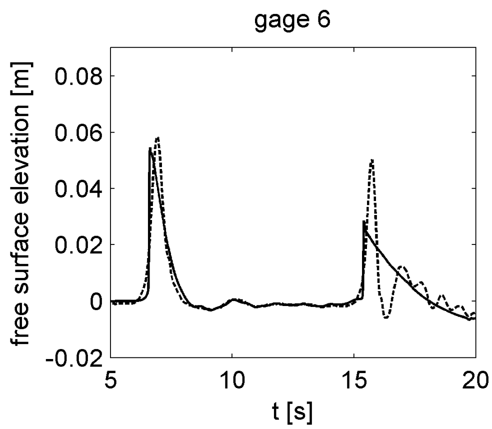

Figure 8-5 Hydrostatic solution for case B. The wave has already broken in the numerical model at gage six. Solid line indicates model results while the dotted line indicates measurements.

The results for the other gages are shown in the appendix but they show a progressively worsening picture.

Using the depth averaged version the non-hydrostatic model the results in Figure 8-6 were obtained. The overall agreement with the measurements is excellent as all gages show that the wave shape and amplitude are well resolved. Only at gage ten there is a significant difference between the measured and calculated amplitude. However, the measured wave appears to have a physically unrealistic shape here and the measurements are most likely in error.

After the wave reflects a small error in the phase is observed and the amplitude is slightly overestimated. Furthermore it is noted that only the leading wave is correctly modelled. The secondary wave, which still has a significant wave height, is present. It has a smaller amplitude and the wave train following these primary waves shows only superficial resemblance to the measurements. Finally it is noted that, similar to case A, using multiple layers resulted in no significant improvement.

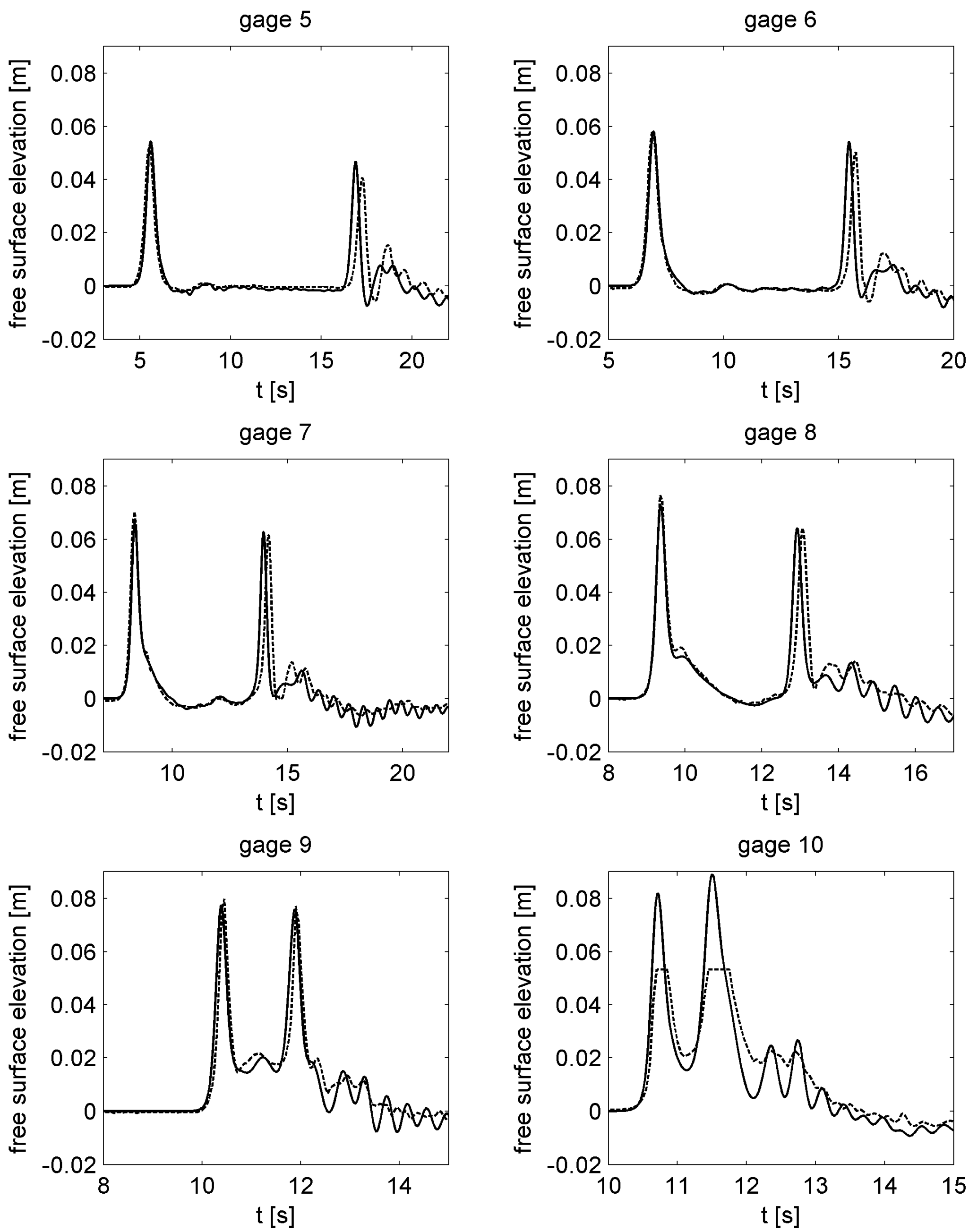

Figure 8-6 Results from the depth averaged non-hydrostatic model for Case B. The solid line indicates model results while the dotted line indicates measurements.

8.3.3. Case C

In the final case the target relative wave height in the experiment was 0.70 while the achieved wave height was very close to this at 0.696. Unfortunately such a highly non-linear solitary wave can no longer be adequately prescribed by the third order solitary wave equations given in (5.11). The main problem with these expressions is that they begin to show new extrema in the velocity components that are not physically realistic.

The problem is that the higher order terms which are neglected are needed to balance the behavior of the lower order terms. Interestingly the free surface profile does not exhibit this behavior and therefore remains acceptable as a solution. To circumvent this problem a first order Boussinesq solution was prescribed as this solution does not contain the oscillatory behavior for higher waves. This does mean that the initial wave deformed significantly which resulted in a larger spurious tail and a significant decrease in amplitude. In order to achieve the correct amplitude at wave gage four some trial and error was therefore involved.

For the results using the hydrostatic approximation the reader is referred to the appendices. The wave is now is significantly non-linear and using the hydrostatic pressure assumption leads to inaccurate results.

Also due to the high initial wave case C is the first case where using two layers visibly produces better results. Here the solution using two layers is presented in Figure 8-7 and the results using the depth averaged model are given in the appendices.

Up until gage eight the results for the wave traveling towards the vertical wall show a good correspondence to the measurements. Wave height, wave form and phase are all consistent with the measurements. However, from the measurements it appears that the wave breaks between gages seven and eight. This is not reproduced in the model as the wave height remains constant in the results.
The model wave height does start to diminish between the gages eight and ten despite the still declining water depth which indicates that wave braking is starting to occur.
The reflective wave is also substantially larger in the model and this is the reason the phase error begins to increase. The final form is reached between the gages four and five where the solution qualitatively agrees with the measurements. Both show a leading wave with a small following trough and a spurious tail.

Concluding it can be said that the main source of errors in this case appears to be the incorrect location of the onset of breaking. It is expected that if this is captured more accurately both subsequent phase and amplitude errors will diminish significantly.

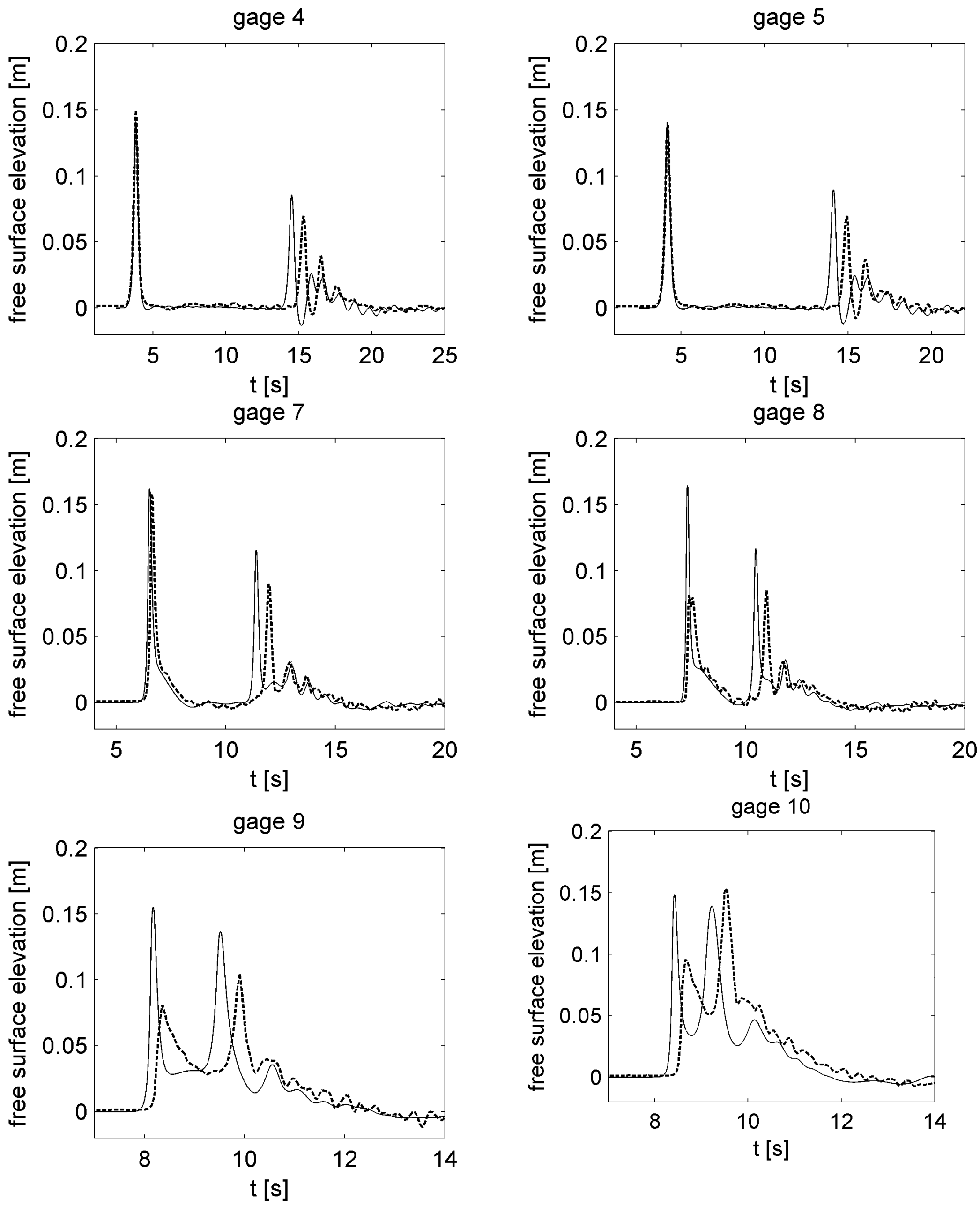

Figure 8-7 Results from the non-hydrostatic model using two layers for Case C. The solid line indicates model results while the dotted line indicates measurements.

8.4. Discussion

The experimental results of the run-up of three different solitary waves on a compound beach ending in a vertical wall where compared to the results produced by the numerical model. Both hydrostatic and non-hydrostatic runs where performed to see the difference, if any, the inclusion of frequency dispersion gives.

It is interesting to see that in all three cases the hydrostatic solutions lead to wave fronts that where steeper than the measured waves and eventually this lead to premature breaking. In cases B and C the differences where so dramatic that the hydrostatic model can no longer be regarded as a viable alternative.

For case A this was different as the incoming wave was much lower and longer which meant that the over steepening typical of the NSWE would not result in very large differences before reflection. For the reflected wave again the NSWE resulted in premature breaking while the measured wave travelling in the off-shore direction still represented a solitary wave.

When using the non-hydrostatic model the waves kept their correct shape and the agreement between the measurements and the numerical results where quite favourable.
Especially case A and case B produced excellent agreement for the leading waves. The agreement for the wave train following the solitary wave after reflection was less good. But it should be mentioned that the back slope of the experimental waves was generated with less accuracy than the front.
In the final case the model actually predicts the breakpoint of the wave a little bit too late. Here the wave continues shoaling while the measurements appear to indicate that the wave broke.

In all three cases the reflected wave appears to have a higher amplitude and it travels slightly faster than the measured wave. The phase difference can readily be explained by noting that higher solitary waves travel faster and therefore if the amplitude is overestimated this automatically leads to phase errors. However, this does not explain the error in amplitude. This might be explained by the lack of viscous damping in the model which could have effected the propagation of the wave in the wave tank.

The comparison between the hydrostatic and non-hydrostatic runs is quite favourable for the non-hydrostatic model. It is therefore tempting to conclude that the non-hydrostatic model is necessary for tsunami run-up in comparable bathymetries. However, as noted before, the modelled waves are rather steep when compared to geophysical tsunamis. Especially case C has little significance, since the incoming wave is at least two orders of magnitude steeper than realistic tsunamis. Even case B is most likely too short and too steep to draw any conclusion on.

Although case A is still steeper and shorter than a typical tsunami it does at least have parameters with similar orders of magnitude. It is quite striking that when using the NSWE

the reflected wave, which has travelled over a relatively modest distance of around four incoming wave lengths, has already broken.
It does appear that the wave which impacts the vertical wall is a good approximation of the incoming wave. This suggests that for local impact assessment the results are acceptable. When the reflected wave is also of interest the non-hydrostatic approach has to be used. This confirms that, in the final stages where the wave becomes strongly non-linear, dispersion might be necessary to prevent the over steepening of the wave front.

In this context the results in this section show that the depth averaged model can provide an attractive alternative that has sufficiently accurate dispersion characteristics to make long waves of permanent form possible.

9. Run-up of solitary waves on a Conical island

The second benchmark test of the tsunami workshop features the run-up of a solitary wave on a conically shaped island. The test was undertaken after the Flores island tsunami of 1992 and the Okushiri island tsunami of 1993 produced unexpectedly large tsunami run-up heights at the lee side of small islands. During the Flores Island tsunami, two villages located on the southern side of the circular Babi Island (Indonesia), whose diameter is approximately 2km, were washed away by the tsunami attacking from the north (see Figure 9-1a).

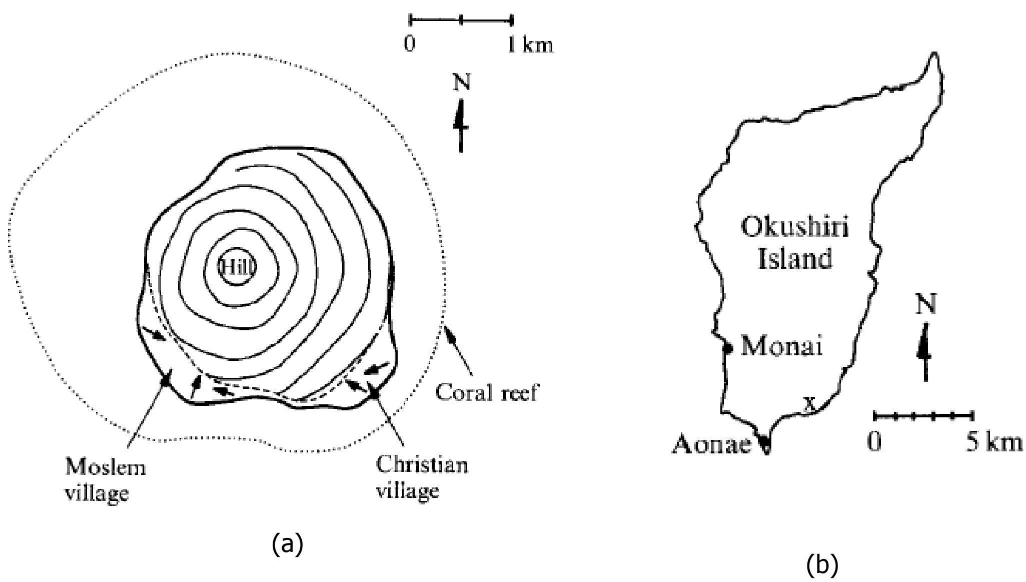

Figure 9-1 **(a)** A sketch of Babi island (Yeh et al 1994). The 1992 tsunami attacked the island from the north while two villages on the lee side of the island where destroyed. **(b)** A sketch of Okushiri Island of Japan (from Hokkaido Tsunami Survey Group 1993). The 1993 tsunami attacked from the northwestern direction. Maximum run-up height reached 30.5 m at Monai which faces the tsunami directly. However, the second largest run-up height (- 20 m) was observed northeast of Aonae in the lee side of the island indicated by x.

Something similar happened during the Hokkaido Island tsunami near Okishiri Island (Japan). Here the pear shaped Okushiri island was attacked from the northwestern direction and caused extensive damage on the southern side of the island. Run-up heights as high as twenty meters where observed at the marked location in Figure 9-1b.

In both instances the highest damages where found on the lee side of the islands. This is apparently not an entirely uncommon and as reported by Bascom(1990): "We discovered that, except for headlands pointing into the tsunami, embayment's facing exactly opposite to the wave direction were likely to be most affected."

At the time, numerical simulations by different international teams produced results that differed substantially from field measurements, often by a factor of ten (see Briggs et. al 1995). Recognizing the need for a better understanding of the important physical parameters involved in three-dimensional run-up, the experimental study by Briggs et al. (1995) was undertaken.

In the experiment a tsunami impact on a small conical island was simulated and the run-up height was measured around the island. Interestingly they found that for certain wave heights the run-up on the lee side could actually become slightly larger than that on the front. Refraction and diffraction cause the wave to bend around the island as edge waves. Because the island and source were symmetric, the wave wraps evenly around the island and produces relatively large run-up on the back side.

The experimental results from this study have since then featured in numerous articles. Examples of these include Fuhrman and Madsen (2007), Titov and Synolakis (1998), Choi et. al (2007) and Lui et al (1995).

9.1. Experimental setup[1]

A physical model of a conical island was constructed in the centre of a 30 m wide and 25 m long flat bottom basin at the U.S. Army Engineer Waterways Experiment Station. The shape of the island was a truncated circular cone with diameters of 7.2m at the toe and 2.2 m at the crest. The vertical height of the island was about 62.5 cm, with a 1:4 beach face. In the experiments test where conducted with two waterdepths, 32 cm and 42 cm. Only the measurements from the 32 cm tests where available and are used here.

The origin of the X-axis of the coordinate system was located at the wave maker and had an orientation perpendicular to the wavemaker while he Y-axis was directed parallel to the wavemaker. (see also **Error! Reference source not found.**). The centre of the island was located at x=12.96m and y= 13.80m.

A total of twenty seven wave gages where used to measure the surface elevation. From these twenty seven gages the time signals from gages 1-4,6,9,16 and 22 are freely available and where used. Their locations are indicated in **Error! Reference source not found.**. Similar

[1] The description of the experimental setup is taken from Briggs et al. (1995)

to the experiment with the vertical wall the gages measuring the incoming wave (1-4) where moved seaward from the toe. The distance moved was equivalent to half-a-wavelength (i.e. L/2) of the wave to be generated. The maximum vertical run-up was measured using a rod and transit at twenty locations around the island.

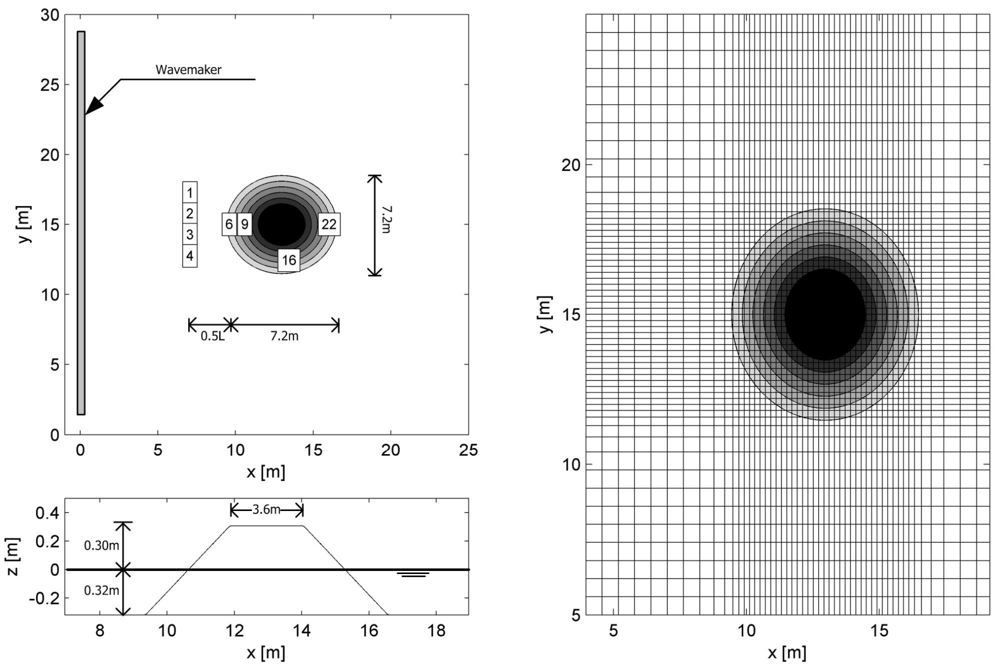

Figure 9-2 Experimental setup of the experiment performed by Briggs (1995) on the left and the numerical grid used on the right. Note that only every fifth line of the grid is shown.

As a model for tsunami waves solitary waves of different amplitudes where generated by the wave maker. A total of three different cases where simulated and the target and achieved relative wave heights are listed in Table 9-1.

Case	**A**	**B**	**C**
Target ζ_0 / d_0	0.05	0.10	0.20
Achieved ζ_0 / d_0	0.045	0.096	0.181
ζ_0 / L	0.0022	0.0063	0.0178
d / L	0.044	0.063	0.089

Table 9-1 Target and achieved incoming wave heights.

The wave parameters are very similar to those in the vertical wall experiment and the comments made there still hold here. The maximum case, case C has the same wave steepens and relative shortness as case B in the previous experiment, while case A is virtually identical to case A of the Vertical wall experiment (see 8.1). Again the cases B and C are steeper than typical geophysical tsunamis while case A might be representative for the leading wave of a medium sized tsunami.

9.2. Numerical Setup

To reduce the problem size only a rectangular sub-domain of the basin was modeled. The wave maker boundary was placed one wavelength away from the first gages while the back boundary was placed one and a half wavelength away from gage 22. On both boundaries a Sommerfeld radiation condition was applied. Both lateral boundaries where placed two wavelengths away from the island centre and where modeled as fully reflecting boundaries. In the original experiment these boundaries where located further away and where coated in wave absorber. Therefore significant deviations from the measurements are expected when the reflections become important. The resulting domain extended from $x = 4m$ to $x = 20m$ and $y = 6.6m$ to $y = 21m$.

The region near the island is expected to contain the largest gradients in the velocity profiles and the free surface. Therefore a higher grid resolution is needed here to achieve comparable accuracy to regions where the solution is smoother. To facilitate this the domain was discretised using a non-uniform grid.

Since flooding and drying is a major feature of this particular experiment only first order approximations where used. To minimize the numerical diffusion inherent to the first order approximations first a 2DV test was run to determine the maximum step size for the flat bed region. This test consisted of a canal, equal in length to the basin, through which the maximum solitary wave to be modeled was propagated. For a grid spacing of 0.04m the numerical diffusion had only small impact on the amplitude of the wave. This was then adopted as the grid spacing in the flat bed region.

The whole region from the centre of the shoal to just beyond the waterline was discretised using $\Delta x = \Delta y = 0.015m$. In this way the whole area where flooding and drying occurred was captured in detail. The region between the fine and coarse grid was covered with a transitional grid defined by (6.1) with a growth factor of 1.1. This ensured a smooth transition between the two grid sizes. The resulting grid contained 592 by 572 points in the horizontal .

The maximum incoming solitary wave has a depth to height ratio of 0.2. This ratio falls right between the waves in case A and case B from chapter 8. Here it was found that the propagation of a solitary wave over a compound beach is well captured using only a singly layer. Although the slopes of the conical island are steeper it is still expected that in this case a single layer will be enough as well. Since the number of gridpoints in the horizontal is already substantial this is a welcome reduction. Furthermore this makes it possible to use the SIP solver which has a smaller memory footprint and is slightly faster than the BiCGSTAB method.

The CFL condition was set to 0.5 which resulted in an averaged timestep of roughly $\Delta t = 0.0016s$. This small timestep is a result of the combination of an explicit method with the need for a high resolution in the area of flooding and drying and is probably not necessary with regard to accuracy. Again each run was conducted with and without the non-hydrostatic pressure correction. Finally it should be mentioned that only the cases B and C where modeled due to time constraints.

9.3. Results

9.3.1. Case B

To facilitate the discussing of the results in the coming sections first a sequence of snapshot type figures presented in Figure 9-3. In this figure snapshots of the contour lines of the free surface are shown which show how the wave refracts around the island.

Starting at t=6.4s the incoming wave starts to shoal in front of the island. At t=7.6s the solitary wave attacks the front side of the island and generates significant amount of run-up. It also starts to separate into a portion of the wave which travels along the top of the island and a wave which travels along the bottom. Due to the bathymetry portions of the wave are still in deeper water where they travel faster than the portions of the wave near the island. This causes the bending of the wave crest which starts to appear at t=7.5s and is clearly visible at t=9.2s.

Between t=9.2s and t=10s the main part of the wave propagates away from the island separating from a small part of the wave which continues to travel alongshore. At t=12.4s both of the trapped waves crash into each other inundating large parts at the back of the island. They then separate again while continuing to propagate alongshore as can be seen at t=13.6s. At this point they continue to leak energy away in the off shore direction which means that their wave height is quickly diminishing from this point onwards. Furthermore reflections from the top and bottom walls now begin to interfere with the results.

What is interesting from these results is that the physics of the problem are qualitatively captured quite well. The incoming solitary wave bends around the island and travels away from the island while portions of the wave become trapped and eventually crash into each other to cause enhanced run-up at the back of the island.

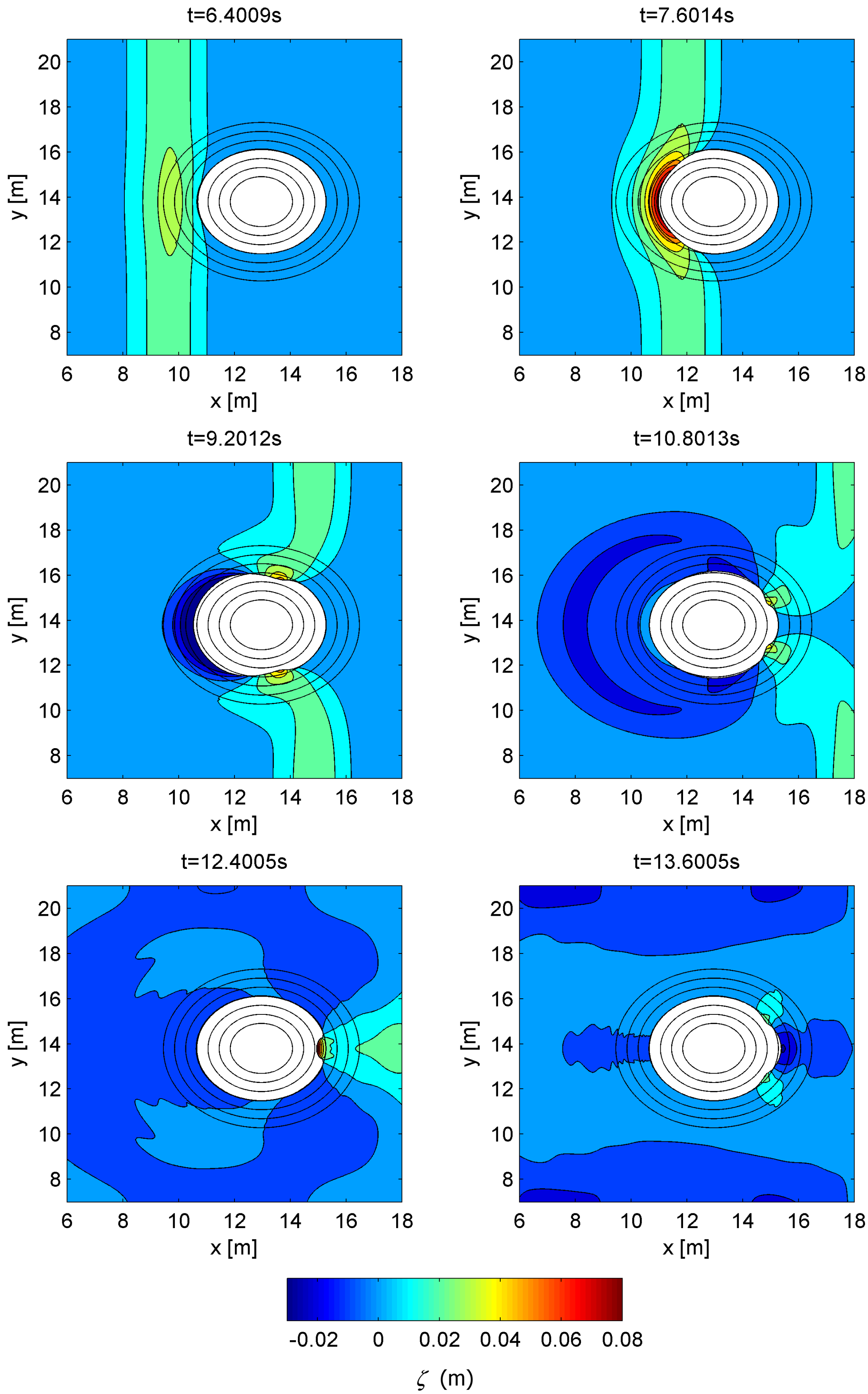

Figure 9-3 Snapshots of the free surface taken at the indicated times for case B.

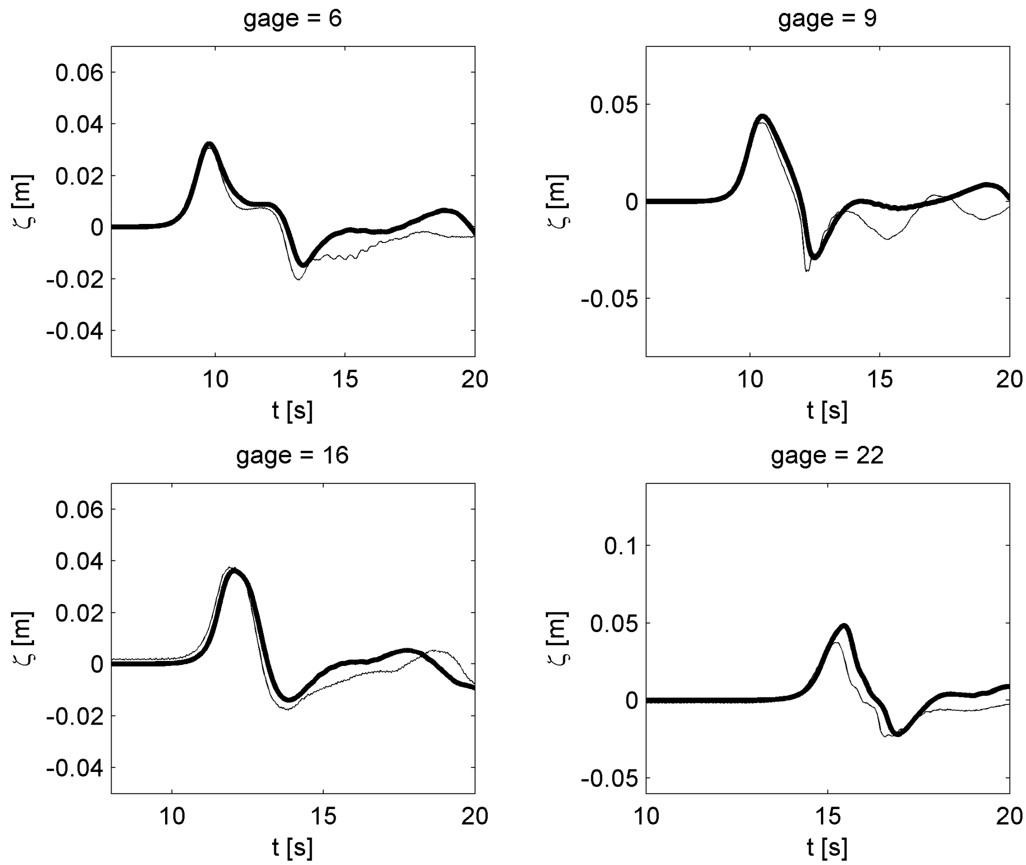

Figure 9-4 Measured (thin line) and calculated (thick line) results at the indicated wave gages for case B.

When comparing the results to the measurements of the four available wave gages the results in front of the island are quite good. In Figure 9-4 the measurements of the gages 6,9,16 and 22 are compared to the computed results. The location of the gages is indicated in **Error! Reference source not found.**. The gages 6 and 9 show the wave as it shoals at the front of the island and partly reflects back. Especially the front of the incoming wave agrees very well with the measurements. At gage 9 the trough of the reflected wave is less deep and sharp as measured, which is also visible at gage 6. Furthermore the depression quickly disappears in the model while the measurements show that the free surface stays below the still water depth for quite some time after the main reflection has passed.

Looking at gage 16, which is located below the island, the arrival time of the wave is predicted well together with its initial amplitude. Again the following depression is slightly less pronounced and has a shorter duration compared to the measurements. Finally at the back of the island at gage 22 again the arrival time of the wave is in excellent agreement. However, the maximum amplitude is over predicted at this location. The wave appears to be significantly larger in the computations than measured, although the shape appears to agree quite well. The amplitude of the following depression is correctly reproduced with a small phase difference.

Finally it should be mentioned that this case was also run hydrostatically and the results for the four wave gages in this case are presented in appendix D.2.1. In these results again the hydrostatic approximation leads to wave fronts which are to steep although the results for gages 6,9 and 16 are very reasonable.

The run-up around the island is also compared to the measured run-up. Both the non-hydrostatic and hydrostatic results will be presented to see how much they differ.

In Figure 9-5 the run-up around the island is shown in a polar plot. The center of the plots correspond to the center of the island. It is clear that the inundation depth is quite similar for the hydrostatic and non-hydrostatic solutions although the hydrostatic solution appears to have traveled a bit further inland at the front of the island.

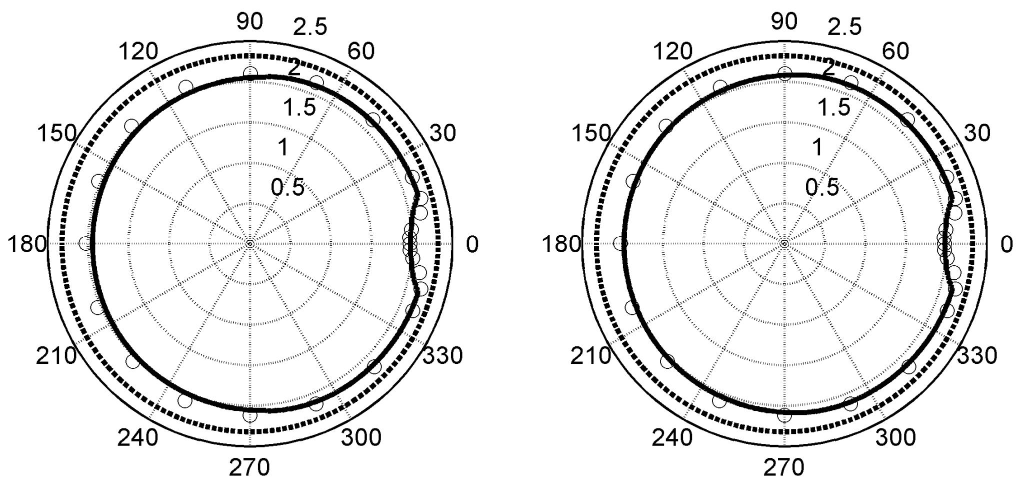

(**a**) (**b**)

Figure 9-5 Computed (solid lne) and measured (circles) maximum inundation depth around the conical island for case B. The dashed line indicates the initial shoreline position. (**a)** depth averaged hydrostatic results, (**b)** depth averaged non-hydrostatic results.

In Figure 9-6 the run-up height around the island is shown for the hydrostatic solution compared to the measurements. Here it is clear that at the front of the island (corresponding to $\pm 180^o$) the run-up is over predicted with more than ten percent. This trend occurs until at the back of the island the run-up is slightly under predicted. Thus the results from the measurements that the run-up height at the back is higher than at the front is not reproduced for the hydrostatic case.

In Figure 9-7 a similar figure is presented for the non-hydrostatic case. Again the run-up at the front of the island is slightly over predicted, but less so than in the hydrostatic case.

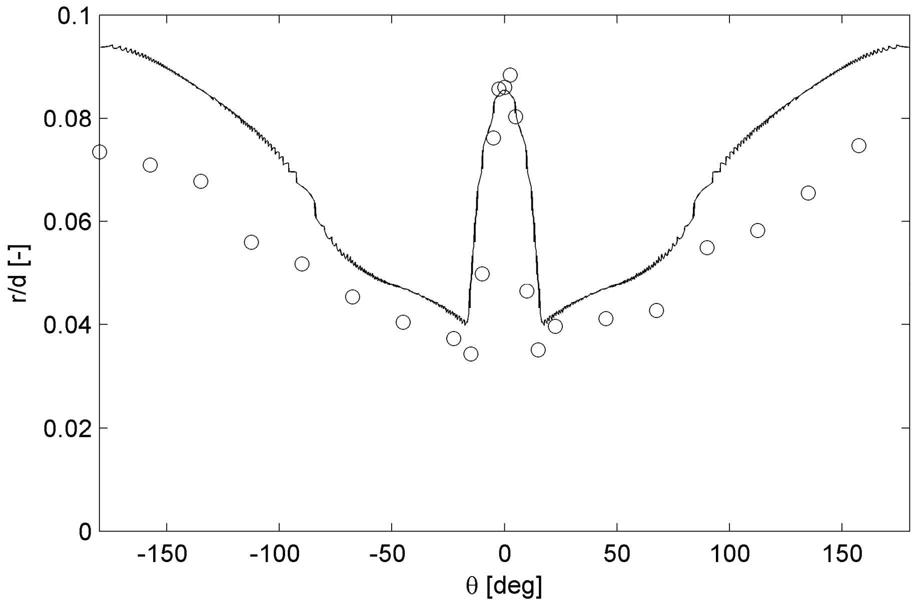

Figure 9-6 Maximum relative run-up around the island for case B in the depth averaged hydrostatic run. Measurements are indicated with a circle while model results are shown as a solid line.

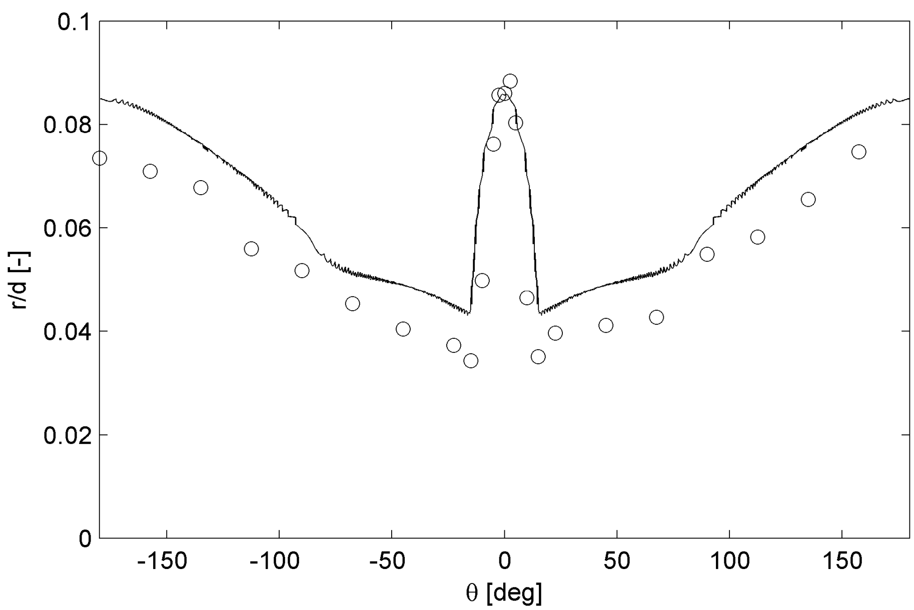

Figure 9-7 Maximum relative run-up around the island for case B in the depth averaged non-hydrostatic run. Measurements are indicated with a circle while model results are shown as a solid line.

The run-up at the back of the island has a similar magnitude as in the hydrostatic case but is now higher than the run-up at the front of the island. All in all the correspondence between run-up and measurements is not great. Qualitatively the solutions agree but the quantitative differences are quite large for both solutions.

9.3.2. Case C

The only difference between case B and C is the different height of the incoming solitary wave. The solution therefore qualitatively behaves in much the same way as the wave in case B and the analysis of the evolution of the wave will not be repeated here.

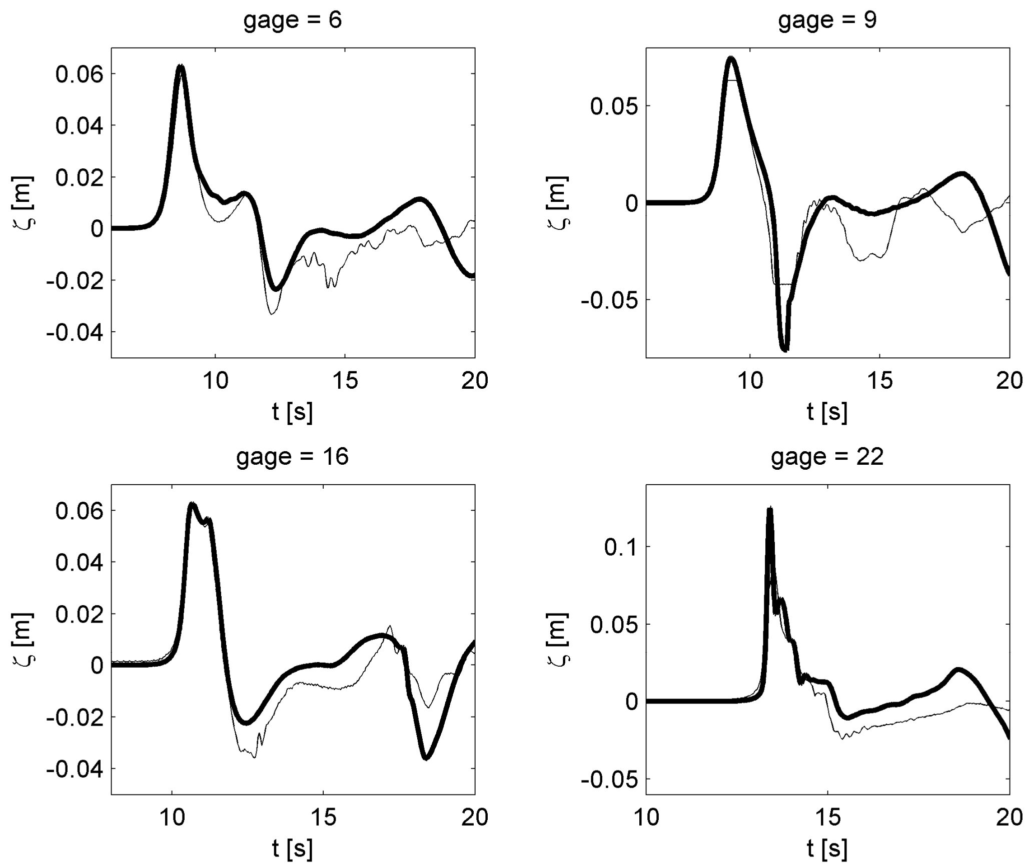

Figure 9-8 Measured (thin line) and calculated (thick line) results at the indicated wave gages for case B.

In Figure 9-8 the measurements from the gages for case C are compared to the numerical results. The results for this case do not differ much from the results in the previous one. Again the incoming wave at the front of the island is captured quite well. At gage 6 both the arrival time and the wave amplitude are predicted excellently. The measured incoming wave signal contained a small trailing trough which is probably the reason why there is a large difference at t=10s. At gage 9 the incoming amplitude is slightly over predicted and this also appears to be the case for the subsequent trough. However, from the shape of the measured signal, which is almost straight here, a more likely explanation is an error in the measurement.

At gage 16 the arrival time of the primary wave and its amplitude are well captured. Even the small secondary maximum, which is also present in the measurements, is accurately represented. Again the reflected depression wave is under predicted in size and duration.

Finally for gage 22 located behind the island the wave appears to have broken or be on the verge of braking. The steepness of the front corresponds well with the measurements in this case but the height is almost 50% too large. However, quickly after the small pronounced peak the two signals correspond again. This would indicate that the real wave broke at an earlier point. Also for this gage the back of the wave is not represented as well as the front.

The hydrostatic results are again presented in the appendices. For this case the hydrostatic approximations resulted in too steep fronts and premature breaking for all gages.

The run-up compared to the measurements for both the hydrostatic and non-hydrostatic cases are presented in Figure 9-9. In this instance the results from the gages showed large differences for the hydrostatic runs when compared to the non-hydrostatic runs.

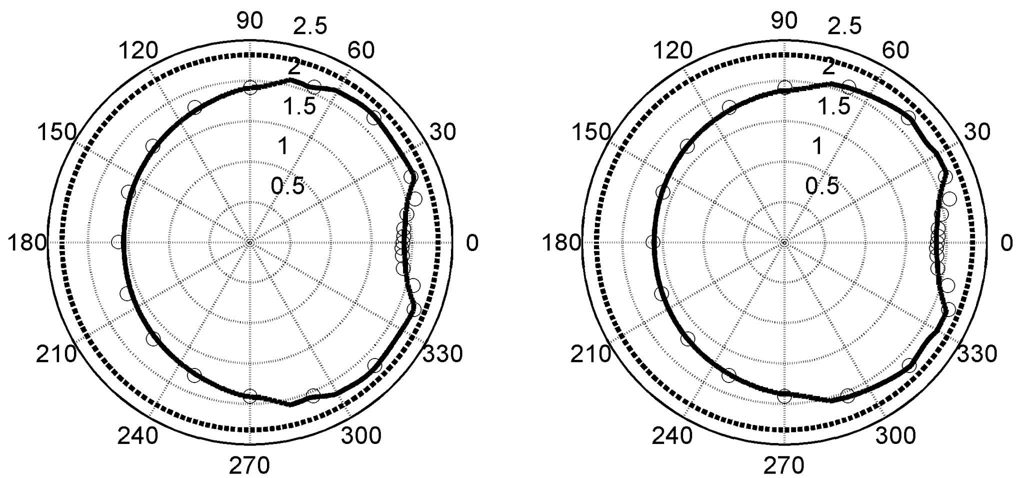

Figure 9-9 Computed (solid lne) and measured (circles) maximum inundation depth around the conical island for case C. The dashed line indicates the initial shoreline position. (**a)** depth averaged hydrostatic results, (**b)** depth averaged non-hydrostatic results.,

Looking at the run-up around the island the hydrostatic results again lead to higher inundation depths than the non-hydrostatic runs. And the difference appears to be the most profound at the front of the island.

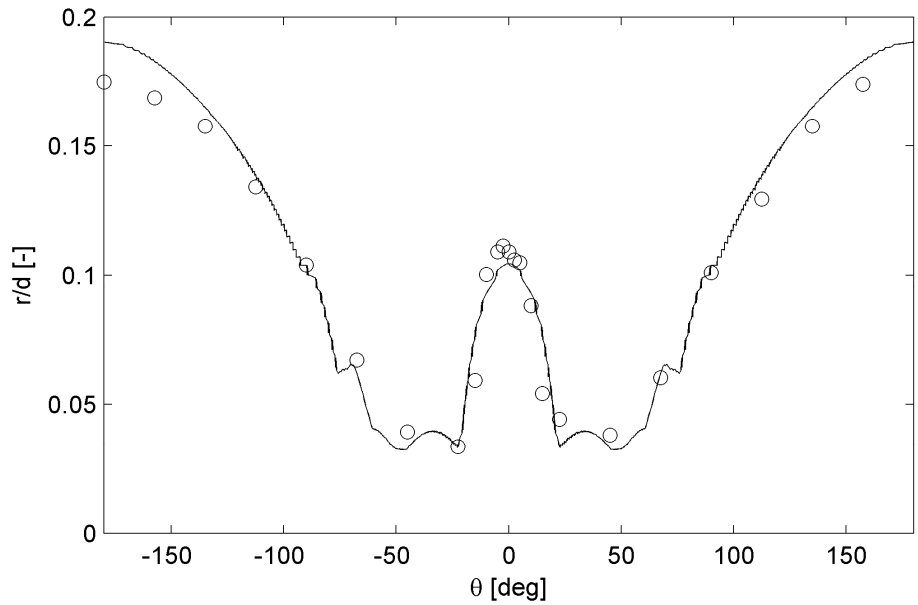

Figure 9-10 Maximum relative run-up around the island for case C in the depth averaged hydrostatic run. Measurements are indicated with a circle while model results are shown as a solid line.

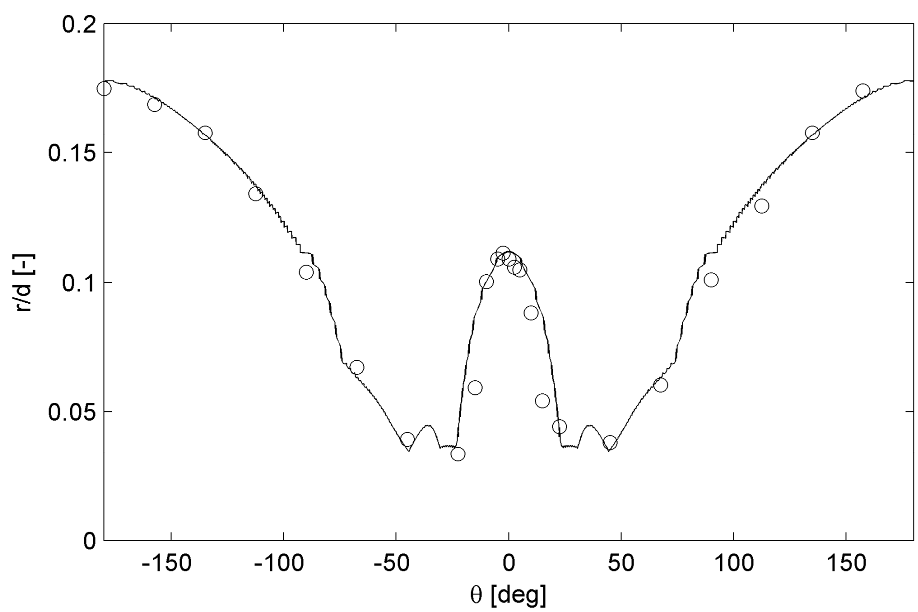

Figure 9-11 Maximum relative run-up around the island for case C in the depth averaged non-hydrostatic run. Measurements are indicated with a circle while model results are shown as a solid line.

In Figure 9-11 and Figure 9-10 the run-up height is compared for the non-hydrostatic and hydrostatic runs. The hydrostatic results show that, similar to case B, the run-up height in front of the island is over predicted while it is slightly under predicted at the back.

For the non-hydrostatic run the results are very good. The run-up height is predicted correctly at the front, back and sides of the island. It appears that the difference between the non-hydrostatic and hydrostatic solutions now has a small but significant influence on the run-up.

9.4. Comparison

As was mentioned in the introduction this particular experiment has served as a verification case for several numerical codes. Here a comparison between the results from this study is made with the results from the studies performed by Fuhrman and Madsen (2007), Choi et. al (2007) and Lui et al (1995).

In Lui at al the first numerical results for this experiment where presented. They used a model based upon the NSWE combined with a simple threshold based flooding and drying scheme. In their report the inundation heights are predicted consistently lower than the measured data. This is in contrast with the results of the hydrostatic results in this study which, at the front of the island, gave significantly higher run-up. However, they also use a much coarser grid ($\Delta x = \Delta y = .1m$) coupled with upwind discretizations. It could very well be that their results would be similar if higher grid resolutions where used as at coarser grid resolutions the present model also predicted smaller run up values. They remark that case C is indeed not suited to be modeled with the NSWE as the results at the gages differ considerably with the measurements.

Fuhrman and Madsen used a higher order Boussinesq model combined with a extrapolation technique at the wet dry interface. They used a more coarse grid ($\Delta x = \Delta y = .15m$) than the one employed in the present study due to the use of higher order spatial schemes. The results they obtained for case B are almost identical to the results obtained in the current study. They also consistently under predict the reflected depression wave and they also over predict the wave height at gage 22. For case C their results are less accurate then the results presented here. Their model fails to resolve the steep braking front at gage 22 and it also over predicts the amplitude at gage 16. Unfortunately the figures they present regarding the run-up heights are unclear which makes a comparison of these impossible.

In Choi et al. a non-hydrostatic model using the true volume of fluid method for the free surface is used. They had an comparable grid size in the horizontal but used a high resolution in the vertical. Their computed run-up heights are comparable to those in this study for both modeled cases. They also find excellent agreement in run-up height for the third case while the second case is less well resolved. Unfortunately they do not make comparisons to the gage data.

9.5. Discussion

9.5.1. Results

The results from the model are, in both cases, in good agreement with the measured results. In particular the results for case C are excellent. The measurements from the wave gages are in good agreement with the results for almost all the gages. Only the final gage 22 shows a significant deviation as the model produces a wave height which is fifty percent higher than the measured wave height. When looking at the run-up the agreement is excellent and form a significant improvement compared to the results of the hydrostatic run.

For case B the comparisons are somewhat less favourable as the agreement in both run-up and measured wave heights is less good. For the wave gages the situation is not to bad as the leading wave is usually quite well captured in the results. The run-up is markedly different from the measurements. Unfortunately time constraints have prevented a detailed investigation into this. It is particularly puzzling that case C has such excellent agreement while this case involves a much higher shorter wave which should be much more difficult to model effectively.

The differences between the hydrostatic and non-hydrostatic solutions are as expected beforehand. The hydrostatic model is no longer applicable for case C while it still gives reasonable results for case B.

When compared to other numerical studies concerning the same experiments the model results stand out quite favourably. Especially the results for case C appear to be better than all the other model results mentioned here. For Case B the results are comparable to those published by others. Only when looking at the efficiency of the model the picture is a lot less favourable.

As with the previous test concerning the vertical wall the comparisons between the hydrostatic and non-hydrostatic runs are not relevant with regards to the need for dispersion under large scale tsunamis. The waves used in the Tsunami benchmarks are not truly representative for large scale tsunamis. The test can however be regarded as an indication that the model will be able to handle the dispersion found under large scale tsunamis.

9.5.2. Model efficiency

In this test for the first time the limitations of a regular grid combined with an explicit time stepping and the need for upwind approximations under flooding and drying show up. These all contributed to the large runtime the model needed for what appears to be a relatively simple setup. In both cases the hydrostatic model took about 26 hours to finish while the non-hydrostatic model needed about 36 hours on a single Athlon 64 1.8 MHz processor. This stands in sharp contrast to for instance Fuhrman and Madsen who report they needed only 4 hours on a single 3.2 MHz Pentium 4 processor.

This large difference can be explained by the need for an extremely small resolution in the run-up zone. Due to the upwind approximations convergence is very slow and high detail is needed to reduce the numerical diffusion.

Secondly, the regular grid used is not very flexible even when a non-uniform approach is taken. In this particular case the need for an high resolution in the flooding and drying zone makes it necessary to reduce the grid size for all cells along a particular row or column. The result is that the parts of the cone, that will never become wet, are covered in the most detailed part of the grid. Also some of the deep parts are now discretised using the small grid size.

Unfortunately these problems mask the fact that the inclusion of the non-hydrostatic model only resulted in a fifty percent increase in time when compared to the hydrostatic solution. This result bodes quite well for the application of the depth averaged model to large areas.

Section V: Conclusions and recommendations

10. Conclusions and recommendations

The objective of this study was to construct a non-hydrostatic numerical model based upon the scheme proposed by Stelling and Zijlema (2003) and investigate if it can be an effective and efficient way to include the effect of frequency dispersion in the modelling of tsunamis in their propagation and run-up.
It was also the intention to show that the employed non-hydrostatic scheme can be easily integrated into an existing shallow water solver. For this purpose the algorithm was added to the XBeach model.
In this section the results found in this study will be presented together with recommendations for future development and research

10.1. Conclusions

10.1.1. Numerical model

The non-hydrostatic model based upon Stelling and Zijlema (2003) appears to have excellent characteristics regarding frequency dispersion. When two layers are used very short waves can be correctly modelled and in this regard it compares very favourably to, for instance, the higher order Boussinesq models.

The most interesting result obtained from the various validation cases is that, using a single layer, weakly dispersive waves can be accurately modelled. This can be seen in for instance the solitary wave test, but also in the oscillating basin tests. The most striking example of this is the Berkoff test. Here a complicated case involving diffraction, refraction and wave shoaling with relatively short incoming waves was modelled very satisfactorily using only a single layer. Using two layers did improve the solution marginally, but the differences could only be found in the details.

Whether one or two layers are employed a large banded matrix needs to be solved. In the 2DV case this can be very efficiently done using Gaussian elimination due to the block like structure of the matrix. However, when three dimensions are involved, Gaussian elimination is no longer possible. In this case either the SIP solver or the BiCGSTAB solver can be used. The SIP solver is only applicable in the depth averaged case, but when it can be used it is substantially faster than the BiCGSTAB method. It is therefore the recommended solver for depth averaged runs.

Regarding flooding and drying the model performs adequately for the validation and verification tests performed. It is unfortunate that the higher order interpolations cause unstable behaviour in the flooding and drying algorithm as they allow for much larger grid sizes in comparison the upwind method.

The final test performed in this thesis really showed the limits of the model in its current form. Here the upwind interpolations required a very fine grid in order for the results to be accurate. This combined with the regular grid and explicit time stepping caused the large difference in computational time: 36 hours for the present model versus 3 hours for the model by Fuhrman and Madsen (2007).

Implementation into XBeach

The original intention, as stated in the objective, was to integrate the non-hydrostatic pressure correction technique into the XBeach model. This was done to show that the non-hydrostatic pressures could be easily implemented into an existing shallow water solver. It also allowed for a shorter development time as the facilities provided by the XBeach modelling environment could be used.

During this study a depth averaged version of this model was successfully constructed which could be used as an add-on to the XBeach model. The XBeach model provided the velocity field based on the non-linear shallow water equations and the non-hydrostatic module would subsequently correct these. Unfortunately the decision to allow for multiple layers meant that the XBeach flow model needed to be rewritten. Besides the possibility of multiple layers also higher order interpolations where implemented to improve the accuracy for wave propagation problems. The final model can therefore no longer function as a simple add-on to the XBeach model.

However, the successful construction of an add-on based on a single layer version proved that in principle the non-hydrostatic pressures can be added to an existing model. Although this is simplest for explicit models it should also be possible, with minor modifications, for implicit models based on the NSWE. In this case a projection based technique as used in for example Zijlema and Stelling (2005) can be used.

10.1.2. Application to tsunamis

For the application to tsunamis two experimental studies where considered. These where featured in a workshop on tsunamis and are regarded as benchmark tests.

The first experiment consisted of the run-up of a solitary wave on a vertical wall. Three cases where modelled, which differed in wave height, and results from the hydrostatic runs where compared to the non-hydrostatic runs. For all three cases the inclusion of the non-hydrostatic pressures improved the results considerably. Especially the higher waves suffered from over steepening in the hydrostatic case. Only the lowest wave could be reasonably modelled using the non-linear shallow water equations.

The second test featured the run up of a solitary wave on a conical island. In both the model and the experiment the waves split into two parts which propagate above and below the island. Parts of the wave became trapped and separated from the main wave which propagates away from the island after passing it. Due to symmetry both of the trapped waves met each other exactly at the back of the island and caused enhanced run-up there. Comparing both gage signals and run-up measurements to the model results resulted in reasonably good to good results. It is somewhat surprising that for the highest incoming wave excellent results where obtained for the run-up around the island, while for the lower wave the agreement was far less good. For both cases enabling the non-hydrostatic pressures improved the result.

However, it is dangerous to draw conclusions based on these benchmarks regarding the importance of frequency dispersion. Even the lowest wave was already quite steep when compared too geophysical tsunamis. For more realistic scenarios it is expected that the differences will be less pronounced. However, they do function as a validation test as the waves can be considered as a worst case scenario. From the test it can be concluded that the depth averaged non-hydrostatic model captures the phenomenon of frequency dispersion sufficiently accurate to justify application towards large scale tsunamis.

This raises the important question if the model is efficient enough to compete with for instance Boussinesq models. From the final test this does not appear to be the case as the model needed far more time to come to a similar answer as a competing Boussinesq model. However, it should be stressed that this had little to do with the non-hydrostatic pressure technique, and everything to do with the first order upwind approximations.

It might be more insightful to look at the additional time the algorithm took when compared to the hydrostatic version of the model. It appears that the model adds roughly fifty percent extra time to the total calculation. And there is definitely room to improve the efficiency of the model.

From this we can conclude that the non-hydrostatic scheme devised by Stelling and Zijlema is indeed applicable for application towards large scale tsunami problems. If the dispersive terms are truly important in these situations needs still to be investigated further. However. it is expected that a depth averaged version will be sufficiently accurate.

10.2. Recommendations

10.2.1. Numerical model

The final test showed that the flooding and drying algorithm in its current form is very inefficient. One of the first things to consider is to try and combine the second order interpolations and the flooding and drying algorithm. It appears that a simple solution for this is available. Due to the higher order interpolations the water level in velocity points is sometimes predicted below the flooding and drying threshold while the surrounding water level points still contain water. This can be prevented by the introduction of a rule which only applies the higher order approximations for cases where either the total depth is sufficiently high or where the higher order approximations lead to an increase in the predicted water level. However. this needs to be investigated further before it can be safely applied.

A second important improvement can be made by using an implicit algorithm. This would increase the stability and would make it possible to vary the grid size while keeping the time step constant. Since a regular grid is employed a very attractive alternative is an ADI type of integration combined with a projection technique for the pressure.

Finally it would be useful to integrate the non-hydrostatic flow model with the existing XBeach code base. In this way the model could be used in the modeling of short waves near shore, coupled with the morphological model this would open up a lot of new possibilities. The easiest way to do this is to use the depth integrated version of the constructed code in XBeach. In this case the non-hydrostatic module functions as an add-on, as was one of the original objectives of this study. However, it is still advised in that the current upwind scheme used in XBeach is replaced with higher order approximations.

10.2.2. Applications to Tsunamis

The first next logical step with regard to the application to tsunamis would be to try and model a real world event. This would build more confidence in the application of the model and also could lead to some interesting insights Furthermore comparisons should be made to existing Boussinesq models.

In the context of tsunami modeling it would also seem very interesting to construct a model which can enable the non-hydrostatic pressures on certain sub-domains. In this way the size of the resulting matrices can be kept small as the non-hydrostatic pressures are only calculated in the regions of the domain where they are important. This is most likely best achieved in combination with an unstructured grid.

References

1 Briggs, J.M., Synolakis, C.E., Harkins, G.S., Green, D.R, 1995 "Laboratory Experiments of Tsunami Run-up on a Circular Island" *Pure and applied Geophysics*; **144**: 569-599

2 Carrier, G.F., Greenspan, H.P., 1957 "Water waves of finite amplitude on a sloping beach" *J. of fluid Mech.*; **24**:641-659

3 Casulli V. 1999 "A semi-implicit finite difference method for non-hydrostatic, free-surface flows." *International Journal for Numerical Methods in Fluids*; **30**:425-440.

4 Casulli, V, Stelling, G.S., 1998 "Numerical simulation of 3D quasi-hydrostatic, free surface flows." *Journal of hydraulic engineering (ASCE)*; **124**:678-686

5 Choi, B.H., Kim, D.C., Pelinovsky, E., Woo, S.B., 2007 "Three-dimensional simulation of tsunami run-up around conical island" *Coastal Engineering*; **54:** 618-629

6 Dingemans, M.W.,1997 "*Water wave propagation over uneven bottom*" Singapore: World scientific publishing.

7 Fenton, J. 1972 "A ninth-order solution for the solitary wave" *J. Fluid Mech*; **53**:257-271

8 Ferziger, J.H. ,Peric,M., "*Computational methods for fluid dynamics"* 3rd ed. Berlin: Springer

9 Fuhrmad, D. R., Madsen, P. A. 2008 "Simulation of nonlinear wave run-up with a high-order Boussinesq model" *Coastal Engineering*; **55**: 139-154

10 Grilli, S. T., Ioualalen, M., Asavanant, J., Shi, F., Kirby, T., and Watts, P., 2007 "Source constraints and model simulation of the December 26, 2004, Indian Ocean Tsunami." *Journal of waterway, port, coastal and ocean engineering*; 414-428

11 Grimshaw, R., 1971 "The solitary wave in water of variable depth. Part 2" . *J. Fluid Mech.*; **46** part 3: 611-622

12 Hammack, J. "A note on tsunamis: their generation and propagation in an ocean of uniform depth*." J. Fluid Mech.* 1973; **60**:769-799

13 Hammach, J., Segur, H., . 1974 "The Korteweg-de Vries equation and water waves. Part 2. Comparison with experiments" *J. of fluid mech.*; **65**:289-314

14 Hammach, J., Segur, H. "Modelling criteria for long water waves" *J. of fluid mech*. 1978; **84**: 359-373

15 Hansen, W., 1956. „Theorie zur Errechnung des Waterstandes und der Stromingen in Randmeeren nebst Anwendungen." *Tellus*; **8:**289–300

16 Haiyang C., 2007 "Non-hydrostatic Numerical modeling of Hydraulic jump over a Weir" *Msc. Thesis*; T.U. Delft

17 Hirsch, C., 2007 "*Numerical Computation of internal and external flows.*" 2nd ed. New York: Wiley

18 Holthuijsen, L., 2007 "*Waves in Oceanic and Coastal Waters*" Cambridge university press

19 Horrillo, J., Zygmunt, K., and Shigihara, Y., 2006 "Wave dispersion study in the Indian Ocean-Tsunami of December 26, 2004." *Marine Geodesy*; **26**:149-166

20 Kulikov, E. 2005 "Dispersion of the Sumatra Tsunami Waves in the Indian Ocean detected by satellite altimetry." *Rep. from P.P. Shirsov Institute of Oceanology*, Russian Academy of Sciences, Moscow.

21 Lui, P. L.F. , Cho,Y.,Briggs,M.J.,Lu,U.K., Synolakis,C.M., 1995 "Run-up of solitary waves on a circular island" *J. of Fluid Mech*; **302**:259-285

22 Lynett,P.J.,Wu,T.R.,Liu,P.L.F.,2002 "Modelling wave run-up with depth averaged equations" *Coastal Engineering*; **46**:89-107

23 Madsen, P.A., Sørensen, O.R., 1992 "A new form of the Boussinesq equations with improved linear dispersion characteristics. Part A slowly varying bathymetry." *Coastal engineering*; **18**:183-204

24 Matsuyama, M.,Ikeno, M., Sakakiyama, T.,Takeda,T. 2007 "A Study of tsunami wave fission in an undistorted Experiment" *Pure appl. Geophys.*; **164**:617-631

25 Mei, C.C., 2005 "*Theory and applications of ocean surface waves*" Singapore: World scientific publishing.

26 Nakamura, N., 2005 "A note on tsunami bore front" *Marine Geodesy*; **28**:305-312

27 Nwogu, O., 1993 "Alternative form of Boussinesq equations for nearshore wave propagation." *Journal of Waterway, Port, Coastal and Ocean Engineering;* **119**:618-638

28 Peregrine, D.H.,1966 "Calculations of the development of an undular bore" *J. Fluid Mech*; **25**:321-350

29 Peregrine, D. H., 1967 "Long waves on a beach" *J. Fluid Mech.;* **27**:815-827

29 Roelving, D., Reniers, A., van Dongeren, D., van Thiel de Vries, J., Lescinski, J., McCall, R. "*XBeach model description and manual*"', UNESCO-IHE Institute for Water Education WL | Delft Hydraulics Delft University of Technology

30 Stansby P.K., Zhou J.G., 1998 "Shallow-water flow solver with non-hydrostatic pressure: 2D vertical plane problems." *International Journal for Numerical methods in Fluids*, **28:** 514-263

31 Stelling, G.S.,Duinmeijer,S.P.A.,2003 "A staggered conservative scheme for every Froude number in rapidly varied shallow water flows" *International journal for numerical methods in fluids*; **43**

32 Stelling, G.S., Van Kester, J.A.T.M.,1994 "On the approximation of horizontal gradients in sigma co-ordinates for bathymetry with steep bottom slopes" *International journal for numerical methods in fluids*; **18**:915-935

33 Stelling, G.S., Zijlema, M., 2003 "An accurate and efficiënt finite-diference algorithm for non-hydrostatic free-surface flow with aplication to wave propagation" *International journal for numerical methods in fluids*; **43**:1-23

34 Sato,S. 1996 "Numerical simulation of 1993 Southwest Hokkaido Earthquake Tsunami around Okushiri Island" *Journal of Waterway, Port, Coastal and Ocean Engineering*; **Sept/Oct**:209-215

35 Synolakis,C.E., 1986 "*The run-up of long waves*" phd. Thesis, Pasadena: California institute of Technology

36 Titov, V.V., Synolakis, C.E., 1998 "Numerical Modeling of Tidal Wave Run-up" *Journal of Waterway, Port, Coastal and Ocean Engineering*; **Juli/Aug**:157-170

37 Tsuji, Y., Yanuma, T.,Murata,I.,Fujiwara,C.,1991 "Tsunami ascending in rivers as an undular bore". *Natural hazards*;**4**:257-266

38 Van Reeuwijk, M., 2002 "*Efficient simulation of non-hydrostatic free surface flows.*" Msc. Thesis T.U. Delft

39 Walters, R.A., 2005 "A semi-implicit finite element model for non-hydrostatic (dispersive) surface waves" *International journal for numerical methods in fluids;* **49**:721-737

40 Yuan, H., Wu, H. C., 2004 "An implicit three-dimensional fully non-hydrostatic model for free-surface flows" *International journal for numerical methods in fluids;* **46**:709-733

41 Zhou J.G., Stansby P.K., 1999, "An arbitrary Lagrangian-Eularian σ (ALES) model with non-hydrostatic pressure for shallow water flows." *Computer Methods in Applied Mechanics and Engineering*; **178**:199-214

42 Zijlema, M., Stelling, G.S. "Further experiences with computing non-hydrostatic free-surface flows involving water waves." *International journal for numerical methods in fluids* 2004; **48**:169-197

43 Zijlema, M., Stelling, G.S. 2008 "Efficient computation of surf zone waves using the nonlinear shallow water equations with non-hydrostatic pressure" *Coastal engineering*

List of main symbols

symbols

ζ	:	Free surface	[*m*]
u	:	Horizontal velocity component in the *x*-direction	[ms^{-1}]
v	:	Horizontal velocity component in the *y*-direction	[ms^{-1}]
w	:	Vertical velocity component	[ms^{-1}]
U	:	Depth averaged velocity in the *x*-direction	[ms^{-1}]
V	:	Depth averaged velocity in the *y*-direction	[ms^{-1}]
q	:	Layer averaged discharge	[m^2s^{-1}]
ω	:	Relative vertical velocity	[ms^{-1}]
ρ	:	Density	[$kg\ m^{-3}$]
h	:	Layer height	[*m*]
H	:	Total water depth	[*m*]
$\Delta x, \Delta y$	:	Grid spacing in the *x*- or *y*-direction	[*m*]
Δt	:	Time step	[*s*]
σ	:	Sigma coordinate	[-]
x	:	Horizontal x-coordinate	[*m*]
y	:	Horizontal y-coordinate	[*m*]
z	:	Vertical coordinate	[*m*]
d	:	Water depth	[*m*]
P	:	Total pressure	[$N\ m^{-2}$]
P	:	Normalized dynamic pressure	[m^2s^{-2}]
p_h	:	Hydrostatic pressure	[$N\ m^{-2}$]
g	:	Gravitational acceleration	[$m\ s^{-2}$]

indeces :

i	:	Index of horizontal grid point in the *x*-direction.
I	:	Maximum number of grid points in the horizontal
j	:	Index of horizontal grid point in the *y*-direction.
J	:	Maximum number of grid points in the horizontal
k	:	Index of vertical grid points.
K	:	Maximum number of grid points in the vertical

Appendices

A. Numerical dispersion relation

A.1. Linearized equations

In order to derive the dispersion relation it is assumed that the initial condition is a small disturbance in which case the non-linear terms can be neglected. Furthermore the bottom is assumed to be flat. In this case the Euler equations are simplified to:

$$\frac{\partial \zeta}{\partial t} + H\frac{\partial u}{\partial x} = 0 \tag{A.1}$$

$$\frac{\partial u}{\partial t} + g\frac{\partial \zeta}{\partial x} + \frac{\partial p}{\partial x} = 0 \tag{A.2}$$

$$\frac{\partial u}{\partial x} + \frac{\partial w}{\partial z} = 0 \tag{A.3}$$

$$\frac{\partial w}{\partial t} + \frac{\partial p}{\partial z} = 0 \tag{A.4}$$

Notice that all advective terms have dropped out. Now a semi-discretisation is performed in the vertical only. It is assumed that there is an equidistant layer distribution with layer thickness $h = \frac{H}{k}$. In this case the equations become:

$$\frac{\partial \zeta}{\partial t} + \sum_{k=1}^{k_{\max}} h\frac{\partial u_k}{\partial x} = 0 \tag{A.5}$$

$$\left.\frac{\partial u}{\partial t}\right|_k + g\frac{\partial \zeta}{\partial x} + \tfrac{1}{2}\left.\frac{\partial p}{\partial x}\right|_{k+\frac{1}{2}} + \tfrac{1}{2}\left.\frac{\partial p}{\partial x}\right|_{k-\frac{1}{2}} = 0 \tag{A.6}$$

$$\left.\frac{\partial u}{\partial x}\right|_k + \frac{w_{k+\frac{1}{2}} - w_{k-\frac{1}{2}}}{H} = 0 \tag{A.7}$$

$$\left.\frac{\partial w}{\partial t}\right|_{k+\frac{1}{2}} + \left.\frac{\partial w}{\partial t}\right|_{k-\frac{1}{2}} + 2\frac{p_{k+\frac{1}{2}} - p_{k-\frac{1}{2}}}{h} = 0 \tag{A.8}$$

For the vertical momentum equation the Keller box has been employed instead of the compact scheme. But as mentioned before, these are essentially equivalent when advection terms are ignored. As there are k momentum and local continuity equations the total number of equations becomes $n = 3k + 1$.

Substituting for each of the variables a single fourier mode with different amplitudes and phases. As a linear superposition different fourier modes will also be a solution this does not mean a loss of generality.

$$\begin{aligned}
\zeta(x,t) &= \hat{\zeta} e^{i(kx-\omega t)} \\
u_k(x,t) &= \hat{u} e^{i(kx-\omega t)} \\
w_k(x,t) &= \hat{w} e^{i(kx-\omega t)} \\
p_k(x,t) &= \hat{p} e^{i(kx-\omega t)}
\end{aligned} \tag{A.9}$$

In order to simplify the expression the amplitudes are taken to be complex and therefore include the phase differences. Using the relations in (A.9) the system of equations (A.5)-(A.8) result into:

$$\begin{aligned}
& -i\omega\zeta + \sum_{k=1}^{k_{\max}} ihku_k = 0 \\
& -i\omega u_k + igk\zeta + \tfrac{1}{2} ikp_{k+\frac{1}{2}} + \tfrac{1}{2} ikp_{k-\frac{1}{2}} = 0 \\
& iku_k + \frac{w_{k+\frac{1}{2}} - w_{k-\frac{1}{2}}}{H} = 0 \\
& -i\omega w_{k+\frac{1}{2}} + -i\omega w_{k-\frac{1}{2}} + 2\frac{p_{k+\frac{1}{2}} - p_{k-\frac{1}{2}}}{h} = 0
\end{aligned} \tag{A.10}$$

With $p_{k_{\max}+\frac{1}{2}} = 0$ and $w_{\frac{1}{2}} = 0$ by virtue of the kinematic boundary condition at the bottom.

A.2. Single layer system

First deriving an expression for the single layer system the equations are written in matrix notation as:

$$\mathbf{Ax} = \mathbf{0} \tag{A.11}$$

Where

$$\mathbf{A} = \begin{pmatrix} -i\omega & ikH & & \\ ikg & -i\omega & & \tfrac{1}{2} ik \\ & ik & H^{-1} & \\ & & -i\omega & -2H^{-2} \end{pmatrix} \quad \mathbf{x} = e^{i(kx-\omega t)} \begin{pmatrix} \hat{\zeta} \\ \hat{u}_1 \\ \hat{w}_{1\frac{1}{2}} \\ \hat{p}_{\frac{1}{2}} \end{pmatrix} \tag{A.12}$$

In order for the system of equations in (A.11) to have more than the trivial solution $\mathbf{x} = \mathbf{0}$ the determinant of the matrix $\mathbf{A}$ has to be equal to zero thus:

$$Det(\mathbf{A}) = \begin{vmatrix} -i\omega & ikH & & \\ ikg & -i\omega & & \tfrac{1}{2} ik \\ & ik & H^{-1} & \\ & & -i\omega & -2H^{-2} \end{vmatrix} = 0 \tag{A.13}$$

A cofactor expansion of the determinant of the matrix yields:

$$Det(\mathbf{A}) = 2\frac{\omega^2}{H^2} - \frac{k^2\omega^2}{2} - 2g\frac{k^2}{H} = 0 \tag{A.14}$$

This expression is precisely zero if the following equation holds:

$$\omega = k\sqrt{\frac{gH}{1+\frac{1}{4}\left(kH\right)^2}} \tag{A.15}$$

This relation between ω and k is the dispersion relation present in the case of a single computational layer.

A.3. Two computational layers

For the two layer system again the equations of (A.10) are written in matrix form resulting in a seven by seven square matrix:

$$\mathbf{A} = \begin{pmatrix} -i\omega & ikh & ikh & & & & \\ ikg & -i\omega & & & & \frac{1}{2}ik & \frac{1}{2}ik \\ ikg & & -i\omega & & & & \frac{1}{2}ik \\ & & & -i\omega & & -\frac{2}{h} & \frac{2}{h} \\ & & & & -i\omega & & -\frac{2}{h} \\ & ik & & \frac{1}{h} & & & \\ & & ik & -\frac{1}{h} & \frac{1}{h} & & \end{pmatrix} \tag{A.16}$$

The determinant of this system can also be determined by a cofactor expansion[1] and results in the following equations:

$$Det\left(\mathbf{A}\right) = -i^3\omega\frac{6\omega^2k^2h^2 + 4\omega^2 + \frac{1}{4}\omega^2k^4h^4 - 2k^4gh^3 - 8k^2gh}{h^4} \tag{A.17}$$

This expression is zero if either $\omega = 0$ or:

$$6\omega^2k^2h^2 + 4\omega^2 + \frac{1}{4}\omega^2k^4h^4 - 2k^4gh^3 - 8k^2gh = 0 \tag{A.18}$$

From equation (A.18) the relation between ω and k becomes:

$$\omega^2 = k^2\frac{\frac{1}{16}\left(kH\right)^2 gH + gH}{1+\frac{3}{8}\left(kH\right)^2 + \frac{1}{256}\left(kH\right)^4} \tag{A.19}$$

Notice that $h = \frac{1}{2}H$ has been substituted here. Equation (A.19) is the dispersion relation present in the two-layer model.

[1] Performed by Maple as the number of computations involved is extensive

B. XBEACH[1]

The XBeach program contains a number of Fortran 90/95 routines for short wave propagation, non stationary shallow water equations, sediment transport and continuity equations that can be coupled in various ways and are designed to cope with extreme conditions such as encountered during hurricanes. Since length scales are short in terms of wave lengths and supercritical flow frequently occurs, the numerical implementation is mainly first order upwind, which in combination with a staggered grid makes the model robust. The model scheme utilizes explicit schemes with an automatic time step based on Courant criterion, with output at fixed or user defined time intervals, which keeps the code simple and makes coupling and parallellization easier, while increasing stability.

The short wave propagation model contains a newly-developed time-dependent wave action balance solver, which solves the wave refraction and allows variation of wave action in x, y, time and over the directional space, and can be used to simulate the propagation and dissipation of wave groups. An added advantage to this set-up, compared to the existing surfbeat model, is that a separate wave model is not needed to predict the mean wave direction, and it allows different wave groups to travel in different directions. Full wavecurrent interaction in the short wave propagation is included. Roelvink (1993) wave dissipation model is implemented for use in the nonstationary wave energy balance (in other words, when the wave energy varies on the wave group time scale).

The Generalised Lagrangean Mean (GLM) approach was implemented to represent the depth-averaged undertow and its effect on bed shear stresses and sediment transport, cf. Reniers et al. (2004). The numerical scheme was updated, in line with Stelling and Duinmeijer method, to improve long-wave run-up and backwash on the beach. Themomentum-conserving form is applied, while retaining the simple first-order approach. The resulting scheme has been verified with the well-known Carrier and Greenspan (1958) test.

Soulsby – Van Rijn transport formulations have been included, which solves the 2DH advection-diffusion equation and produces total transport vectors, which can be used to update the bathymetry. The pickup function follows Reniers et al (2004) was implemented. An avalanching routine was implemented with separate criteria for critical slope at wet or dry points. The model has been validated against a number of analytical and laboratory tests, both hydrodynamic and morphodynamic.

[1] Description taken from Dano Roelvink et al (2008)

C. strongly implicit procedure

The basis for the SIP method lies in the observation that an LU decomposition is an excellent general purpose solver, which unfortunately cannot take advantage of the sparseness of a matrix. Secondly, in an iterative method, if the matrix **M** is a good approximation to the pressure coefficient matrix **A**, rapid convergence results. These observations lead to the idea of using an approximate LU factorization of **A** as the iteration matrix **M**. i.e.:

$$\mathbf{M} = \mathbf{LU} = \mathbf{A} + \mathbf{N} \qquad (1.20)$$

Where **L** and **U** are both sparse and **N** is small. For asymmetric matrices the incomplete LU (ILU) factorisation gives such an decomposition but unfortunately converges rather slowly. In the ILU method one proceeds as in a standard LU decomposition. However, for every element of the original matrix **A** that is zero the corresponding elements in **L** or **U** is set to zero. This means that the product of **LU** will contain more nonzero diagonals that the original matrix **A.** Therefore the matrix **N** must contain these extra diagonals as well if (1.20) is to hold.

Stone reasoned that if the equations approximate an elliptic partial differential equation the solution can be expected to be smooth. This means that the pressure points corresponding to the extra diagonals can be approximated by interpolation of the surrounding points. By allowing **N** to have more non zero entries on all seven diagonals and using the interpolation mentioned above the SIP method constructs an **LU** factorization with the property that for a given approximate solution ϕ the product $\mathbf{N}\phi \approx 0$ and thus the iteration matrix **M** is close to **A** by relation (1.20). To solve the system of equations the following iterations is performed, starting with an initial guess for the pressure vector $\mathbf{p}^s$ an iteration is performed solving:

$$\mathbf{Up}^{s+1} = \mathbf{L}^{-1}\mathbf{Np}^s + \mathbf{L}^{-1}\mathbf{Q} \qquad (1.21)$$

Since the matrix **U** is upper triangular this equation is efficiently solved by back substitution. An essential property which makes the method feasible is that the matrix **L** is easily invertible. This iterative process is repeated until convergence is reached. Note that when the solution of is identical to the original problem.

D. Tsunami run up

D.1. Run up on a vertical wall

D.1.1. Case A

Hydrostatic Results

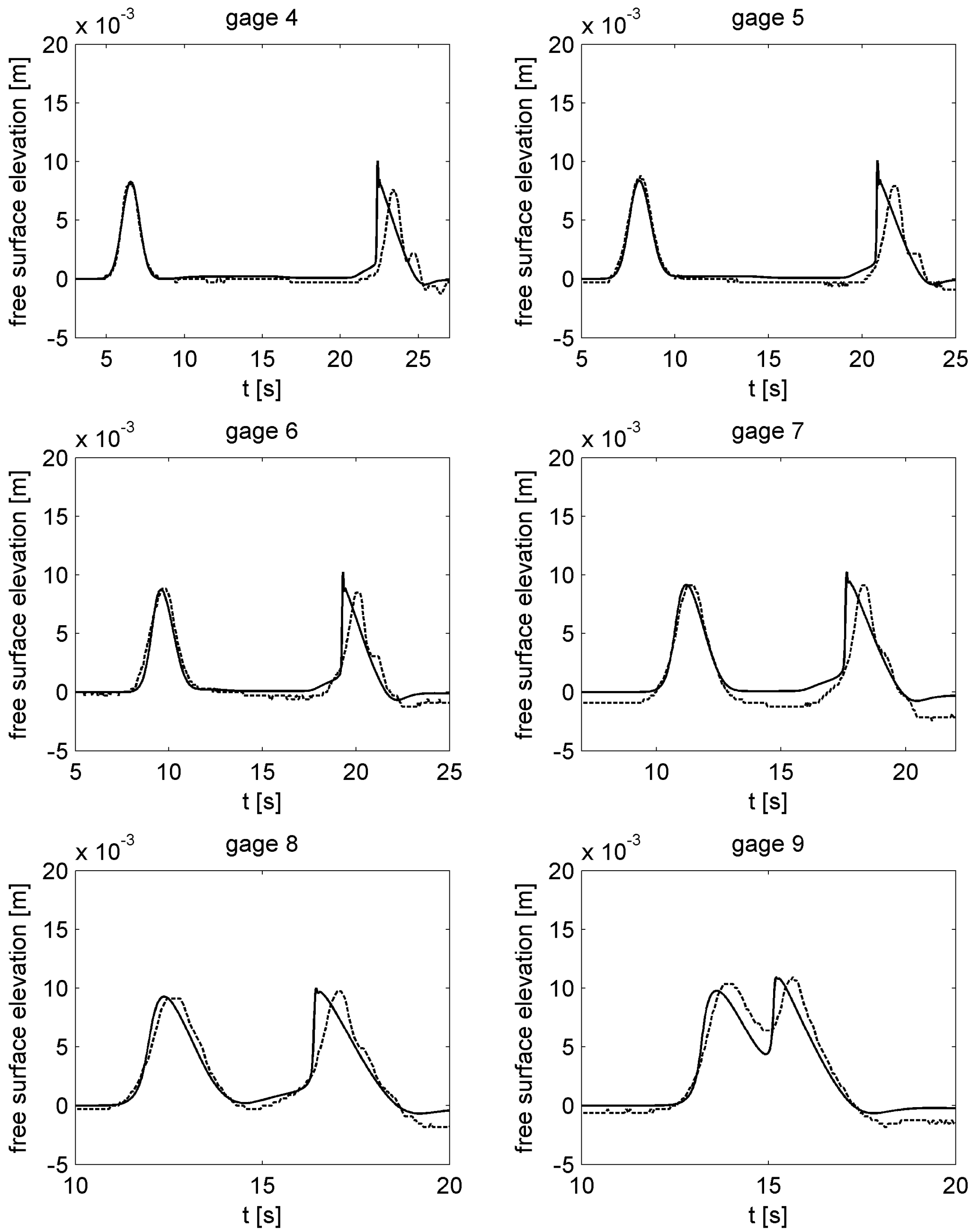

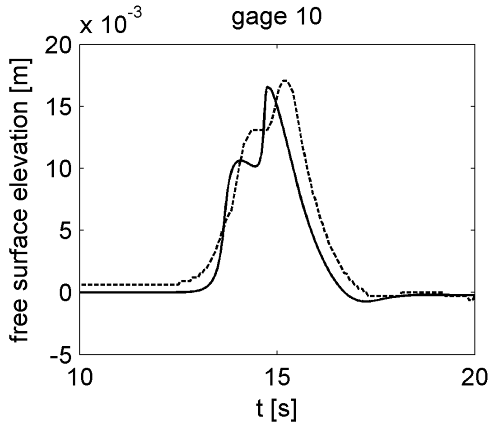

Non-hydrostatic 1-layer

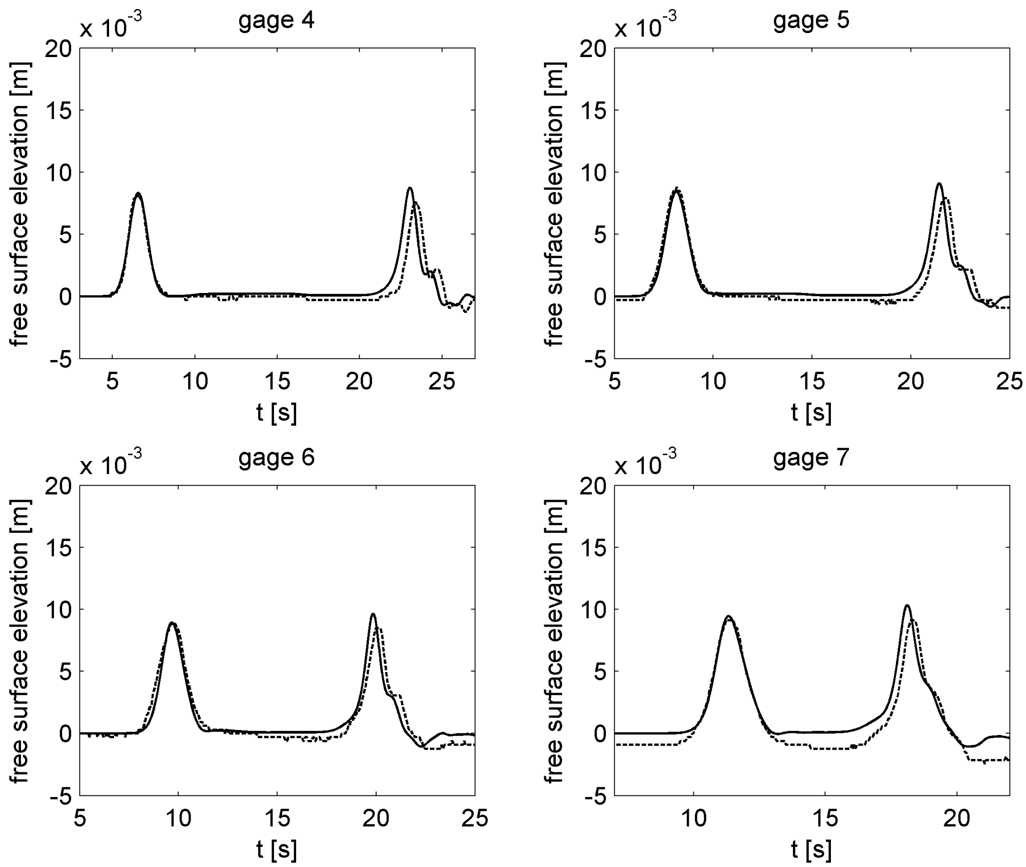

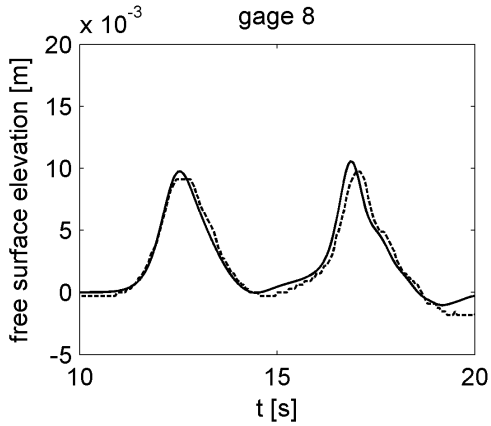

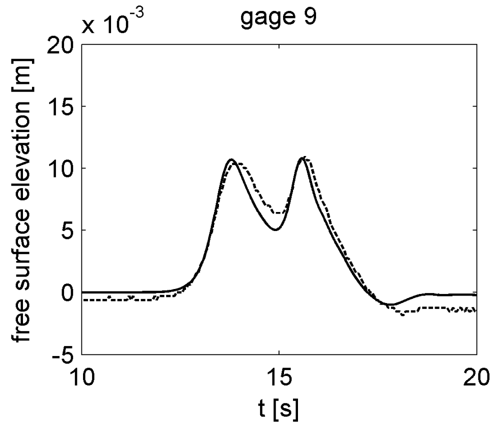

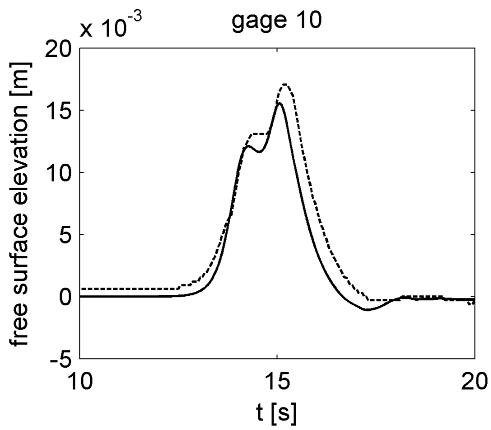

Non-hydrostatic 2 layer

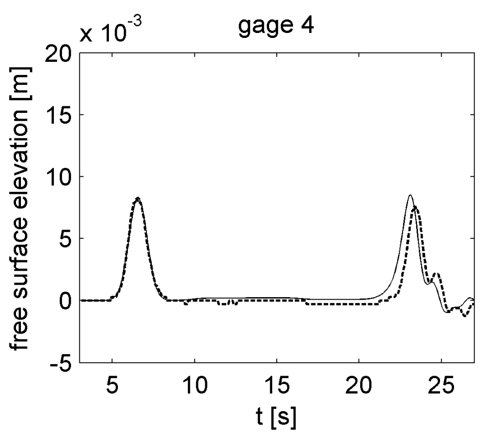

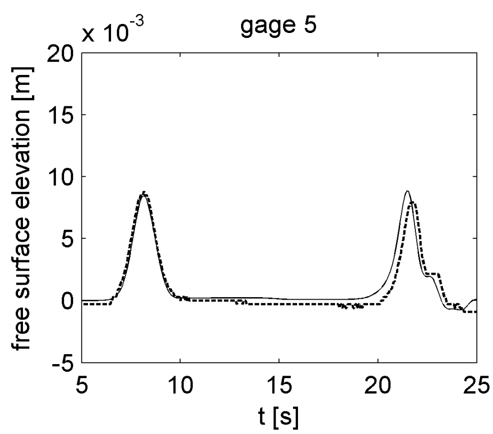

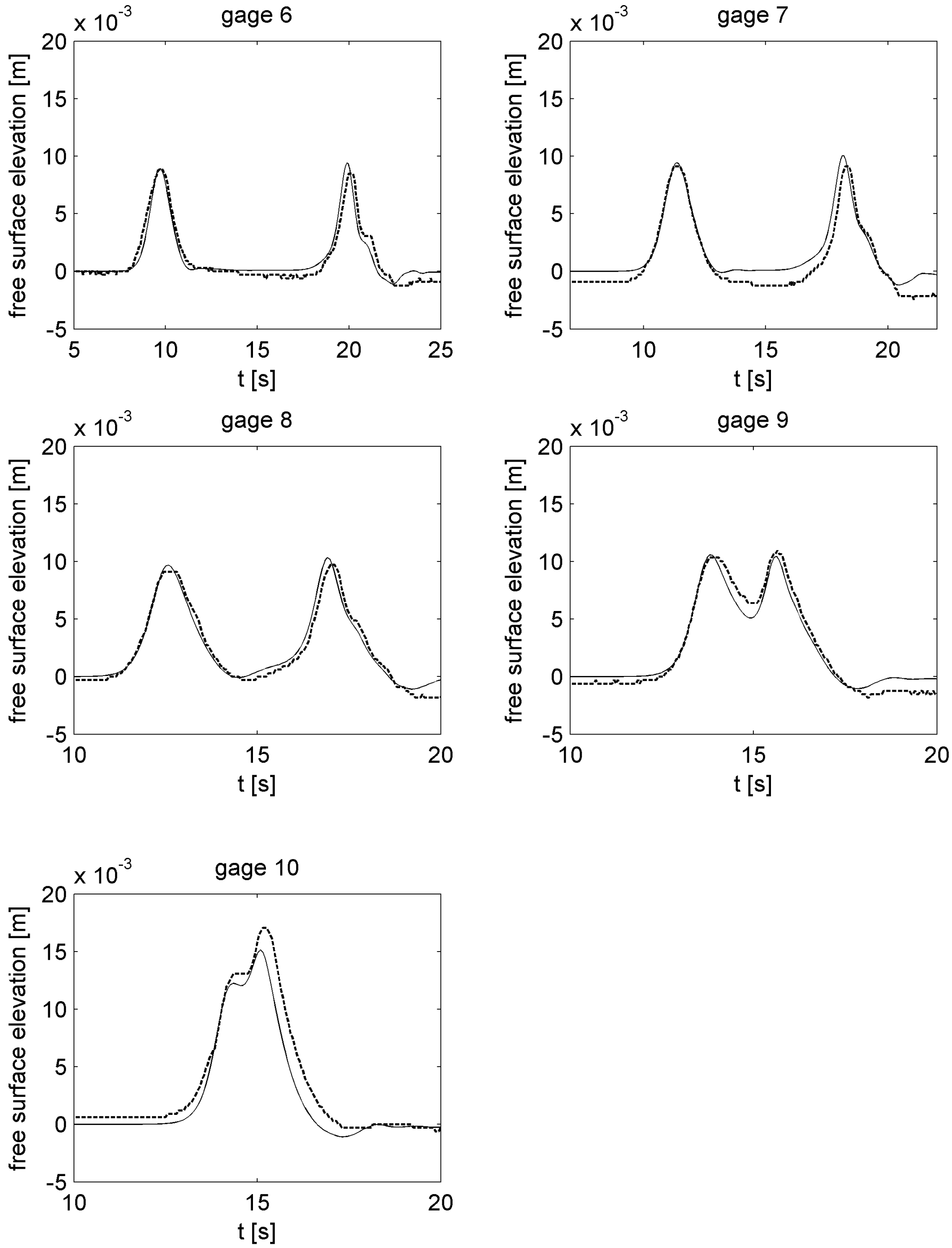
gage 6
gage 7
gage 8
gage 9
gage 10
x 10^-3
free surface elevation [m]
t [s]

D.1.2.Case B

Hydrostatic run

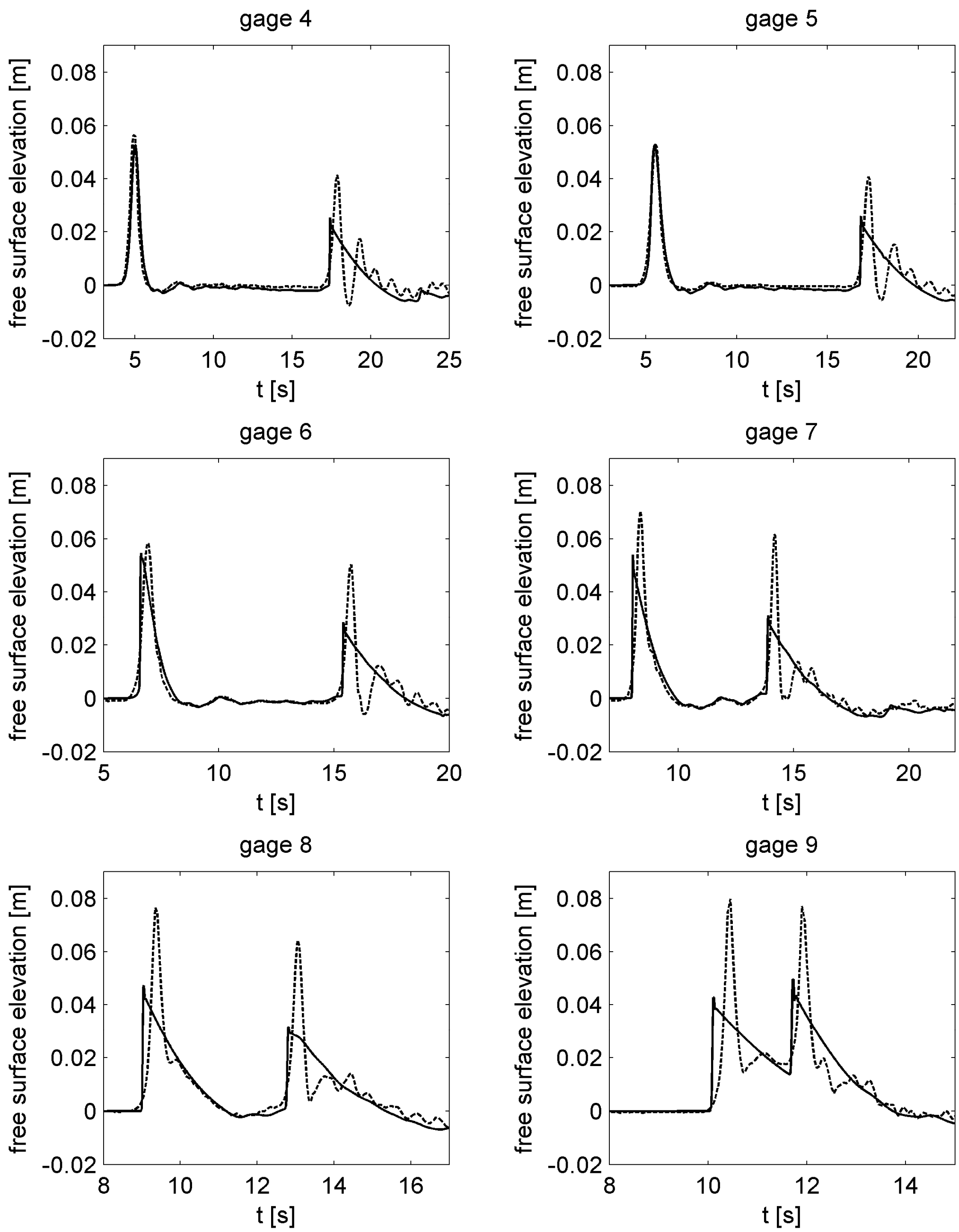

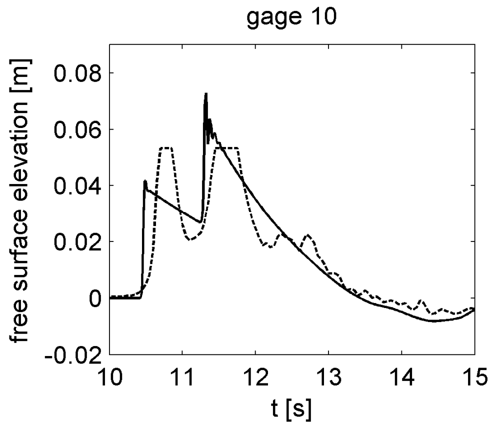

Non-hydrostatic 2-layer

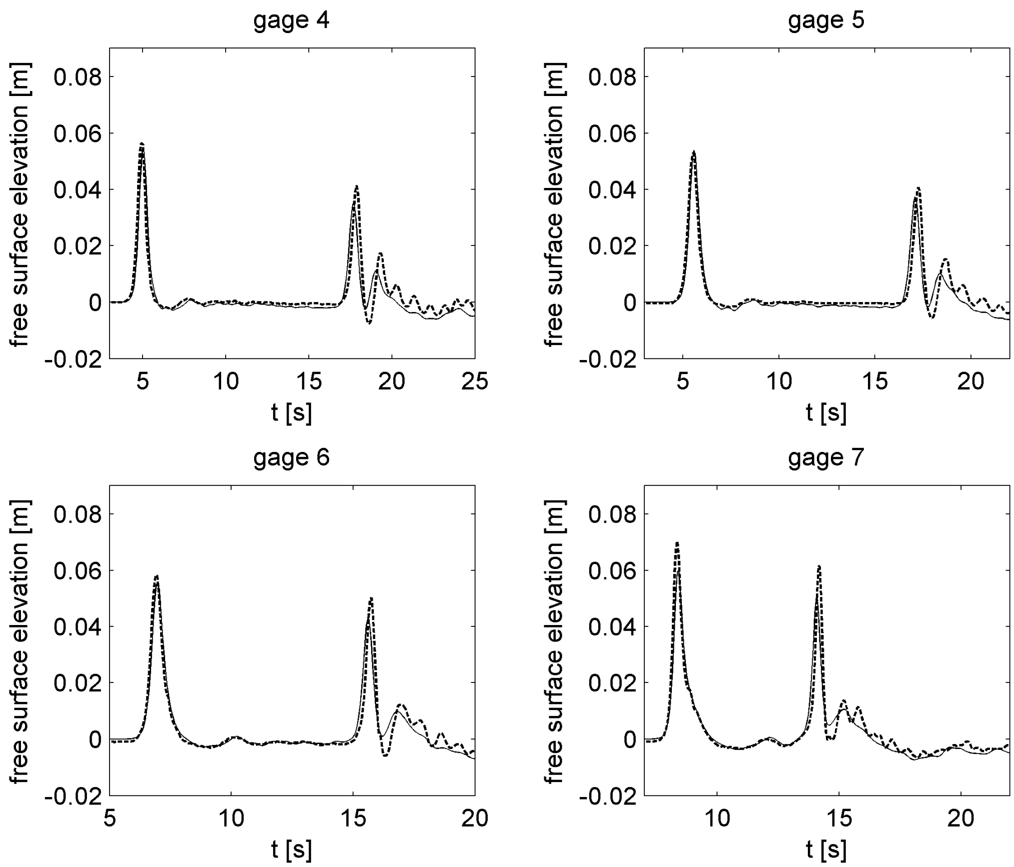

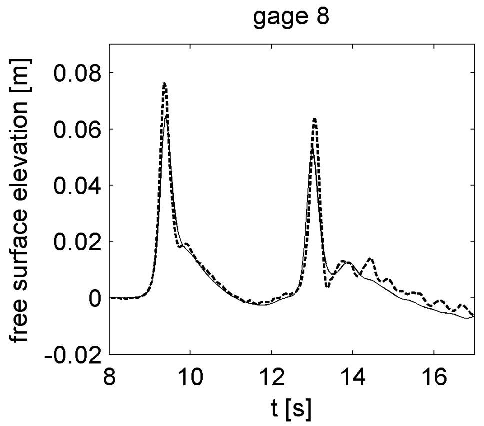

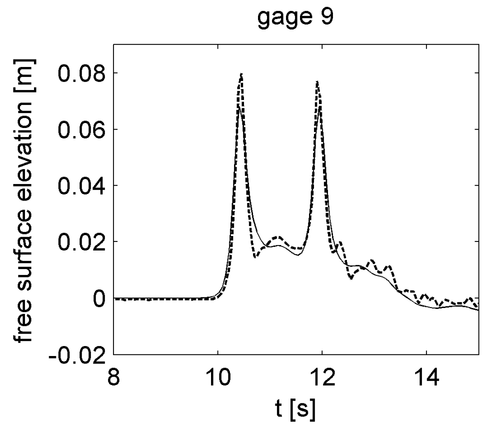

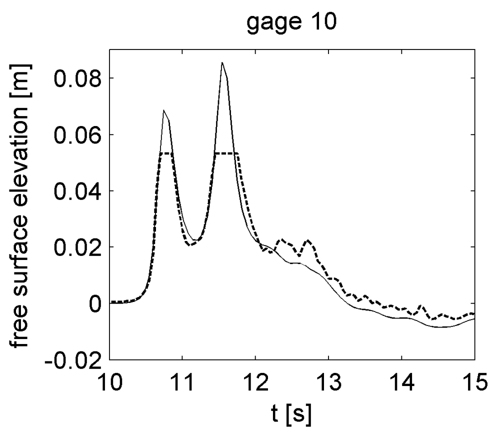

D.1.3.Case C

Hydrostatic

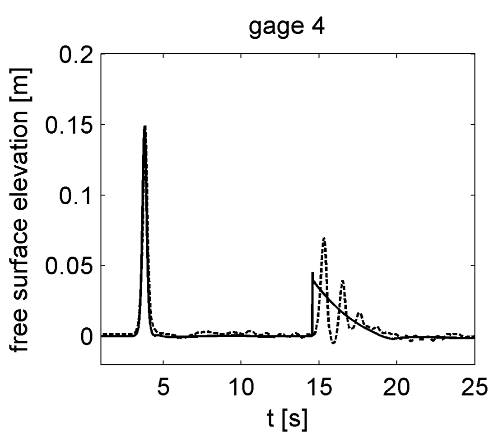

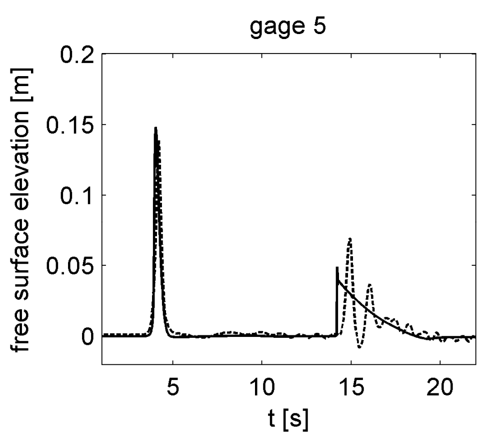

v

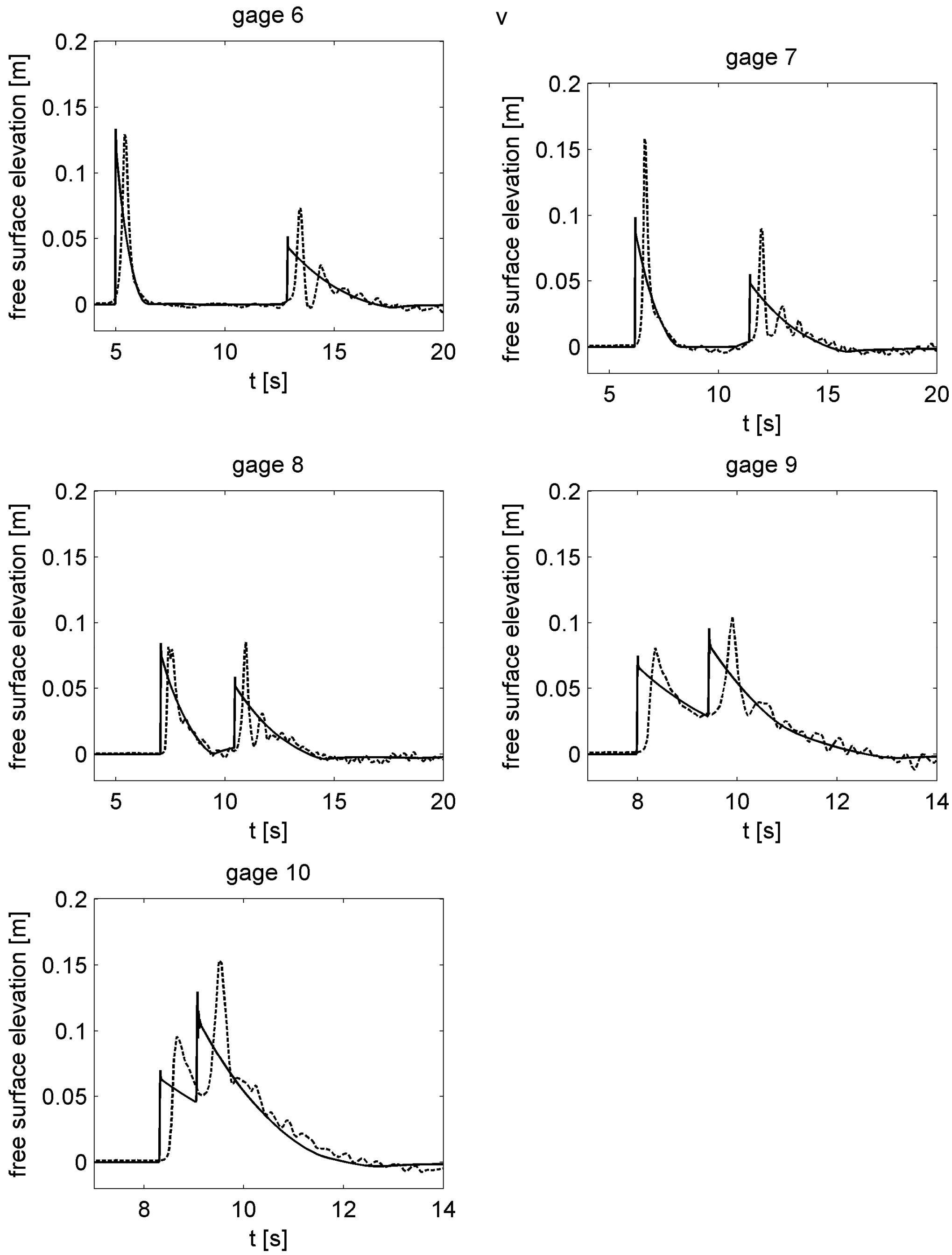

Non-hydrostatic 1-layer

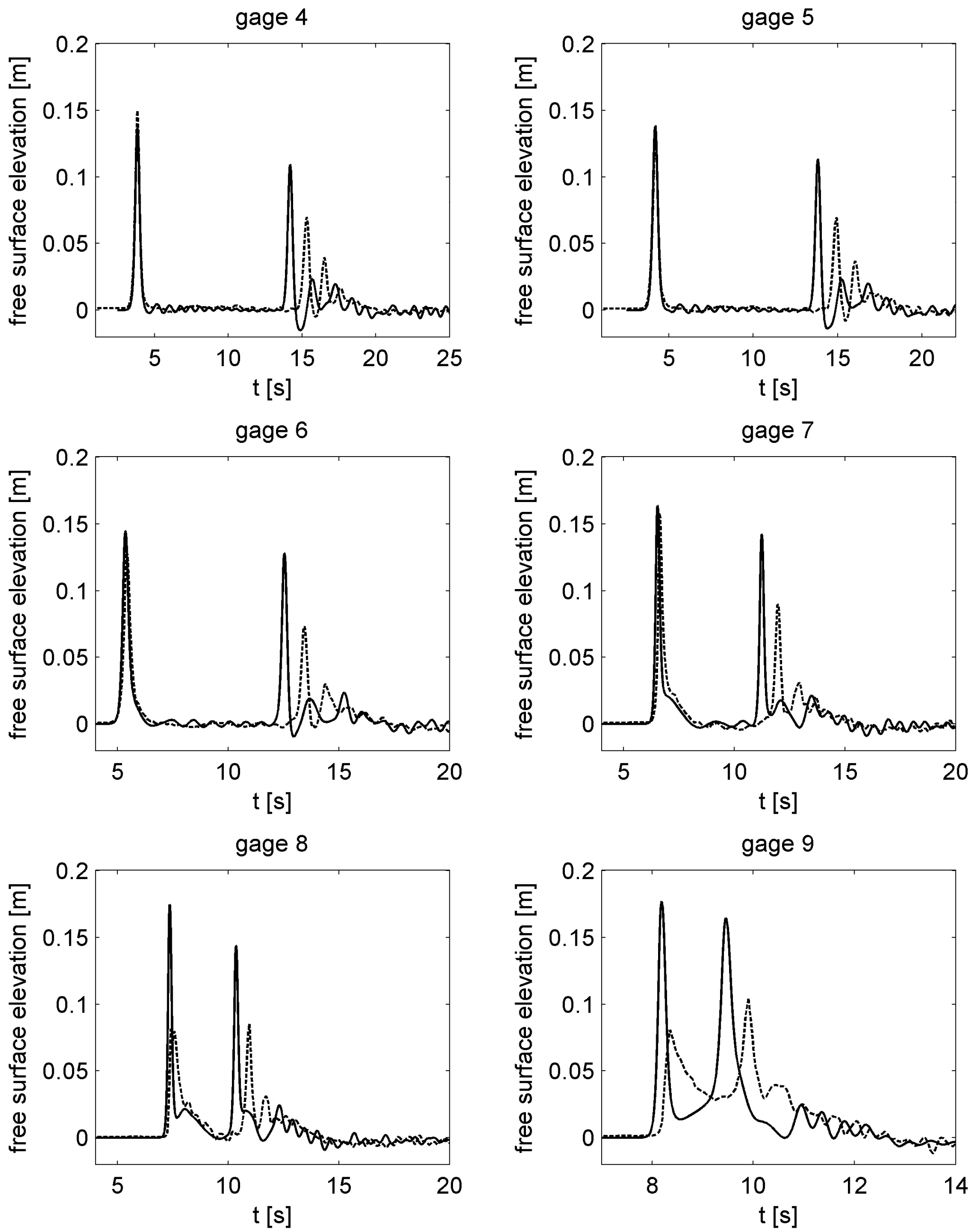

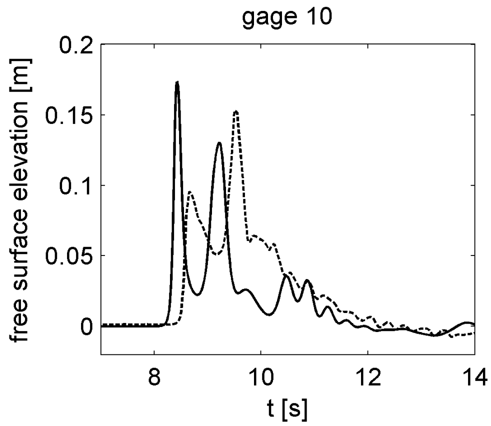

D.2. Run up of solitary waves on a Conical island

D.2.1. Timeseries Case B

Hydrostatic

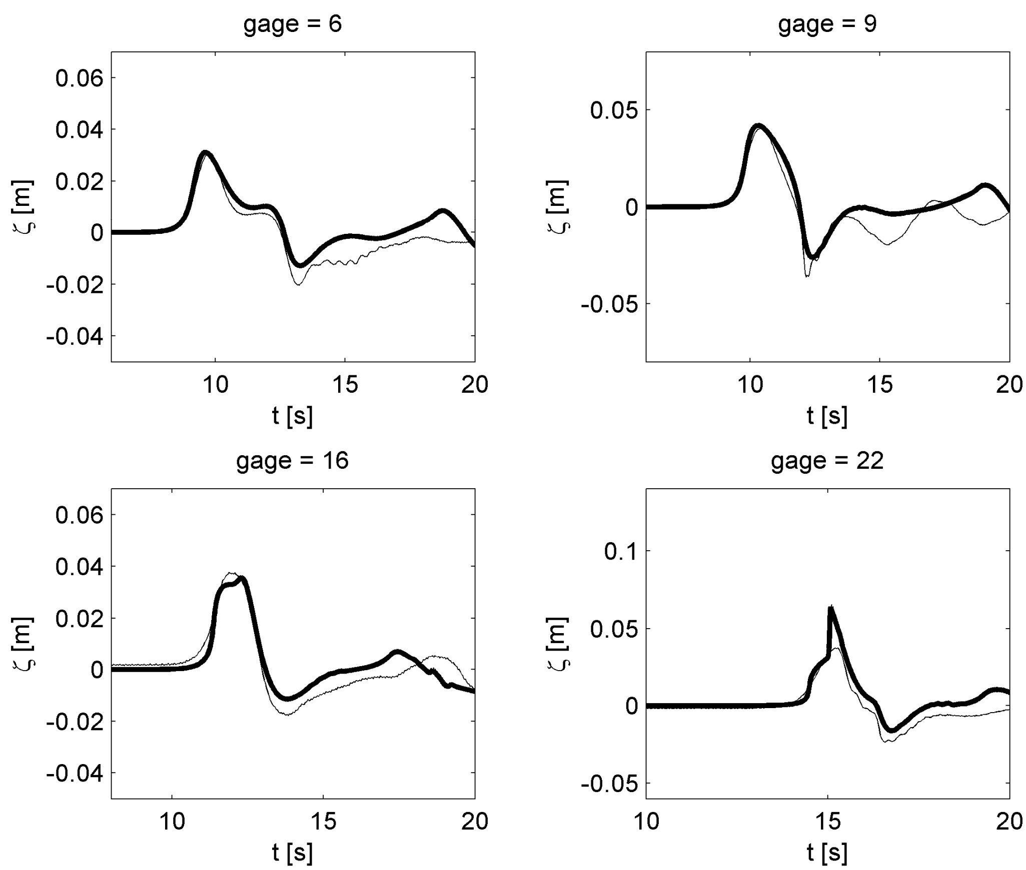

Non-hydrostatic

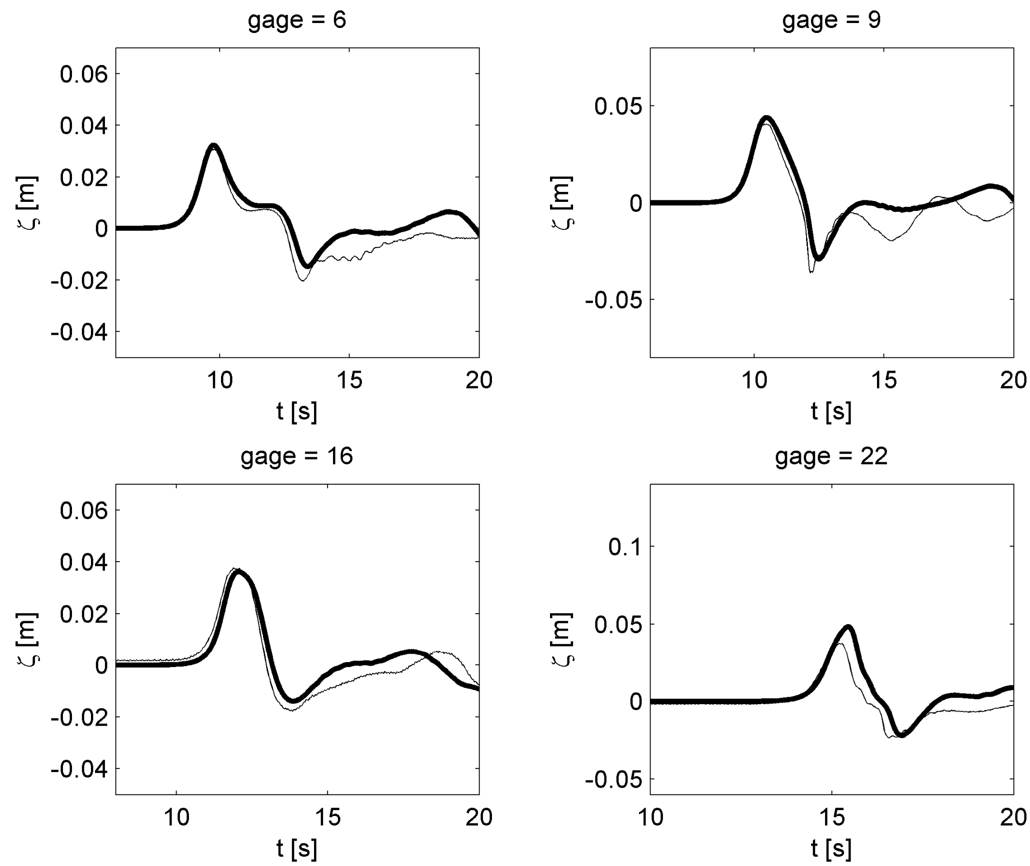

D.2.2. Timeseries Case C

Hydrostatic

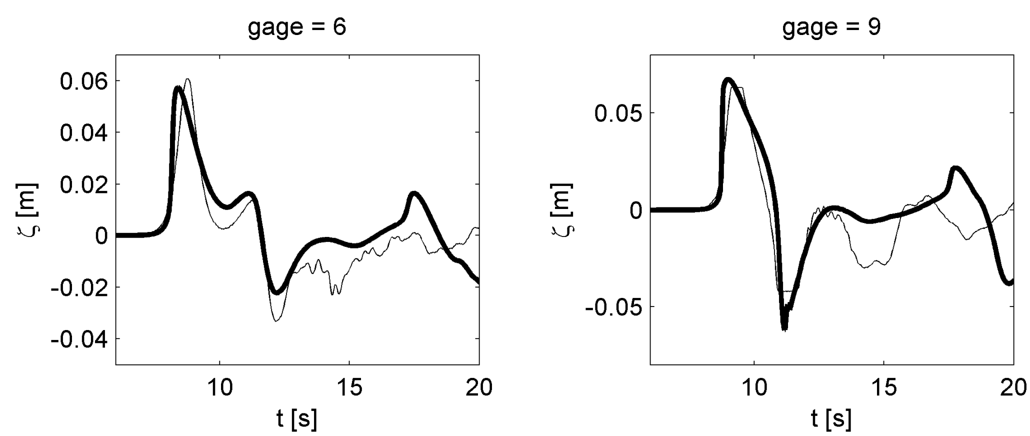

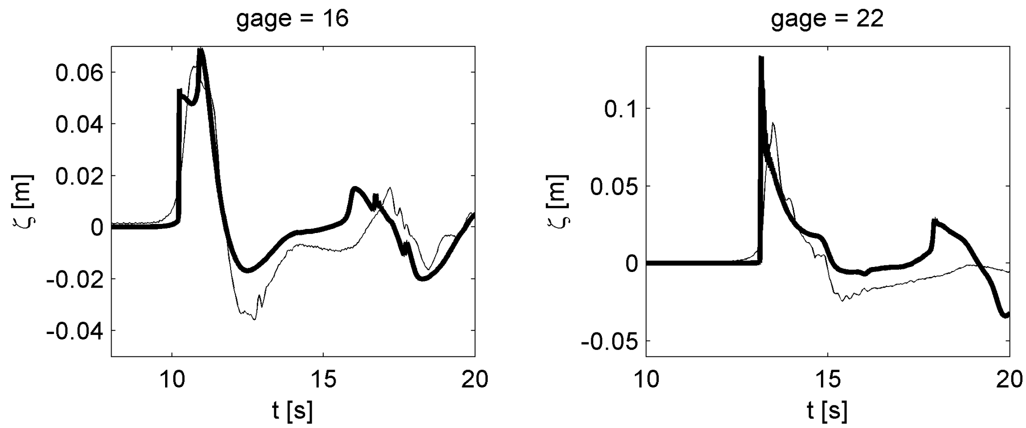

Non-hydrostatic